



# 31<sup>st</sup> Conference of the South African Society for Atmospheric Science

21 to 22 September 2015

Hennops River Valley, South Africa

***SPONSORED BY***

*UNIVERSITY OF PRETORIA*

*SOUTH AFRICAN WEATHER SERVICE*

*INTERMET AFRICA*

*NATIONAL RESEARCH FOUNDATION*

*MOMENTUM*

*CENTRE FOR HIGH PERFORMANCE COMPUTING*

All rights reserved. No part of this publication may be reproduced or copied in any form – graphic, electronic, or mechanical, including photocopying, taping, or information storage and retrieval systems – without the prior written permission of the publisher. Contact SASAS for permission pertaining to the overall collection. Authors retain their individual rights and should be contacted directly for permission to use their material separately. The manuscripts reproduced herein are a collection of refereed (conference proceedings) and unrefereed (short abstracts) presented at the 31st Conference of the South African Society for Atmospheric Science. The peer reviewed conference proceedings in this collection constitute formal publication. The index for these papers are represented by the “S” code assigned to each presentation in the programme.

Peer review conference proceedings: ISBN 978-0-620-67825-4

## FOREWORD BY THE PRESIDENT

Dear Delegates,

I welcome you to the 31th conference of the South African Society for Atmospheric Sciences. After the successful 30th conference presented by the North-West University in Potchefstroom last year it is a great pleasure to welcome you all in Lanseria in such a nice location and to be hosted by an all-female team, a first in the history of SASAS. They are Liesl Dyson from the University of Pretoria, Stephanie Landman from the South African Weather Service, Christien Engelbrecht from the Agricultural Research Council, Nita Pienaar from MMI and as a private consultant Emsie Klopper. The SASAS conference is truly international and every year we get delegates from Africa, Europe, USA, South America and Asia. This year we are for the first time going to award a medal for excellence in science, education and technology on top of the usual Stanley Jackson Award for best peer review paper and the usual best posters and best presentation awards. I remind you that the aim of SASAS is to stimulate interest and support for all branches of atmospheric sciences, to encourage research and education in the atmospheric sciences and to promote collaboration between organisations and institutions interested in atmospheric science in southern Africa. Atmospheric sciences include meteorology, agro-meteorology, climatology, air quality, ocean-atmosphere interaction, troposphere-stratosphere interaction, hydroclimatology, numerical modelling, and instrumentation. SASAS also welcome contributions from physical oceanography, applications modelling and user interactions. The conference proceedings of the conference are peer reviewed and have an ISBN number which could draw funding. Former conference papers and abstract are available on the SASAS web site. A newsletter is also produced by its members. SASAS has a web site <http://www.sasas.org.za>. At the end of the day, although we compete for grants, for discoveries, for papers, for awards, we agree or disagree on how to run things, but SASAS unites everybody and the conference is one of the longest running annual conferences in Africa. These conferences are also where we spot young talent. I encourage everybody to fill in the membership form that you will find in your bag and hand it to any of the Council members before the assembly and prize giving which I also encourage you to attend. We need to grow the Society and therefore welcome any suggestions to improve it. I also remind you that we do have a constitution that can be amended through a vote by Council. Here is your chance to change things and help the Society to progress.

Professor Mathieu Rouault

*SASAS President*

# COMMITTEES

## Event Organizing Committee

Liesl Dyson (University of Pretoria)

Christien Engelbrecht (Agricultural Research Council)

Emsie Klopper (Consultant)

Stephanie Landman (South African Weather Service)

Nita Pienaar (MMI)

*Special note of gratitude to Erik Becker for editing and compiling the reviewed and short abstracts for the conference proceedings.*

## Review Processes and Panel Members

The South African Society for Atmospheric Sciences' annual meeting provide the opportunity for scientists to publish their work in the conference proceedings. All the papers in this proceedings underwent a blind review process in order to improve quality, performance and provide credibility to the research. Each paper was send to a member of the following review panel: The reviewer's comments and authors' correspondence were addressed through a review convener. Based on the reviewer's comments, the convener decided on the acceptance or rejection of the abstracts. Only one abstract was demoted into a short non reviewed abstract.

Prof Willem Landman (Council for Scientific and Industrial Research, SA) – Review Convener

Dr Mary-Jane Bopape (University of Reading, UK)

Prof Natalie Burls (George Mason University, USA)

Dr Rebecca Garland (Council for Scientific and Industrial Research, SA)

Dr Scott Hersey (North-West University, SA and Olin College of Engineering, USA)

Dr Andries Kruger (South African Weather Service, SA)

Dr Thando Ndarana (Council for Scientific and Industrial Research, SA)

Riëtha Oosthuizen (Council for Scientific and Industrial Research, SA)

Prof George Philander (University of Princeton, USA)

Prof Stuart Piketh (University of North-West, SA)

Dr Eugene Poolman (South African Weather Service, SA)

Dr Warren Tennant (Met Office, UK)

Prof Sivakumar Venkataraman (University of KwaZulu-Natal, SA)

Prof Sue Walker (Crops for the Future Research Centre, Malaysia)

Dr Caradee Wright (South African Council for Medical Research, SA)

## **SASAS Medal Committee**

Chairman: Prof Willem Landman, CSIR

Members:

Dr Simon Mason, International Research Institute for Climate and Society, USA

Dr Babatunde Abodiun, CSAG, UCT

Dr Thando Ndrana, CSIR

Prof Stuart Piketh, School of Geo and Spatial Science, North West University

Ass. Prof Marcello Vichi, Department of Oceanography, UCT

Prof El Hassan Bencherif Universite de La Reunion

## KEY NOTE SPEAKERS

### Dr Florian Pappenberger



European Centre for Medium Range Weather Forecasts

Research Interests: Hydro-meteorology, ensemble

forecasting, uncertainty analysis

Key note: Supporting sectorial adaptation to climate change through weather forecasts and natural hazard application

E-mail: [florian.pappenberger@ecmwf.int](mailto:florian.pappenberger@ecmwf.int)

### Dr Declan Conway



Grantham Research Institute

Research interests: Water security, Adaptation and development, Water-energy-food, China, Nile Basin and Climate Change

Key Note: Climate and water resources in Africa

E-mail: [d.conway@lse.ac.uk](mailto:d.conway@lse.ac.uk)

### Dr Eugene Poolman



South African Weather Service

Research Interests: Disaster Risk Forecasting, Risk reduction, Severe Weather Forecasting, Early warning systems

Key Note: Toward impact-based early warning services: forecasting the risk of adverse societal impacts of flash floods

E-mail: [eugene.poolman@weathersa.co.za](mailto:eugene.poolman@weathersa.co.za)

**PROGRAMME: 21 September 2015**  
**Morning Sessions**

<b>REGISTRATION AND OPENING:</b>		<b>Chairperson:</b> Stephanie Landman
07:30 - 08:30	<b>Registration</b>	
08:45 - 09:00	<b>Welcome and opening:</b> SASAS President: Prof Mathieu Rouault	
<b>SESSION 1: Noteworthy Scientists - Africana</b>		<b>Chairperson:</b> Stephanie Landman
09:00 - 09:30	<b>Key Note address</b> <b>K1: Pappenberger: Supporting sectorial adaptation to climate change through weather forecasts and natural hazard application</b>	S1.1
09:30 - 09:50	<b>Rouault:</b> Origin, development and demise of a Benguela Nino in the tropical Atlantic in 2010 and 2011	S1.2
09:50 - 10:10	<b>Venkataraman:</b> A new 2-D scan portable Durban LiDAR for atmospheric studies – system description and first scientific result	S1.3
10:10 - 10:30	<b>Engelbrecht F:</b> Antarctic stratospheric ozone and seasonal predictability over southern Africa	S1.4
<b>10:30 - 11:00</b>	<b>Tea Break</b>	

<b>PARALLEL SESSION 2A: Developing scientists A - Africana</b>		<b>Chairperson:</b> Nita Pienaar
11:00 - 11:20	<b>Msomba:</b> Evaluation of the ERA Interim precipitation products over eastern Tanzania*	S2a.1
11:20 - 11:40	<b>Mpanza:</b> Comparison of January 1981 and January 2014 cut-off low pressure systems*	S2a.2
11:40 - 12:00	<b>Van Loggerenberg:</b> Microstructure of rainfall events on the southern African Highveld *	S2a.3
12:00 - 12:20	<b>Hauptfleisch:</b> Evaluating a rain gauge network's ability to characterize the spatial variability of rainfall *	S2a.4
12:20 - 12:40	<b>Swart:</b> Effect of meteorological factors and emission reduction on pollution in the Vaal Triangle Airshed priority area *	S2a.5
12:40 - 13:00		
<b>13:00 - 14:00</b>	<b>Lunch</b>	

<b>PARALLEL SESSION 2B: Developing scientists B - Marlotti</b>		<b>Chairperson:</b> Dawn Mahlobo
11:00 - 11:20	<b>Guehaz:</b> Demonstrating LiDAR technique on forest fire detection in Algiers and Durban: A preliminary study *	S2b.1
11:20 - 11:40	<b>Mulumba:</b> Climate change impact on contributing tropospheric ozone sources over in southern Africa and the adjacent Indian Ocean Islands *	S2b.2
11:40 - 12:00	<b>Ogunniyi:</b> Temporal variation in solar radiation, UV index and its effect on ozone variations over Durban, South Africa – initial result *	S2b.3
12:00 - 12:20	<b>Shikwambana:</b> Five year climatological trends of AOD over coastal and inland towns of South Africa retrieved by MODIS *	S2b.4
12:20 - 12:40	<b>Sovara:</b> Simulations of the meridional overturning circulation using the parallel cubic ocean model (PCOM): The spin-up phase *	S2b.5
12:40 - 13:00	<b>Schilperoort:</b> The effect of the Agulhas current on SAR derived wind fields *	S2b.6
<b>13:00 - 14:00</b>	<b>Lunch</b>	

\*Indication of student presentation

**PROGRAMME: 21 September 2015**  
**Afternoon Sessions**

<b>SESSION 3: Recent doctorates - Africana</b>		<b>Chairperson:</b> Christien Engelbrecht
	<b>Key Note address</b>	
14:00 - 14:30	<b>K2: Poolman: Towards impact-based early warning services: forecasting the risk of adverse societal impacts of flash floods</b>	S3.1
14:30 - 14:50	<b>Dieppois:</b> Decadal variability of summer southern African rainfall	S3.2
14:50 - 15:10	<b>Gierens/Josipovic:</b> Observing the atmospheric boundary layer structure over the Highveld using a ceilometer	S3.3
15:10 - 15:30	<b>Malherbe:</b> Acknowledging decadal to intraseasonal variability in support of agriculture – the 2014/15 maize production season	S3.4
15:30 - 15:50	<b>Adesina:</b> Variability of aerosol optical depth over Richard’s Bay (South Africa) based on MODIS, OMI satellite and GOCART model measurements	S3.5
15:50 – 16:10	<b>Longandjo:</b> Toward better understanding of interannual rainfall variability over central Africa and its relation with its surrounding tropical oceans	S3.6
<b>16:10 – 16:30</b>	<b>Tea</b>	

<b>Session 4: Immanent doctorates - Africana</b>		<b>Chairperson:</b> Lynette van Schalkwyk
16:30 - 16:50	<b>Mkhwazi:</b> Downscaled climate change projections over northeastern South Africa: Implications for streamflow	S4.1
16:50 - 17:10	<b>Ngwana:</b> Predictability of synoptic types over southern Africa	S4.2
17:10 - 17:30	<b>Nkoana:</b> Last glacial maximum simulations over southern Africa using a variable-resolution global model: synoptic-scale verification	S4.3
17:30 - 17:50	<b>Engelbrecht C:</b> Seasonal forecasting of synoptic type variability: potential intraseasonal predictability relevant to the Cape south coast of South Africa	S4.4
17:50 - 18:10	<b>Mphesha:</b> Predicting the extreme 2015/16 El Nino event	S4.5
<b>18:10 - 19:00</b>	<b>Posters viewing - Africana</b>	
<b>19:00</b>	<b>SASAS CONFERENCE BANQUET</b>	

**PROGRAMME: 21 September 2015**  
**Poster Presentations**

Student	Main Author	Title
	<b>Adesina</b>	Study of aerosol indirect effect and its impact over a coastal city on South Africa
*	<b>Beraki</b>	Recent developments on the SAWS seasonal forecast suite
	<b>Bulo</b>	The impact of storms in our society, impact mitigation
*	<b>Claassen</b>	Describing the life cycle of the continental tropical low that caused heavy rainfall over the eastern parts of South Africa in January 2013
	<b>Coetzee</b>	The Dobson Spectrophotometers from the South African Weather Service: 25 Years of atmospheric total column ozone monitoring
*	<b>De Wit</b>	Analysis of anomalous propagation conditions affecting the S-band Doppler radar at the Irene weather station.
*	<b>Engelbrecht E</b>	Utilizing standardized anomalies to predict rare synoptic scale events over South Africa
*	<b>Fourie</b>	Causal Factors related to peak solar UVR readings at De Aar, Northern Cape, South Africa
	<b>Garland</b>	Modelled southern African biomass burning aerosol particle transport and recirculation over the southern Atlantic Ocean
*	<b>Hamad</b>	Evaluation of the performance of CORDEX- Regional Climate Models on simulating extreme rain events in Tanzania
*	<b>Harvey</b>	Volcanic Forcing: new initiatives to establish its impacts on climates of the Southern Hemisphere
*	<b>Hughes</b>	Forecasting the local-scale lower tropospheric convection
*	<b>Ingram</b>	Sounding parameters associated with significant amounts of hail claims over the Gauteng Province during 2006-2014
*	<b>Khwashaba</b>	Vulnerability and resilience in the Mopani District Municipality in a changing climate
*	<b>Kijazi</b>	Verification of conformal cubic atmospheric model seasonal forecasts
	<b>Landman S</b>	Can home-based weather observations be reliable?
*	<b>Malekela</b>	The impact of ozone depletion on the kinetic energy aspects of the Lorenz energy cycle of the Southern Hemisphere
*	<b>Maluleke</b>	Estimating a dynamically adjusted Carrying Capacity Output for Limpopo Province using seasonal forecasts and remote sensing products
*	<b>Middleton</b>	Investigating Severe Convective Storm Environments over southern Africa
*	<b>Mosha</b>	Evaluation of regional Unified model over Tanzania
	<b>Muthige</b>	Impacts of spectral nudging on the simulation of present-day rainfall patterns over southern Africa
*	<b>Nchabeleng</b>	Calculation of the Air Pollution concentration field from the Industrial Emission Sources in North West Province
	<b>Ndarana</b>	Numerical agroweather prediction
	<b>Olivier</b>	The Intertropical Convergence Zone and its association with seasonal southern African rainfall
*	<b>Senyagwa</b>	Bias-correction of satellite precipitation products based on probability distributions with application in hydrometeorology
*	<b>Sibiya</b>	Spatial and Temporal distribution of O <sub>3</sub> Pollutant Concentration over South Africa as Predicted by the NAME III Modelling System
*	<b>Smith</b>	Analysis of SO <sub>2</sub> , CO and PM <sub>10</sub> levels at Welgegund station in 2011 and 2013
*	<b>Tongwane</b>	Estimation of reference evapotranspiration in the northeastern region of the Free State Province, South Africa
*	<b>Vogel</b>	Using benzene/toluene ratios as a means for tracing vehicular emissions
	<b>Waagsaether</b>	Climate information websites – what information is out there and how is it delivered?
	<b>Wolski</b>	Accounting for heterogeneity in spatial correlation of climate fields in optimization of country-scale climatological network
	<b>Xulu</b>	Formation and propagation of landfalling tropical cyclones over the Southwest Indian Ocean: 1960-2012

\*Indication of student poster

## PROGRAMME : 22 September 2015

<b>SESSION 5: Striking Scientists - Africana</b>		<b>Chairperson:</b> Coleen Vogel
08:30 - 9:00	<b>Key Note address</b> <b>K3: Conway: Climate variability and water resources in Africa</b>	S5.1
09:00 - 09:20	<b>Landman:</b> Ranking seasonal rainfall forecast skill of emerging and developing economies	S5.2
09:20 - 9:40	<b>Pegram:</b> Comparing interpolated daily gauge rainfall over RSA with TRMM to determine possible bias correction for hydrological applications	S5.3
09:40 - 10:00	<b>Moeletsi:</b> Weather effects on maize production in the eastern Free State: Case study of the 2013/14 and 2014/15 agricultural seasons	S5.4
10:00 - 10:20	<b>Wright:</b> Solar UVR instrument inter-comparison focussing on measurement interval recording setting and solar zenith angle as important factors	S5.5
<b>10:20 - 10:50</b>	<b>TEA BREAK</b>	

<b>SESSION 6: Young scientists - Africana</b>		<b>Chairperson:</b> Rebeca Garland
10:50 - 11:10	<b>Phakula:</b> Predictability of the intra-seasonal rainfall characteristics variables over South Africa	S6.1
11:10 - 11:30	<b>Dedekind:</b> High resolution rainfall modelling over the eastern escarpment of South Africa	S6.2
11:30- 11:50	<b>Gijben:</b> A lightning threat index for South Africa using numerical weather prediction data	S6.3
11:50 - 12:10	<b>Ramkilowan:</b> Application of a commercial Lidar-ceilometer to studies of aerosols in the atmospheric boundary layer	S6.4
12:10 - 12:30	<b>Mahlobo:</b> A local diagnosis of the Hadley circulation over South Africa	S6.5
12:30 - 12:50	<b>Pienaar:</b> Atmospheric anomalies during the 2012/13 extreme hail season over Gauteng	S6.6
<b>12:50 – 13:40</b>	<b>LUNCH</b>	

<b>SESSION 7: Health scientists - Africana</b>		<b>Chairperson:</b> Caradee Wright
13:40 - 14:00	<b>Albers:</b> Solar ultraviolet radiation levels measured under umbrellas in relation to ambient conditions and sun angle	S7.1
14:00 - 14:20	<b>Oosthuizen:</b> From a historical journey of air pollution to responsible choices that will mitigate climate change and improve the health of the nation	S7.2
14:20 - 14:40	<b>John:</b> Understanding of extreme temperature events by environmental health stakeholders in South Africa	S7.3

<b>14:50 - 16:00</b>	<b>Prize giving and SASAS ANNUAL GENERAL MEETING</b>
<b>16:00</b>	<b>THANKS AND FAREWELL -</b>
<b>16:00 – 16:30</b>	<b>Tea and Game viewing</b>

## AUTHOR INDEX

Surname	Name	Affiliation	Email	Abstract Nr
<b>A</b>				
Abiodun	Babatunde	UCT	<a href="mailto:babiodun@csag.uct.ac.za">babiodun@csag.uct.ac.za</a>	
Adesina	Joseph	UKZN	<a href="mailto:jadesina173@gmail.com">jadesina173@gmail.com</a>	S3.5
Albers	Patricia	SA MRC	<a href="mailto:palbers@mrc.ac.za">palbers@mrc.ac.za</a>	S7.1
<b>B</b>				
Beraki	Asmerom	SAWS	<a href="mailto:asmerom.beraki@weathersa.co.za">asmerom.beraki@weathersa.co.za</a>	
Bulo	Bubele	SAWS	<a href="mailto:Bubele.bulo@weathersa.co.za">Bubele.bulo@weathersa.co.za</a>	
<b>C</b>				
Claassen	Elani	UP	<a href="mailto:claassen.elani@hotmail.com">claassen.elani@hotmail.com</a>	
Coetzee	Gerrie	SAWS	<a href="mailto:gerrie.coetzee@weathersa.co.za">gerrie.coetzee@weathersa.co.za</a>	
Conway	Declan	GRI	<a href="mailto:d.conway@lse.ac.uk">d.conway@lse.ac.uk</a>	S5.1
<b>D</b>				
De Wit	Jaco	UP	<a href="mailto:frodjabulani@yahoo.com">frodjabulani@yahoo.com</a>	
Dedekind	Zane	CSIR	<a href="mailto:zdedekind@csir.co.za">zdedekind@csir.co.za</a>	S6.2
Dieppoiss	Bastien	Coventry Univ, UK	<a href="mailto:Bastien.dieppoiss@gmail.com">Bastien.dieppoiss@gmail.com</a>	S3.2
Djolov	Georges-Noel	UP	<a href="mailto:george.djolov@up.ac.za">george.djolov@up.ac.za</a>	
Duba	Thama	DUT	<a href="mailto:thamadub@dut.ac.za">thamadub@dut.ac.za</a>	
Dyson	Liesl	UP	<a href="mailto:liesl.dyson@up.ac.za">liesl.dyson@up.ac.za</a>	
<b>E</b>				
Engelbrecht	Francois	CSIR	<a href="mailto:fengelbrecht@csir.co.za">fengelbrecht@csir.co.za</a>	S1.4
Engelbrecht	Edward	UP	<a href="mailto:ehengelbrecht@gmil.com">ehengelbrecht@gmil.com</a>	
Engelbrecht	Christien	UP	<a href="mailto:c10.engelbrecht@gmail.com">c10.engelbrecht@gmail.com</a>	S4.4
<b>F</b>				
Fourie	Celeste	UP	<a href="mailto:Lilafourie18@gmail.com">Lilafourie18@gmail.com</a>	
<b>G</b>				
Garland	Rebecca	CSIR	<a href="mailto:RGarland@csir.co.za">RGarland@csir.co.za</a>	
Gijben	Morné	UP	<a href="mailto:morne.gijben@weathersa.co.za">morne.gijben@weathersa.co.za</a>	S6.3
Griffith	Derek	CSIR/DPSS	<a href="mailto:dgriffith@csir.co.za">dgriffith@csir.co.za</a>	
Guehaz	Riad	UKZN	<a href="mailto:rguehaz@cdta.dz">rguehaz@cdta.dz</a>	S2b.1
<b>H</b>				
Hamad	Asya	UP	<a href="mailto:asyooo@yahoo.com">asyooo@yahoo.com</a>	
Henrikson	Svante	NWU PUKKE	<a href="mailto:Svante.henriksson@fmi.fi">Svante.henriksson@fmi.fi</a>	
Harvey	Pamela	WITS	<a href="mailto:pamjharvey14@gmail.com">pamjharvey14@gmail.com</a>	
Hauptfleisch	Reinhardt	NWU PUKKE	<a href="mailto:22449345@nwu.ac.za">22449345@nwu.ac.za</a>	S2a.4
Hughes	Rebekah	UCT	<a href="mailto:beckyhugs@gmail.com">beckyhugs@gmail.com</a>	
<b>J</b>				
John	Juanette	CSIR	<a href="mailto:jjohn@csir.co.za">jjohn@csir.co.za</a>	S7.3
Josipovic	Micky	NWU PUKKE	<a href="mailto:Micky.Josipovic@nwu.ac.za">Micky.Josipovic@nwu.ac.za</a>	S3.3
<b>K</b>				
Khwashaba	Marubini	None	<a href="mailto:marubinikh@gmail.com">marubinikh@gmail.com</a>	
Kijazi	Lawrence	UP	<a href="mailto:Martin.kijazi@yahoo.com">Martin.kijazi@yahoo.com</a>	
Klopper	Emsie	UP	<a href="mailto:emsie@lawwindow.co.za">emsie@lawwindow.co.za</a>	
<b>L</b>				
Landman	Stephanie	SAWS	<a href="mailto:stephanie.landman@weathersa.co.za">stephanie.landman@weathersa.co.za</a>	

Landman	Willem	CSIR	<a href="mailto:WALandman1981@gmail.com">WALandman1981@gmail.com</a>	S5.2
Longandjo	Georges-Noel	UCT	<a href="mailto:gntiers@gmail.com">gntiers@gmail.com</a>	S3.6
Lotter	Daleen	CSIR	<a href="mailto:dlotter@csir.co.za">dlotter@csir.co.za</a>	
<b>M</b>				
Mahlobo	Dawn	SAWS	<a href="mailto:Dawn.mahlobo@weathersa.co.za">Dawn.mahlobo@weathersa.co.za</a>	S6.5
Malekela	Charles	UP	<a href="mailto:cosbyjohnson@yahoo.com">cosbyjohnson@yahoo.com</a>	
Malherbe	Johan	ARC	<a href="mailto:johan@arc.agric.za">johan@arc.agric.za</a>	S3.4
Maluleke	Phumzile	UP / ARC	<a href="mailto:malulekep@arc.agric.za">malulekep@arc.agric.za</a>	
Mazibuko	Sabelo	ARC	<a href="mailto:mazibukosm@arc.agric.co.za">mazibukosm@arc.agric.co.za</a>	
Middleton	Coleen	UCT	<a href="mailto:col_mid@mweb.co.za">col_mid@mweb.co.za</a>	
Mkhwanazi	Musa	SAWS	<a href="mailto:musa.mkhwanazi@weathersa.co.za">musa.mkhwanazi@weathersa.co.za</a>	S4.1
Moeletsie	Mokhele	ARC	<a href="mailto:moeletsim@arc.agric.za">moeletsim@arc.agric.za</a>	S5.4
Mosha	Nestory	UP	<a href="mailto:nestorymosha@yahoo.com">nestorymosha@yahoo.com</a>	
Mpanza	Msawenkosi	UP	<a href="mailto:thbms17@gmail.com">thbms17@gmail.com</a>	S2a.2
Mpheshea	Lerato	CSIR	<a href="mailto:lmpheshea@csir.co.za">lmpheshea@csir.co.za</a>	S4.5
Msomba	Elewa	UP	<a href="mailto:korrosso@yahoo.com">korrosso@yahoo.com</a>	S2a.1
Mulumba	Jean Pierre	UKZN	<a href="mailto:204517461@stu.ukzn.ac.za">204517461@stu.ukzn.ac.za</a>	S2b.2
Muthige	Muvhungu	CSIR	<a href="mailto:mmuthige@csir.co.za">mmuthige@csir.co.za</a>	
<b>N</b>				
Nchabeleng	Precious	UP	<a href="mailto:nchabeleng.precious@yahoo.com">nchabeleng.precious@yahoo.com</a>	
Ndarana	Thando	CSIR	<a href="mailto:tndarana@csir.co.za">tndarana@csir.co.za</a>	
Ngwana	Isaac	SAWS	<a href="mailto:isaac.ngwana@weathersa.co.za">isaac.ngwana@weathersa.co.za</a>	S4.2
Nkoana	Ramapulana	CSIR NMMU	<a href="mailto:rnkoana@csir.co.za">rnkoana@csir.co.za</a>	S4.3
<b>O</b>				
Ogunniyi	Jeremiah	UKZN	<a href="mailto:jerryogunniyi@yahoo.com">jerryogunniyi@yahoo.com</a>	S2b.3
Olivier	Cobus	SAWS	<a href="mailto:cobus.olivier@weathersa.co.za">cobus.olivier@weathersa.co.za</a>	
Oosthuizen	Riëtha	CSIR	<a href="mailto:roosthui@csir.co.za">roosthui@csir.co.za</a>	S7.2
<b>P</b>				
Pappenberger	Florian	ECMWF	<a href="mailto:Florian.pappenberger@ecmwf.int">Florian.pappenberger@ecmwf.int</a>	S1.1
Pegram	Geoffrey	Pregram & Ass	<a href="mailto:pegam@ukzn.ac.za">pegam@ukzn.ac.za</a>	S5.3
Phakula	Steven	SAWS	<a href="mailto:stevenphakula@weathersa.co.za">stevenphakula@weathersa.co.za</a>	S6.1
Pienaar	Nita	Momentum	<a href="mailto:npienaar@momentum.co.za">npienaar@momentum.co.za</a>	S6.6
Poolman	Eugene	SAWS	<a href="mailto:Eugene.poolman@weathersa.co.za">Eugene.poolman@weathersa.co.za</a>	S3.1
<b>R</b>				
Ramkilowan	Arshath	CSIR/DPSS	<a href="mailto:aramkilowan@csir.co.za">aramkilowan@csir.co.za</a>	S6.4
Reasson	Chris	UCT	<a href="mailto:chris.reason@uct.ac.za">chris.reason@uct.ac.za</a>	
Rouault	Mathieu	UCT	<a href="mailto:Mathieu.Rouault@uct.ac.za">Mathieu.Rouault@uct.ac.za</a>	S1.2
<b>S</b>				
Schilperoort	Daniel	UCT	<a href="mailto:schdano23@myuct.ac.za">schdano23@myuct.ac.za</a>	S2b.6
Senyagwa	Rose	UP	<a href="mailto:kerinseny@yahoo.com">kerinseny@yahoo.com</a>	
Shikwambana	Lerato	UKZN	<a href="mailto:lshikwambana@gmail.com">lshikwambana@gmail.com</a>	S2b.4
Sibiya	Bheki	CSIR	<a href="mailto:Bsibiya@csir.co.za">Bsibiya@csir.co.za</a>	
Smith	Lauren	UP	<a href="mailto:smith.lauren16@gmail.com">smith.lauren16@gmail.com</a>	
Sovara	Mthetho	CSIR	<a href="mailto:mvsovara@gmail.com">mvsovara@gmail.com</a>	S2b.5
Swart	Anzel	UP	<a href="mailto:anzelswart44@gmail.com">anzelswart44@gmail.com</a>	S2a.5
Sweijd	Neville	CSIR	<a href="mailto:nsweijd@access.ac.za">nsweijd@access.ac.za</a>	
<b>T</b>				
Tongwane	Mphethe	ARC	<a href="mailto:tongwanem@arc.agric.za">tongwanem@arc.agric.za</a>	

**V**

van

Loggerenberg	Juan	NWU PUKKE	<a href="mailto:21714355@nwu.ac.za">21714355@nwu.ac.za</a>	S2a.3
van Schalkwyk	Lynette	eNews	<a href="mailto:lynvanschalkwyk@gmail.com">lynvanschalkwyk@gmail.com</a>	
van der Merwe	Kobus	CSIR	<a href="mailto:jhvdmerwe@csir.co.za">jhvdmerwe@csir.co.za</a>	
Venkataraman	Sivakumar	UKZN	<a href="mailto:venkataramans@ukzn.ac.za">venkataramans@ukzn.ac.za</a>	S1.3
Vogel	Coleen	WITS	<a href="mailto:Coleen.vogel@gmail.com">Coleen.vogel@gmail.com</a>	
Vogel	Aileen	TUT	<a href="mailto:vogela@tut.ac.za">vogela@tut.ac.za</a>	

**W**

Waagsaether	Katinka	CSAG	<a href="mailto:katinka@csag.uct.ac.za">katinka@csag.uct.ac.za</a>	
Wolski	Piotr	CSAG UCT	<a href="mailto:wolski@csag.uct.ac.za">wolski@csag.uct.ac.za</a>	
Wright	Caradee	SA MRC	<a href="mailto:cwright@mrc.ac.za">cwright@mrc.ac.za</a>	S5.5

# Study of aerosol indirect effect and its impact on precipitation over a coastal city in South Africa

Joseph A. Adesina<sup>1\*</sup>, V. Sivakumar<sup>1</sup>, Kanike R. Kumar<sup>2</sup>, Jeremiah A. Ogunniyi<sup>1</sup>, Priyanka Singh<sup>1</sup>

<sup>1</sup>Discipline of Physics, School of Chemistry and Physics, College of Agriculture, Engineering and Science, Westville Campus, University of KwaZulu-Natal, Durban 4000, South Africa.

<sup>2</sup>Key Laboratory for Aerosol-Cloud-Precipitation of China Meteorological Administration, School of Atmospheric Physics, Nanjing University of Information Science and Technology, Nanjing 210044, Jiangsu, China

\*corresponding author: [jadesina173@gmail.com](mailto:jadesina173@gmail.com)

## Abstract

The indirect effect of anthropogenic aerosols on cloud is such that it modifies cloud albedo and cloud lifetime and can sometimes lead to suppression of precipitation. This study based on three years data (2010 – 2012) reveals that high aerosol optical depth (AOD) does significantly affect the cloud and the precipitation pattern over the study location. Its effect on the selected cloud parameters showed that aerosol has a strong negative correlation with cloud effective radius (CER), cloud optical depth (COD) and cloud fraction (CF), having correlation coefficient R equals -0.85, -0.85, -0.99 respectively and its decrease causes an appreciable increase in rainfall over Durban.

Key Words: Aerosol Index, Cloud optical depth, Cloud effective radius, Aerosol optical depth, Rainfall

## I. Introduction

The role aerosol plays in climate change has become a point of focus in atmospheric science and in meteorology in particular. These aerosols which come from both natural and anthropogenic origin have direct effect on earth's radiation budget by causing scattering and absorption of incoming solar radiation and indirect effect by modification of the radiative properties of the cloud through altering the cloud microphysical properties (Gunaseelan et al., 2014). Due to rain wash out, gravitational settling, etc., the lifetime of tropospheric aerosol is very short. This study is intended to find how aerosol optical depth (AOD) is associated with precipitation and cloud parameters over Durban (29°57'S, 30°56'E, 8 m), South Africa using three years of dataset. Durban has a hot Mediterranean/ dry-summer subtropical climate (Köppen-Geiger classification: Csa) that is mild with moderate seasonality. Summers are dry and hot due to the domination of subtropical high pressure systems; while winters experience moderate temperatures and changeable rainy weather due to the polar front. The study first consider aerosols effect on cloud and then on rainfall. A major limitation of the study is that it does not separate the effect of

meteorology from aerosol-induced effect.

## II. Dataset

The parameters AOD<sub>550</sub>, Angstrom exponent (AE), cloud optical depth (COD), and cloud effective radius (CER) are retrieved from the monthly MOD08\_M3.051 Terra MODIS (Moderate resolution imaging spectroradiometer) Level 3 gridded at 1° × 1° product for the period of January 2010 to December 2012. The estimated uncertainty of the MODIS AOD product was reported to be ±0.05 ±0.15 (±mean±SD) over land (Remer et al., 2005). Aerosol index (AI), which gives more weight between the most cloud effective particles and aerosol fine mode (than AOD alone) was derived from the product of AOD and AE (Constantino and Breon, 2012). The Tropical Rainfall Measuring Mission monthly TRMM\_3B43\_ACC.007 accumulated rain [mm] data using the time series download at (1° × 1°) resolutions from 2010-2012 are used in this study to examine the relationship between AOD and rainfall.

## III. Results and Discussion

### a. AOD and Cloud parameters

Twomey's theory suggests a direct modification of cloud

microphysics when decrease in CER causes increase in AI. The modification causes a decrease of the cloud droplet mean size as aerosol particles interacts with the cloud acting as cloud condensation nuclei (CCN) (Lohmann and Lesins, 2002; Twomey et al., 1984). In Fig 1a we considered two periods one from January-December (the whole data) and the period when high values of AOD were noticed. This is from August to October every year and these high values correspond to the biomass season in South Africa. The linear correlation using Pearson's correlation coefficient between CER and AI for January to December was - 0.16 but when high aerosol loading period (August to October) was considered the value was - 0.86 which was a very strong negative correlation in contrast to that of the whole data. The impact of aerosol on CER can be quantified by the linear regression slope of the CER-AI log-log relationship (Costantino and Bréon, 2012). The best fit slope of the linear regression between CER and AI for all the months was - 19 but when only the high aerosol months was considered it was - 0.18 giving a significant change of a ratio of about 23 times. In Fig 1b the correlation between AI and COD for all the months was 0.33 but for the high aerosol months it was -0.86 showing that for the high AOD period there was a significant impact of AOD on COD. When aerosol are mixed and interacting with cloud, the slope of COD and AI is particularly small and slightly negative but when the layers are well separated the slope though may be small but is positive (Costantino and Bréon, 2012). Thus during the high AOD period, aerosol is mixed and interacting with the cloud as the slope is negative (- 8.9) while it seems that generally in many months they are well separated as the linear regression slope was positive (10). In Fig 1c the correlation of CF with AI is 0.2 for the whole data and -0.99 for the period of high AOD while the linear regression slope goes from 0.2 for the whole data to - 0.5 for the months of high AOD. Although the positive relationship between CF-AI has not been fully explained in literature, some explanations have been proffered like the increase in aerosol concentration as a result of low tropospheric stability and secondly that when precipitation is

suppressed by cloud active aerosols, longer-lived clouds results but the negative relationship is seen as aerosol located within well-mixed boundary layer causing a decrease both in cloud liquid water path and cloud fraction due to large simulation of stratocumulus clouds (Costantino and Bréon, 2012).

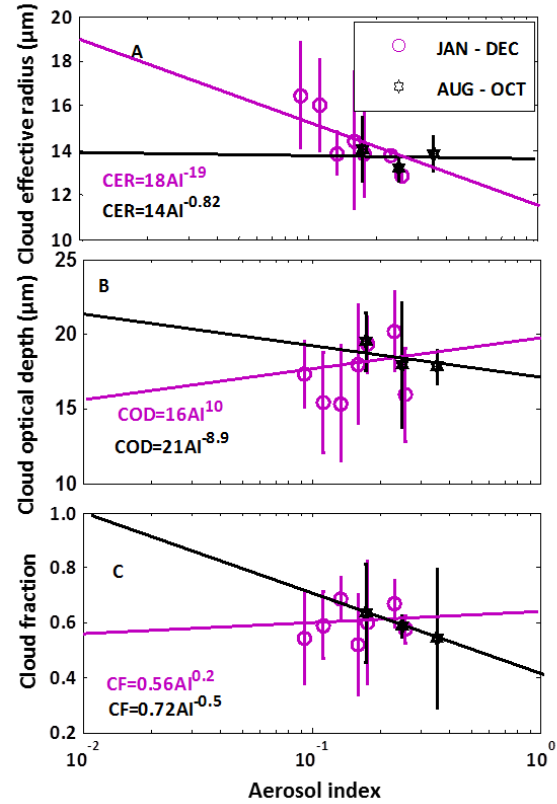


Fig 1: Cloud parameters averaged over constant bin of Aerosol Index (AI) represented with the standard deviations in log-log scale over Durban. The purple plot is averaged data for all the months during entire study period (2010–2012), while the black is averaged over August–October only during 2010–2012 to study the case high aerosol loading.

#### b. AOD and Rainfall

The effect of aerosol on cloud-droplet number concentration is termed the first indirect effect while the suppression of rainfall due to increase in anthropogenic aerosol is called the second indirect effect (Rotstayn et al., 2000). We now proceed to study this second indirect effect. In fig 2a AOD showed a decreasing trend of  $-0.00015/\text{month}$  over the study period. Highest values of AOD occurred in 2010 and lower values in 2011 and 2012. Rainfall on the other hand showed an

increasing trend of 2.2/month over the study period with low values in 2010 but high values in 2011 and 2012. Fig 2b shows the variation of AOD with rainfall for the months which are generally of high values (August – October) of the years under study. It is seen that high AOD values generally goes with low rainfall. Table 1 gives the statistical relationship between these two quantities using Pearson correlation coefficient. In 2010 the average AOD for (Jan – Dec) was  $0.14\pm 0.06$  and the total rainfall was 651.5 mm, the correlation coefficient (R) between AOD and Rainfall was - 0.22. The average AOD value for Aug – Oct was  $0.24\pm 0.03$  and R was - 0.62, but  $R^2$  which is the coefficient of determination indicated that the decrease in rainfall was due to other factors and not particularly AOD. It is most likely that the low rainfall for this year was due to other meteorological factors like temperature, relative humidity, wind speed etc. In 2011, yearly average AOD was  $0.11\pm 0.03$  and the total rainfall was 1144.7 mm. R value for that year was - 0.27 and the R value for Aug – Oct of same year with average AOD of  $0.15\pm 0.04$  was - 0.85.  $R^2$  indicated that 46% of the factors responsible for the strong negative correlation to the rainfall can be explained by the decrease in the AOD i.e. low AOD was partly responsible for the increase in Rainfall. In 2012, average AOD was  $0.12\pm 0.05$  and total rainfall was 1150 mm. R was - 0.12 considering the whole year but for Aug - Oct with AOD of  $0.17\pm 0.04$  R was - 0.89 and again  $R^2$  indicated that 58% of the factor responsible for the increase in rainfall was the AOD. When the three years was considered together, R for the whole data was - 0.16 and for August to October it was - 0.49 with  $R^2$  showing that about 13% of the factor responsible for the correlation being the effect of AOD. It is well to note that whenever the whole data was been considered, apart from the poor correlation between AOD and rainfall,  $R^2$  indicated for all the years that the relationship cannot be explained by changes in AOD. Generally, it was discovered that aerosols can either suppress or favor rainfall depending on aerosol types. Aerosols that are hygroscopic tend to enhance cloud formation and consequently favor rainfall while those that hydrophobic suppress rainfall since

they are not good enough for cloud condensation nuclei (Gunaseelan et al., 2014).

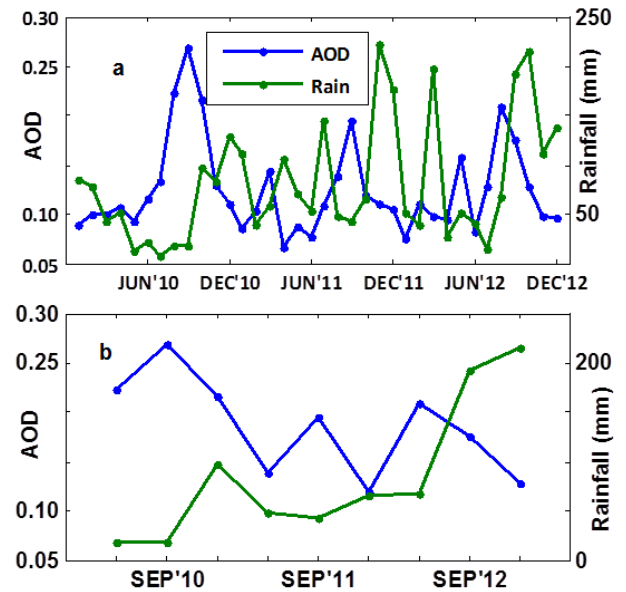


Fig 2 Monthly variations of aerosol optical depth with rainfall over Durban for (a) January 2010 to December 2012 and (b) August to October for 2010, 2011 and 2012.

Table 1 showing the statistical relationship between AOD and Rainfall over Durban for 2010-2012

Year	JAN-DEC				AUG-OCT			
	AOD	Rain (mm)	R	$R^2$	AOD	Rain (mm)	R	$R^2$
2010	$0.14\pm 0.06$	651.5	-0.22	-0.05	$0.24\pm 0.03$	134.4	-0.62	-0.22
2011	$0.11\pm 0.03$	1144.7	-0.27	-0.01	$0.15\pm 0.04$	157	-0.85	0.46
2012	$0.12\pm 0.04$	1150.1	-0.12	-0.08	$0.17\pm 0.04$	475.4	-0.89	0.58
2010-2012	$0.12\pm 0.05$	2946.3	-0.16	0.00	$0.19\pm 0.05$	766.8	-0.49	0.13

#### IV. Conclusion

Aerosol indirect effect over Durban has been studied from three years data (2010 – 2012), the effect of aerosols on cloud properties is seen to be significant during high aerosol regime. Considering the relationship between Aerosol index and cloud parameters, it was shown that aerosol caused modification of cloud microphysics and decrease in cloud fraction as it is well mixed and interacting with the cloud. The effect on rainfall was such that the decrease in AOD causes its increase so that while AOD had a negative trend over the study period, rainfall had a positive trend.

## V. Acknowledgement

The authors are thankful to NASA for providing MODIS satellite data and TRMM rainfall data from Giovanni website (<http://disc.sci.gsfc.nasa.gov/>). We want to thank the reviewer of the paper for the comments which contributed to the improvement of the paper.

## References

- Costantino, L. and Bréon, F.-M. (2012). Aerosol indirect effect on warm clouds over South-East Atlantic, from co-located MODIS and CALIPSO observations. *Atmospheric Chemistry & Physics Discussions*, 12, 14197-14246.
- Gunaseelan, I., Bhaskar, B. V. and Muthuchelian, K. (2014). The effect of aerosol optical depth on rainfall with reference to meteorology over metro cities in India. *Environmental Science and Pollution Research*, 21(13), 8188-8197.
- Lohmann, U. and Lesins, G. (2002). Stronger constraints on the anthropogenic indirect aerosol effect. *Science*, 298(5595), 1012-1015.
- Remer, L. A., Kaufman, Y., Tanré, D., Mattoo, S., Chu, D., Martins, J. V., Li, R.-R., Ichoku, C., Levy, R. and Kleidman, R. (2005). The MODIS aerosol algorithm, products, and validation. *Journal of the atmospheric sciences*, 62(4), 947-973.
- Rotstayn, L. D., Ryan, B. F. and Penner, J. E. (2000). Precipitation changes in a GCM resulting from the indirect effects of anthropogenic aerosols. *Geophysical Research Letters*, 27(19), 3045-3048.
- Twomey, S. A., Piegrass, M. and Wolfe, T. (1984). An assessment of the impact of pollution on global cloud albedo. *Tellus B*, 36(5), 356-366.

## Supporting sectorial adaptation to climate change through weather forecasts and natural hazard applications

Florian Pappenberger<sup>1,\*</sup>, Rebecca Emerton<sup>1,2</sup>, Di Francesca Giuseppe<sup>1</sup>, Jesus San-Miguel<sup>3</sup>, Hannah L. Cloke<sup>2</sup>, Vera Thiemi<sup>3</sup>, Feyera A. Hirpa<sup>3</sup>, Fredrik Wetterhall<sup>1</sup>, Emmanuel Dutra<sup>1</sup>, Paul J. Smith<sup>1</sup>, Ervin Zsoter<sup>1</sup>, Louise Arnal<sup>1,2</sup>, Callum Baugh<sup>1</sup>, Elisabeth Stephens<sup>2</sup>, Peter Salamon<sup>3</sup>, Juergen Vogt<sup>3</sup>, Paulo Barbosa<sup>3</sup>, Christophe Lavaysse<sup>3</sup>, Beatriz Revilla-Romero<sup>3,4</sup>, Thomas Petrolia<sup>3</sup>, Giorgio Liberta<sup>3</sup>, Jutta Thielen<sup>3</sup>

<sup>1</sup>European Centre for Medium Range Weather Forecasts, Reading, UK

<sup>2</sup>University of Reading, Reading, UK

<sup>3</sup>European Commission, Joint Research Centre (JRC), Institute for Environment and Sustainability (IES), Ispra, Italy

<sup>4</sup>Utrecht University, Faculty of Geosciences, Utrecht, the Netherlands

### Abstract

Climate variability and climate change impact a large number of societal sectors including water, energy, agriculture and forestry, health, tourism and infrastructure. Medium to long term numerical Weather Prediction (NWP) in combination with application-specific forecasting systems present an ideal “soft” adaptation strategy in contrast to “hard” measures which are often more costly. This requires a continuous improvement and increasing lead time of the NWP and applications systems in particular in terms of increasing lead time. In this paper the current status of the ECMWF forecast system is presented alongside imminent future developments such as a spatial resolution upgrade. Examples of flood, drought, malaria and fire forecasts are used to illustrate how the ECMWF NWP forecasts can be used as a soft adaptation tool to reduce loss of life and economic damage during extreme events. Particular focus is given on the African continent where climate change is expected to increase both frequency and impact of severe weather events in the future.

**Keywords:** Numerical Weather Prediction, Sectorial applications, ECMWF, Copernicus, multi-hazard early warning, Africa, soft adaptation strategy

### 1. Introduction

Responding to environmental and societal challenges associated with climate variability requires combining observations of the climate system with the latest science to develop authoritative, quality-assured information about the past, current and future states of the climate worldwide. The European Commission has launched the Copernicus Climate Change and Emergency service to respond to these challenges<sup>2</sup>. The Services will provide comprehensive information covering a wide range of components of the Earth system and timescales spanning days to centuries. They will maximise the use of past, current and future earth observations (from *in-situ* and satellite observing systems) in conjunction with modelling, supercomputing and networking capabilities. This wealth of information will be the basis for generating a wide variety of sectoral impact indicators aimed at supporting climate adaptation and mitigation policies in a number of sectors; namely Water, Energy, Agriculture and Forestry, Health, Coastal Areas, Insurance, Tourism and Infrastructure.

It is important that scientists and policy makers work together to develop appropriate solutions to keep climate change within manageable limits, to assess the benefit of structural measures to minimise negative impacts (hard adaptation measures), while at the same time developing early warning systems to reduce the residual risks associated with extreme weather events (soft adaptation measures). Early warning systems allow anticipating events and their consequences, allowing decision makers to take appropriate actions to reduce the impact on the short as well as longer terms and are therefore part of both disaster risk reduction as well as climate change adaptation strategies. Adaptation and mitigation strategies for the agricultural sector that are based on weather forecasting show great potential. Winsemius et al. (2014) demonstrated an adaptation and mitigation strategy in the agricultural sector by investigating how the frequency of extreme events (dry spells and heat stress conditions) may change in the future due to climate change over southern Africa and the predictability in seasonal forecasts. Wetterhall et al. (2015a; 2015b) find that seasonal forecasts have the potential to be used in a probabilistic forecast system for

\* Corresponding author: Tel: +44 118 9499 000, florian.pappenberger@ecmwf.int

<sup>2</sup> Regulation (EU) No 377/2014 of the European Parliament and of the Council of 3 April 2014 establishing the Copernicus Programme and repealing Regulation (EU) No 911/2010 Text with EEA relevance

drought-sensitive crops, indicating that there is potential for a successful adaptation strategy. This could be replicated for other natural hazards such as floods, droughts and tropical cyclones, especially in the developing world (Pappenberger *et al.*, 2013; Webster, 2013).

Different types of Numerical Weather Prediction (NWP) products will be important for different types of natural hazards. For example, many hazard indices rely on climatologies, derived from reanalyses or reforecasts, to build early warning indicators such as the Extreme Forecast Index (Dutra *et al.*, 2013a; Zsoter *et al.*, 2015) or understand the probabilities of events occurring in the form of return periods (Alfieri *et al.*, 2013b; Cloke *et al.*, 2013; Pappenberger *et al.*, 2015b; Pappenberger *et al.*, 2013; Pozzi *et al.*, 2011). The

appropriate forecast lead time depends on the time footprint of that type of hazard and also end user requirements. For example, floods and fires mostly require sub-seasonal to seasonal forecasts (Pappenberger *et al.*, 2013; Thielen-Del Pozo *et al.*, 2009) whilst droughts and malaria tend to focus on the seasonal time scale (Dutra *et al.*, 2013b; Lavaysse *et al.*, 2015; Mwangi *et al.*, 2014). In Table 1 ECMWF forecast products are related to hazard. The skill of any hazard forecasting system will thus be closely linked to the skill of the driving weather forecasts products in terms of their time range.

**Table 1:** Potential use of ECMWF products in forecasting of some natural hazards

ECMWF Product	Time Range	Floods	Wildfire	Droughts	Malaria	Wind storms	Cyclone
High Resolution	Up to 10 days	✓	✓			✓	✓
Ensemble	Up to 15 days	✓	✓			✓	✓
Monthly	Up to 42 days		✓	✓	✓		✓
Seasonal	Up to 6/12 months		✓	✓	✓		
Re-Analysis	1900-today (ERA 20C)						
	1979-today (ERAInterim, Era 5)	✓	✓	✓	✓		✓

## ECMWF Forecasts: Recent and Future Developments

### Current Status

The ECMWF high resolution forecast has a lead time of 10 days and a horizontal resolution of ~16 km (ECMWF, 2015b). Weather forecasts are often based on ensemble techniques to adequately represent uncertainties (Buizza *et al.*, 2008; Leutbecher and Palmer, 2008; Shutts *et al.*, 2011) and the ECMWF ensemble consists of 51 forecasts issued twice a day with a lead time of 15 days. The monthly forecast is integrated into this 15-day forecast by extending the forecast range to 32 days twice a week. The seasonal

forecasting system is run once a month with a lead time up to 12 months (Kim *et al.*, 2012; Molteni *et al.*, 2011). These systems are supplemented with a set of reforecasts, which are forecasts run for the past 20 years with the current prediction model. Reforecasts are used to calculate model climatologies, or to calibrate the forecast before its use in driving applications. In addition to forecasting products, ECMWF produces re-analysis products, which can be used for real-time monitoring, or for analysis of past events. Re-analysis produces global fields of atmospheric, land and ocean properties using available observations assimilated by the NWP system. The current ECMWF re-analysis product is called ERA-Interim (Dee *et al.*, 2011) and is available from

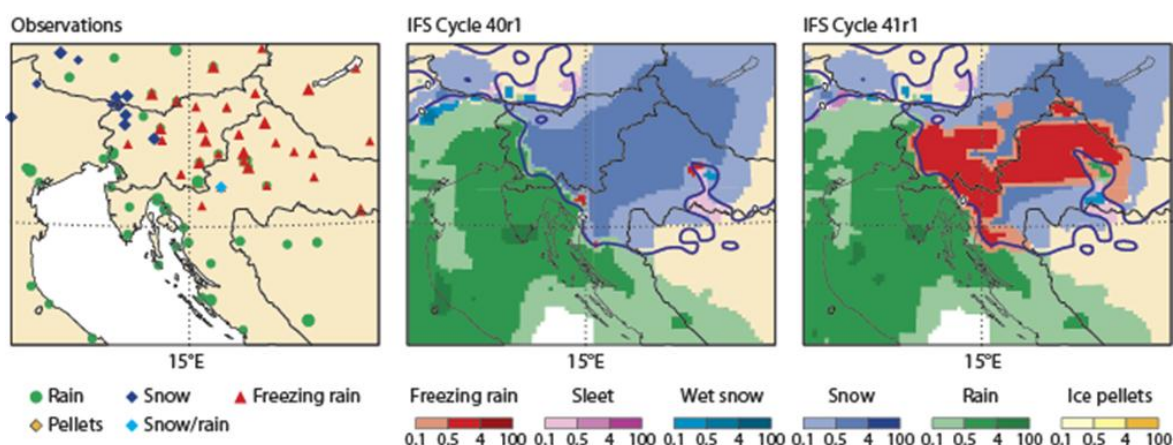


Figure 1 Freezing rain event in Slovenia and Croatia on 2 February 2014. The panels show observed precipitation type (left); precipitation type and rate (mm/hour) forecast by IFS Cycle 40r1 (middle); and precipitation type and rate forecast with the new physics (right)

1979 until today with a spatial resolution of ~80 km. ERA-Interim superseded the earlier ERA-40 (Uppala *et al.*, 2005). The next generation re-analysis product will be ERA-20C, a global re-analysis for the whole 20th century and ERA-5 which will replace ERA-Interim (ECMWF, 2015a).

ECMWF launched a new model cycle on 12 May 2015 with a range of improvements, such as changes to the assimilation of observations and modelling of atmospheric processes, the introduction of a new lake model and the extension of the high-resolution wave model, which previously covered Europe and the North Atlantic, to the whole globe. These changes have resulted in various improvements to forecast performance, particularly for cloud cover and precipitation. The occurrence of drizzle has been reduced when forecasting rainfall from extensive cloud sheets, and precipitation amounts have increased when forecasting heavy rainfall. Further improvements are seen for the 2-metre temperature and humidity in parts of the northern hemisphere and the tropics, and new output parameters have been introduced such as precipitation type, including freezing rain which has been shown to significantly increase forecast quality, as shown in figure 1

### Future Status

Science and innovation activities cover data assimilation, model development and predictability. Future enhancements to the NWP system are likely to include model parameterisations, new schemes to calculate radiation tendency and the integration of cloud and turbulence parameterisations and new aerosol climatologies. Research into data assimilation includes the evaluation of hybrid ensemble/variational methods, while a new non-hydrostatic

version of the Integrated Forecasting System (IFS) is progressing as numerical methods are being developed. Alongside the new model version, the ensemble method is being further developed, focussing on how to include model error estimation within data assimilation and ensemble forecasting, and development of a new coupled ocean-atmosphere model for extended-range predictions is ongoing. This includes a higher resolution ocean model as well as interactions between surface waves and upper-layer ocean mixing. In terms of predictability, research is focussing on large-scale circulation patterns. A future model cycle will include a horizontal resolution upgrade, with a trade-off between resolution and computational costs in mind, using a cubic, spectral octahedral grid. The anticipated upgrade will have a horizontal resolution that translates to ~9km in the outer loop of 4D-Var and the high resolution forecast, and to ~16km for the ensemble forecast up to day 10. ECMWF has extended collaboration with 10 international partners by launching a data portal for sub-seasonal to seasonal (S2S) weather forecasts to help researchers study predictability on time-scales of up to 60 days, which is anticipated to improve forecast verification through multi-model comparison; <https://software.ecmwf.int/wiki/display/S2S/Home>

### Applications: Recent and Future Developments

The improvements in the atmospheric modelling components are mirrored in improvements in applications. In this section, we highlight current and future developments in four key applications: floods, drought, malaria and wild fire,

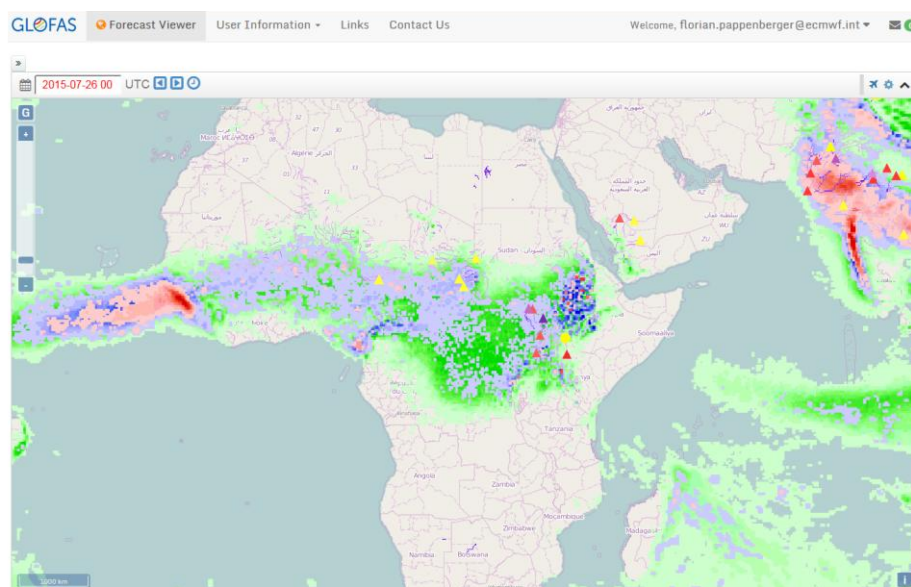


Figure 2 Forecast of the Global Flood Awareness System with a forecast issued on the 26/07/2015 00UTC

with a particular focus on Africa reflecting the desire for closer collaboration through the Africa disaster reduction fund<sup>3</sup>.

### Floods

Being prepared for major flood events on local, national and international level is key in making our global population more resilient to disasters (Stephens and Cloke, 2014). The Global Flood Awareness System (GloFAS, [www.globalfloods.eu](http://www.globalfloods.eu), see Figure 2) is a flood information system providing the European Commission and international aid organisations with daily ensemble forecasts with a horizon of 30 days across a global river network (Alfieri *et al.*, 2013a). GloFAS builds upon the knowledge and success of the European Flood Awareness System (EFAS, Thielen *et al.*, 2009a), which is operated under the Copernicus Emergency Management Service, providing early flood warnings across Europe. EFAS has undergone substantial testing and development (Alfieri *et al.*, 2014a; Alfieri *et al.*, 2014b; Bartholmes *et al.*, 2009; De Roo *et al.*, 2011; Demeritt *et al.*, 2013; Kalas *et al.*, 2008; Thielen *et al.*, 2009b; Thielen *et al.*, 2009c; Thiemig *et al.*, 2010; Wanders *et al.*, 2014; Wetterhall *et al.*, 2013; Younis *et al.*, 2008). Multiple recent floods (Haiden *et al.*, 2014; Thielen *et al.*, 2014) have demonstrated the benefits of these early flood warnings. Moreover, it has been demonstrated that an early flood warning systems can provide considerable monetary benefit (about 400 Euros for every 1 Euro invested in the case of EFAS) (Pappenberger *et al.*, 2015a). Recently, the

methodology was extended to develop a pan-African early flood forecasting system (Thiemig *et al.*, 2014; Thiemig *et al.*, 2010). Thiemig *et al.* (2014) showed that such a system can detect ~70% of the reported flood events correctly. In particular, the system showed good performance in predicting riverine flood events of long duration (>1 week) and large affected areas (>10 000 km<sup>2</sup>) well in advance, with clear limitation for small-scale and short duration flood events.

### Droughts

There has been considerable effort and research into using ECMWF's seasonal forecasts for drought predictions (Dutra *et al.*, 2013b; Dutra *et al.*, 2014; Lavaysse *et al.*, 2015; Mwangi *et al.*, 2014; Naumann *et al.*, 2014; Pozzi, 2014; Trambauer *et al.*, 2014; Werner *et al.*, 2014; Wetterhall *et al.*, 2015a; Winsemius *et al.*). Barbosa *et al.* (2013) developed a pan-African map viewer for drought monitoring and forecasting enabling better access to a large range of drought related information (<http://edo.jrc.ec.europa.eu/ado/ado.html>, see figure 3). Mwangi *et al.* (2014) evaluated seasonal drought forecasts in East Africa, showing that the forecast for the October–December rainy season has higher skill than for the March–May season. The forecasts, in particular when they are complemented by indicators such as the Standard Precipitation Index, can add value to the consensus forecasts produced during the Greater Horn of Africa Climate Outlook Forum (GHACOF), which is the present operational product for precipitation forecasts over East Africa. Forecasting on the continental scale is extremely challenging, in particular in

<sup>3</sup> <http://www.unisdr.org/archive/45134>

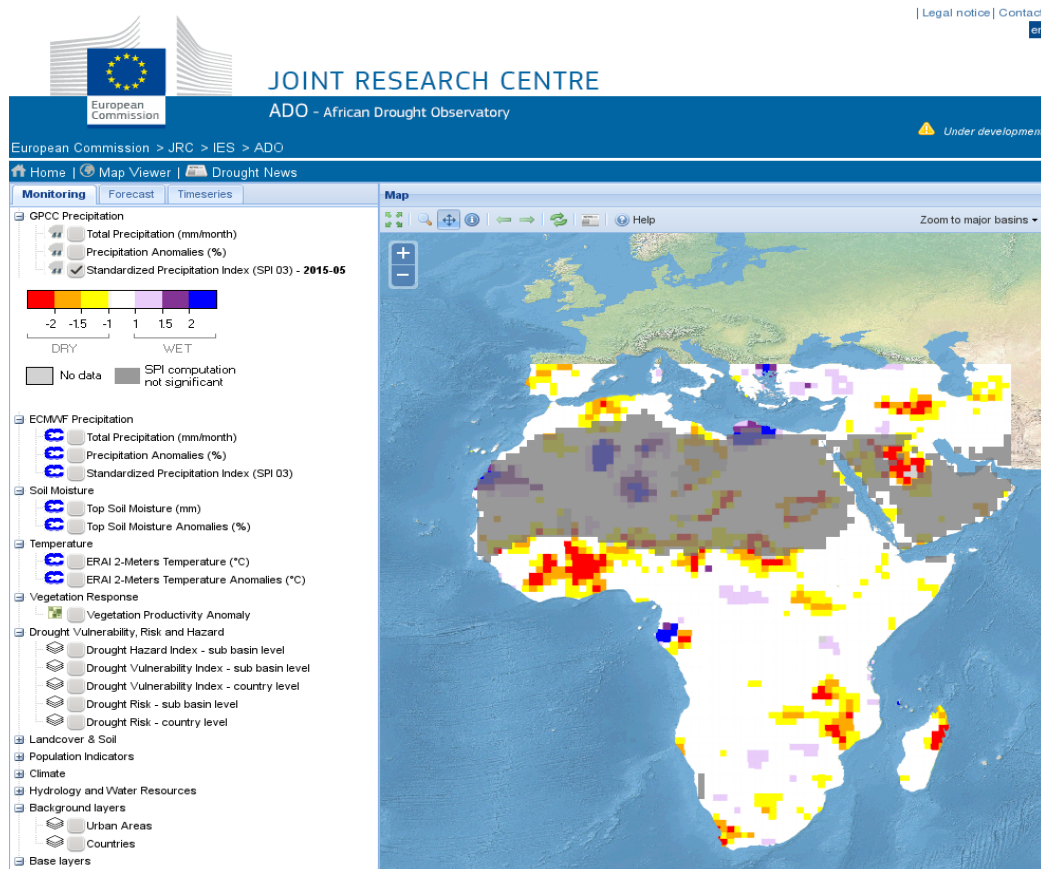


Figure 3 African Drought Observatory Interface (see <http://edo.jrc.ec.europa.eu/ado/ado.html>)

the complex and highly variant nature of Africa (Masih *et al.*, 2014).

### Malaria

ECMWF's forecasts have been used to develop a pan-African malaria risk forecast integrating a malaria model (Tompkins and Ermert, 2012) and bias-corrected merged monthly and seasonal forecasts (Di Giuseppe *et al.*, 2012). Forecasts are merged with reforecasts to detect anomalous transmission conditions (see figure 4). The system has shown the potential for skilful malaria predictions up to 4 months in advance over wide areas that were identified to have highly variable transmission for specific months of the year (Tompkins and Di Giuseppe, 2015). Tompkins and Di Giuseppe (2015) compare the forecasts to outpatient data of the highland regions of south-western Uganda and western Kenya showing considerable skill of the forecast system. The next phase is under way, in collaboration with two health ministries in Africa, in which a detailed evaluation of the system at the health-district level is conducted.

### Wild Fire

Wildfires can have significant impacts on the economy, environment, heritage and social fabric of rural areas. A

global fire climatology has recently been published (Field *et al.*, 2014) and it could be shown that there is skill in predicting fires on the seasonal scale in Asia (Spessa *et al.*, 2015). In Europe, the European Commission operates the European Forest Fire Information System (Camia *et al.*, 2006) to monitor and forecast fire danger and fire behaviour. Forecasts are primarily based on the Canadian Fire Weather Index (FWI) and deterministic, single value atmospheric forecasts. Recent research funded by the Joint Research Centre (EC) has coupled ECMWF medium range forecasts to alternative fire modules (US Forest Service National Fire Danger Rating System, Australian McArthur rating system and FWI) to produce fire hazard forecasts for the globe (Di Giuseppe *et al.*, submitted), demonstrating that the systems are able to identify conditions of danger for fire events. The predictions are particularly accurate where fire events are mainly controlled by persistent drought conditions (Boreal Forests, Mediterranean region, South America and Central Africa). The very promising results show that climate model simulation may usefully extend the early warning available from environmental monitoring (see figure 5).

### Conclusions

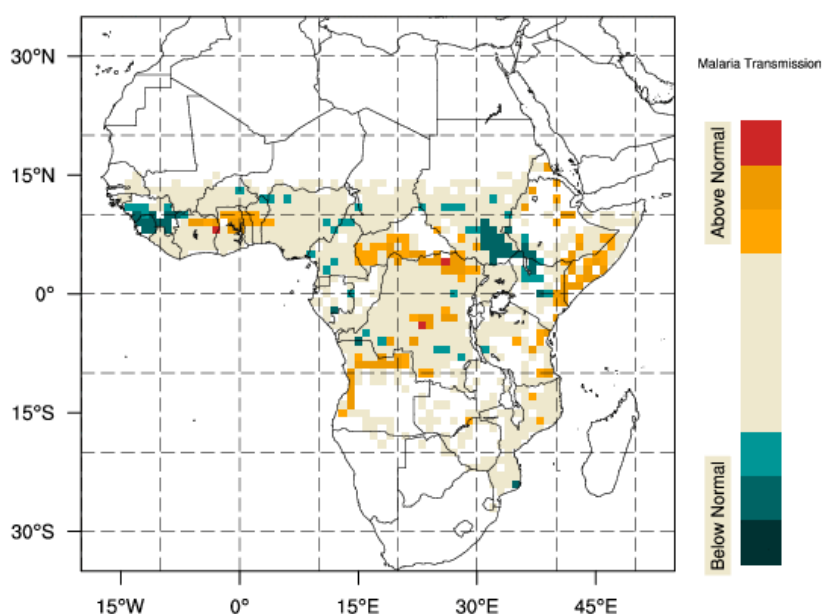


Figure 4: Forecast of malaria transmission risk from the 16 May to 13 June with a forecast lead time of 2 months.

Variability and change in our climate requires adaptation along different time scales. One flexible and therefore “soft” key adaptation strategy is that of improving forecasting capabilities, enabling the anticipation of extreme events so that appropriate actions can be taken to reducing impact and damage. In particular, weather forecasting systems have great potential for the reduction of the impact of disasters if they are coupled to other downstream forecasting services. In all areas, the potential benefits are significant given adequate technical infrastructure. In this paper, the current statuses of the ECMWF forecasting systems are outlined alongside future developments and ongoing research. Four application areas (floods, droughts, malaria and fire) are described, all of which currently use ECMWF forecasts. These coupled systems show considerable potential for improved early warning of natural hazards and hence clear potential for further uptake in climate adaptation and mitigation strategies.

## References

- Alfieri, L., Burek, P., Dutra, E., Krzeminski, B., Muraro, D., Thielen, J., Pappenberger, F., 2013a. GloFAS-global ensemble streamflow forecasting and flood early warning. *Hydrology and Earth System Sciences*, 17(3): 1161-1175.
- Alfieri, L., Pappenberger, F., Wetterhall, F., 2013b. The extreme runoff index for flood early warning in Europe. *Natural Hazards and Earth System Sciences Discussions*, 14: 1505-1515, doi:10.5194/nhess-14-1505-2014.
- Alfieri, L., Pappenberger, F., Wetterhall, F., Haiden, T., Richardson, D., Salamon, P., 2014a. Evaluation of ensemble streamflow predictions in Europe. *Journal of Hydrology*, 517: 913-922.
- Alfieri, L., Salamon, P., Bianchi, A., Neal, J., Bates, P., Feyen, L., 2014b. Advances in pan-European flood hazard mapping. *Hydrological Processes*, 28(13): 4067-4077.
- Barbosa, P., Naumann, G., Valentini, L., Vogt, J., Dutra, E., Magni, D., De Jager, A., 2013. A Pan-African map viewer for drought monitoring and forecasting. 14th Waternet Symposium, Dar es Salaam, Tanzania, 30 October to 1 November 2013.
- Bartholmes, J.C., Thielen, J., Ramos, M.H., Gentilini, S., 2009. The european flood alert system EFAS - Part 2: Statistical skill assessment of probabilistic and deterministic operational forecasts. *Hydrology and Earth System Sciences*, 13(2): 141-153.
- Buizza, R., Leutbecher, M., Isaksen, L., 2008. Potential use of an ensemble of analyses in the ECMWF Ensemble Prediction System. *Q. J. R. Meteorol. Soc.*, 134: 2051-2066.
- Camia, A., Barbosa, P., Amatulli, G., San-Miguel Ayanz, J., 2006. Fire danger rating in the European Forest Fire Information System (EFFIS): current developments, Proceedings of 5th International Conference on Forest Fire Research, November 27-30 2006, Coimbra, Portugal.
- Cloke, H.L., Wetterhall, F., He, Y., Freer, J.E., Pappenberger, F., 2013. Modelling climate impact on floods with ensemble climate projections. *Q.J.R. Meteorol. Soc.*, 139(282-297, doi: 10.1002/qj.1998).
- De Roo, A., Thielen, J., Salamon, P., Bogner, K., Nobert, S., Cloke, H., Demeritt, D., Younis, J., Kalas, M., Bodis, K., Muraro, D., Pappenberger, F., 2011. Quality control, validation and user feedback of the European Flood Alert System (EFAS). *International Journal of Digital Earth*, 4: 77-90.

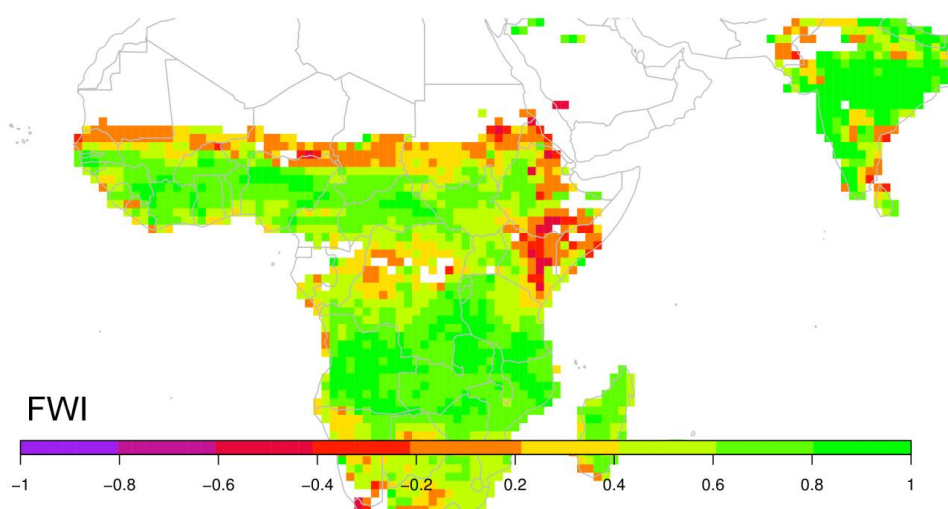


Figure 5 Extreme Dependency Index for Fire Weather Index. The Extreme Dependency Index takes the value of 1 for perfect forecasts and 0 for random forecasts. Values above zero could be considered skilful. For details see (Di Giuseppe et al., submitted)

- Dee, D.P., Uppala, S.M., Simmons, A.J., Berrisford, P., Poli, P., Kobayashi, S., Andrae, U., Balmaseda, M.A., Balsamo, G., Bauer, P., Bechtold, P., Beljaars, A.C.M., van de Berg, L., Bidlot, J., Bormann, N., Delsol, C., Dragani, R., Fuentes, M., Geer, A.J., Haimberger, L., Healy, S.B., Hersbach, H., Hólm, E.V., Isaksen, I., Kållberg, P., Köhler, M., Matricardi, M., McNally, A.P., Monge-Sanz, B.M., Morcrette, J.J., Park, B.K., Peubey, C., de Rosnay, P., Tavolato, C., Thépaut, J.N., Vitart, F., 2011. The ERA-Interim reanalysis: configuration and performance of the data assimilation system. *Quarterly Journal of the Royal Meteorological Society*, 137(656): 553-597.
- Demeritt, D., Nobert, S., Cloke, H.L., Pappenberger, F., 2013. The European Flood Alert System and the communication, perception, and use of ensemble predictions for operational flood risk management. *Hydrological Processes*, 27(1): 147-157.
- Di Giuseppe, F., Molteni, F., Tompkins, A.M., 2012. A rainfall calibration methodology for impacts modelling based on spatial mapping. *Quarterly Journal of the Royal Meteorological Society*: doi:10.1002/qj.2019.
- Di Giuseppe, F., Pappenberger, F., Wetterhall, F., Krzeminski, B., Cania, A., Liberta', G., San-Miguel, J., submitted. Assessment of global fire risk using ECMWF ERA-Interim reanalysis. *Journal of Climate*.
- Dutra, E., Diamantakis, M., Tsonevsky, I., Zsoter, E., Wetterhall, F., Stockdale, T., Richardson, D., Pappenberger, F., 2013a. The extreme forecast index at the seasonal scale. *Atmospheric Science Letters*, 14(4): 256-262.
- Dutra, E., Giuseppe, F.D., Wetterhall, F., Pappenberger, F., 2013b. Seasonal forecasts of droughts in African basins using the Standardized Precipitation Index. *Hydrology and Earth System Sciences*, 17(6): 2359-2373.
- Dutra, E., Pozzi, W., Wetterhall, F., Di Giuseppe, F., Magnusson, L., Naumann, G., Barbosa, P., Vogt, J., Pappenberger, F., 2014. Global meteorological drought - Part 2: Seasonal forecasts. *Hydrology and Earth System Sciences*, 18(7): 2669-2678.
- ECMWF, 2015a. Climate Reanalysis, <http://www.ecmwf.int/en/research/climate-reanalysis>, last accessed 22/07/2015.
- ECMWF, 2015b. Key characteristics of the forecasting system, <http://www.ecmwf.int/en/forecasts/documentation-and-support/key-characteristics-forecasting-system>, last accessed 22/07/2015.
- Field, R., Spessa, A., Aziz, N., Camia, A., Cantin, A., Carr, R., de Groot, W., Dowdy, A., Flannigan, M., Manomaiphiboon, K., others, 2014. Development of a global fire weather database for 1980-2012. *Natural Hazards and Earth System Sciences Discussions*, 2(10): 6555-6597.
- Haiden, T., Magnusson, L., Tsonevsky, I., Wetterhall, F., Alfieri, L., Pappenberger, F., de Rosnay, P., Muñoz-Sabater, J., Balsamo, G., Albergel, C., Forbes, R., Hewson, T., Malardel, S., Richardson, D., 2014. ECMWF forecast performance during the June 2013 flood in Central Europe. *ECMWF Technical Memorandum*, 723.
- Kalas, M., Ramos, M.-H., Thielen, J., Babiakova, G., 2008. Evaluation of the medium-range European flood forecasts for the March-April 2006 flood in the Morava river. *Journal of Hydrology and Hydromechanics*, 56(2): 116-132.
- Kim, H.-M., Webster, P., Curry, J., 2012. Seasonal prediction skill of ECMWF System 4 and NCEP CFSv2 retrospective forecast for the Northern Hemisphere Winter. *Clim Dyn*, 39(12): 2957-2973.
- Lavaysse, C., Vogt, J., Pappenberger, F., 2015. Early warning of drought in Europe using the monthly ensemble system from ECMWF. *Hydrology and Earth System Sciences Discussions*, 12(2): 1973-2009.

- Leutbecher, M., Palmer, T.N., 2008. Ensemble forecasting. *J. Comp. Phys.*, 227: 3515-3539.
- Masih, I., Maskey, S., Mussá, F.E.F., Trambauer, P., 2014. A review of droughts on the African continent: a geospatial and long-term perspective. *Hydrol. Earth Syst. Sci.*, 18(9): 3635-3649.
- Molteni, F., Stockdale, T., Balmaseda, M., Balsamo, G., Buizza, R., Ferranti, L., Magnusson, L., Mogensen, K., Palmer, T., Vitart, F., 2011. The new ECMWF seasonal forecast system (System 4). ECMWF Technical Memorandum, 656.
- Mwangi, E., Wetterhall, F., Dutra, E., Di Giuseppe, F., Pappenberger, F., 2014. Forecasting droughts in East Africa. *Hydrology and Earth System Sciences*, 18(2): 611-620.
- Naumann, G., Dutra, E., Barbosa, P., Pappenberger, F., Wetterhall, F., Vogt, J.V., 2014. Comparison of drought indicators derived from multiple data sets over Africa. *Hydrology and Earth System Sciences*, 18(5): 1625-1640.
- Pappenberger, F., Cloke, H.L., Parker, D.J., Wetterhall, F., Richardson, D.S., Thielen, J., 2015a. The monetary benefit of early flood warnings in Europe. *Environmental Science & Policy*, 51: 278-291.
- Pappenberger, F., Jendritzky, G., Staiger, H., Dutra, E., Di Giuseppe, F., Richardson, D., Cloke, H., 2015b. Global forecasting of thermal health hazards: the skill of probabilistic predictions of the Universal Thermal Climate Index (UTCI). *International journal of biometeorology*, 59(3): 311-323.
- Pappenberger, F., Wetterhall, F., Dutra, E., Di Giuseppe, F., Bogner, K., Alfieri, L., Cloke, H.L., 2013. Seamless forecasting of extreme events on a global scale. *Climate and Land Surface Changes in Hydrology*, edited by: Boegh, E., Blyth, E., Hannah, DM, Hisdal, H., Kunstmann, H., Su, B., and Yilmaz, KK, IAHS Publication, Gothenburg, Sweden: 3-10.
- Pozzi, W., 2014. Global meteorological drought-Part 1: Probabilistic monitoring. *Hydrology and Earth System Science (HESS)*, 18: 2657-2667.
- Pozzi, W., de Roo, A., Vogt, J., Lawford, R., Pappenberger, F., Heim, R., Stefanski, R., 2011. Group on Earth Observations (GEO) Global Drought Monitor Portal: Adding Capabilities for Forecasting Hydrological Extremes and Early Warning Networking. AGU Fall Meeting Abstracts, 1: 04.
- Shutts, G.J., Leutbecher, M., Weisheimer, A., Stockdale, T., Isaksen, L., Bonavita, M., 2011. Representing model uncertainty: stochastic parametrization at ECMWF. *ECMWF Newsletter(129)*: 19-24.
- Spessa, A., Field, R., Pappenberger, F., Langner, A., Enghart, S., Weber, U., Stockdale, T., Siegert, F., Kaiser, J., Moore, J., 2015. Seasonal forecasting of fire over Kalimantan, Indonesia. *Natural Hazards and Earth System Science*, 15(3): 429-442.
- Stephens, E., Cloke, H., 2014. Improving flood forecasts for better flood preparedness in the UK (and beyond). *The Geographical Journal*, 180(4): 310-316.
- Thielen-Del Pozo, J., Pappenberger, F., Bogner, K., Kalas, M., de Roo, A., 2009. Seamless Flood Forecasting Based on Monthly, Medium-Range and Short-Range Ensemble Prediction Systems, EGU General Assembly Conference Abstracts, pp. 8650.
- Thielen, J., Annunziato, A., Andreadakis, I., McCormick, N., Kalas, M., Kechagioglou, X., Kucera, J., Muraro, D., Probst, P., Salamon, P., Thiemig, V., 2014. Balkans' worst floods for more than 100 years HEPEX blog: <http://hepex.irstea.fr/balkans-worst-floods-for-more-than-100-years/>, last accessed 23.07.2015.
- Thielen, J., Bartholmes, J., Ramos, M.-H., de Roo, A., 2009a. The European Flood Alert System textendash Part 1: Concept and development. *Hydrology and Earth System Sciences*, 13: 125-140, doi:10.5194/hess-13-125-2009.
- Thielen, J., Bartholmes, J., Ramos, M.H., de Roo, A., 2009b. The European Flood Alert System - Part 1: Concept and development. *Hydrology and Earth System Sciences*, 13(2): 125-140.
- Thielen, J., Bogner, K., Pappenberger, F., Kalas, M., del Medico, M., de Roo, A., 2009c. Monthly-, medium-, and short-range flood warning: testing the limits of predictability. *Meteorological Applications*, 16(1): 77-90.
- Thiemig, V., Bisselink, B., Pappenberger, F., Thielen, J., 2014. A pan-African Flood Forecasting System. *Hydrol. Earth Syst. Sci.*, 19, 3365-3385, doi:10.5194/hess-19-3365-2015, 2015..
- Thiemig, V., Pappenberger, F., Thielen, J., Gadain, H., de Roo, A., Bodis, K., Del Medico, M., Muthusi, F., 2010. Ensemble flood forecasting in Africa: a feasibility study in the Juba-Shabelle river basin. *Atmospheric Science Letters*, 11(2): 123-131.
- Tompkins, A.M., Di Giuseppe, F., 2015. Potential Predictability of Malaria in Africa Using ECMWF Monthly and Seasonal Climate Forecasts. *J. Appl. Meteor. Climatol.*, 54(521-540).
- Tompkins, A.M., Ermert, V., 2012. A regional-scale, high resolution dynamical malaria model that accounts for population density, climate and surface hydrology. *Malaria Journal*, 12(65): doi:10.1186/1475-2875-12-65.
- Trambauer, P., Maskey, S., Werner, M., Pappenberger, F., Van Beek, L.P.H., Uhlenbrook, S., 2014. Identification and simulation of space-time variability of past hydrological drought events in the Limpopo river basin, Southern Africa. *Hydrology and Earth System Sciences Discussions*, 11, 2014.
- Uppala, S.M., Kållberg, P.W., Simmons, A.J., Andrae, U., Bechtold, V.D.C., Fiorino, M., Gibson, J.K., Haseler, J., Hernandez, A., Kelly, G.A., Li, X., Onogi, K., Saarinen, S., Sokka, N., Allan, R.P., Andersson, E., Arpe, K., Balmaseda, M.A., Beljaars, A.C.M., Berg, L.V.D., Bidlot, J., Bormann, N., Caires, S., Chevallier, F., Dethof, A., Dragosavac, M., Fisher, M., Fuentes, M., Hagemann, S., Hólm, E., Hoskins, B.J., Isaksen, L., Janssen, P.A.E.M., Jenne, R., McNally, A.P., Mahfouf, J.F., Morcrette, J.J., Rayner, N.A., Saunders, R.W., Simon, P., Sterl, A., Trenberth, K.E., Untch, A., Vasiljevic, D., Viterbo, P., Woollen, J., 2005. The ERA-40 re-

- analysis. *Quarterly Journal of the Royal Meteorological Society*, 131(612): 2961-3012.
- Wanders, N., Karssenber, D., de Roo, A., de Jong, S.M., Bierkens, M.F.P., 2014. The suitability of remotely sensed soil moisture for improving operational flood forecasting. *Hydrology and Earth System Sciences*, 18(6): 2343-2357.
- Webster, P.J., 2013. Meteorology: Improve weather forecasts for the developing world. *Nature*, 493(7430): 17-19.
- Werner, M., Trambauer, P., Winsemius, H., Maskey, S., Dutra, E., Pappenberger, F., 2014. Assessing the skill of seasonal forecasting of streamflow and drought in the Limpopo basin, Southern Africa. *AGU Fall Meeting Abstracts*, 1: 0920.
- Wetterhall, F., Pappenberger, F., Alfieri, L., Cloke, H.L., Thielen-del Pozo, J., Balabanova, S., Danhelka, J., Vogelbacher, A., Salamon, P., Carrasco, I., Cabrera-Tordera, A.J., Corzo-Toscano, M., Garcia-Padilla, M., Garcia-Sanchez, R.J., Ardilouze, C., Jurela, S., Terek, B., Csik, A., Casey, J., Stankunavicius, G., Ceres, V., Sprokkereef, E., Stam, J., Anghel, E., Vladikovic, D., Eklund, C.A., Hjerdt, N., Djerv, H., Holmberg, F., Nilsson, J., Nystrom, K., Susnik, M., Hazlinger, M., Holubecka, M., 2013. HESS Opinions "Forecaster priorities for improving probabilistic flood forecasts". *Hydrology and Earth System Sciences*, 17(11): 4389-4399.
- Wetterhall, F., Winsemius, H., Dutra, E., Werner, M., Pappenberger, F., 2015a. Corrigendum to "Seasonal predictions of agro-meteorological drought indicators for the Limpopo basin" published in *Hydrol. Earth Syst. Sci.*, 19. *Hydrol. Earth Syst. Sci.*, 19: 2637–2637.
- Wetterhall, F., Winsemius, H.C., Dutra, E., Werner, M., Pappenberger, E., 2015b. Seasonal predictions of agro-meteorological drought indicators for the Limpopo basin. *Hydrol. Earth Syst. Sci.*, 19: 2577-2586, doi:10.5194/hess-19-2577-2015.
- Winsemius, H., Dutra, E., Engelbrecht, F., van Garderen, E.A., Wetterhall, F., Pappenberger, F., Werner, M., Exploring the potential of adapting to climate change through seasonal prediction of meteorological drought indicators.
- Winsemius, H.C., Dutra, E., Engelbrecht, F.A., Archer Van Garderen, E., Wetterhall, F., Pappenberger, F., Werner, M.G.F., 2014. The potential value of seasonal forecasts in a changing climate in southern Africa. *Hydrology and Earth System Sciences*, 18(4): 1525–1538.
- Younis, J., Ramos, M.-H., Thielen, J., 2008. EFAS forecasts for the March-April 2006 flood in the Czech part of the Elbe River Basin - a case study. *Atmospheric Science Letters*, 9(2): 88-94.
- Zsoter, E., Pappenberger, F., Richardson, D., 2015. Sensitivity of model climate to sampling configurations and the impact on the Extreme Forecast Index. *Meteorological Applications*, 22(2): 236-247.

## Origin, development and demise of a Benguela Niño in the tropical Atlantic in 2010 and 2011

Mathieu Rouault<sup>1,2</sup>, Joke Lübbecke<sup>3</sup>, Serena Illig<sup>4,1</sup>, Rodrigue Anicet Imbol Kounge<sup>1,2</sup>

<sup>1</sup> Department of Oceanography, MARE Institute, University of Cape Town, South Africa

<sup>2</sup> Nansen-Tutu Center for Marine Environmental Research, University of Cape Town

<sup>3</sup> IMF GEOMAR, Kiel Germany

<sup>4</sup> ICEMASA, IRD, France

A Benguela Niño started in November 2010 and lasted for 5 months along the Angola and Namibian coastline in the Angola Benguela current system. Maximum amplitude was reached in January 2011 with an SST anomaly of up to 4° C at the monthly scale. Consistent with previous Benguela Niños, the event was generated by a relaxation of the trade winds in the western equatorial Atlantic triggering an equatorial Kelvin wave that propagated eastward along the equator and then southward along the south-west African coast as a coastal Kelvin wave. The warming was then advected further south as far as 25 °S by an anomalously strong poleward subsurface current.

### 1. Introduction

The South-western African coast is characterized by a strong temperature gradient between the warm tropical Atlantic and the cold Benguela current. Every few years, sea surface temperatures (SSTs) off the coast of Angola and Namibia reach values of up to 5°C higher than typical for the season. These warm events have been named Benguela Niños (Shannon et al., 1986). These have large impacts on local fisheries (Boyer and Hampton, 2001) and on rainfall variability over south-western Africa (Rouault et al., 2003). While local wind forcing might play a role in the development of some of the events (Richter et al., 2010), especially in the Benguela upwelling, it has been shown that they are mainly generated by wind stress changes in the western equatorial Atlantic (Rouault et al., 2007; Lübbecke et al., 2010). Understanding and potentially forecasting their development is thus of high socioeconomic importance and the lead time between decrease in wind speed along the Equator and development of SST anomalies along the Angolan and Namibian coastline offer predictability. In this study, we will analyse the evolution of the 2010/2011 Benguela Niño event using direct observations from the PIRATA array of mooring, satellite estimate of SST and altimetry derived sea surface height (SSH), ERA Interim reanalysis wind stress, an Ocean Linear Model and an Ocean General Circulation Model

### 2 Origin, development and demise of the warm event

In October 2010, weaker than normal easterly wind occurred in most of the Tropical Atlantic from 5 °N

to 10 °S and from 50 °W to 0 °W. According to ERA Interim Reanalysed climate data, it was the largest decrease in zonal wind speed since at least 1982 at the monthly scale along the equator with positive anomaly above 2 standard deviation. Following the decrease in easterly wind speed a deepening of the thermocline of up to 30 m was observed by the PIRATA array of mooring propagating from East to West from early October, taking a month to reach the African coastline. PIRATA derived monthly anomalies of the 20 °C isotherm, measured dynamic height monthly anomaly from 0 to 500 Db and altimetry derived detrended monthly anomaly of sea surface height.

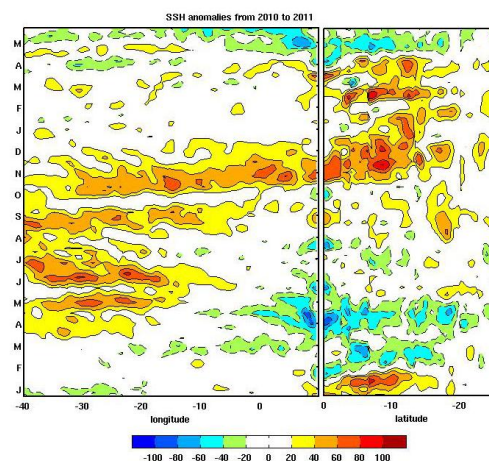


Fig 1: Hovmöller diagram of altimetry derived SLA anomalies from monthly climatology along the equator (averaged over 1°S to 1°N, left) from 40 °W to the African coastline and along the Southern African coast (averaged from coast to 2° offshore, right) from 0 to 25 °S from January 2010 (bottom) to May 2011 (top).

Fig 1 confirms the propagation of subsurface temperature anomalies across the basin, the deepening of the thermocline and the duration of the

events that lasted for two months along the Equator in October/November 2010. Fig 1 is a Hovmöller diagram of monthly anomalies of SSH along the equator (left) from 40 °W to the African coast and from 0° S to 30° S along the coast (right). Data is averaged from 1°N to 1°S along the equator and from the coast to 2° degree offshore along Southern Africa from January 2010 (bottom) to December 2011 (top). The propagation of above normal SSH along the Equator is followed by a poleward propagation of SSH positive anomalies along the African coastline from 0 °S to 20 °S. A difference from the equatorial region is that the SSH anomalies are observed from November 2010 to April 2011. In May 2011 abnormal negative anomaly of SSH are detected along the eastern equator and along the African coastline, putting an abrupt end to the warm. Figure 2 is the same Hovmöller diagram as Figure 1 but for TRMM TMI Sea surface temperature monthly anomalies.

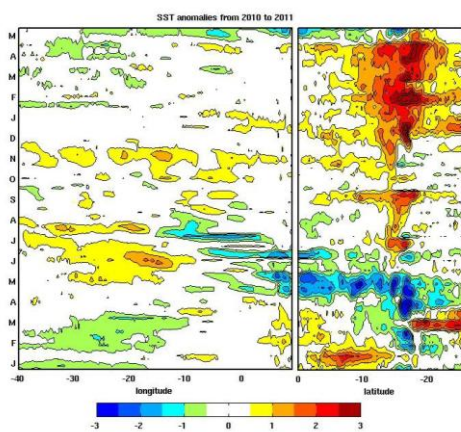


Fig 2: Hovmöller diagram of TRMM TMI SST anomaly from January 2010 (bottom) to May 2011 (top) along the equator (left) and along the South West African coast.

Along the Equator, a moderate increase in SST is visible from October to December along the equator with SST anomaly of up to 1.5 C but along the coast of Africa and especially at the Angola Benguela Frontal zone the increase is more substantial and lasts for a few months all the way to 25 °S in the Northern Benguela upwelling with a maximum SST positive anomaly of 4 °C. An SST anomaly of more than 1 °C is first observed at the Angola Benguela front in November 2010 and seems to spread southward and northward until May 2011 when the warm event suddenly stops. When considering SST from 1982 to 2014, that warm event was the highest austral summer warm event in Angola and Northern Namibia and also the longest since the famous 1995 Benguela Niño and it was the warmest event at the Angola Benguela Front since at least 1982 with SST anomaly above 3 standard deviations. This warm events is clearly on par with major warm events that occurred in Austral summer since 1982 such as 1984

(January to June) 1994/1995 (November to July), 1997/1998 (October to January) or 2001 (February to April). A peculiarity of the 2010/2011 warm event is that it started quite early in the austral summer season.

### 3 Southward advection of warm tropical water

As for previous Benguela Niño's, the warming was not restricted to the Angola Benguela Frontal zone where the coastal tropical thermocline outcrop but occurred as far as 25°S. Rouault (2012) argued that this southward expansion is related to an anomalous poleward advection of warm water in the Benguela upwelling. Looking at NCEP/GODAS modelled meridional transport volume transport monthly anomaly in Sverdrup at the Angola Benguela Front from 0 to 250 m depth and 8.75°E to the coast at 11.5°E, we find that there is indeed an enhanced southward transport across 17°S in late 2010 (Fig. 3).

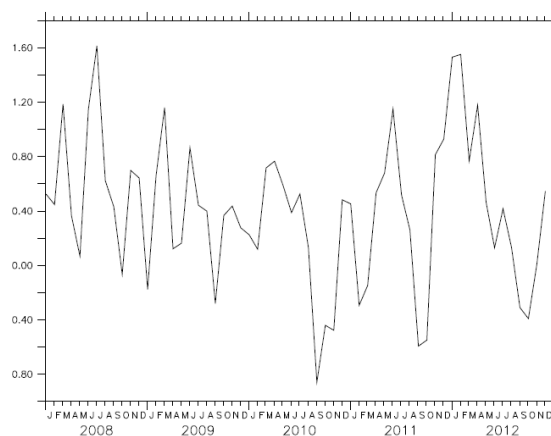


Fig.3: GODAS modelled transport monthly anomaly across the Angola Benguela Front at 17 °S anomalies from GODAS (positive values denote northward i.e. equatorward transport anomalies)

There is also a secondary modelled anomalous poleward advection of warm water in February. The deepening of the thermocline in late 2010 along the Equator is also well modelled by GODAS. In May, at the Angola Benguela Front an abnormal transport this time equatorward is modeled by GODAS at the same time that of the demise of the warm events along the African coast. It means that a cold event involving stronger zonal wind speed along the Equator that will lead to shallower thermocline propagating all the way the Angola Benguela front is a mean to interrupt a warm event in Angola and Northern Namibia,

### 4 Role of Kelvin and Rossby waves in the origin of the events

In order to investigate equatorial wave propagations, we used the Equatorial Atlantic Ocean Linear Model (OLM) developed by Illig et al. (2004) and used in Rouault et al (2007). We focus on the modelled SSH signal along the equator and in particular on the gravest baroclinic mode (1 and 2) long equatorial Kelvin wave components. Model was run with no reflection of Kelvin wave and Rossby wave (not shown) at the border allowed versus reflection at the border allowed to highlight and calculate the contribution of reflected Rossby and Kelvin waves to overall signal.

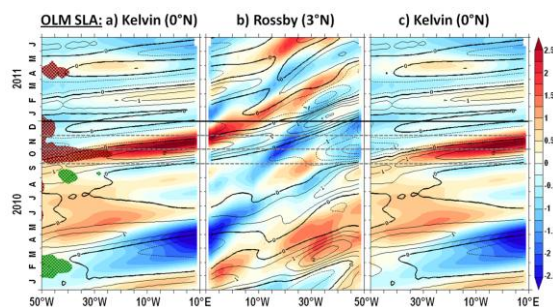


Fig. 4: Panel a (b): Longitude–time Hovmöller diagrams of the eastward (westward) propagating Kelvin (Rossby) wave contribution to the monthly SLA along the equator (at 3°N) from the Ocean Linear Model from January 2010 to June 2011. The second baroclinic Kelvin wave contribution (dominant mode) is in colour, while contours denote the first baroclinic Kelvin wave contribution (fastest mode). Unit is cm. Note that Kelvin is repeated in panel c and the longitude axis in the Rossby is reversed in order to appreciate the reflexion at the meridional boundaries of the basin. In panel a, orange (green) shadings corresponds to zonal wind stress anomalies along the equator (averaged between 2°S–2°N)

The results highlight the role of Kelvin and Rossby waves in the origin of the event. It confirms that anomalies of zonal wind stress in October 2010 is the main forcing of thermocline anomaly along the Equator and confirm the PIRATA observation and Altimetry results. Moreover, wind forcing of Kelvin waves in October 2010 is simultaneous with reflected Rossby waves at the Brazilian border in the Western part of the basin. The latter were forced by Kelvin waves reflecting in Rossby waves at the African border in April 2010 for Kelvin wave mode 1, while for mode 2 Rossby wave seemed to be forced by positive anomalies of meridional wind stress in austral winter 2010. There is a lag of one month between the arrival of Kelvin wave mode 1 and Kelvin wave mode 2 at the African border. Kelvin wave mode 1 arrived at the end of October 2010 while Kelvin wave mode 2 arrived at the end of November 2010. Together with the reflected Rossby wave, this could explain the anomaly in

thermocline depth and subsurface anomaly in November 2010 observed with PIRATA. Reflections at the meridional boundaries explain 20 % of the SSH anomaly along the Equator in November/December 2010.

### Acknowledgements

MR wants to thanks ACCESS, NRF, WRC and the Nansen Tutu for Marine Environmental Research for funding. The research leading to these results received funding from the EU FP7/2007–2013 under Grant Agreement No. 603521.

### References

- Boyer, D. C. and I. Hampton (2001), An overview of the living marine resources of Namibia, South Afr. J. Mar. Sci., 23, 1, 5–35.
- Illig, S., Dewitte, B., Ayoub, N., du Penhoat, Y., Reverdin, G., De Mey, P., Bonjean, F., Lagerloef, G.S.E., 2004. Interannual long equatorial waves in the Tropical Atlantic from a high resolution OGCM experiment in 1981–2000. J. Geophys. Res. 109 (C2), C02022. doi:10.1029/2003JC001771
- Lübbecke, J. F., C. W. Böning, N. S. Keenlyside, and S.-P. Xie (2010), On the connection between Benguela and equatorial Atlantic Niños and the role of the South Atlantic Anticyclone, J. Geophys. Res., 115, C09015, doi:10.1029/2009JC005964.
- Rouault, M., P. Florenchie, N. Fauchereau, and C. J. C. Reason (2003), South East tropical Atlantic warm events and southern African rainfall, Geophys. Res. Lett., 30, doi:10.1029/2003GL018440.
- Rouault, M., S. Illig, C. Bartholomae, C. J. C. Reason, and A. Bentamy (2007), Propagation and origin of warm anomalies in the Angola Benguela upwelling system in 2001, J. Mar. Syst., 68, 473–488.
- Rouault, M. (2012), Bi-annual intrusion of tropical water in the northern Benguela upwelling, Geophys. Res. Lett., 39, L12606, doi: 10.1029/2012GL052099.
- Shannon, L. V., A. J. Boyd, G. B. Brundrit, and J. Taunton-Clark (1986), On the existence of an El Niño–type phenomenon in the Benguela system, J. Mar. Sci., 44, 495–520.

## A new 2-D Scan portable Durban LiDAR for atmospheric studies – System Description and first scientific result

Venkataraman. Sivakumar\*, Jeremiah A. Ogunniyi, Joseph A. Adesina, Priyanka. Singh  
and Lerato. Shikwambana

*Discipline of Physics, School of Chemistry and Physics, University of KwaZulu-Natal, Durban 4000,  
South Africa*

\*corresponding author: [venkataramans@ukzn.ac.za](mailto:venkataramans@ukzn.ac.za)

### Abstract

In this paper, we explore the atmosphere, by using the new 2 dimensional (x-y) Scan LiDAR measurements for aerosol, smoke, clouds and water vapour. The integrated X-Y scanner will provide improved mapping of the target (smoke, clouds or pollutants) to study smoke/plume/pollutant dispersion. The system shall be used for different field campaign measurements in the country.

Keywords: Zenith, Azimuth, Measurements, Transmission, Backscatter

### 1. Introduction

Light Detection and Ranging (LiDAR) studies on particulate matter (0.5 and 0.3 microns) elucidate their distribution and concentration in the atmosphere. Particulate matter plays a key role in atmospheric physical and chemical processes from local to global scale (Kanike and Sivakumar, 2015). The complexities of these processes have been reviewed in literature and LiDAR measurements have greatly contributed to a better understanding of atmosphere dynamics and particle microphysics. By making observations on a pre-determined spatial scale (from sites to regions), it will be possible to calculate atmospheric mass transport, and, through trajectory analysis, it is possible to back-track the location of plume sources, e.g. biomass burning. The atmospheric backscatter measurements of aerosols (solid particles floating in the air and formed by combination of different pollutants), can be used to identify the stratification of pollutants and will enable the classification of the source regions, such as industrial, biological and anthropogenic sources (Střížik 2008 and Sivakumar, 2012). The science behind the optical and microphysical properties of aerosols, is currently considered as ‘low level’ within the climate change scientific community but it is intricately involved in global warming (see Fifth Assessment report of the IPCC, 2013, Stocker et al., 2013).

Though, the LIDAR has been exploited for atmospheric measurements in many countries, LIDARs in the African continent are limited to two including the mobile LIDAR system developed at CSIR-NLC (Sivakumar, 2012). Hence, the portable and 2-D scan LIDAR is yet to be considered a state-of-the-art for South Africa and African countries. A recent survey made on identifying the

scan LiDAR which are in operational not only for atmosphere or environmental application. Fig. 1 depicts the number of available stations where the 2-D scan LiDAR has been employed based on survey. It further confirms that there is no 2-D scan LiDAR in the continent (Africa) and in the country, except the one which we have now procured [see. Fig. 1].

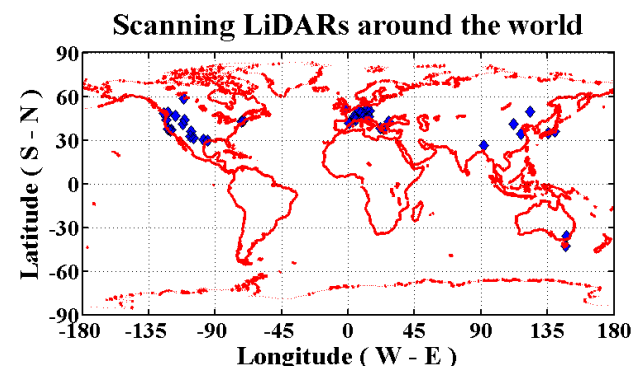


Figure-1: Geo-graphical position of 2-D scan LiDAR employed in the world.

### 2. UKZN 2-D Scan LiDAR – System Description

More recently, a portable 2-D scan LiDAR system is being procured at University of KwaZulu Natal, Durban (29°82' S; 30°94' E), South Africa. The system is primarily aimed for atmospheric backscatter measurements in the lower troposphere region (0 to 8 km). The complete system is planned to be transported through a flexible trailer and thus possible to make measurements at any place of interest. More technical details about the system are given here.

In general, the system consists of four main sections, such as, transmission, reception, data-acquisition and 2-D scan devices. Fig. 2 illustrates the system block diagram and describes how the system is being integrated.

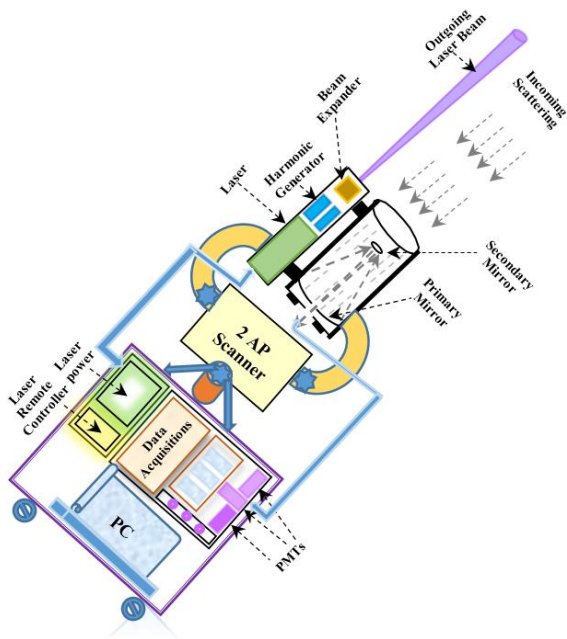


Figure-2 : A schematic sketch of UKZN 2-D scan LiDAR.

An Nd:YAG laser is used for transmission which is presently employed at the third harmonic (355 nm) at a repetition rate of 20 Hz with an energy of 35 mJ. The initial laser beam of 3.4 mm has been expanded into 10 times (i.e., 34 mm) and it reduces the beam divergence into 0.097 mrad. It also further allows the laser to be eye safe (due to reduction in energy) and thus it does not require any prior air-space permission.

The receiver system employs a Cassegrain telescope configuration with a 200 mm primary and 48 mm secondary mirror. A multimode optical fiber is used to couple the received backscatter optical signal from the telescope to the PMT. A Hamamatsu® R7400-U20 is used, which operates in the 300 nm to 900 nm wavelength range and has a fast rise time response of 0.78 ns. The data acquisition is performed by a LiDAR Computing and Electronics (LICEL) transient recorder which communicates with a host computer for storage and offline processing of data. The system is favoured due to its capability of simultaneous analogue and photon counting detection, which makes it highly suited to LIDAR applications by providing high dynamic range. A software interface is included with the LICEL system which allows the user to acquire signals without the need for any immediate programming. The system

has capabilities of receiving backscattered signal from 355 nm, 387 nm (Raman shifted signal) and their polarized (parallel and perpendicular to the laser transmission) components. The Raman-shifted backscatter measurements at 387 nm stands for  $N_2$  molecules and customarily used for measuring lower atmosphere temperature. The simultaneous temperature measurements assists to improve the aerosol-extinction calculations at different wavelengths, as presently we have been employing a model for retrieving the molecule (Rayleigh) contributions.

The integration of a scanner in the LiDAR system assists us in terms of (a) X-Y dimensional mapping of the atmosphere (horizontal or vertical cross-section), (b) focusing the target (industrial smoke or cloud of pollutants) and (c) to study the plume (say smoke, biomass burning and etc), haze and aerosol/pollutant dispersion.

### 3. Measurements and Observations

There were number of *insitu* measurements made at the UKZN Westville campus using 2-D portable LiDAR. However, here we present an obtained first result to illustrate the capability of the system. The selected measurements were made on 07 April 2014 at different modes of operation (vertically upwards) and using the scanner both in Azimuth and Zenith directions.

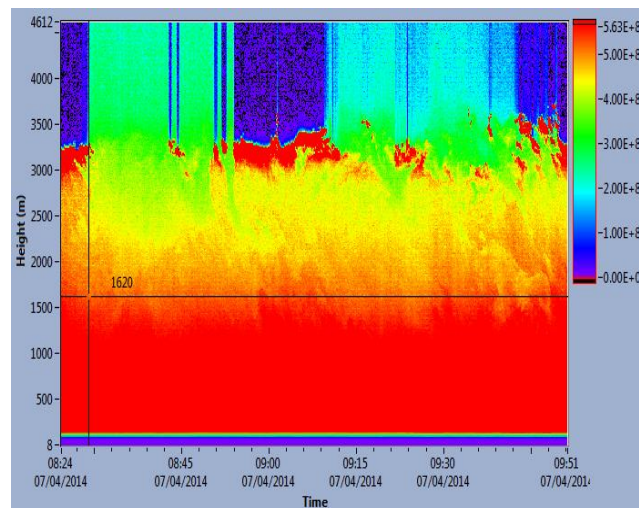


Figure-3 : Range-Time color map of range corrected backscattered signal for the day of 07 April 2014.

Fig. 3 illustrates the obtained backscattered signal (photon counts) for the day 07 April 2014. The system time has been adjusted to GMT, and the corresponding local time is GMT+2 hrs. Though, there are intermittent clouds observed, the backscattered signal can be inferred for the

height region up to 5 km. Note that the system is capable of archiving the information up to 122 km, but due to our interest, the results are shown here for addressing the boundary layer evolution. Further, depends on the type of cloud (optically and physically thick or thin), the laser may penetrate through and provides/not the backscattered signal. It is clear from the figure that the lower height region illustrates the boundary layer evolution, and at above 3 km, there were some low altitude clouds with varying thickness and structure.

As mentioned earlier, the system has also been operated in Zenith and Azimuth direction with angular resolution of  $5^\circ$ . Fig. 4 shows the obtained Azimuth (horizontal) scan measurements. It is also clear from the measurements, the system capability for addressing horizontal and vertical scan and addresses more in-sight features. It is visible from the figure that cloud passage over 3 to 5 km especially in  $10^\circ$  and  $20^\circ$  angle slots. Also, note that the system capable of making measurements with a possible minimum angular resolution of  $0.00025$  deg, in both azimuth and zenith direction. Here, the total number of shots indicates the actual period of the observations, i.e., 100 shots equivalent to 5 seconds of the measurements.

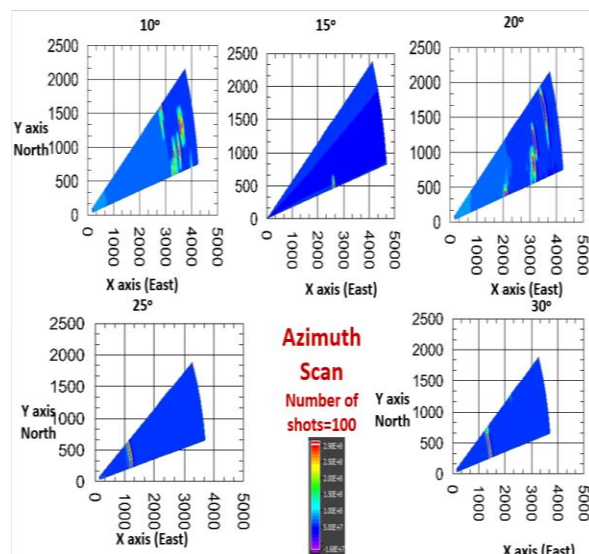


Figure-4 : An Azimuth scan of 2-D Portable LiDAR measurements for the day 07 April 2014. X and Y axis scales are range (m) from the transmission.

## 4. Summary

Here, we have presented the system description and technical details of the new 2-D portable scan LiDAR system. The first initial results illustrate the capability of the system. It has been planned to make more continuous measurements over the site at first, thereafter, planned to address measurements in different places in South Africa.

## 5. Acknowledgements

The authors sincerely thank UKZN, for funding the equipment. This work partly supported by the National Research Foundation (NRF–South Africa) bi-lateral research grants (UID: 786820), African Laser Centre and CSIR-DST Rental Pool programme. We also acknowledge Miss. Lulu Raxangana for assisting during the LiDAR observation time.

## 6. References

- Kanike R K and Sivakumar V, Remote Sensing of Aerosols using Sun-Photometer: Optical properties, Aerosol Types and Sources, Book, Lambert Academic Publishing, Germany, ISBN 978-3-659-70622-6., 2015.
- Sivakumar V , CSIR - NLC Mobile LIDAR for Atmospheric Remote Sensing, Advanced Techniques and Platforms, Dr. Boris Escalante (Ed.), ISBN: 978-953-51-0652-4, InTech, Available from: <http://www.intechopen.com/books/remote-sensing-advanced-techniques-and-platforms/csir-nlc-south-africa-mobile-lidar-for-atmosphere-remote-sensing>, 2012.
- Štrížik M, Zelinger Z and Sivakumar V and Pavel E, LiDAR for ground- and airborne trace gas detection, Chapter-6 in a text book, 'Lasers in Chemistry', Wiley-VCH publications, ISBN-10: 3-527-31997-2; -13: 978-3-527-31997-8, Germany, 2008.
- Stocker, T. F., Qin, D., Plattner, G.-K., Tignor, M., Allen, S. K., Boschung, J., Midgley, P. M. (2013). Climate change 2013: The physical science basis. *Intergovernmental Panel on Climate Change, Working Group I Contribution to the IPCC Fifth Assessment Report (AR5)*(Cambridge Univ Press, New York)

# Antarctic stratospheric ozone and seasonal predictability over southern Africa

Francois A. Engelbrecht<sup>1,2</sup>, Thando Ndarana<sup>1</sup>, Yushi Morioka<sup>3</sup>, Swadhin Behera<sup>3</sup>, Marcus Thatcher<sup>4</sup> and John L. McGregor<sup>4</sup>

<sup>1</sup>CSIR Natural Resources and the Environment – Climate Studies, Modelling and Environmental Health, Pretoria, South Africa

<sup>2</sup>Department of Environmental Sciences and Management, North West University, South Africa

<sup>3</sup>Japanese Agency for Marine Earth Science and Technology, Yokohama, Japan

<sup>4</sup>Oceans and Atmosphere Flagship, Commonwealth Scientific and Industrial Research Organisation, Melbourne, Australia

## *Abstract*

The impact of time-varying Antarctic stratospheric ozone on southern African summer climate variability is explored through atmospheric global circulation model (AGCM) sensitivity experiments. A control experiment following the design of the Atmospheric Model Intercomparison project (AMIP) was performed first, generating 12 different ensemble members using a lagged-average forecasting approach. These simulations are shown to be skilful in representing southern African summer-season inter-annual variability. This skill can be improved upon, over the entire southern African region, by replacing the climatological ozone distributions in the AMIP experiment by realistic time-varying ozone concentrations.

Key words: seasonal predictability, Antarctic stratospheric ozone, southern Africa, global atmospheric model

## INTRODUCTION

The objective of this paper is to explore the Antarctic stratospheric radiative forcing of climate variability over southern Africa, through a number of novel climate simulation experiments. An atmospheric global circulation model (AGCM), the conformal-cubic atmospheric model (CCAM), is used to perform these experiments. The main hypothesis is that the inclusion of time-dependent radiative forcing in the form of stratospheric ozone in climate models can improve skill in simulating inter-annual variability over southern Africa, in particular for the summer season. Specifically, the notion that summer-season predictability may be improved, stems from recent theoretical and observational studies, which have demonstrated a clear link between Antarctic stratospheric ozone depletion in spring and a lagged response in high- to mid-latitude tropospheric circulation in summer (e.g. Thompson and Solomon, 2002). However, in most state-of-the-art seasonal forecasting or climate simulation systems applied to predict/simulate Southern Hemisphere climate variability, this form of time-varying radiative forcing is not included - the long-term climatological averages are used instead. One possible reason for the current situation is the assumption that seasonal forecast skill largely exists due to tropical sea-surface temperature (SST) forcing of the atmosphere. Due to the large heat capacity of the ocean, this SST forcing can be readily included in seasonal forecasting systems based on AGCMs, using either persisted SST anomalies or predicted SSTs. This paper explores the hypothesis that more-realistic depiction of the atmosphere's ability to absorb and release radiation, through the representation of the time-varying concentrations of stratospheric ozone, can improve the model's skill to simulate/forecast inter-annual summer-circulation variability over southern Africa.

## THE CONFORMAL-CUBIC ATMOSPHERIC MODEL AND EXPERIMENTAL DESIGN

CCAM is a variable-resolution global atmospheric model, developed by the Commonwealth Scientific and Industrial Research Organisation (CSIRO) (McGregor, 2005). It employs a semi-implicit semi-Lagrangian method to solve the hydrostatic primitive equations. The model includes a fairly comprehensive set of physical parameterizations. The GFDL parameterizations for long-wave and short-wave radiation are used, with interactive cloud distributions determined by the liquid and ice-water scheme of Rotstajn (1997). A stability-dependent boundary layer scheme based on Monin Obukhov similarity theory is employed (McGregor et al., 1993), together with the non-local treatment of Holtslag and Boville (1993). In these simulations CCAM was integrated coupled to the dynamic land-surface model CABLE (CSIRO Atmosphere Biosphere Land Exchange Model). The cumulus convection scheme uses a mass-flux closure, as described by McGregor (2003), and includes downdrafts, entrainment and detrainment. CCAM may be applied at quasi-uniform resolution, or alternatively in stretched-grid mode to obtain high resolution over an area of interest. The simulations described here were performed on a C48 quasi-uniform grid (about 200 km resolution in the horizontal), and with 27 levels in the vertical. The CCAM atmosphere is about 50 km deep, and although a higher number of levels in the vertical is certainly preferable to better resolve stratospheric processes, the current spacing does result in realistic simulations of the Southern Hemisphere polar vortex.

A number of simulations in the style of the Atmospheric Model Intercomparison Project (AMIP) have

been performed to explore the impacts of time-varying ozone forcing on southern African climate. A control experiment was performed first, which followed the specifications of a traditional AMIP simulation: CCAM was forced with observed SSTs and sea-ice at its lower boundary, climatological specifications of CO<sub>2</sub> and stratospheric ozone were applied, and aerosol forcing was set to zero. The simulation was performed for the period February 1978 to December 2005. An ensemble of 12 members was obtained for the control experiment settings, with each member initialized using different initial conditions in February 1978 (using a lagged-average forecasting approach). These simulations were used to establish the baseline skill of the model in simulating inter-annual variability over southern Africa. An additional set of AMIP-style simulations was subsequently performed, also consisting of 12 members, but with the climatological ozone description replaced by the observed time-varying concentrations. The latter were obtained from the Coupled Model Intercomparison Project Phase Five (CMIP5) archive. It may be noted that performing the simulations was computationally- and time-intensive, and relied on the use of a computer cluster of the Centre for High Performance Computing (CHPC) of the CSIR.

## DISCUSSION

The model skill in simulating year-by-year summer 850 hPa geopotential anomalies over southern Africa (control simulation) is shown in Fig. 1. Skill is measured in terms of the Ranked Probability Skill Score (RPSS), where the climate for 1978-2005 is used as the reference forecast. Prior to this calculation, the geopotential values at each grid point, over the 27 December to February (DJF) seasons between 1978 and 2005, were divided into below-normal, normal and above-normal categories (as defined by terciles). Positive values in Fig. 1 indicate that the model simulations have skill over the reference forecasts based on climatology, whilst negative values indicate areas where the model forecasts are not skilful over climatology. The simulations of summer circulation anomalies are highly skilful, with maximum skill found over the interior regions of tropical Africa and eastern southern Africa. The simulations are less skilful over the western parts of southern Africa, but are still skilful over climatology. The simulations are the least skilful over the Southern Ocean, where the westerly wind regime and fast-propagating frontal systems prevail.

The inclusion of time-varying ozone instead of climatological ozone leads to an improvement in simulation skill over southern and tropical Africa for summer (Fig. 2), compared to the control experiment (Fig. 1). Here the change in skill is depicted in terms of the

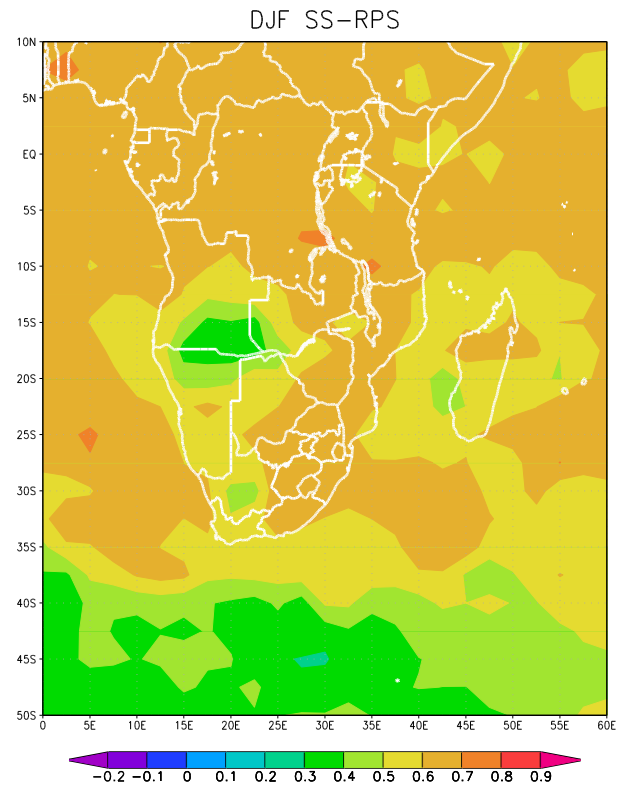


**Fig. 1.** CCAM skill in simulating summer 850 hPa geopotential height anomalies over southern Africa, for the control experiment. The Ranked Probability Skill Score (SS-RPS) is shown, with climatological circulation used as the reference forecast.

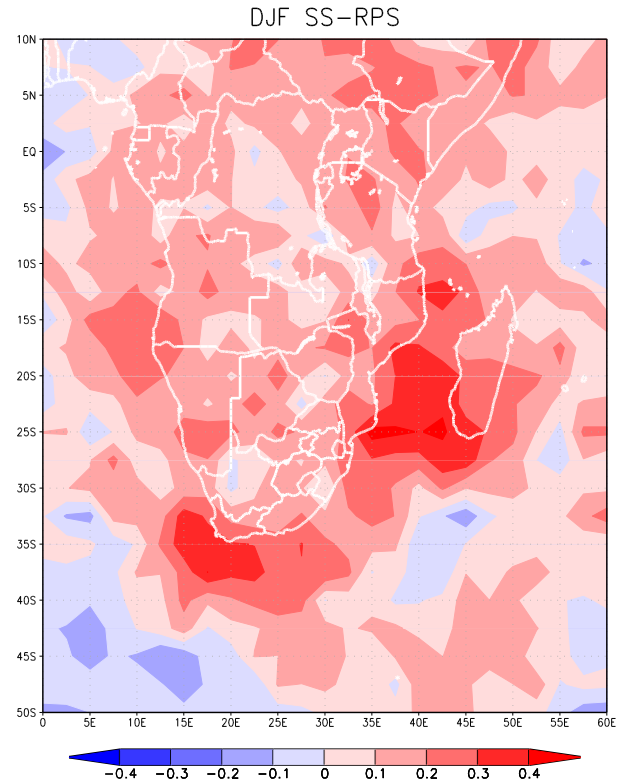


**Fig. 2.** Change in CCAM skill in simulating summer 850 hPa geopotential anomalies over southern Africa, for the case of time-varying ozone forcing relative to climatological radiative forcings.

RPSS, but with the CCAM simulations of the control experiment used as the reference forecast. A marked and spatially homogeneous improvement in skill is obtained across the southern African region. This result is consistent with the existing understanding that stratospheric ozone forcing in spring over Antarctica has a chain reaction in the mid-latitudes in the troposphere, lasting into the summer months. However, the propagation of this forcing effect deep into the subtropics and tropics of southern Africa, as suggested by the results obtained, has previously been unknown. It is possible, however, that the improvement in skill obtained is not the result of specifically Antarctic stratospheric ozone forcing, but rather of stratospheric forcing emanating directly from the subtropical and tropical atmosphere. However, similar improvements in skill have not been obtained for the autumn, winter and spring seasons, at least not over the southern African domain. This is demonstrated in Fig. 3, which shows the area-averaged SS-RPS over a southern African domain spanning the region 35 S to 10 S and 10 E to 40 E, for the summer, autumn (March to May, MAM), winter (June to July, JJA), spring (September to October, SON) and summer seasons.

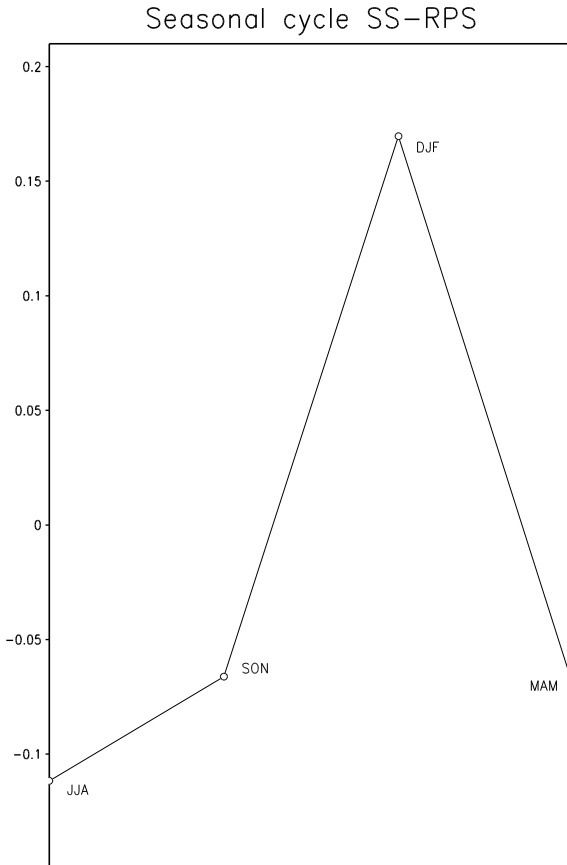


**Fig. 3.** Area-averaged change in CCAM skill in simulating seasonal 850 hPa geopotential anomalies over southern Africa, for the case of time-varying ozone forcing relative to climatological radiative forcings. The southern African domain covers the region 35 °S to 10 °S and 10 °E to 40 °E.

The reductions in skill obtained for the autumn, winter and spring seasons from the inclusion of time-varying stratospheric ozone suggests that the specification of the

time-varying ozone values in the tropics and subtropics is deficient. It also strengthens the deduction that the enhanced skill for summer is obtained due to Antarctic stratospheric ozone forcing in spring. This is an aspect that requires further investigation in future model development research to be performed at the CSIR.

## CONCLUSION

The AGCM CCAM was used to perform AMIP-style simulations designed to investigate the effects of the inclusion of time-varying radiative forcing in the form of stratospheric ozone in improving model skill in representing the inter-annual variability of the seasonal circulation anomalies over southern Africa. The AMIP-style simulations performed span the period 1978-2005. The simulations of the inter-annual variability of seasonal circulation anomalies are skilful for the austral summer in the control experiment. The inclusion of time-varying stratospheric ozone concentrations improves the simulation skill of circulation variability over southern Africa in summer. This result is consistent with dynamic circulation theory, according to which stratospheric forcing over Antarctica in spring has a pronounced mid-latitude response in summer. This study is the first to demonstrate that this response actually reaches the subtropical latitudes of southern Africa. It also implies the potential for an improvement in seasonal forecast skill over southern Africa, in forecasting systems that are initialised in spring using observed stratospheric ozone concentrations.

## ACKNOWLEDGEMENTS

The research is supported by the Water Research Commission Project K5/2163 and the SATREPS-IDEWS collaboration between Japan and South Africa.

## REFERENCES

- Holtstlag, A.A.M. and Boville, B.A. (1993). Local versus non-local boundary layer diffusion in a global climate model. *J. Climate* **6** 1825-1842.
- McGregor, J.L. (2003). A new convection scheme using a simple closure. In "Current issues in the parameterization of convection", *BMRC Research Report* **93**, 33-36.
- McGregor, J.L. (2005). C-CAM: Geometric aspects and dynamical formulation. CSIRO Atmospheric research Tech. Paper No. 70, 43 pp.
- McGregor, J.L., Gordon, H.B., Watterson, I.G., Dix, M.R. and Rotstayn, L.D. (1993). The CSIRO 9-level atmospheric general circulation model. CSIRO Div. Atmospheric Research Tech. Paper No. 26, 89 pp.
- Rotstayn, L.D. (1997) A physically based scheme for the treatment of stratiform clouds and precipitation in large-scale models. I: Description and evaluation of the microphysical processes. *Quart. J. Roy. Meteor. Soc.* **123** 1227-1282.
- Thompson, D.W.J. and Solomon, S. (2002). Interpretation of recent southern hemisphere climate change. *Science* **296**: 895-899.

# Evaluation of the ERA Interim Precipitation Products over Eastern Tanzania

Elewa B Msomba<sup>1</sup> and Christien J Engelbrecht<sup>1,2</sup>

<sup>1</sup>Department of Geography, Geo-informatics and Meteorology, University of Pretoria, Pretoria, South Africa

<sup>2</sup>Agricultural Research Council, Institute for Soil, Climate and Water, Pretoria, South Africa

## Abstract

Tanzania is a country rich in many natural resources such as forest reserves and farming fields. The rainfall networks in Tanzania has challenges with regard to their network distribution. Rainfall reanalysis has the potential to supplement observed rainfall in a data scarce area. Era-interim precipitation data was verified over the eastern parts of Tanzania. The correlation coefficient was stronger in the annual cycles than it was for inter-annual rainfall data. The test statistic of  $r = 0.97, 0.79$  and  $0.97$  for annual was significant for three stations and  $r = 0.40, 0.66$  was significant for two stations in the inter-annual rainfall cycle.

Key words: Eastern Tanzania, performance, annual and inter-annual

## INTRODUCTION

Tanzania possess large area rich in natural resources such as forests reserves, game reserves, water bodies and agricultural land. The country borders Mozambique and Malawi to the South, Uganda and Kenya in the North, Rwanda, Burundi and Democratic Republic of Congo to the West, Zambia to the Southwest and Indian Ocean to the east. The economic setup of the country is highly dependent on agriculture. The agricultural sector is directly affected by the distribution of seasonal rainfall. The understanding of the Intra-annual and annual rainfall cycles can help the farming community in planning for planting, diseases and pest control (Kijazi and Reason, 2004). Tanzania has two main rainfall seasons, short (Vuli) and long rainfall seasons (Masika) in various localities. The shortage of rainfall during a wet seasons can lead to shortage in agricultural production. Both increase and decrease in rainfall have a serious implication to socio-economic sectors with agriculture being affected most (Timiza, 2011).

This study focus on the eastern coast of the country. The short and long rain seasons are associated with the movement of the Inter Tropical Convergence Zone (ITCZ). The north coast experience two rain seasons and the south one rainfall season (Mhita and Nassib, 1987). Tanzania is located in East Africa between latitudes 1°S and 12°S and longitudes 29°E to 41°E. The red borders in figure 1 surrounds rainfall

stations of which four of them were used in this study (Timiza, 2011; 2013).

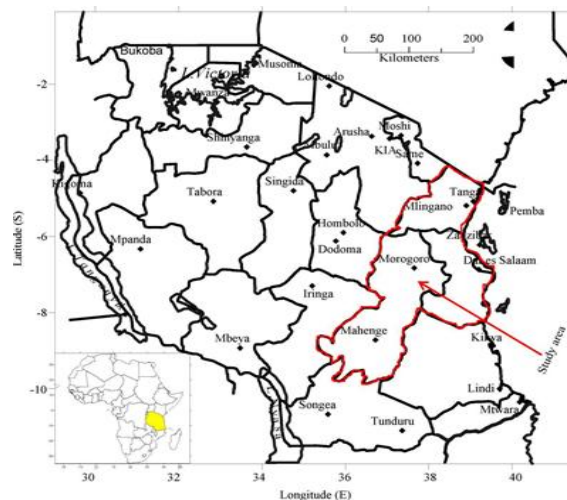


Figure 1: The map of Tanzania showing the distribution of rainfall stations and the area of study surrounded by red boundary.

Rainfall stations network over Tanzania, as of the most of Africa, has challenges with regards to spatial density. With climate variability and climate change impacting on agricultural activities monitoring of rainfall is important. With the sparseness of rainfall stations the alternative was to make use of gridded rainfall re-analysis or estimation products. In our study

<sup>1</sup>Tel: +27782955966 Email: [korrosso@yahoo.com](mailto:korrosso@yahoo.com)

<sup>1,2</sup>Tel: +27(12)3102676 Email: [engelbrecht@arc.agric.za](mailto:engelbrecht@arc.agric.za)

we evaluated the Era-interim precipitation data against observed rainfall station data. Reanalysis rainfall data was also used in restoration of rainfall observational networks to fill up gaps in the dataset (Chamberlain *et al.*, 2014; Leeuw *et al.*, 2014). This was a further motivation for assessing gridded rainfall products to rainfall station data.

Therefore, this study aims at evaluation of one of the Era-interim precipitation products (Total daily precipitation) and to assess the performance of the model data as compared to observations.

## DATA AND METHOD

In this study 36-years of daily data from 1979 to 2014 were used to calculate monthly and yearly rainfall totals for both Era-interim and rainfall stations data. Daily observed rainfall data was provided for four stations by the Tanzania Meteorological Agency (TMA). Data quality control was used to check for consistency of the data and missing data removed. Data is missing when data is not available for a particular station at that particular time. Data for one station (Mahenge) was missing up to 1992, therefore in the analysis for Mahenge presented here, 1993-2014 was analyzed. Mahenge station was established in late 1992.

The three hourly reanalysis of data from European Centre for Medium Range Weather Forecast (ECMWF) was used as gridded rainfall dataset to be evaluated. For this purpose it was needed to extract the rainfall data from the same geographical location as data of the corresponding weather station. To do that, a square grid box of  $0.75^{\circ} \times 0.75^{\circ}$  was constructed around each station. The data was then read and extracted from the four corners of the grid box using Grid Analysis and Display System (GrADS). Average value of the four points was taken to represent reanalysis rainfall for that grid. After quality control, the available data was then used to evaluate reanalysis data on each grid. The inter-annual rainfall and annual rainfall cycle was evaluated.

Data analysis and programming was done using FORTRAN programming, Grid Analysis and Display System (GrADS) as well as the Quantum Geographic Information System (QGIS) software.

Correlation between average monthly and annual rainfall totals between the datasets was performed. The Pearson's correlation coefficient ( $r$ ) lies between -1 and +1. The interpretation of the relationship follows that higher values of the correlations indicated that the datasets had strong relationships. The correlation coefficient is a measure of co-fluctuation

between observed rainfall and Era-interim precipitation (Hennemuth *et al.*, 2013).

## RESULTS AND DISCUSSION

Comparison of monthly average precipitation for both data sets was performed. The correlation were calculated for each station.

Annual rainfall correlation coefficients were calculated between Era-interim and rain-gauge observations. Both stations show positive correlations. The significant correlations are  $r = 0.97$ ,  $0.79$  and  $0.97$  representing Morogoro (Mor), Mahenge (Mah) and Dar es Salaam (Dar) respectively. The data have strong positive relations for three stations except for Tanga which show weak relation between the two datasets. The significance of the relationships between the datasets are well explained in a section explaining test statistics of  $r$ .

The stations in figure 2 are assigned short names as TanO, MorO, MahO and DarO representing observed rainfall for Tanga, Morogoro, Mahenge and Dar es Salaam respectively as given series names in figure 2. For the model reanalysis data the position of O is replaced by M indicating Era-interim precipitation data for each station. The data covers time from 1979 to 2014 for all stations except for Mahenge (Mah) which starts from 1993 to 2014. The Era-interim is a result of 3 times step with initial time 00 at a model resolution of  $0.75^{\circ}$  (Figure 2).

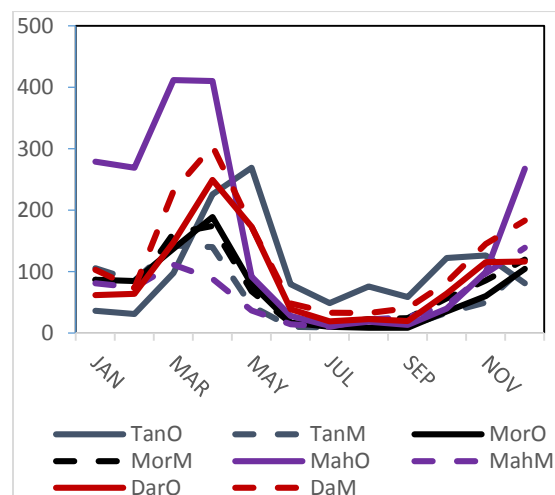


Figure 2: Monthly average precipitation (O) from surface land Meteorological stations and Era-interim precipitation (M). Solid lines indicate observed annual rainfall totals (O) and dashed lines indicate annual Era-interim precipitation totals.

Inter-annual correlation between observed station rainfall and Era-interim precipitation datasets was

much weaker than the correlation for the annual rainfall cycle. Their correlations were  $r = 0.06, 0.40, 0.26$  and  $0.66$  for Tanga (Tan), Morogoro (Mor), Mahenge (Mah) and Dar es Salaam (Dar) respectively. The two datasets still show positive relationship which have significant correlation for  $r = 0.4$ , and  $r = 0.66$  with Tanga station having the weakest relation (Figure 3). The observed rainfall is represented by TanO, MorO, MahO and DarO representing observed rainfall for Tanga, Morogoro, Mahenge and Dar es Salaam respectively as they appear in series names in figure 3. The symbol M is assigned for the Era-interim precipitation data and takes the position of O for the each station.

For the model reanalysis data the position of O is replaced by M indicating model reanalysis data for each station. Figure 3 shows observed (O) and model (M) reanalysis rainfall data for all stations from 1979-2014 except for Mahenge that has time range from 1993-2014.

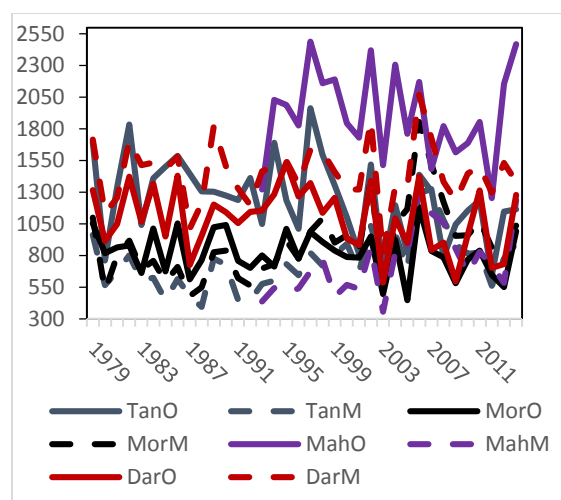


Figure 3: Comparison of annual Era-interim precipitation to observed annual station rainfall totals. Solid lines indicate observed rainfall totals (O) and dashed lines indicate Era-interim precipitation totals.

#### TEST STATISTICS OF SIGNIFICANCE OF CORRELATION ( $r$ )

The results from the regression analysis between observed precipitation and Era-interim on annual and inter-annual time scales (Figure 2 and 3) were statistically tested at a significant level of  $\alpha = 0.05$ . The investigation of the significance of  $r$  were carried out by using student t-test by assuming that both precipitation types (observations and Era-interim) had equal sample size. The data samples were normally distributed and the population correlation coefficient being zero ( $\rho = 0$ ) (Shaw and Wheeler, 1994). The

hypothesis were described by stating Null and alternative hypothesis of the correlation  $r$  for sample and population as shown below.

$H_0: \rho = 0$  This Null hypothesis means there is no correlation between observed and Era-interim precipitation.

$H_1: \rho \neq 0$  This Alternative hypothesis means that there is a significant correlation between the observed and Era-interim precipitation.

The interpretation of the significance of correlation  $r$  followed that if the calculated test statistic  $T$  is greater than the  $t$ -value then the null hypothesis was rejected in favour of the alternative hypothesis. The opposite was true for  $T < t$ -value. Table 1 summarizes the results for none significant and significant correlation  $r$  based on test statistic  $T$  and  $t$ -value.

The results of annual rainfall totals indicate three stations (Morogoro, Mahenge and Dar es Salaam) having significant correlation  $r$  while correlation for Tanga was not statistically significant. Therefore, there is a significance relationship between the observed and Era-interim annual precipitation for three stations (Table 1).

The results indicated that significant relations for Inter-annual rainfall totals were observed for Morogoro and Dar es Salaam. A further analysis showed that inter-annual rainfall totals for Tanga and Mahenge were not significant (Table 1).

Table 1. Statistical significance results of t-test for annual and inter-annual rainfall totals. The table shows the correlation ( $r$ ),  $t$ -value and significance ( $\text{sig}^*$ ) of the correlation.

Annual			
Station	$r$	$t$ -value	$\text{Sig}^*$
Tanga	0.18	0.58	NS
Morogoro	0.97	12.62	S
Mahenge	0.79	4.08	S
Dar es Salaam	0.97	12.62	S
Inter-annual			
Station	$r$	$t$ -value	$\text{Sig}^*$
Tanga	0.06	0.35	NS
Morogoro	0.40	2.55	S
Mahenge	0.26	1.20	NS
Dar es Salaam	0.66	5.12	S

The test statistic  $T$  is 2.228 for annual rainfall totals, and for inter-annual  $T = 2.032$  tabulated for Tanga, Morogoro and Dar es Salaam and  $T = 2.086$  for Mahenge. The correlation was tested at a significant

level of  $\alpha = 0.05$  for a 95% confidence interval. The degree of freedom was computed from the relations  $df = n-2$ , where  $n$  stands for sample number. In table 1, the significant correlation is represented by S (S = significant) and N (N= Not significant).

## CONCLUSION

The study evaluated 36-years of reanalysis data using annual cycles and inter-annual time series. Annual cycles indicate that the data have similar pattern. Annual cycles show stronger correlation for all stations as compared to annual time series. Although both annual and inter-annual rainfall totals have positive correlations the relations between observed rainfall and Era-interim precipitation is stronger with the annual rainfall that it is for inter-annual. The significance of relation is also observed to be strong for annual. In conclusion, the performance of rainfall products had a peak trend in March, April and May which signify a wet season.

## REFERENCES

Chamberlain, J.M., Bain, Boyd, D.F.A., McCourt,K., Butcher,T & Palmer,S. (2014). Forecasting storms over Lake Victoria using a high resolution model. *Meteorological Applications* 21:419-430.

Hennemuth, B., Bender, S., Bülow, K., Dreier, N., Keup-Thiel, E., Krüger, O., Mudersbach, C., Radermacher, C., Schoetter, R. (2013). Statistical methods for the analysis of simulated and observed climate data, applied in projects and institutions dealing with climate change impact and adaptation. CSC Report 13, Climate Service Center, Germany.

Kijazi, A.L and Reason, C.J. (2004). Relationships between intraseasonal rainfall variability of coastal Tanzania and ENSO. *Theor. Appl. Climatol.* 82, 153–176 DOI 10.1007/s00704-005-0129-0.

Leeuw, J.D., Methven, J & Blackburn, M. (2014). Evaluation of Era-interim reanalysis precipitation products using England and Wales observations. *Q. J. R. Meteorol. Soc:* DOI:10.1002/qj.2395.

Mhita, M.S and Nassib, I.R. (1987). The onset and end of rain in Tanzania. *Proc. 1<sup>st</sup> Tech. Conference. Meteor Res Eastern and Southern Africa*, Nairobi, pp 101–115.

Timiza, W. (2011). Climate variability and satellite – observed vegetation responses in Tanzania. Master thesis Physical Geography and Ecosystem Analysis, Lund University, Seminar series 205, 30 ECTS.

Timiza, W. (2013). Status and priority needs of monitoring and predicting climate Anomalies and extremes in Tanzania: Tanzania Meteorological Agency (TMA): Regional workshop on Climate Monitoring and Analysis on Climate Variability, Pretoria,, South Africa.

Shaw, G. and Wheeler, D. (1994). *Statistical Techniques in Geographical Analysis* (2nd Ed.) David Fulton Publishers Ltd, London.

## Comparison of January 1981 and January 2014 cut-off low pressure systems

Msawenkosi A T Mpanza

Department of Geography, Geo-informatics and Meteorology, University of Pretoria, South Africa

Liesl L Dyson

Department of Geography, Geo-informatics and Meteorology, University of Pretoria, South Africa

### Abstract

A comparison of two cut-off low pressure system, January 1981 and January 2014 is carried out using National Center for Environmental prediction data. This study attempts to identify key similarities and differences of these two systems. The results show that in both systems the ridging high caused strong on-shore flow into the south and south east coasts. In 1981 the on-shore flow was stronger than the 2014 case. The 2014 COL was deeper than the 1981 COL and there was very little westward tilt with height while the 1981 one had a clear westward tilt with height. Convergence of moisture was high in the 1981 case as compared to the 2014 case. Both systems reached their maximum depth 24hrs before maximum rainfall occurred. The 2014 COL produced more rainfall than the 1981 COL over the south Western Cape.

Key words: COL, Moisture flux, Ridging high, Onshore flow, Divergence.

### Introduction

Cut-off lows (COLs) are high impact weather systems that have a significant influence on the society due to their association with violent weather (Favre *et al.*, 2011). Singleton and Reason (2007) stated that COLs cause severe weather due to intrusion of stratospheric air into the troposphere which causes deep moist convection (DMC). DMC can results in significant amount of rainfall over a short period of time which increases the possibility of flash flooding (Singleton & Reason, 2007).

However not all COLs are associated with heavy rainfall. It is only when there is enough moisture and a correct balance in the dynamic forcing such as low level convergence, strong vertical motion and divergence that heavy rainfall does occur (Zhao & Sun, 2007). Taljaard (1985) stated that only one in five systems results in flooding, mainly over the south and eastern coastal belts.

In this paper the cut-off low of 1981 was compared to the one which occurred in 2014 by investigating dynamic and moisture parameters. Emphasis is placed on moisture flux, wind divergence, moisture flux divergence and rainfall. The two weather systems are worth comparing since they both occurred in January and both caused heavy rainfall over the Southwestern

Cape. They both had a northerly displacement to be situated over the border<sup>1</sup> of Namibia and South Africa when the heaviest rainfall occurred.

### Instrumentation and Method

The National Center for Environmental Prediction-National Center for Atmospheric Research (NCEP-NCAR) reanalysis-2 data were used (Kanamitsu *et al.*, 2002). This dataset has a spatial resolution of 2.5° ×2.5° and temperature, geopotential height, zonal and meridional winds and relative humidity were obtained on all pressure levels. Rainfall data for January 1981 and 2014 were obtained from the South African Weather Service (SAWS). Grids analysis and display system (GRADS) was used extensively for calculating and visualization of meteorological parameters (Doty 2014). Calculations were carried out at the following levels 1000, 850,500,400 and 200 hPa. The table below shows meteorological parameters that were used for comparison and the levels in which calculations were done.

---

<sup>1</sup> Email: thbms17@gmail.com

Table.1 Meteorological parameters.

parameter	Equation	units	Level (hPa)
Geopotential Height	$\int_0^h g(\phi, z) dz$	gpm	850,500
Moisture flux	$q\bar{V}$	$kg.kg^{-1}.ms^{-1}$	1000-850
Moisture flux convergence	$\nabla \cdot (q\bar{V})$	$kg.kg^{-1}.s^{-1}$	1000-850
Divergence	$\nabla \cdot \bar{V}$	$s^{-1}$	400-200

QGIS was used to plot rainfall maps.

## Results and Discussions

On January 25<sup>th</sup> 1981 heavy rainfall occurred over the Southwestern Cape (Fig. 1a). Several stations recorded above 100 mm in 24 hrs. The highest rainfall recorded was 181 mm at Concordia rainfall station. A COL located close to Springbok and had a depth of 5700 gpm at 500 hPa (Fig. 2a). A well-developed surface low at 850 hPa was situated over the Northern Cape and had a depth of 1460 gpm. East of the surface low was a northerly flow which was rich in moisture as it had a tropical origin. To the south, a ridging high was inducing a south easterly flow which amalgamated with the north-easterly flow coming from the Mozambique Channel. What is also seen from Fig. 3a is that this low level moisture was converging over this region, which is favorable for rainfall formation. The hovmoller diagram in Fig. 4a also shows how the flow changed anticlockwise, from a south easterly into an easterly flow.

In the upper air strong divergence was taking place above the region of low level moisture flux convergence as it can be seen on Fig. 5a. These conditions generated a large scale dynamic ascent. Since moisture was abundant heavy rainfall over south Western Cape occurred. The white triangle in Fig. 3a, 4a and 5a indicates the position of the Concordia station which recorded 181 mm during this day.

On January 6<sup>th</sup> 2014 heavy rainfall occurred over the Western Cape. Also in this event several stations recorded above 100 mm of rainfall in 24 hrs (Fig. 1b). The highest rainfall recorded was 201.8 mm in 24 hrs at Swellendam, which marginally exceeds the rainfall of 1981 case over the southwestern Cape. Fig. 2b shows a COL positioned over Alexander Bay with a depth of 5680 gpm. This 500 hPa low was slightly deeper and further north than the one of 1981. However the gradient of the 1981 was tighter over the interior of South Africa. At 850 hPa the circulation

was characterized by two low pressure systems. The low over the western interior was directly underneath the 500 hPa low making it equivalent barotropic. Fig. 3b shows that moisture flux was more southerly. The main area of moisture flux convergence was over the central interior but it was also occurring over the Southwestern Cape Fig. 3b. The moisture flux and moisture flux convergence for 2014 COL are slightly weaker than those associated with the 1981 COL Fig. 4b. The white triangle in Fig. 3b, 4b and 5b indicates Swellendam rainfall station where 201.8 mm of rainfall.

Upper air divergence was taking place south east of the 500 hPa low almost in the same region as that of 1981 COL (Fig. 5b). This upper air divergence region was overlaying the moisture flux convergence at the surface. These conditions contributed to dynamical ascent, which resulted in heavy precipitation.

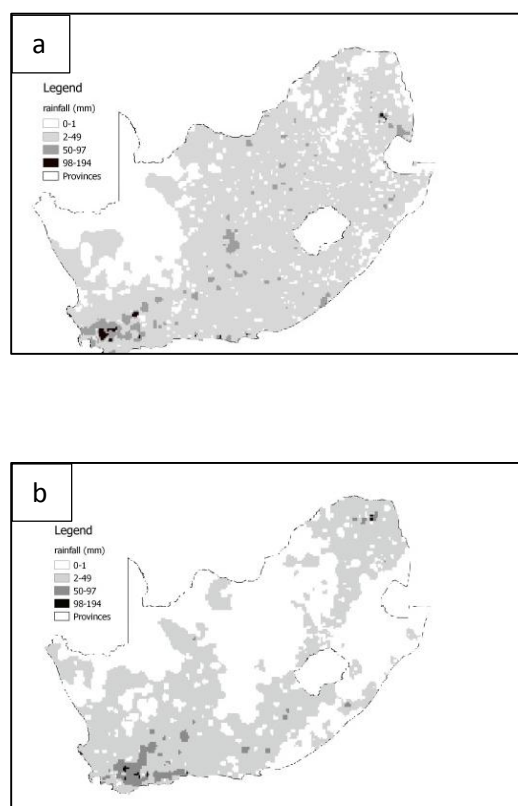


Figure 1: 24 hrs daily rainfall maps (mm) on (a) 25 January 1981 and (b) 06 January 2014.

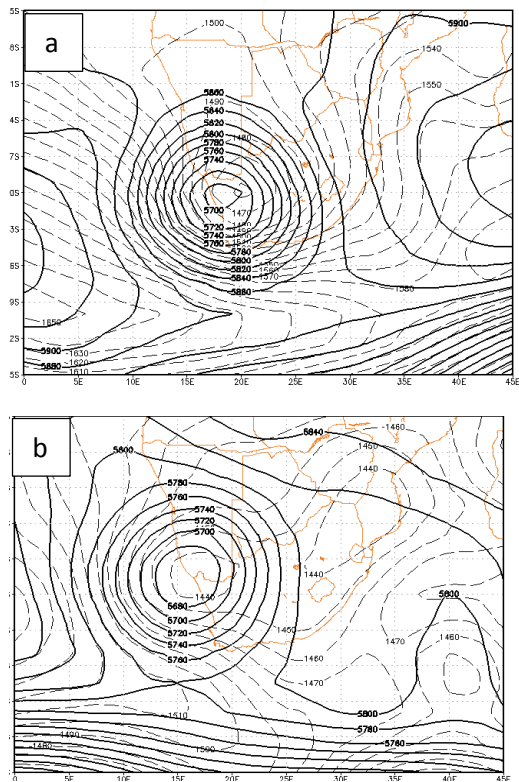


Figure 1: Geopotential height (gpm) at 500 hPa (solid lines) and 850 hPa dashed lines on (a) 25 January 1981 and (b) 06 January 2014.

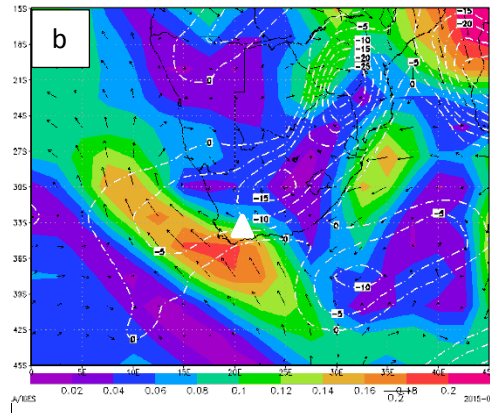
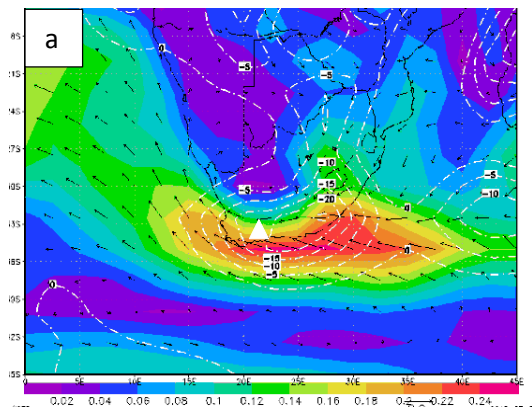


Figure 3: Average (1000-850 hPa) moisture flux vector (arrows), Average (1000-850 hPa) moisture flux magnitude (shading) and Average (1000-850 hPa) moisture flux divergence ( $\times 10^7$ ) (dotted lines) on (a) 25 January 1981 at 12Z and (b) 06 January 2014 at 12Z. Location of heaviest rainfall (white triangle).

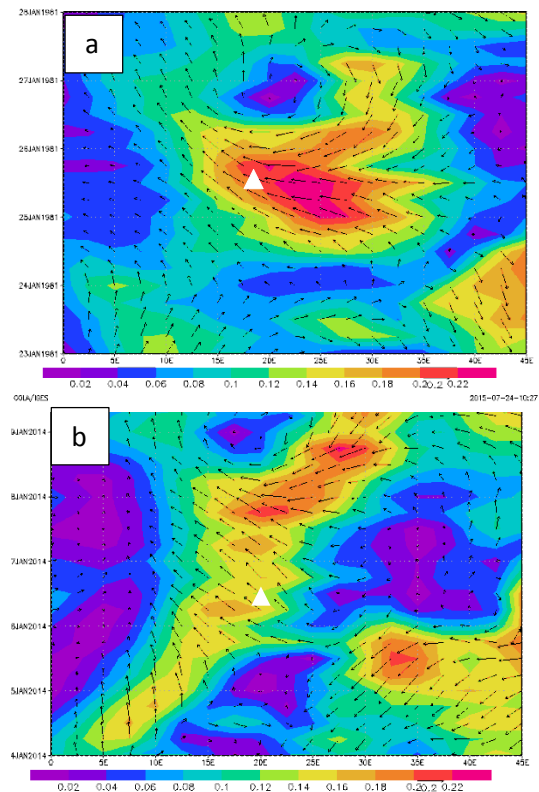


Figure 4: Hovmoller diagram of Average (1000-850 hPa) moisture flux (shading) and Average (1000-850 hPa) moisture flux vectors (arrows) on (a) 23-25 January 1981 and (b) 04-08 January 2014. Location of heaviest rainfall (white triangle)

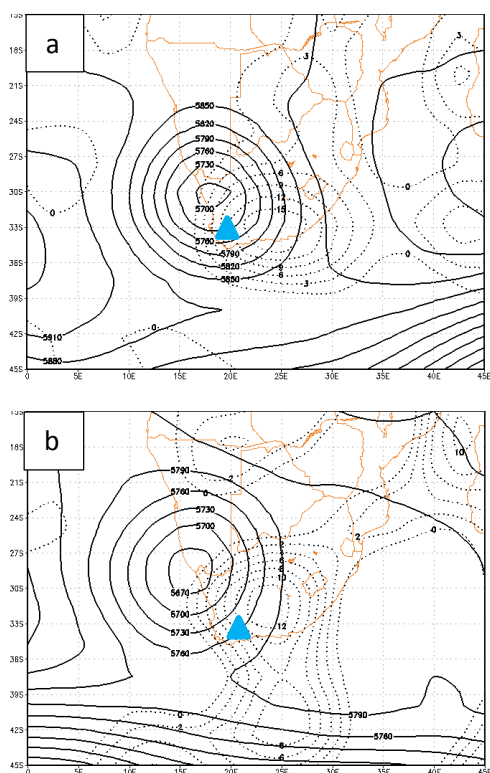


Figure 5: Geopotential height (gpm) at 500 hPa solid lines, Average (400-200 hPa) divergence ( $\times 10^5$ ) (dotted lines) on (a) 25 January 1981 at 12Z and (b) 06 January 2014 at 12Z. Location of heaviest rainfall (blue triangle)

## Conclusions and Recommendations

The COLs of 1981 and 2014 both reached their minimum depth 24 hrs before the heaviest rainfall occurred. In both cases intense moisture flux occurred when the south Atlantic high was ridging south of the country. Heaviest rainfall is distributed over the same region, when the two systems were marginally at the same location over the Northern Cape. The COLs differ in that the gradient of the 1981 COL was stronger than the 2014 COL. The 1981 COL had more moisture flux Figs. 4(a) and (b) and larger moisture flux convergence than the 2014 Figs. 3(a) and (b). 1981 COL lasted three days while the 2014 COL lasted four days.

It is recommended that other dynamical parameters such as temperature advection, vorticity advection, and static energy are investigated to infer and compare the development and the movement of the two systems.

## Acknowledgements

The SAWS is greatly acknowledged for providing rainfall data.

## References

- Doty, B.E. (2014). Grid Analysis and Display System (GrADS), Center for Ocean Land – Atmosphere Interaction, Institute of Global Environment and Society, 149 pp.
- Favre, A., Hewitson, B., Lennard, C., Cerezo-Mota, R., Tadross, M. (2011). Relationship between cut off lows and semiannual and the southern oscillation. *Clim Dyn.* 38:1473–1487.
- Kanamitsu, M., Ebisukazi, W., Woollen, J., Kengyang, S., Hnilo, J., Fiorino, M., Potter, G.L. (2002). NCEO-DOE AMIP-II REANALYSIS (R2):AN updated NCEP/NCAR reanalysis covering 1971-present feature new physics and observed soil moisture forcing and also eliminates several previous errors (2002) *American Meteorological society, BAMS.*83:11-1631.
- Singleton, A.T., Reason, C.J.C. (2007). Variability in characteristics of cut off low pressure systems over subtropical Southern Africa. *Int. J. Climatol.*2: 295–310.
- Taljaard, J.J. (1985). Cut-off lows in the South African region. *South African Weather Bureau, Technical paper no:14.*
- Treigaardt, D.O., Terblanche, D.E., Van Heerden, J., Laing, M.V. (1988). The Natal Floods of 1987. *Weather Bureau Technical paper no:19.*
- Zhao, S. and Sun, J. (2007). Study on cut-off low-pressure systems with floods over Northeastern Asia. *Meteorol Atmos Phys.* 96:159-180

# Microstructure of rainfall events on the southern African Highveld

**J van Loggerenberg, SJ Piketh, RP Burger and E Becker**

*1. North West University, School of Geography and Environmental Management, Private Bag X6001, Potchefstroom, 2520, South Africa*

*2. South African Weather Service (SAWS), Pretoria, South Africa*

## Abstract

Rainfall is highly variable over space and time. This is due to changes in the composition of the drop size distribution (DSD) from one location to another and between events. To understand the DSD high resolution data is needed. South Africa has an extensive network of weather radars. It includes 9 single polarized S band radars, 1 dual polarized S band weather radar, 2 mobile dual polarized X band radars and 5 C band radars. Combining data measured by radars, disdrometers and rain gauges can improve the accuracy and reliability of data. In this study radar rainfall estimates was improved by stratifying events into convective and stratiform rainfall. A high density rain gauge network and a parsivel disdrometer are used to evaluate different rainfall algorithms. 109 events have been measured with 180mm of rain observed. Implementing a new unique Z-R relation to 3 different case studies showed an increase in accuracy compared to the Marshall and Palmer. For mixed precipitation the data improved from 66% to 87% compared to rain gauge data. For convective events correlation improved from 80% to 95% and for stratiform from 49% to 50%.

## Introduction

Rainfall has a high variability over space and time. Extreme rainfall events occur from time to time over the interior of South Africa which cause large scale damage to infrastructure and even in some cases death (Dyson, 2009). Therefore understanding the microphysical processes within clouds, cloud dynamics and synoptical conditions associated with these events will improve the prediction and forecasting thereof. This will help in water resource management, agricultural management, disaster management etc. Improving radar rainfall estimates is therefore very important especially over the interior and Highveld of South Africa due to its importance in agricultural activities and the large number of citizens living in highly dense neighbourhoods within this area.

The climate of the world is a dynamic and complex system which undergoes changes and can vary between years. Models are showing us that in the future the frequency of extreme events will increase (Mason et al., 1999). The amount of rainfall does not necessarily change but the rain rate does. Therefore daily rainfall data will limit the ability to study the small scale variability of microphysical processes within clouds. High resolution data will give the ability to study changes and trends of rain rates which is mostly the contributing factor in the occurrence of flash flood, landslides, sinkhole, erosion and other natural disasters. High resolution data and quality observation is needed to accurately measure rainfall (Nikolopoulos et al., 2008).

This paper includes a thorough analysis of data from the disdrometer and the radars to determine the variability of the DSD and the effect that it has on rainfall rates. The outline of this paper is as follows. Section 2 sets out the methodology. Then a discussion on how remote sensing estimates of rainfall will help better the accuracy of data and the microphysical properties within clouds. Lastly a discussion of the data will be done and the variation of the DSD will be discussed.

## Methodology

The South African Weather Service operates three weather radars which cover the interior and Highveld of South Africa. This includes the Irene and Ottosdal weather radar which is S band single polarized radars and the Bethlehem weather radar which is a state of the art dual polarized radar (Figure 1). Data from these radars were compared to different ground based instruments. This includes a Parsivel disdrometer (Figure 2A) which was situated in Potchefstroom at the North West University and a high density rain gauge network (Figure 1) situated north of Potchefstroom which consist of 20 tipping bucket rain gauges over an area of 3294 sq.

The Parsivel disdrometer is an optical rain gauge that uses cutting edge laser technology to measure each particles size and velocity as it moves through the laser beam (Figure 2B). It consists of two housing units which hold the receiver and the transmitter. With a sampling area of 54cm<sup>2</sup> it can

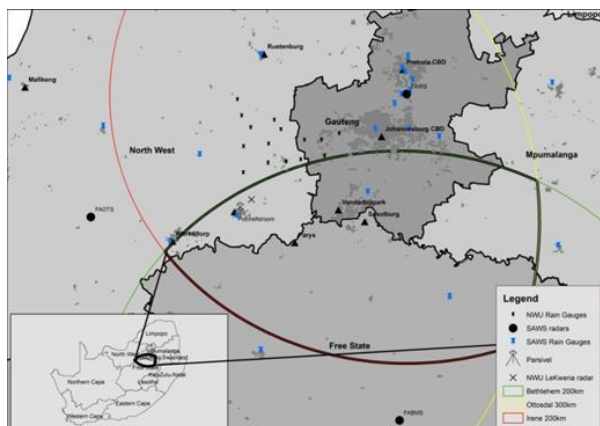


**Figure 1**

*Placement of the radars, disdrometer and rain gauges*

measure particle up to 25mm in diameter and velocities between 0.2 and 20m/s. The particles are then categorised into 1024 classes of size and velocity and is displayed on a  $32 \times 32$  matrix. The Parsivel was also placed in close proximity to a tipping bucket rain gauge for calibration purposes (Figure 2A). One of the greatest advantages of using a Parsivel disdrometer is the ability to measure reflectivity and rain rate simultaneously.

Events were stratified into convective and stratiform events by using TITAN (Thunderstorm Identification, Tracking, Analysis and Nowcasting) which is a program that supports storm properties analysis. This was done to calculate a unique Z-R relation for each event. A unique Z-R relation was also measured for mixed precipitation. Radar rainfall estimates was then measured by using the different relations and compared to the ground truth data. The South African Weather Service uses a default Z-R relation to estimate rainfall. This Z-R relation called the Marshall and Palmer is widely recognized around the world as the most accurate for the most number of climates and events (Nikolopoulos et al., 2008; Tenorio et al., 2010; Uijlenhoet, 2001; Ulbrich and Lee, 1999).

The North West Province has a mean annual precipitation of 400mm. The rainfall season occurs mid-summer with most of the rain between January to March (Schulze, 1997). The data in this paper was measured from the 21st of February to the 31st of March 2014. This is a total of 39 days and in this time there was 109 events measured. Events were defined by a 15min gap between measurements. The rain amount for these 39 days was 180mm.

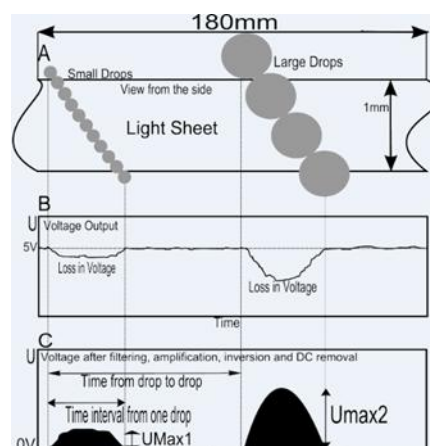


**Figure 2**

*The Parsivel disdrometer deployed in close proximity to a tipping bucket rain gauge.*

### Radar Rainfall Estimates

Remote sensing is extremely important in the measurement of rainfall and the microphysical processes of clouds. It involves the process of gathering information from a distance and measuring an object without being in contact with it (Campbell, 1996). Radars work by sending out powerful electromagnetic waves into the atmosphere and listening for the waves returning made by raindrops. This returning power is directly related to a physical quantity called reflectivity (dbz) measured in  $\text{mm}^6/\text{m}^3$  (Krajewski and Smith, 2002). These instruments provide the opportunity to observe large areas with a minimal infrastructure footprint which is extremely important especially in the study of cloud dynamics. The measurements made by radars on rainfall are very important for models of flood predictions, validation of satellite data and the analysis of extreme rainfall events (Krajewski and Smith, 2002). There are also a number of errors associated with weather radar measurements. At large distances radars tend to underestimate events due to the beam of the lowest cappi (constant altitude plan position indicator)

increasing in height above sea level as distance from the radar increases (Ulbrich et al., 1999) (Figure 3). Some other errors and limitations associated with the use of radars include ground and sea clutter, mountains, shallow rain, partial beam blocking, the bright band etc. (Doviak and Zrnic, 1993; Rinehart, 1997).

Tipping bucket rain gauges (TBR) and weather radars have been used for centuries in studying rainfall. However, these conventional methods have their limitations and specialized instruments such as the Parsivel disdrometer are playing an increasingly bigger role due to its ability to measure both the reflectivity and the rain rate (Nikolopoulos et al., 2008; Krawjeski and Smith, 2002; Krawjeski et al., 2002; Tokay et al., 2003). The Parsivel uses the shadow of the particle created by the laser of the transmitter and received by the receiver to convert it into the size and velocity of the particle (Figure 4).

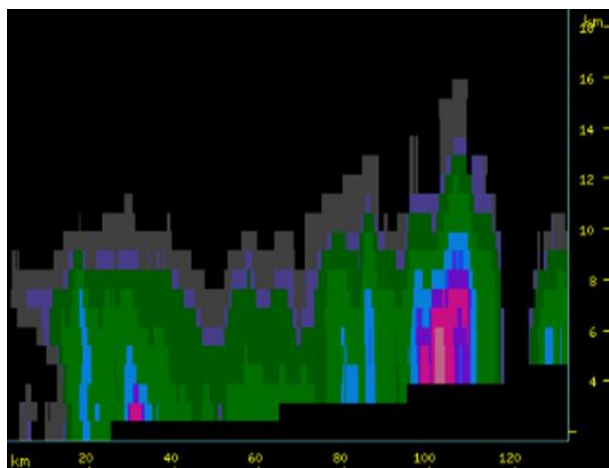


**Figure 3**

*Cross section of radar measurements at large distances*



**Figure 4**

*Parsivel process from above*

The biggest challenge in radar rainfall estimates is the conversion of radar reflectivity measure by the radar aloft to rain rate on the ground (Uijlenhoet, 2001). Rain intensity and radar reflectivity are products derived from the drop size distribution (DSD) (Tokay et al., 2003). The DSD represents a body of particles within a cloud with its different sizes and distributions. The DSD is a fundamental part of rainfall and is highly variable over time and

space (Jaffrain and Berne., 2010). Determining the variability of the DSD involves how the relationship between the reflectivity and the rain rate changes. This is known as the Z-R relation of the form (equation 1).

$$Z=AR^b \quad (1)$$

Z represents the reflectivity, R represents the rain rate and A and b are coefficients that may vary from one location to another and between seasons (Ulbrich and Miller, 2000; Kajewski and Smith, 2000). Due to the Z-R relation that changes between events and location most radar rainfall estimates is done by using a theoretical Z-R relation (equation 2)

$$Z=200R^{1.6} \quad (2)$$

which is widely recognized as the most accurate for the most events and climates (Marshall and Palmer, 1948).

Therefore stratifying events into convective and stratiform rainfall will improve the accuracy of rainfall estimates. Convective events are characterized by their high rain rate, short, strong horizontal reflectivity gradients and large vertical velocity duration. These events are normally very localized and has strong up and down drafts whereas stratiform events has lower rain rates, weak horizontal reflectivity gradients, a bright band near the melting layer, weak vertical velocity, longer in duration and is widely distributed (Cui et al., 2007; Houghton, 1968; Atlas et al., 2000).

#### **Comparison using Radar, Disdrometer and Rain Gauge data**

The frequency of large convective events occurring over the interior of South Africa is increasing and this can lead to infrastructure damage and even loss of human life. The need for improved radar rainfall estimates has never been greater in Africa due to wide spread poverty and people vulnerable to natural disasters. The South African weather Service has invested millions of rand in improving the weather radar network of South Africa and therefore using them to their maximum potential is extremely important.

Radar rainfall estimates in South Africa has over the years been measured by using the theoretical Z-R relation (equation 2). Never before has the measurement of new unique Z-R relation for different events and locations been explored. This is important due to the high variability of the Z-R relation over space and time. The paper aims at deriving a unique relation for each event and

comparing this to the theoretical relation used by the South African Weather Service. This will be done by using the data obtained from the Mooi River catchment rain gauge network situated north from Potchefstroom which consists of 20 tipping bucket rain gauges (Figure 1). These rain gauges will resemble the ground truth and will be used as a reference instrument. New Z-R relations were measured by the Parsivel as it has the ability to measure reflectivity (Z) and rain rate (R) on the ground simultaneously. Therefore it is the ideal instrument to improve radar rainfall estimates.

TITAN (Thunderstorm Identification, Tracking, Analysis and Nowcasting) is a program that has the ability to identify different events. Convective events was measured on the 5<sup>th</sup> of March 2014. A large number of scattered events, identified by TITAN, occurred over the interior of South Africa (Figure 5).

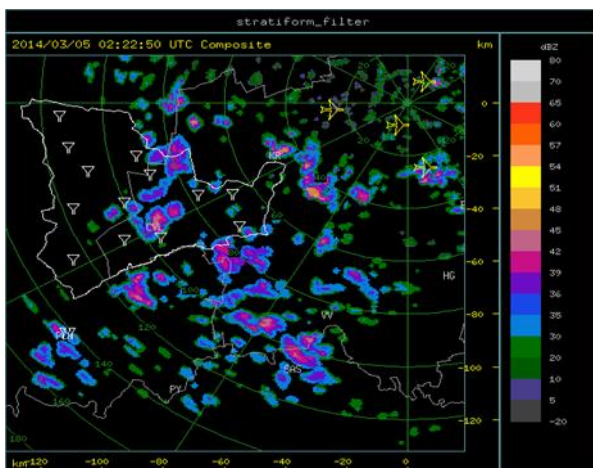


**Figure 5**

*Convective events identified by TITAN over the interior of South Africa on the 5<sup>th</sup> of March 2014*

These events was measured by the Parsivel and a new unique relation,

$$Z=186R^{1.6} \quad (3)$$

has been derived (Figure 6).

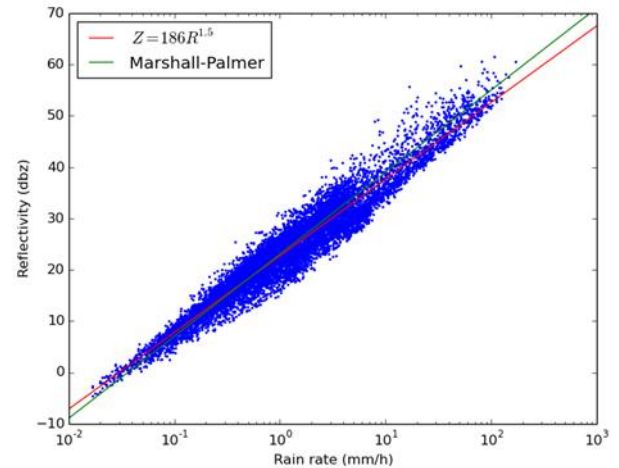


**Figure 6**

*Convective events as measured by the Parsivel disdrometer*

These convective events often occur in the summer over South Africa when the easterly movement of air brings warm moist air from the equator. This easterly low pressure creates condition that is favourable for uplifting which cause widespread convective events.

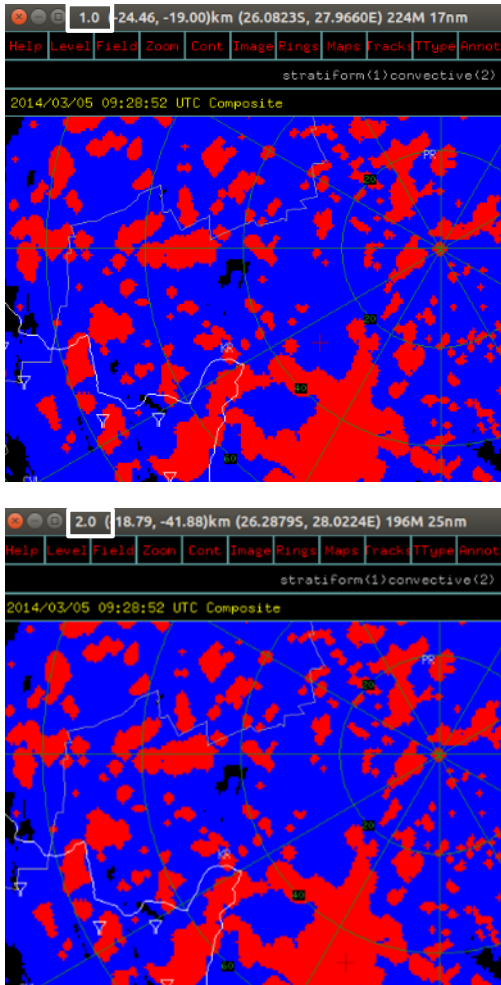
Stratiform events are widespread evenly distributed rainfall which is also a frequent occurrence over South Africa. TITAN has the ability to identify convective and stratiform events when the reflectivity of a pixel exceeds a specified dbz threshold. A number is then assigned to the pixel which stratifies the pixel into stratiform (1) or convective (2) events (Figure 7).

Figure 7 show that stratiform events cover a large area over South Africa. Using the Parsivel disdrometer a new unique Z-R relation,

$$Z=241R^{1.5} \quad (4)$$

has been measured for stratiform events (Figure 8). These events also mainly occur in the summer when the South Atlantic high pressure system of the coast of South Africa brings warm moist air over the warm Indian Ocean to the continent. Orographic processes cause the air to rise and cools. Eventually large scale evenly distributed rain is observed. These events are often under estimated by radars due to the fact that it consists of low lying clouds (Figure 3).

Mixed precipitation includes both convective and stratiform events. The entire 39 days of data measured by the Parsivel was analysed and a Z-R relation was measured (Figure 9). Between the 21st of February and the 31st of March 180mm of rain was measured. The new Z-R relation measured by the



**Figure 7**

*Convective and stratiform events identified by TITAN. Top: Stratiform events assigned the number 1. Bottom: Convective events assigned the number 2.*

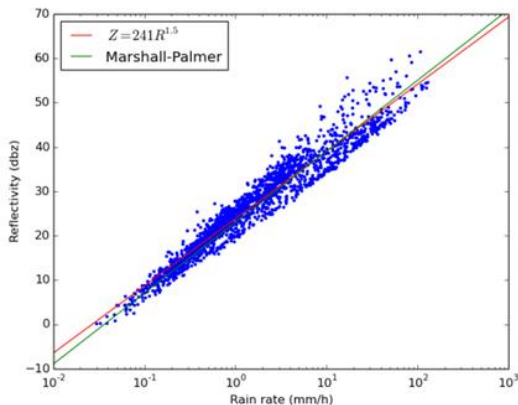


**Figure 8**

*Stratiform events as measured by the Parsivel disdrometer*

disdrometer was (Figure 10):

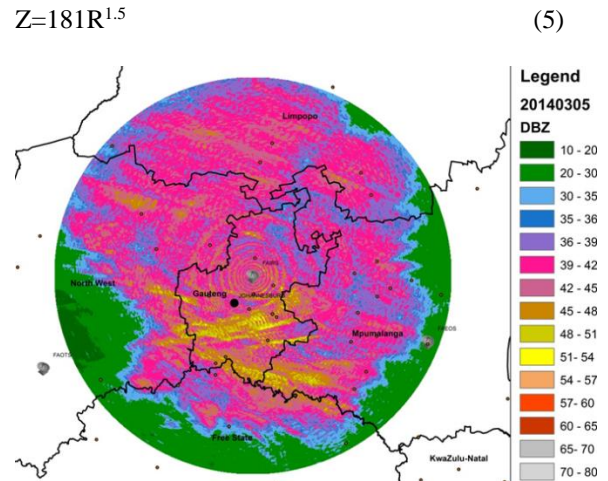


**Figure 9**

*Mixed Precipitation measured by the Irene weather radar between the 21<sup>st</sup> of February and the 31<sup>st</sup> of March 2014*

Using the new Z-R relation and comparing to rainfall estimates measured by the theoretical Z-R relation showed an increase in correlation for all three precipitation categories. Ground truth data was measured by a tipping bucket rain gauge situated within the Mooi River catchment approximately 30km from where the Parsivel was placed.

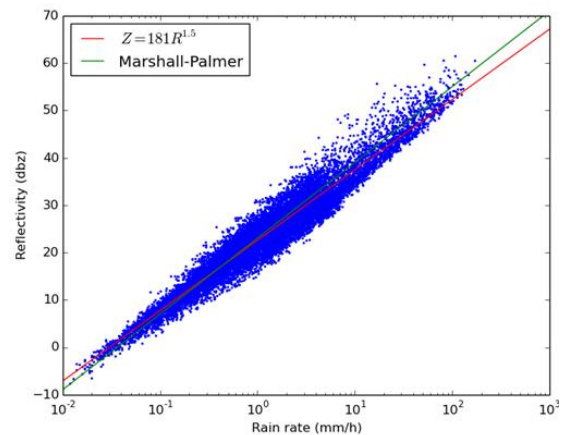


**Figure 10**

*Mixed Precipitation measured by the disdrometer*

Table 1 shows a summary of radar rainfall estimates measured by using different Z-R relation. These measurements were then compared to ground truth data and the correlation of each was determined. N(RG) shows the number of tips measured by the rain gauge and N(R) the number of volume scans made by the radar.

	Date	Time	N(RG)	N(R)	H(RG)(mm)	H(R) Marshall and Palmer (mm)	$\Delta$ (mm)	A	b	H(R)(mm)	$\Delta$ (mm)
Mixed Precipitation	2014/12/19	12:00:00-16:15:00	135	43	27.2	18.21	-8.99	181	1.5	23.7	-3.5
Convective	2015/01/09	23:00:00-23:59:59	111	9	22.4	18.14	-4.26	186	1.5	23.5	1.1
Stratiform	2015/01/27	21:00:00-23:59:59	36	27	2.6	5.3	2.7	241	1.5	5.2	2.6

**Table 1**

*Radar rainfall estimates compared to ground truth measurements*

Table 1 shows a summary of radar rainfall estimates measured by using different Z-R relation. These measurements were then compared to ground truth data and the correlation of each was determined. N(RG) shows the number of tips measured by the rain gauge and N(R) the number of volume scans made by the radar. The rainfall accumulation (H(RG)) measured by the rain gauge is the ground truth and is assumed to be the most accurate. Rainfall estimates measured by the radar is presented by H(R) using different Z-R relations (A and b).

Implementing a new unique Z-R relation to all three different case studies showed an improvement in radar rainfall estimates. Convective events showed an improvement in the correlation from 80% to 95% compared to rain gauge measurements. Mixed precipitation had an improvement from 66% to 87% and stratiform from 49% to 50%.

### Conclusion

The need for improved radar rainfall estimates in Africa has never been greater. Technological advances in rainfall research in the last decades has provided us with innovative instruments such as disdrometers and dual polarized radars that uses cutting edge processes to measure rainfall more accurately and provides the scientific community with more reliable data. South Africa has the most advanced radar network in Africa but these radars are not always operated to their full potential. Weather radar is extremely important due to its ability to measure atmospheric processes at large distance with a small infrastructure footprint. It has been found in this study that variations in the A and b coefficients is evident especially between different events. This has been demonstrated through comparison between different Z-R relations and ground truth data. It has been found that using

KRAJEWSKI WF and SMITH JA (2002) Radar hydrology: rainfall estimation. *Advances in Water Resources* **22** 1387-1394

unique Z-R relations will improve the data. However problems with the radar often occur because of hardware problems and often needs technical maintenance.

### References

ATLAS D, ULBRICH CW, MARKS FD, BLACK RA, AMITAI E, WILLIS PT AND SAMSURY CE (2000) Partitioning tropical oceanic convective and stratiform rain by draft strength. *Journal of Geophysical Research* **105** (D2) 2259-2267

CAMPBELL JB (1996) *Introduction to remote sensing*. Taylor & Francis, London. 625pp.

CUI X, ZHOU Y and LI X (2007) Cloud microphysical properties in tropical convective and stratiform regions. *Meteorology and Atmospheric Physics* **98** (1-2) 1-11

DOVIK RJ and ZRINIC DS (1993) *Doppler Radar and Weather Observations*. Dover Publications, New York. 562pp.

DYSON LL (2009) Heavy daily-rainfall characteristics over the Gauteng Province *Water SA* **35** (5) 627-637

HOUGHTON HG (1968) On Precipitation Mechanisms and their Artificial Modification. *Journal of Applied Meteorology and climatology* **7** (5) 851-859

JAFFRAIN J and BERNE A (2010) Experimental Quantification of the Sampling Uncertainty Associated with Measurement from PARSIVEL disdrometer. *Journal of Hydrometeorology* **12** (3) 352-370

MARSHALL JS and PALMER WM (1948) The distribution of raindrops with size. *J. Meteorol* **5** 165-166

MASON SJ, WAYLEN PR, MIMMACK GM, BALAKANAPATHY R and HARRISON JM (1999) Changes in Extreme Rainfall events in South Africa. *Climate Change* **41** 249-257

NIKOLOPOULOS EI, KRUGER A, KRAJEWSKI WF, WILLIAMS CR and GAGE KS (2008) Comparative rainfall data analysis from two vertically pointing radars, an optical disdrometer, and a rain gauge. *Nonlinear Processes in Geophysics* **15** 987-997

RINEHART RE (1997) *RADAR for Meteorologists*. Rinehart Publications, Columbia. 428pp

UIJLENHOET R (2001) Raindrop size distributions and radar reflectivity-rain rate relationships for radar hydrology. *Hydrology and Earth System Sciences* **5** (4) 615-627

SCHULZE RE (1997) South African Atlas of Agrohydrology and –Climatology. Water Research Commission, Pretoria, Report TT82/96

TENORIO RS, DA SILVA MORAES C and KWON BH (2010) Raindrop Distribution in the Eastern Coast of Northeastern Brazil using Disdrometer Data. *Revista Brasileira de Meteorologia* **25** (4) 415-426

TOKAY A, WOLFF DB, WOLFF KR and BASHOR P (2003) Rain Gauge and Disdrometer Measurements during the Keys Area Microphysics Project (KAMP). *Journal of Atmospheric and Oceanic Technology* **20** (11) 1460-1477

ULBRICH CW and LEE LG (1999) Rainfall Measurement Error by WSR-88D Radars due to Variations in Z-R Law Parameters and the Radar Constant. *Journal of Atmospheric and Oceanic Technology* **16** (8) 1017-1024

UIBRICH CW and MILLER NE (2000) Experimental Test of the Effects of Z–R Law Variations on Comparison of WSR-88D Rainfall Amounts with Surface Rain Gauge and Disdrometer Data. *Weather and Forecasting* **16** (3) 369-374

# Evaluating a rain gauge network's ability to characterize the spatial variability of rainfall

Reinhardt G Hauptfleisch\*, Stuart J Piketh and Roelof Burger

Unit for Environmental Sciences and Management, North-West University, Potchefstroom, 2520, South Africa

## Abstract

Rainfall varies in space and time. Rain gauges, configured in a network are traditionally used to make direct measurements of rainfall. However, even though rain gauges can provide accurate measurements of point rainfalls at very fine temporal scale, the spatial variability of rainfall is very difficult to estimate without a network with enough density in space. In this study the capability to accurately measure rainfall in a catchment of an existing rain gauge network is evaluated by determining the spatial correlation between rain gauges in a network.

**Keywords:** Rain gauge network evaluation, Rainfall variability, Rainfall estimation, Rain gauges

## Introduction

Rainfall measurements are commonly used for many applications in hydrological and meteorological modelling. Rainfall is however a very irregular occurrence that exhibits large spatial and temporal variation. South Africa is especially vulnerable to variations in rainfall. The variability of rainfall impacts on agriculture, water management, disaster management and urban design (Reason et al., 2003).

Traditionally rainfall is measured with rain gauges that measure the true rainfall that falls over a small area of a few squared decimeters. Direct measurements of rainfall are best achieved with rain gauges, and rain gauge networks are usually used to characterize the spatial and temporal variability of rainfall over a certain area. However, even though rain gauges are regarded to make the most accurate measurement of rainfall at very fine resolution in time, it is still very difficult to characterize the spatial variability of rainfall without a dense enough rain gauge network in the area under investigation (Cheng et al., 2007).

The optimization of a rain gauge network is generally done in order to improve the accuracy of rainfall measurements by the network. In most cases the performance evaluation of a network is usually focused on reducing the estimation variance of areal rainfall and not on point rainfall across a study area.

\*Correspondence to: RG Hauptfleisch, Tel.: 073 189 5486. E-mail address: [reinhardt.hauptfleisch@gmail.com](mailto:reinhardt.hauptfleisch@gmail.com)

Correlation coefficient is the quantitative measurement of the linear dependency between two or more random variables. Correlations between rain gauges are widely used to characterize the spatial variability of rainfall (Habib et al., 2001; Jensen and Pedersen., 2005; Tokay et al., 2014; Srinivasan and Nair., 2005; Gires et al., 2014).

The purpose of this study is to evaluate the ability of a rain gauge network to characterize the spatial variability of rainfall and in doing so determine if the existing network is dense enough in space.

## Data collection and Methods

The Mooi river network that is situated in the Highveld of South Africa between 25 and 26° S latitude and 25 and 27° E longitude (Figure 1).

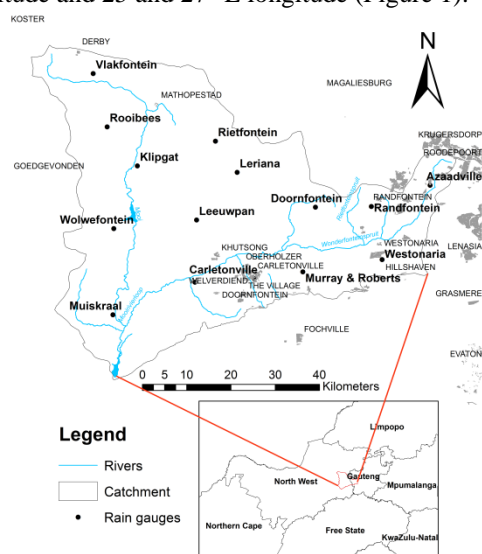
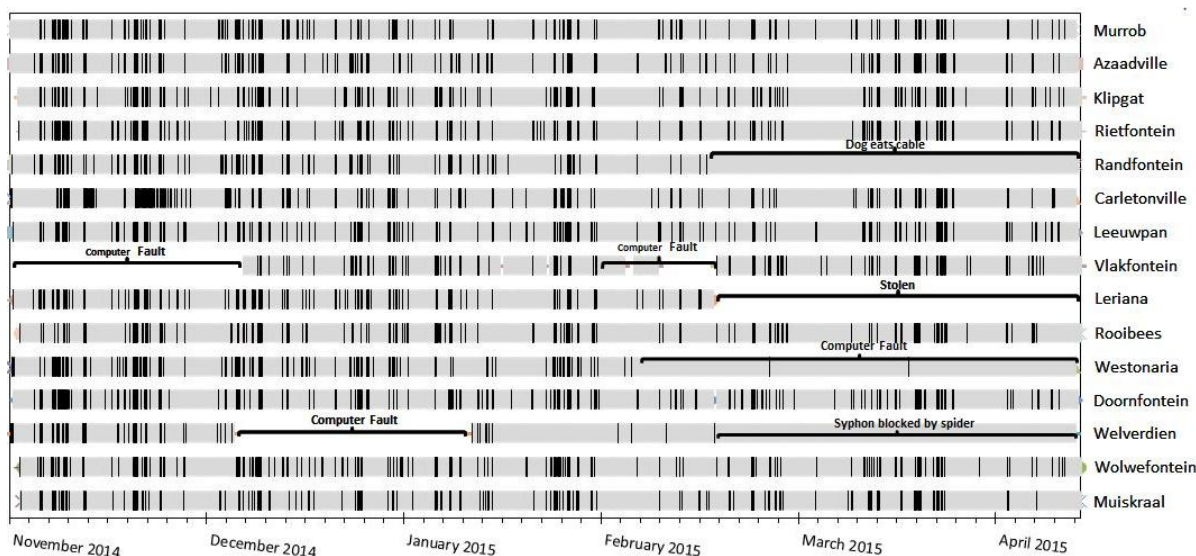


Figure 1: The study area and rain gauge locations.



**Figure 2:** Each tip of the rain gauge bucket is represented by a stipe and the grey indicates the period of rainfall measurements taken successfully by each rain gauge in the Mooi river network.

The climate of the catchment is moderate with predominately summer rainfall occurring between the months of October and March (Lynch et al., 2001 and Schulze, 1997).

This network became fully operational at the beginning of the summer of 2014/2015. The Mooi river network is a conglomerate of tertiary catchments that forms part of the Primary Vaal river basin.

A total of 15 tipping bucket rain gauges are installed over the catchment with a maximum inter gauge distance of < 80 km.

Because the network is so new, it does not yet have the ability to give a proper climatic record of the area and it is prone to various external errors and faults that can be seen in Figure 2 and Table 1.

**Table 1:** Percentage of time that each rain gauge in the were either offline or working between November 2014 and April 2015

Site	Name	Percentage time	
		Offline	Working
1	Muiskraal	0	100
2	Wolwefontein	0	100
3	Welverdiend	67	33
4	Doornfontein	0	100
5	Westonaria	43	57
6	Rooibees	0	100
7	Leriana	34	66
8	Vlakfontein	30	70
9	Leeuwpán	0	100
10	Carletonville	6	100
11	Randfontein	35	65
12	Rietfontein	0	100
13	Klipgat	0	100
14	Azaadville	0	100
15	Murrob	0	100

As indicated by Figure 3, variable amounts of rain were recorded of between 300 and 600 mm of rainfall by each rain gauge. With the exception of the gauge at Site 3 which is the Welverdiend gauge that experienced various computer faults and blockages thus reporting much less rainfall than the rest of the gauges as can be seen in Figure 2.

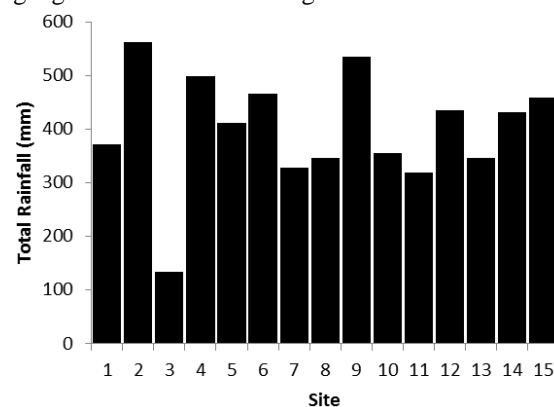


**Figure 3:** Cumulative total of rainfall recorded by the Mooi river network between: November 2014 – April 2015.

To determine the spatial variability of rainfall over the Mooi river network, Pearson's correlation was applied to 77 pairs of gauge records

$$r(X, Y) = \frac{\overline{XY} - \bar{X}\bar{Y}}{\sqrt{(\overline{X^2} - (\bar{X})^2)(\overline{Y^2} - (\bar{Y})^2)}}$$

Where  $r(X, Y)$  gives the Pearson product-moment sample coefficient, derived from number of pair scores  $N$ . The over bars indicate the average values of the sample size  $N$  (Habib et al., 2001)

## Results

The Pearson's correlation coefficient was estimated for all possible gauge combinations and then plotted as a function of inter gauge distance for daily and 12 hourly rainfall as shown in Figure 4 and 5.

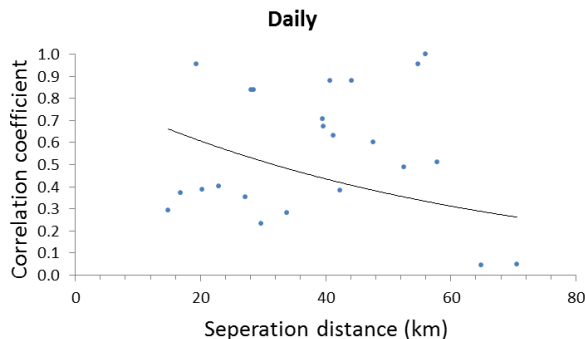


**Figure 4:** Intergauge correlations (dots) and the fitted exponential function (curve) for daily rainfall totals.

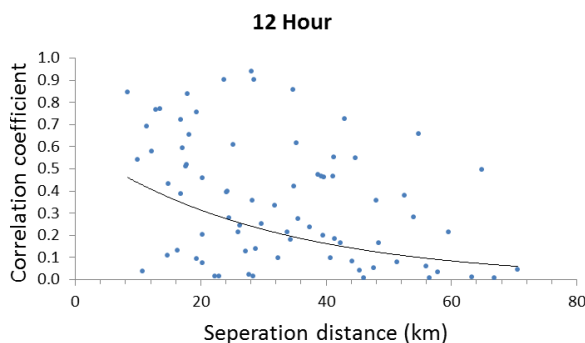


**Figure 5:** Intergauge correlations (dots) and the fitted exponential function (curve) for 12 hourly rainfall totals.

Results of the daily and 12 hourly rainfall analysis show that there is considerable spatial variation in rainfall. It is however evident that over longer temporal scales there is less spatial variation as shown by figure 4. The daily rainfall correlation varies less over distance than the 12 hourly correlations. For the daily analysis in Figure 4, correlations range between 0.9 and 0.4 for separation distance < 60 km. The 12 hourly analysis (Figure 5) correlations exhibit a much stronger downward curve with weaker correlation at longer distances between 40 km and 80 km as opposed to the daily analysis.

## Conclusions

The aim of this paper was to determine if the existing rain gauges in the Mooiriver network is dense enough to quantify the spatial variability of rainfall.

In figure 4 and 5, we can see the difference that temporal scale has on the spatial variability. For longer accumulation periods such as the daily data, it can be seen that the rainfall totals is more uniform with less variation in correlation between rain

gauges. At the shorter temporal scale of 12 hours there is more variation in rainfall correlations between rain gauges.

Therefore it is important that rain gauge networks that are designed for a specific purpose is carefully evaluated in order to determine what resolution of data is needed and what is the network's ability to capture the spatial variability of rainfall. If the purpose of a network is to provide information on long term climate, a less dense network will be sufficient as the variability of rainfall is less over longer period, as shown if Figure 4. However if a network is designed for calibration of other weather sensors such as radar and satellites, high resolution spatial and temporal data will be needed, thus a more rain gauges will have to be installed in the existing network.

## References

- Cheng, K.s., Lin, Y.C. and Liou, J.J. (2007). Rain-gauge network evaluation and augmentation using geostatistics. *Hydrological Processes* 22: (2008) 2554-2564.
- Gires, A., Tchiguirinskaia, I., Schertzer, D., Schellart, A., Berne, A. and Lovejoy, S. (2014). Influence of Small Scale Rainfall Variability on Standard Comparison Tools Between Radar and Rain Gauge Data. *Atmospheric Research*. 138: 125-138.
- Habib, E., Krajewski, W.F. and Caich, G.J. (2001). Estimation of Rainfall Interstation Correlation. *Journal of Hydrometeorology*. 2: 621-629.
- Jensen, N.E. and Pedersen, L. (2005). Spatial Variability of Rainfall: Variations within a Sinle Radar Pixel. *Atmospheric Research*. 77: 269-277.
- Lynch, S.D., Zulu, J.T., King, K.N. And Knoesen D.M. (2001). The analysis of 74 years of rainfall recorded by the Irwins on two farms south of Potchefstroom. *Water SA* 27 (4) 559-564.
- Reason, C.J.C., Jagadheesha, D and Tadross, M. (2003). A Model Investigation of Inter-Annual Winter Rainfall Variability Over Southwestern South Africa and Associated Ocean-Atmosphere Interaction. *South African Journal of Science*. 99: 75-80.
- Schulze, R.E. (1997). South African Atlas of Agrohydrology and Climatology. *Water Research Commission*, Pretoria, Report TT82/96.
- Srinivasan, G. and Nair, S. (2005). Daily Rainfall Characteristics from a High Density Rain Gauge Network. *Current Science*. 88(06): 942-946.
- Tokay, A., Roche, J.R. and Bashor, P.G. (2014). An Experimental Study of Spatial variability of Rainfall. *Journal of Hydrometeorology*. 15: 801-812.

# ***Effect of Meteorological Factors and Emission Reduction on Pollution in the Vaal Triangle Airshed Priority Area***

***Anzel Swart and George Djolov***

***Department of Geography, Geoinformatics and Meteorology, University of Pretoria.***

The atmosphere has no boundaries; pollution can be carried away from its origin at large distances and air pollution dispersion models are capable of studying its effects. The Vaal Triangle Airshed Priority Area in South Africa is an area with high pollution levels where emission reduction strategies have been implemented. Arcelormittal South Africa Vanderbijlpark Works is an industrial plant located in this priority area which specialises in producing iron and steel and is a source of high levels of PM<sub>10</sub> emissions. The influence of different meteorological conditions on pollution dispersion is studied using the USA Environmental Protection Agency regulatory model AERMOD. The effect of the emission reduction programme in Arcelormittal South Africa is quantified. Two types of extreme atmospheric conditions, very stable and unstable are evaluated. The planetary boundary layer stability is defined using the Monin-Obukov Length. At both stratifications the effect of the planned 40% reduction of emission levels is quantified. The study illustrates that with unstable stratification the maximum pollution level is closer to the emission sources and the opposite is valid at stable stratification. The emission reduction of 40% leads in general to proportioned reduction of the concentration levels at the sensitive areas in the region.

***Keywords – AERMOD, Monin-Obukov length, PM<sub>10</sub>, Pollution Dispersion Modelling***

## ***Introduction***

South Africa is the largest producer of emissions in Africa, and contributes 1.47% to the total emissions of the world (Carbon Dioxide Information Analysis Center, 2013). The Vaal Triangle was declared a pollution priority area as a result of the poor air quality and raised pollutant concentrations. Arcelormittal South Africa (AMSA) Vanderbijlpark Works, is an industrial iron and steel plant in the Vaal Triangle Airshed Priority Area (VTAPA) (Jagathlal, 2012). It is a significant source of PM<sub>10</sub> pollution which have negative impacts on human health.

Determining the effect of meteorological factors on the dispersion of pollution is of significance in this priority area. After the declaration of the VTAPA, air quality targets were proposed and an emission reduction plan was set into place for this area (Department of Environmental Affairs and Tourism, 2009). The major meteorological factors influencing the dispersion of emissions is wind direction, wind speed and the stability regime in the planetary boundary layer. In this study, the AERMOD pollution dispersion model was used to evaluate the role that meteorological factors play on ambient concentrations in this area.

The first aim of this paper is to use an appropriate air pollution dispersion model to evaluate the role of meteorological conditions on the air quality in the study area. This aim was reached by statistical analysis of the stability conditions over the region for the year of 2010 and by obtaining and running AERMOD.

The second aim is to investigate the effect of previously implemented emission reduction strategies at the AMSA Vanderbijlpark Works on the air quality in the area. This aim was reached by studying air pollution with emission

data before and after the implementation of emission reduction strategies with use of an air pollution dispersion model.

## ***Instrumentation and Method***

The model uses meteorological information to calculate the necessary dynamic and turbulent characteristics of air pollution and the convective mixing heights of the planetary boundary layer. Midnight soundings (TD-2061 format) from Irene upper-air station and hourly surface weather data (SAMSON format) from O.R. Tambo International Airport for the year of 2010 were obtained. ERA-interim reanalysis data was used together with the upper-air sounding data to complete the data set and to account for missing hours of data. The data is for 365 days and contains 8760 hours of meteorological information.

This research project focuses solely on point source emissions from AMSA. The emission data for these point sources are validated by AMSA each month before being recorded and the archived. The emission data used in this research project was obtained from the thesis of S. Jagathlal. Emission rates from the year 2010 was used as input. Source characteristics needed by the model is the stack height, stack diameter, exit velocities of emissions and the stack temperatures of each of the point sources. The emission rate is measured in grams per second (g/s).

The Environmental Protection Agency Regulatory Model (AERMOD) is used. AERMOD is based on the Gaussian equation and assumes Gaussian distribution of pollution. This model is thoroughly validated; it is the governing dispersion model for the EPA and recommend in South Africa. AERMOD is also suited to handle rural and urban areas, flat and complex terrains, surface or elevated

releases of emissions, multiple emission sources and downwash caused by nearby buildings (US Environmental Protection Agency, 2009).

AERMOD assumes Gaussian concentration distribution in the vertical and horizontal directions when conditions are stable. In the convective boundary layer this model assumes Gaussian distribution in the horizontal direction and distribution in the vertical direction is defined with a bi-Gaussian probability density function (Cimorelli et al., 2004).

$$C(x, y, z) = \frac{Q}{2\pi\sigma_y^2\sigma_zU} \exp\left(\frac{-y^2}{2\sigma_y^2}\right) \left( \exp\left(\frac{-(z-h)^2}{2\sigma_z^2}\right) + \exp\left(\frac{-(z+h)^2}{2\sigma_z^2}\right) \right)$$

**Equation 1:** Gaussian equation on which AERMOD is based (Cimorelli et al., 2004).

In the Gaussian equation (Eq. 1), C is the concentration of pollution at the location x,y,z measured in micrograms per cubic meter ( $\mu\text{g}/\text{m}^3$ ). Q is the rate at which emissions exit the source and is measured in grams per second (g/s). U is the average wind speed measured at the top of the stack in meters per second (m/s).  $\sigma_y$  is the standard deviation of concentration distribution in the horizontal and  $\sigma_z$  is in the vertical. These two parameters are measured in meters (m). H represents the combination of the height of the stack and the rise of the plume as it exits the stack (measured in meters). x is the distance downwind from the stack, y is the crosswind distance from the plume centerline and z is the vertical distance from the surface of the earth. x, y, z are all measured in meters (m) (Stockie, 2011).

The AERMOD dispersion model was run for 4 different scenarios. First the dispersion model for a stable stratified atmosphere was run and secondly for an unstable atmosphere. Next the AERMOD dispersion model was run for the entire year of 2010. Lastly, the dispersion model was run for stable stratified and unstable atmospheric conditions with emissions for each source group reduced by 40%. This 40% reduction in emissions represents the possible implementation of reduction strategies.

The grid used when running AERMOD starts at -10 000 m in the -x and -y direction and has steps of 1000 m between each point on the grid. Altogether there are 21 points between -10 000 and 10 000 grid points on the x-axis, and the same is true for the y-axis. Included in this grid are 7 polar receptor points.

AERMOD is considerably flexible when it comes to the specification of point receptor locations. A grid point receptor network was specified for the model runs. Receptors were also placed at 7 “sensitive” locations in the area. The locations of the 7 receptors used in this research project are all located at schools in a populated area or community (Fig. 1).



**Figure 1:** Locations of receptor points (black) and AMSA (red) (Adapted from Google Earth, 2013).

Monin-obukhov length is the stability parameter calculated by AERMET (the meteorological pre-processor to AERMOD) when the meteorological data is prepared for AERMOD. One stable case and one unstable case was chosen based on the predominant hourly stability regime.

These two types of atmospheric conditions have an influence of the way in which pollution disperses in the Planetary Boundary Layer (PBL). A stable atmosphere will ideally result in the “fanning” of pollutants while an unstable atmosphere will cause pollutants to “loop”.

At night-time and in winter during the day, stable conditions with little convection prevails. Fanning of pollution takes place under these atmospheric conditions. The unstable PBL is present during the day when convection dominates. Looping of pollution takes place under these atmospheric condition.

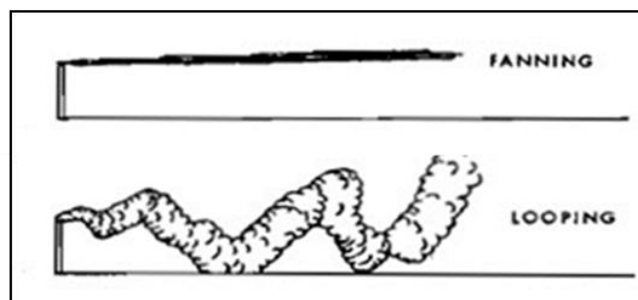


**Figure 2:** The effect of two types of atmospheric conditions on pollutant dispersion in the PBL (Datafedwiki, 2011).

The research project is aimed at investigating emissions originating from stacks at AMSA steel works located in Vanderbijlpark. These emission concentrations will be studied at different meteorological conditions before and after the implementation of reduction strategies. This will be accomplished by using an appropriate air pollution dispersion model together with meteorological, emission and terrain data.

### Results and Discussion

A statistical analysis of the stability conditions over the region for the year of 2010 (Fig.3) was done. This is

important in order to compare the distribution of stable and unstable hours throughout the year.

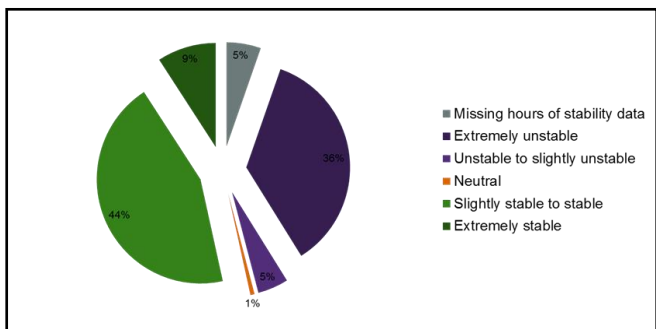


**Figure 3:** Distribution of stability classes (based on Monin-Obukhov Length values) for every hour of the year 2010.

Figure 2 shows that slightly stable to stable conditions were dominant throughout the year and occurred in 44% of the hours of the year. Extremely unstable hours occurred in 36% of the hours. Neutral atmospheric conditions were only present for 1% of the hours for the year of 2010.

All concentrations contained in the following results are 24 hour averages for the 10 source groups. There are 7 receptors, they are named POL1 to POL7. Each of these receptor point are located at nearby schools in the area. Receptor points are at different distances away from the source and also placed in different directions from AMSA.

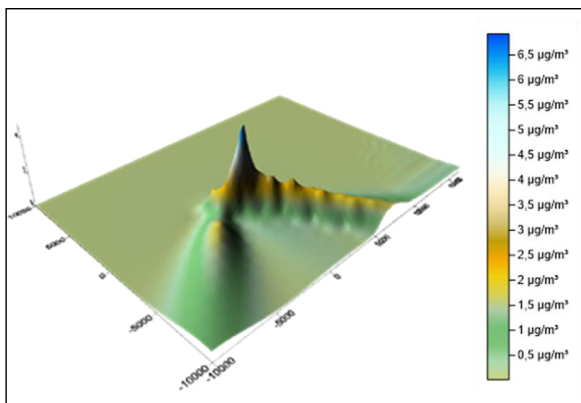


**Figure 4:** PM<sub>10</sub> concentration fields for the stable case. This was modelled by AERMOD and plotted by Surfer.

The maximum daily concentration for this case (Fig. 4) with normal emissions is 5.27µg/m<sup>3</sup>, and located at 1000x;-1000y on the grid. The maximum daily concentration for the same case but with 40% reduction in emissions is 3.16µg/m<sup>3</sup> and located at the same position.

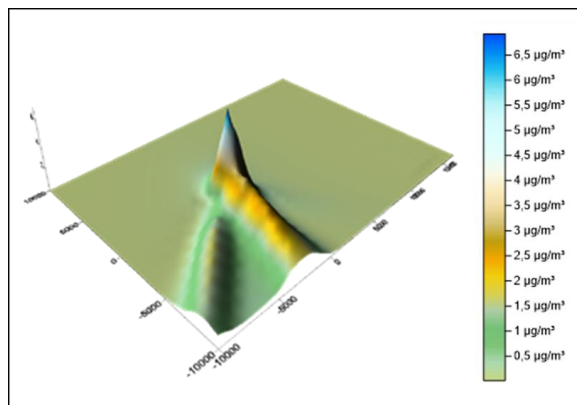


**Figure 5:** PM<sub>10</sub> concentration fields for the unstable case. This case was modelled by AERMOD and plotted by Surfer.

The maximum daily concentration for this case (Fig. 5) with normal emissions is 6.93µg/m<sup>3</sup>, and located at 0x;0y on the grid. The maximum daily concentration for the same case but with 40% reduction in emissions is 4.16µg/m<sup>3</sup> and located at the same position.

The difference in location of maximum daily concentration between the stable (Fig.4) and the unstable (Fig.5) cases confirms that the turbulent mixing process in the case of unstable air is more intensive (maximum located closer to the origin) than for stable air (maximum located further from the origin) in observational data.

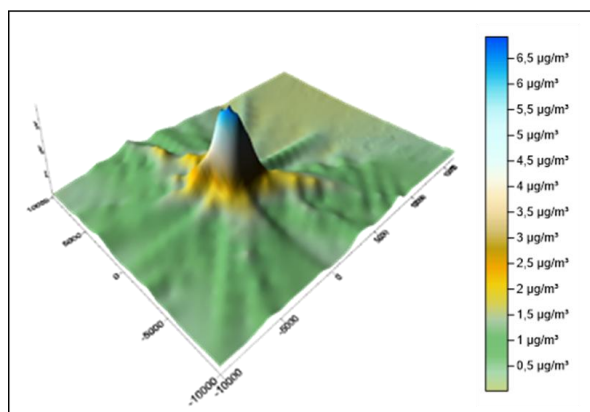


**Figure 6:** PM<sub>10</sub> concentration fields for the year of 2010. This was modelled by AERMOD and plotted by Surfer.

The maximum annual concentration for the year (Fig. 6) was 19.80µg/m<sup>3</sup> and located at 0x;0y on the grid. The maximum annual concentration when the emissions were reduced by 40% was 11.88µg/m<sup>3</sup> and located at the same position.

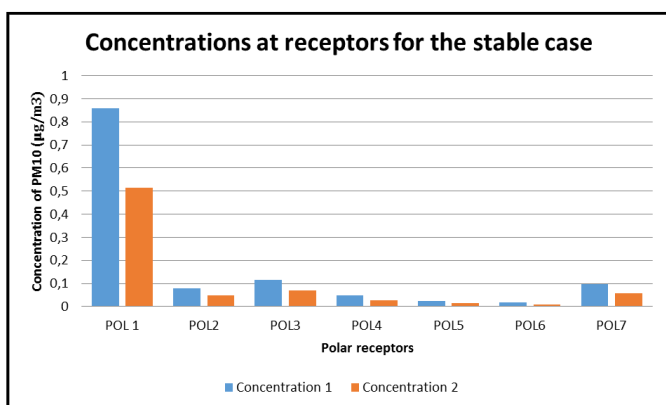


**Figure 7:** Concentrations of PM<sub>10</sub> at receptor points before (blue) and after (orange) emissions were reduced by 40% for the stable case.

Concentrations at polar receptor 1 are higher than concentrations at the other receptors (Fig. 7). This can be attributed to the fact that POL 1 is located relatively close to AMSA (4.6 km). The lower concentrations at the other POL 2 to POL 7 is because the dominating wind direction on the stable day was North-West to North North-West.

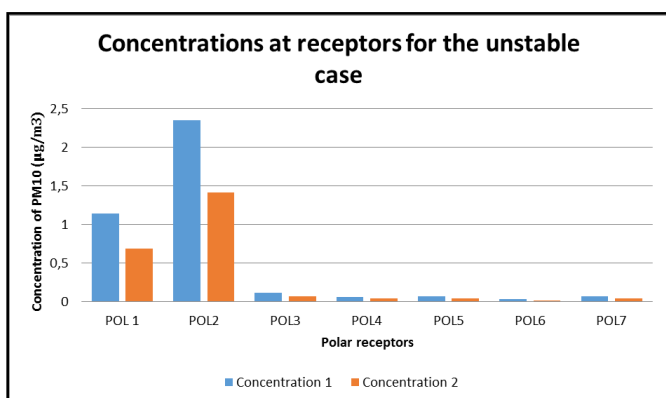


**Figure 8:** Concentrations of PM<sub>10</sub> at 7 receptor points before (blue) and after (orange) emissions were reduced by 40% for the unstable case.

Concentrations at polar receptor 1 and 2 are significantly higher than concentrations at the other receptors (Fig. 8). The high concentrations at POL 1 are attributed to the fact that it is located relatively close to AMSA (4.6 km). POL 1 and POL 2 are both situated in the direction of the dominant wind direction of the unstable day.

### Conclusions

Concentration level for the unstable case is higher near the source as opposed to the stable case, this complies with the physics of the phenomenon in the PBL.

As indicated by the Gaussian equation, a reduction in emissions will lead to a proportional reduction in concentration of pollution at a point. 40% reduction in emissions at sources led to an approximate 40% reduction in concentrations at each grid point and polar receptor.

Under the specified conditions and with the point source emission data used it can be concluded that the

concentrations of PM<sub>10</sub> at the 7 receptors are below the South African Air Quality Standards for daily concentrations of PM<sub>10</sub> (180 µg/m<sup>3</sup>).

The fact that the calculated concentrations don't exceed the air quality standards should be interpreted only as that the AMSA emission reduction measures from point sources give satisfactory results. This research project focused solely on the point source emissions from AMSA. There are many other emission sources associated with AMSA and many other pollutants in the VTAPA area.

To attain a realistic representation of pollution concentrations at the sensitive receptors in the study area the modelling used in this project should be extended to cover all emission sources in the VTAPA area. This will allow to obtain a realistic assessment of the VTAPA air quality conditions - the total concentration at any point being a sum of the concentrations from all sources in the area.

An air pollution dispersion model is an excellent tool to model air quality in the VTAPA because it illustrates a relationship between industrial and meteorological factors and show their effect on the air pollution condition in an area.

### References

- Carbon Dioxide Information Analysis Center (CDIAC). 2013. "Fossil-Fuel CO<sub>2</sub> Emissions." May 2013, 10 May 2014. <[http://cdiac.ornl.gov/trends/emis/meth\\_reg.html](http://cdiac.ornl.gov/trends/emis/meth_reg.html)>
- Cimorelli, A. J., S.G. Perry, A. Venkatram, J. C. Weil, R. J. Paine, R. B. Wilson, R. F. Lee, W. D. Peters, R. W. Brode, and J. O. Paumier. (2004). AERMOD: Description of Model Formulation, EPA-454/R-03-004. U.S. Environmental Protection Agency, Research Triangle Park, NC.
- Datafedwiki. 2011. "Atmospheric stability." Jan 2011. 10 March 2014. <[datafedwiki.wustl.edu/index.php/2011-01-27:\\_Atmospheric\\_stability](http://datafedwiki.wustl.edu/index.php/2011-01-27:_Atmospheric_stability)>
- Department of Environmental Affairs and Tourism (DEAT). 2009. National Environmental Management: Air Quality Act (No. 39 of 2004) Vaal Triangle Airshed Priority Area Air Quality Management Plan. Government Gazette No. 32263.
- Google earth. 2013. "Vanderbijlpark and surrounding areas." -26.669206° S and 27.86924° E. December 14, 2013. May 20, 2014.
- Jagathlal, S. 2012. Assessing the PM<sub>10</sub> footprint of an Iron and Steel plant on ambient air quality: Modelling PM<sub>10</sub> emissions from the Arcelormittal Vanderbijlpark works iron and steel plant. Master of Science. University of the Witwatersrand, Johannesburg, South Africa.
- Stockie, J. M. 2011. The mathematics of atmospheric dispersion modelling. Siam Review, Vol 53(2), pp 349-372.
- US Environmental Protection Agency (EPA). 2009. AERMOD Implementation Guide. Office of Air Quality Planning and Standards. Air Quality Assessment Divisions Environmental Protection Agency. Research Triangle Park, NC.

### Acknowledgements

I would like to acknowledge my study leader Professor George Djolov for all his assistance and time and Roelof Burger from the North West University for supplying the upper-air and hourly meteorological data.

# Demonstrating LiDAR Technique on Forest Fire Detection in Algiers and Durban: A preliminary study

R. GUEHAZ<sup>1,2\*</sup>, M. TRAICHE<sup>1</sup>, V. SIVAKUMAR<sup>2</sup>

1. Centre de Développement des Technologies Avancées, PB 17, Cité 20 Août 1956, Baba Hassen, Algiers, Algeria.

2. Discipline of Physics, School of Chemistry and Physics, University of KwaZulu Natal, Westville Campus, Private Bag X54001, Durban 4001, South Africa.

\**Email*: rguehaz@cda.dz

## ABSTRACT

Forest fires can cause serious environmental and economic damage. We investigate the tracing of plume evolution that is generated in the fire smoke. As a preliminary study, we use a single shot detection to study the smoke plume at distances varying from 50 to 150 meters by using emitted pulses from a Q-S Nd: YAG laser with second harmonic generation at 532nm optical wavelength. The backscattered radiation power is used to retrieve the target position and other parameters.

**Key-Words:** LIDAR, Forest Fires, Smoke plume, Mie Scattering.

## 1. INTRODUCTION

The LiDAR (Light Detection and Ranging) technique has been one of the most sophisticated active remote sensing techniques over the last 50 years. It has been applied to the study of the atmosphere and, as a powerful tool, to detect even the tenuous smoke plumes produced by forest fires [1].

Many experimental and theoretical investigations are used to study smoke plumes produced by forest fires. Andreucci et al. (1993a) [2] and - (1993b) [3] made the smoke plume model and its detection performance. Experiments by Bellecci et al. [4] and Utkin et al. [5] dealt with the feasibility and fundamentals of forest fire detection by smoke sensing with single-wavelength LiDAR. In another application, Kehui Huang et al. [6] have used Doppler weather Radar detecting smoke plumes from forest fires with almost the same principle as the LiDAR.

In Algeria, we are developing a dual mobile LiDAR system for environmental studies. The detection of forest fire in continuous mountainous forests in north Algeria is the primary focus of this application [7]. Especially, in those hilly and inaccessible zones where the risk factor of a forest fire is high in summer. The purpose of this application is to identify the signature up of smoke on the laser pulse. A backscattering of smoke was estimated by using wavelength 532 nm. The

experiment has been conducted in an open space in CDTA campus, Algeria, by the LiDAR team and in an open space in UKZN campus in South Africa with atmospheric research team.

## 2. METHODOLOGY

In principle, a LiDAR consists of a transmitter, a receiver and a Data acquisition. Short light pulses with lengths of a few nanoseconds are generated by the laser. The beam at output has a width of 8 mm. We also use a PIN photodiode as a detector. It is followed by an optical analyzing system which, depending on the application, selects specific wavelengths.

The experimental parameters used in CDTA are given in the following table:

Transmitter	LiDAR
Laser Source	Brilliant B (Nd:YAG + SHG)
Operating Wavelength	532 nm
Energy per pulse (mJ)	Up to 400 mJ
Beam Expander	× 5/3
Pulse length (ns)	5 ns
Pulse repetition rate	10 Hz
Beam divergence (mrad)	0.3

The receiver is set as a lens of 20 cm in diameter. A Tektronics Scope interfaced on a laptop is utilized for the return signals acquisition. The acquisition speed is 5 GS/s allowing for a space sampling every 3 cm interval.



**Fig.1** This photo shows a recent experiment conducted in CDTA to characterize the smoke signature on return pulses in an open space.

At UKZN, the automatic portable LiDAR system, whose some results are presented in this paper consists of a transmission, a receiving system and a data acquisition unit. The transmitter system based on a compact Q-switched Nd: YAG laser source operating at three wavelengths: 1064 nm, 532 nm and 355 nm.

### 3. RESULTS

The experiment of smoke plume detection with Nd:YAG laser sources operating at wavelength 532 nm. The backscattered signal is collected by a photodiode and then transferred to the oscilloscope, where the signal acquisition is shown by a LeCroy digital oscilloscope. As a rule, the simplest LiDAR methods are not sufficiently sensitive to characterize molecular interaction. However, for solid targets and aerosols, the technique is successfully investigated. Specifically, direct-detection LiDAR provides information on particle distribution and aerosols in smoke plumes. Early fire detection and automatic forest-fire surveillance are among its prospective applications, competing with passive methods based on IR and video imaging [8].

The experimental data used in this work were obtained indirectly by estimating the smoke density distribution from LiDAR backscattering, obtained by scanning the laser beam through real-fire smoke plumes. The LiDAR signal contains information about the particle concentration in the smoke plume, which is proportional to the local backscattered radiation collected by the LiDAR receiver optics, plotted as a function of time.

The figure 2, from an experiment in CDTA (Algiers) with one pulse detection, shows the backscattered signals from the smoke and from a wall as solid target in the background. The figure shows an emitted pulse (Ch-4), scattered back by the ambient air close to the detector. The second pulse is due to the smoke. Here the diverging part of the smoke is scattering the beam back. The third pulse is the return from the wall after a double crossing of the smoke. The 2<sup>nd</sup> pulse is larger than the 3<sup>rd</sup> pulse, indicating a smoke of 3.75 meter in size.

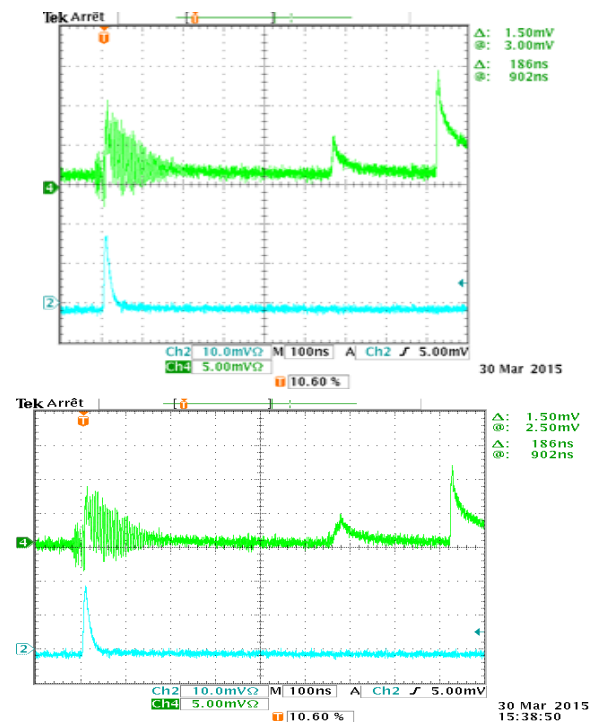


**Fig.2** The signal acquisition by digital oscilloscope in an open space at CDTA with a wall in the background.

Fig.3 shows a repeated experiment CDTA (Algiers) where we had a smoke plume but no background. Like in fig.2 the 1<sup>st</sup> pulse on Ch-4 is the emitted pulse, scattered back by the ambient air close to the receiving photodiode. The second

pulse is the reflection from the smoke. The pulse on Ch-2 is the emitted pulse in a reliable form.

The time  $t$  elapsed from the moment of the laser-pulse emission until the detection moment is related to the distance  $R$  from the radiation source to the target by the equation :  $t = 2R/c$

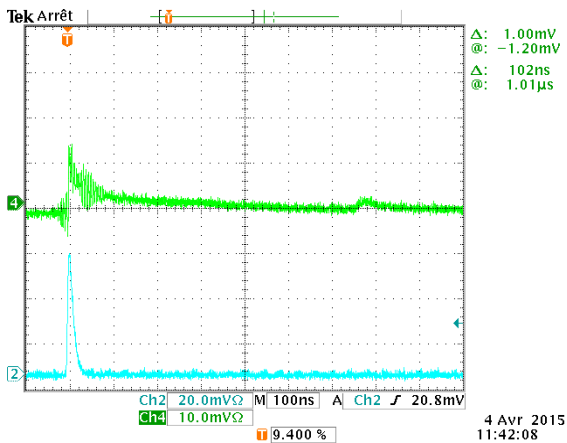
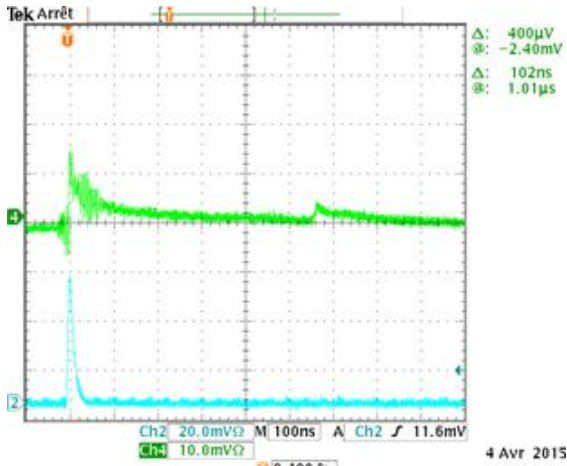


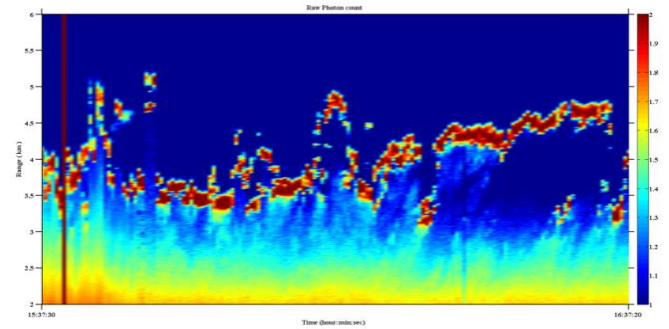
**Fig.3.** The signal acquisition by a digital oscilloscope in an open space at CDTA without background obstacle (wall).

Where ‘ $c$ ’ is the velocity of light and the distance is doubled as light propagates twice through the same distance.

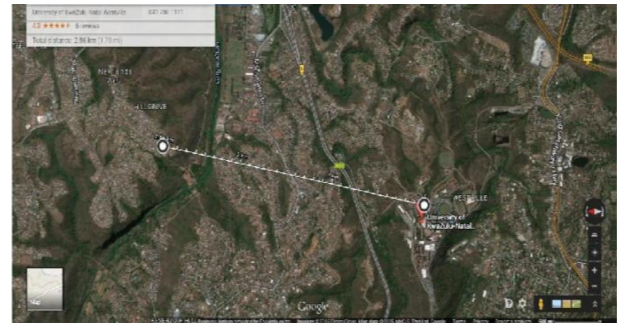
The temporal evolution of the backscattered LiDAR signals allows to depict the smoke evolution in time. This has been experimented at UKZN campus with our partner LiDAR group led by Prof. Sivakumar. Figure 4 illustrates the different forms of the signal— analog, photon count and glued photon count.

Fig 5 illustrates the location of the fire smoke detected in Durban next to UKAN campus (~3.8 km away and a natural

fire). It shows that LiDAR technique could be extremely useful in forest fire detection.



**Fig.4** Backscattered signals illustrating the smoke evolution at a 3-4.8 km range.



**Fig.5** Location of a natural fire captured about 3.8 km from UKZN (almost horizontal)

**4. Scaling-up towards LiDAR real time detection**

The experiments depicted above were planned to prove the possibility of fire smoke detection from:

- Accumulated  $n$  signals capable of generating a signal to noise ratio  $SNR \sqrt{n}$  times better in value. This allowed detecting even tenuous smokes at a few kilometers of range [9] based upon the results from UKZN experiments.
- Single return pulses, allowing capability to perform earlier fire detection: in a couple of minutes, based on CDTA experiments.

Future work is to resolve the smoke from its features on the return signal patterns. Figure 6 shows a record of the on-going pulse on channel 2 and the return pulse showing the smoke signature in terms of a peak-valley structure. This structure and/or the broadening of the return pulse/on-going pulse, has been used in a numerical program under Python to recognize

the smoke existence from a single pulse. This has been experimented with almost no fault alarms. The information on the fire start, its range to the system and its size, has been put on the mobile networks after only one minute or less using Twilio. This was successful as a bread-board LiDAR for a single-pulse-based detection.

The next step is to perform again the same experiments by scanning the horizon and ensure effective detection for an unknown fire. The CDTA LiDAR system details has been provided in our earlier communication [10].

## 5. CONCLUSION

In this work, we have demonstrated two LiDAR experiments carried out at CDTA campus in Algiers and at ULZN campus in Durban. We demonstrated the LIDAR capability to detect even tenuous smokes from forest fires at a very early stage. In case of a detection based on a single laser pulse, the return pulse length broadening serves as a first parameter to recognize the smoke. Other parameters are drawn by pattern recognition.

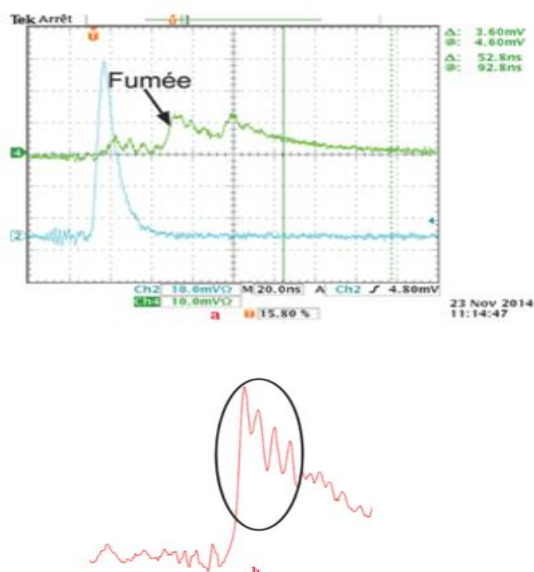


**Fig.6** Pattern recognition of the smoke signature on the return pulse.

Right: the scope record, left: the peak-valley structure describing the plume convection in the smoke.

## REFERENCES

[1] P.GAUDIO and al. "A portable LIDAR system for the early detection: FFED system - a case study".

- [2] F. ANDREUCCI and al. « A Study on Forest Fire Automatic Detection Systems I.- Smoke Plume Model." *IL NUOVO CIMENTO VOL. 16 C*, N.1.35 Gennaio-Febraio 1993a.
- [3] F. ANDREUCCI and M. V. ARBOLINO "A Study of Forest Fire Automatic Detection Systems II.- Smoke Plume Detection Performance" *IL NUOVO CIMENTO VOL. 16 C*, N. 1.51 Gennaio-Febraio 1993b.
- [4] Bellecci C, Francucci M, Gaudio P, Gelfusa M, Martellucci S, Richetta M. "Early detection of small forest fire by dial technique". *SPIE EurIntSymp Remote Sensing 2005:5914-76* [Bruges, Belgium].
- [5] Utkin et al "feasibility of forest-fire smoke detection using LiDAR" *international journal of wildland fire*, 2003, 12, 159-166.
- [6] Kehui Huang et al. the method of forest fires recognition by using Doppler weather radar" *Eighth Symposium on Fire and Forest Meteorology 13-15 October 2009, Kalispell, Montana*.
- [7] M. Traïche and A. Kedadra "A dual LiDAR development for environmental studies in Algeria" 21 June 2013, *SPIE Newsroom*. DOI: 10.1117/2.1201306.004801.
- [8] A.Lavrov and all "Evaluation of smoke dispersion from forest fire plumes using lidarexperiments and modeling" *International Journal of Thermal Sciences* 45 (2006) 848-859.
- [9] A. Kedadra and M. Traïche: "Photomultiplier and avalanche photodiode detection performance for LiDAR application to environment studies," *J. Appl. Remote Sens.*, 8(1), 083568 (2014).
- [10] M. Traïche, A. Kedadra: "A Dual LiDAR development for environmental studies in Algeria," *Peer reviewed conference proceedings of South African Society of Atmospheric Sciences 29<sup>th</sup> Annual Meeting SASAS-2013, September 2013*.

# Climate change impact on contributing tropospheric ozone sources over in southern Africa and the Adjacent Indian Ocean Islands

Jean-Pierre Mulumba<sup>1</sup>, Sivakumar Venkataraman<sup>2</sup> and Thomas Joachim Odhiambo Afullo<sup>3</sup>  
 College of Agriculture, Engineering and Science. School of Chemistry and Physics and School of Electrical and Electronical Engineering  
 University of KwaZulu Natal/ Durban South Africa

1

## Abstract

There is very less information regarding sources contributing to tropospheric ozone formation in Southern Africa and the Adjacent Indian Ocean Islands with regard to their dynamic and occurrence. Information from few measurement campaigns undertaken in the region (SAFARI-92, TRACE A, MOZAIC, DECAFE, SHADOZ, etc), reveal a seasonal increase of tropospheric ozone apparently due to five main contributing sources including stratospheric tropospheric exchange, biomass burning, and urban industrial, biogenic and lightning. As tropospheric ozone variability sharply depends on local or regional prevailing meteorological conditions, it is assumed that these conditions may have a crucial role on ozone transport and chemistry which determine the lifetime of ozone precursor's species in the atmosphere. There is no a particular emission inventory for ozone contributing sources for southern Africa. Existing emission inventory encompassing African continent shows that biomass burning is the largest source of trace gas emission with 38% followed by biogenic and lightning emissions with 25% and 17% respectively. However, almost 52% of annual tropospheric ozone in originates from STE and lightning emissions which may be exacerbated by climate change.

**Key words:** *Climate change, Ozone, Production, Sources, Tropospheric,*

## 1. Background

Seasonal variability of tropospheric ozone levels over southern Africa and Adjacent Indian Ocean has been attributed to photochemical ozone formation from various sources including biomass burning (Fishman *et al.* 1996, Randriambelo *et al.* 2000), biogenic and lightning emissions as well as stratospheric ozone intrusion (Baray *et al.* 1998). However, a comprehensive review of these contributing sources, their dynamic as well as and their subsequent influence on regional environment is still lacking. As these sources contribution fairly depend on meteorological factors it is believed that recent changes observed on regional and global climate are luckily to affect tropospheric ozone formation and dynamic.

Therefore the objective of this work is to review the dynamic of the main tropospheric ozone contributing sources over southern African and Adjacent Indian Ocean Islands, and to consider climate change impacts scenarios on individual sources. This work is partitioned into four sections. The first provides the background on the research question. The second exposes the material and method used to achieve the objective of this work. The third deals with contributing sources and their dynamic on the formation of tropospheric ozone over southern Africa and Adjacent Indian Ocean with emphasis on climate change impacts. Assumptions on possible scenarios due to change in climate dynamic are examined in the last section, which also draws a conclusion and provides suggestions for future studies.

## 2. Materials and Method

The material used for the achievement of this work was made of scientific journal papers with sound critical view pertaining to the objective of our research key questions (Levis and Ellis, 2006). Descriptive and critical approach from background information leading to new methods and techniques related to the identification of sources contributing to ozone formation and their dynamic have been used to elucidating individual sources occurrence and magnitude over the region under investigation. Results from recent findings will be used to discuss and sustain the objective of this work.

## 3. Tropospheric ozone sources

### 3.1 Stratospheric tropospheric exchange

Stratospheric and Tropospheric Exchange (STE) as a dynamic process includes chemical and radiative coupling reactions that play a crucial role in prediction of global atmospheric change (Holton *et al.* 1995). Its contribution to tropospheric ozone enhancement in southern Africa and Adjacent Indian Ocean was widely assumed to occur in upper troposphere in twofold. The dynamic process which is responsible for transport of trace chemical species from anthropogenic and natural emissions (Holton *et al.* 1995), and the chemical processes which influence the radiative flux balance in the troposphere and lower stratosphere in many ways (Ramaswamy *et al.* 1992; Toumi *et al.* 1994). Change in climate

parameters such as temperature increase and relative humidity and wind patterns may significantly affect both dynamical (Butchart and Scaife 2001) and chemical capacity of the troposphere (Lelieveld and Dentener 2000). Therefore, the duration of vertical transport due to STE is dependent on the state of the atmosphere in similar altitude range. This may take months, a year or more and is more often accompanied by radiative heating or cooling (Holton *et al.* 1995). This explains the rapid increase in ozone mixing ratio and the rapid decrease in water vapour mixing ratio with altitude observed just above the tropopause. It is under this approach that thermal and chemical behaviour of the tropopause was a key indicator of the contribution of lower stratosphere ozone into the troposphere. This intrusion, which takes place under certain particular meteorological conditions such as Brewer Dobson circulation, determines the bulk of air downward through the extra tropical tropopause. This confirms recent research conclusion on the effect of climate change on the tropopause dynamic (Collins *et al.* 2003; Lelieveld and Dentener, 2000, Butchart and Scaife 2001).

### 3. 2. Photochemical tropospheric ozone sources

#### 3.2.1 Biomass burning

Biomass burning which plays a crucial economic and social role in both in rural and urban areas in Africa is also a contributing source to ozone formation in southern Africa and Adjacent Indian Ocean. Research (Andreae 1997, van der Werf *et al.* 2003, van der Werf *et al.* 2006) has proven that it does not generate large amounts of ozone in a global sense but the burning yields larger upsurges in other important trace gases. Therefore tropospheric ozone produced from biomass burning is primarily a regional effect within and near the burning with most generated ozone lying in the low troposphere depending on prevailing meteorology for its dispersion or sink at local or regional levels.

#### 3.2.2 Anthropogenic emission

Anthropogenic emissions due to human activities including energy-use in industry, transportation, mining, construction, and in the household are set to increase and therefore contribute more on ozone enhancement due to fastest growing human population and urbanisation (IPCC, 1996). Since air pollution control remains at the very low stage in the region, much efforts are needed for the implementation of national and regional air quality standards as well as stringent air quality management plan for controlling emissions of ozone precursors from domestic and industrial operators.

#### 3.2.3. Biogenic emission

The role of biogenic emissions to the formation of tropospheric ozone formation in southern African and Adjacent Indian Ocean originates from forests and

savannas where important quantities are most observed in austral spring corresponding to the rainy season in the Southern Hemisphere (Diab *et al.* 2004). As the precedent sources, biogenic emissions likewise depend on meteorological conditions (high temperature and humidity) coupled with vegetation types. Despite the scarcity of data, and large uncertainties on emission rate (Nyamadzawo *et al.* 2012) the most important factor in determining biogenic emissions is the response to environmental changes occurring during the year (Delon *et al.* 2008).

#### 3.2 4. Lightning emission

Lightning emissions were less accounted as source of ozone precursors until the finding made by Pickering *et al.* (1998) and Otto *et al.* (2010) who showed that NO<sub>x</sub> from lightning was crucial for the formation of upper tropospheric ozone as greenhouse gas. Furthermore, Thompson *et al.* (2000), Martin *et al.* (2002b), Edwards *et al.* (2003), and Sauvage *et al.* (2007) suggested that lightning generated NO<sub>x</sub> (LNO<sub>x</sub>) was instrumental on understanding of the dominant features in tropical tropospheric ozone distribution, and even over downwind of mid-latitude continents where anthropogenic sources are strongest. It is evident that high density lightning are located at low latitude central equatorial region and low to medium density near and below 20° south latitude. The role of NO<sub>x</sub> in the tropospheric ozone formation is especially critical (Yuan *et al.* 2012) as it accounts amongst natural sources of ozone precursors although accurate source strength of LNO<sub>x</sub> and its variability is poorly documented.

### 4. Inventory of sources contribution estimates

There is no particular inventory of source contributing to tropospheric ozone for southern Africa and Adjacent Indian Oceans. For the purpose of this study Table 1 presents annual trace gas emissions from various sources for Africa such as performed by Marufu *et al.* (2000). Biomass burning is the largest source of trace gas emission in Africa with (38%) followed by biogenic and lightning emissions with 25 and 17% respectively. This inventory shows that almost 42% of trace gas emission originates from natural sources, which may be exacerbate by climate change as discussed above.

Relative emission source contributions to the annual average tropospheric ozone and ozone abundance over Africa are presented in Table 2. A large percentage of tropospheric ozone in Africa originates from STE which represents 26.8% followed by lightning emission with 26.7%.

**Table 1.** Annual trace gas emission from various sources for Africa

Source	Emissions, yr <sup>-1</sup>				
	CO <sub>2</sub> , Tg C	CO, Tg C	CH <sub>4</sub> , Tg C	NMHC, Tg C	NO <sub>x</sub> , Tg N
Biofuel*	181	16.3	0.8	1.3	0.4
Other biomass burning†	156	79.6	5.4	11.8	2.7
Industry‡	228.9	4.0	2.3	4.7	1.0
Biogenic§	...	11.9	9.6	105.2	1.8
Lightning	...	...	...	...	1.2
Total	565.9	112	18.1	123	7.1
Other estimates (biofuels) <i>Olivier et al. [1996]</i>	262	19.2	2.8	6.2	0.3

\*Own inventory (see text).  
†Includes savanna burning, agricultural waste burning, and deforestation fires. For CO<sub>2</sub> only deforestation fires have been considered.  
‡Includes fossil fuel burning and industrial processes.  
§Includes soil and vegetation emissions.

Source: Marufu *et al.* (2000)

Industry emissions as well as biomass burning occupy the third and fourth position with 19.2 % and 12.7% respectively. This finding confirms the impact climate change may have on natural sources such STE and lightning which present higher abundance contribution in the whole troposphere. With regard to the abundance in Boundary Layer, biomass burning as well as industry emissions have the higher percentage as these deeply depend on prevailing meteorology for their dispersion in the atmosphere. This assumption matches recent findings made by Mulumba *et al.* (2015) who modeled tropospheric ozone climatology relationship with meteorological parameters at Irene for the period 1998-2013.

**Table 2.** Relative emission source contribution to the annual average tropospheric Ozone abundance over Africa (i.e., in Region Below 100hPa based on “Marked tracer” Approach.

Source	Contribution to Ozone Abundance in Whole Troposphere		Contribution to Ozone Abundance in Boundary Layer	
	Tg O <sub>3</sub>	Percent Total	Tg O <sub>3</sub>	Percent Total
Biofuel	0.75	2.9	0.15	3.7
Other burning	3.33	12.7	0.84	20.4
Industry	5.1	19.2	1.14	27.8
Biogenic	3.10	11.7	0.66	16.0
Lightning	7.03	26.7	0.78	19.0
Stratospheric	7.05	26.8	0.54	13.1
Total	26.32	100	4.11	100

Source: Marufu *et al.* 2000

## 5. Conclusion

The main focus of this review was to provide a comprehensive review of sources contributing to tropospheric ozone over southern Africa and Adjacent Indian Ocean Islands in order to find sound critical understanding of their occurrence and dynamic. Five main contributing sources including stratospheric tropospheric exchange (STE), Biomass burning (BB), anthropogenic emissions (AE), biogenic emissions (BE) and lightning emissions (LE) have been identified and discussed with regard

to their respective contribution to tropospheric ozone enhancement observed over the region. Their likelihood impact in the regional tropospheric ozone formation with the changing climate has also been discussed for a better prediction of future regional atmospheric changes. The dynamic of these sources is responsible in a given region for the chemistry, transport and radiative flux balance in the troposphere at the lower stratosphere at a given altitude and latitude. Accordingly it was then stipulated that the role of NO<sub>x</sub> in the tropospheric ozone formation is especially critical, as it accounts amongst natural sources of ozone precursors although accurate source strength of LNO<sub>x</sub> and its variability is poorly documented.

## 5. References

- Andreae, M. O. (1997). Emissions of trace gases and aerosols from southern African savanna fires, in *Fire in the Southern African Savannas: Ecological and Environmental Perspectives*, edited by B. W. van Wilgen *et al.*, pp. 161– 183, Witwatersrand Univ. Press, Johannesburg, South Africa.
- Baray, J. L., Ancellet, G., Taupin, F. G., Bessafi, M., Baldy, S., and Keckhut, P., (1998) Subtropical tropopause break as a possible stratospheric source of ozone in the tropical troposphere, *J. Atm. Sol.-Terrestr. Phys.*, 60 (1), 27–36.
- Butchart, N., and A. A. Scaife, (2001). Removal of chlorofluorocarbons by increased mass exchange between the stratosphere and troposphere in a changing climate, *Nature*, 410, 799– 802.
- Collins, W. J., Derwent, R. G., Garnier, B., Johnson, C. E., Sanderson, M. G., and Stevenson, D. S., (2003). Effect of stratospheretroposphere exchange on the future tropospheric ozone trend, *J. Geophys. Res.*, 108, 8528, doi:10.1029/2002JD002617.
- Diab, R. D., Thompson, A. M., Mari, K., Ramsay, L., and Coetzee, G. J. R. (2004): Tropospheric ozone climatology over Irene, South Africa, From 1990 to 1994 and 1998 to 2002, *J. Geophys. Res.*, 109, D20301, doi:10.1029/2004JD004793, 2004.
- Delon, C., Serc, a, D., Boissard, C., Dupont, R., Laville, P., de Rosnay, P., and Delmas, R., (2007). Soil NO emissions modeling using artificial neural network, *Tellus B*, 59B, 503–513.
- Edwards, D. P., *et al.* (2003), Tropospheric ozone over the tropical Atlantic: A satellite perspective, *J. Geophys. Res.*, 108(D8), 4237, doi:10.1029/2002JD002927.
- Fishman Jr., J., Bendura, R. D., McNeal, R. J., and Kirchhoff, V.W. J. H.: NASA GTE TRACE A Experiment (September–October 1992). (1996). Overview, *J. Geophys. Res.*, 101, 23 865–23 880.

- Holton, J. R., Haynes, P. H., McIntyre, M. E., Douglass, A. R., Rood, R. B. and Pfister, L. (1995). Stratosphere-troposphere exchange. Review of Geophysical Sciences, 33, 403–439.
- Intergovernmental Panel on Climate Change (IPCC) (1996). Climate Change 1995: The Science of Climate Change, edited by J. T. Houghton *et al.*, Cambridge Univ. Press, New York.
- Levy, Y. and T. J. Ellis, (2006). A Systems Approach to Conduct an Effective Literature Review in Support of Information Systems Research. Informing Science Journal Volume 9, 1-32.
- Martin, R. V., *et al.*, (2002b). Interpretation of TOMS observations of tropical tropospheric ozone with a global model and in situ observations, *J. Geophys. Res.*, 107(D18), 4351, doi:10.1029/2001JD001480.
- Marufu, L., *et al.*, Photochemistry of the African troposphere, (2000). Influence of biomass burning emission, *J. Geophys. Res.*, 105, 14,513-14,15 30.
- Mulumba, J.P., Venkataraman, S., Afullo, T.J.O. (2015). Modelling Tropospheric Ozone climatology over Irene using retrieved remote sensing and ground based measurement data. *J. Geophys. Remote Sens.* vol.4 issue 3. <http://dx.doi.org/10.4172/2169-0049.1000151>
- Nyamadzawo, G., N. Chirinda, F. Mapanda, J. Nyamangara, M. Wuta, P. Nyamugafata and J.E. Olesen (2012). African Crop Science Journal, Vol. 20, Issue Supplements, pp. 553 – 564.
- Otto, L., K. Pickering, G. Stenchikov, D. Allen, A. Decaria, B. Ridley, R. Lin, S. Lang, and W. Tao, (2010). Production of lightning NO<sub>x</sub> and its vertical distribution calculated from three-dimensional cloud-scale chemical transport model simulations, *J. Geophys. Res.*, 115, D04301, doi:10.1029/2009JD011880.
- Pickering, K. E., Y. S. Wang, W. K. Tao, C. Price, and J. F. Muller, (1998). Vertical distributions of lightning NO<sub>x</sub> for use in regional and global chemical transport models, *J. Geophys. Res.*, 103(D23), 31,203–31,216, doi:10.1029/98JD02651.
- Ramaswamy, V., M. D. Schwarzkopf, and K. Shine, (1992). Radiative forcing of climate from halocarbon-induced global stratospheric ozone loss, *Nature*, 355, 810-812.
- Randriambelo, T., Baray, J.-L., and Baldy, S., (2000). Effect of biomass burning, convective venting, and transport on tropospheric ozone over the Indian Ocean: Reunion Island field observations, *J. Geophys. Res.*, 105 (D9), 11 813–11 832.
- Sauvage, B., R. V. Martin, A. Van Donkelaar, and J. R. Ziemke, (2007). Quantification of the factors controlling tropical tropospheric ozone and the South Atlantic maximum, *J. Geophys. Res.*, 112, D11309, doi:10.1029/2006JD008008.
- Thompson, A. M., B. G. Doddridge, J. C. Witte, R. D. Hudson, W. T. Luke, J. E. Johnston, B. J. Johnston, S. J. Oltmans, and R. Weller, (2000). A tropical Atlantic paradox: Shipboard and satellite views of a tropospheric ozone maximum and wave-one in January-February 1999, *Geophys. Res. Lett.*, 27(20), 3317–3320, doi:10.1029/1999GL011273.
- Toumi, R., S. Bekki, and K. S., (1994). Law, Indirect influence of ozone depletion on climate forcing by clouds, *Nature*, 372, 348-351.
- Van der Werf, G.R., Randerson, J.T., Collatz, G.J. and Giglios, L., (2003). Carbon emissions from fires in tropical and subtropical ecosystems, *Global Change Biology*, 9, 547-562.
- Van der Werf, G.R., Randerson, J.T., Giglio, L., Collatz, G.J., Kasibhatla, P.S., and Arellano, A.F., (2006). Interannual variability in global biomass burning emissions from 1997 to 2004, *Atmospheric Chemistry and Physics*, 6, 3423-3441.
- Wilgen *et al.*, pp. 161– 183, Witwatersrand Univ. Press, Johannesburg, South Africa.
- Yuan, T., Lorraine A. Remer, Huisheng Bian, Jerald R. Ziemke, *et al.* (2012). Aerosol indirect effect on tropospheric ozone via lightning. *Journal of Geophysical Physical Research*, Vol. 117, D18213, doi:10.1029/2012JD017723.

## Temporal Variation in Solar Radiation, UV index and its effect on Ozone variations over Durban, South Africa – Initial result

Jeremiah A. Ogunniyi<sup>1\*</sup> Venkataraman Sivakumar<sup>1</sup> and Paulene Govender<sup>1</sup>

<sup>1</sup>Discipline of Physics, School of Chemistry and Physics, College of Agriculture, Engineering and Science, Westville Campus, University of KwaZulu-Natal, Durban 4000, South Africa

\*Corresponding Author: [jerryogunniyi@yahoo.com](mailto:jerryogunniyi@yahoo.com); +27617489684

### Abstract

Global solar radiation has a significant role in the balance of ground surface radiation, exchange of energy between the earth and its surface as well as the development of weather and climate systems in different regions. In this work, we studied the monthly global, direct and diffuse radiation over Durban, South Africa. The aim is also to study solar radiation and their effect on ozone over Durban using both ground-based and satellite observations between 2013 and 2014. The initial result shows similar inter-annual variation pattern as well as seasonal maximum in summer and minimum during winter for both solar radiation as well as the UV Index.

Key Words: Global, Direct, Diffuse, Irradiance, Seasons

### Introduction

The importance of ozone and solar ultraviolet radiation has been discussed by researchers over the last few decades. Though ozone is almost negligible in atmospheric concentration, change in its concentration has adverse effects on all living organisms on earth. Ozone absorbs the most energetic part of the solar ultraviolet radiation spectrum, thus preventing this harmful radiation from penetrating the atmosphere to the earth's surface. Ozone has been found to decrease in both the northern and southern hemisphere over the past decades due to anthropogenic emissions of ozone-depleting substances which in turn increases the amount of active ultraviolet radiation reaching the earth's surface (Musil et al., 2003). The variability of ozone has great effect on the solar ultraviolet radiation measured on the earth surface. This, however, depends on wavelength since ozone absorption increases with decreasing wavelengths. Data reported for over two decades (1979 to 1998) showed that there was significant increase in solar ultraviolet radiation attributed to a decrease in the amount of stratospheric ozone (Fahey 2006). This was based on the assumption that other factors that influence the amount of solar ultraviolet radiation reaching the earth surface are unchanged. This increase in solar ultraviolet radiation on the earth surface is of adverse effect to living organism on earth. According to the United Nations Environmental Programme, increase in solar ultraviolet radiation could induce up to a million cases of blindness due to cataracts, and poses great threat to the aquatic ecosystem, plant growth, and photosynthesis among others. Earlier, Duigan et al (1993) measured UVB over Durban between February and December 1993 and compared measurements obtained from a Yankee systems

pyranometer with theoretically generated values. They obtained good correlation coefficient between the two models using regression analysis. Their study also revealed that the damage burn time of the skin on sunny days is under 40 minutes and not hours as many would have thought. Later, Bodeker and Scourfield (1998) estimated both the past and the future of UV radiation based on the trends of total column ozone (TCO) at five locations in South Africa. They showed that TCO level was reducing at a statistically insignificant trend which corresponds to increase in surface erythema irradiance. They developed a statistical model for accounting for changes in TCO trend, however, they warned that their predictions should be taken with caution. They then emphasized the need for ground based UV monitoring network over South Africa. As well as solar ultraviolet radiation, a number of scientists have researched in the variation of ozone over South Africa. Thompson et al (1996) analysed a campaign measurement over Southern Africa between 1992 and 1993. Their result showed that the variation of ozone was mainly due to ozone annual cycle, Quasi Biennial Oscillation (QBO) transport processes as well as biomass burning. This study therefore provides a more recent report on the variation of total ozone with solar ultraviolet radiation as well as the ultraviolet radiation index (UVI).

### Datasets

The radiometric data used for this study was obtained from the University of KwaZulu-Natal (UKZN) Westville campus radiometry station in Durban (S29°49'2", E30 56'40"). The station is situated on the roof of the Physics building (205m above mean sea level), with an unobstructed view of the horizon. The station comprises a Kipp and

Zonen Normal Incidence Pyrheliometer (NIP) for direct radiation measurements and shaded and unshaded pyranometers for diffuse and global measurements, respectively. All instruments are mounted on a Solys2 automatic sun tracker. The data sampling rate is 1 second, thereafter minute, hourly and daily averages are produced. The instruments are subject to regular cleaning and maintenance. Data for this study is restricted to the period of 2013 and 2014 due to frequent electricity disruptions experienced at the station during 2015. The Westville radiometry station is one of ten radiometry stations within the South African Universities Radiometric Network (SAURAN), whose primary aim is to provide long-term, high-quality radiometric data (Brooks et al., 2015). Total column Ozone values are obtained from the Ozone Monitoring Instrument (OMI) over Durban. The UVI datasets over Durban are collected from the Global Ozone Monitoring Experiment (GOME-2). The datasets can be obtained from [http://www.temis.nl/uvradiation/SCIA/stations\\_uv.html](http://www.temis.nl/uvradiation/SCIA/stations_uv.html)

## Results and Discussion

The monthly variation in solar radiation was obtained by grouping the datasets in terms of months irrespective of the years and the mean was obtained. Fig 1 shows the monthly variation in global, diffuse and direct solar radiation in Westville, Durban, South Africa. The result reveals the seasonal variation in solar radiation with the summer months having the highest global corresponding to  $\sim 1300 \text{ W/m}^2$ , diffuse  $870 \text{ W/m}^2$  and direct  $580 \text{ W/m}^2$  solar radiation in January and the minimum in the winter months corresponding to  $600 \text{ W/m}^2$ ,  $420 \text{ W/m}^2$  and  $210 \text{ W/m}^2$  for global, diffuse and direct solar radiation, respectively, in July. During these winter months, the averaged minimum ozone values are also obtained for the combined two year period of measurement as shown in Fig 2. This can be attributed to the fact that most ozone is produced as a result of the photolysis of oxygen which basically takes place when there is much sunshine (Arne Dahlback 2008). There was a gradual increase from winter through summer and then spring in solar ultraviolet radiation. These seasonal changes also correspond to changes in ozone level during this period. However, there are other contributing factors to the variation of ozone. The correlation coefficients between global and direct radiation was 0.46 while those of global and diffuse as well as between diffuse and direct are 0.31 and 0.01, respectively.

Power and Mills (2005) evaluated both the temporal and spatial variability in global, diffuse as well as direct irradiance at eight South African stations. The result showed that both the global and

direct irradiance decrease from northwest to south east while diffuse irradiance increase towards the east. These trends are attributed to the presence of tropical temperate troughs which are associated with cloud bands. They also observed a statistically significant long-term trend in five of those stations, including Durban, in annual averaged global irradiance. However, there was no significant trend in the averaged diffused irradiance.

However, it is quite difficult to determine the trend of solar radiation from the current study, long-term datasets would be required to determine solar radiation trend in Durban, South Africa. However, according to Arne Dahlack (2008), the levels of solar ultraviolet radiation in most stations in the Southern Hemisphere have been decreasing since the late 1990s in accordance with the observed ozone. Although some stations in the Northern Hemisphere showed increase in solar radiation due to long term changes in other factors affecting solar radiation mainly aerosols, total column ozone and cloud cover.

The ultraviolet radiation data was available from 2002 till present. However, for the purpose of this study, the data used was limited to 2013 and 2014. The monthly variation in ultraviolet index was obtained by grouping the daily measurements in terms of months and their respective mean was obtained. The result revealed that UVI was minimum during winter which is expected due to minimum solar ultraviolet radiation and maximum during spring as shown in Fig 3. According to the United States Environmental Protection Policy, a UVI index of 11 is considered extreme and it was recommended that during these extreme days or months, protective equipment should be worn to prevent the sun burns and long term effects of skin cancer and cataracts. During summer months over Durban, the average peak, midday UVI is about 13 which is very high.

## Conclusion

The study showed that there is better relationship between global and direct solar radiation compared to either global and diffuse or diffuse and direct solar radiation based on their correlation coefficients. For global, diffuse and direct solar radiation, maximum irradiance was during summer while minimum was in winter while for ozone, maximum was measured in spring while the minimum was in autumn. The long term trend of global, diffuse and direct solar radiation in Durban could not be determined due to the lack of long term datasets. The result of the UVI showed very high values during the summer months and it is highly recommended that protective clothing and other products should be worn during this period to

prevent both the short term and long term effect of this radiation on the skin as well as the eyes.

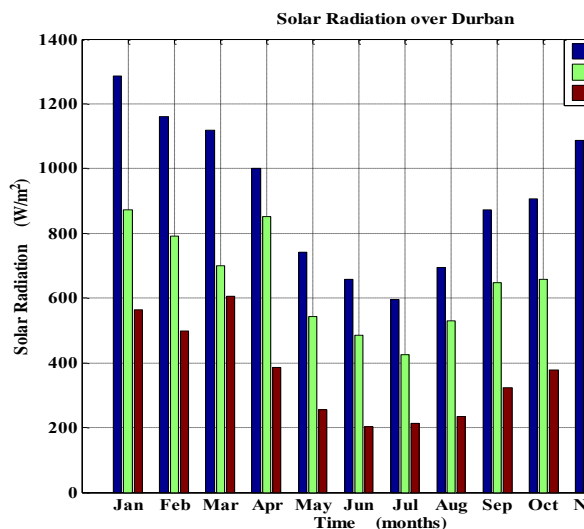


Figure 1 Monthly mean of Global, Diffuse and Direct Solar radiation over Durban, South Africa for 2013 and 2014

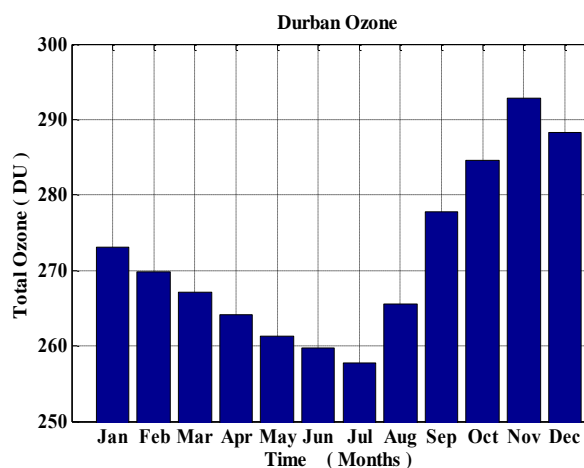


Figure 2 Monthly mean of total column ozone over Durban, South Africa for 2013 and 2014

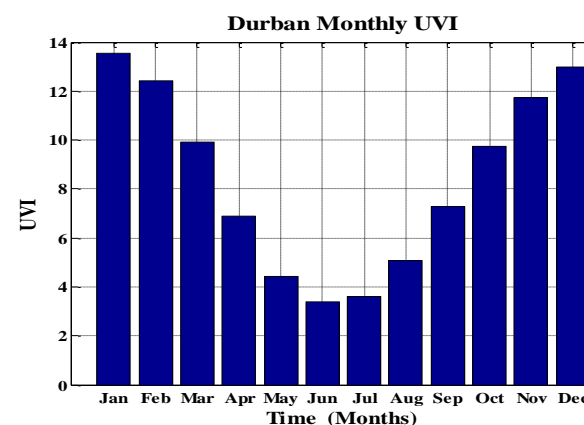


Figure 3 Monthly mean ultraviolet radiation index over Durban between 2013 and 2014

List of Figures

Figure 1 Monthly mean of Global, Diffuse and Direct Solar radiation over Durban, South Africa for 2013 and 2014

Figure 2 Monthly mean of total column ozone over Durban, South Africa for 2013 and 2014

Figure 3 Monthly mean ultraviolet radiation index over Durban between 2013 and 2014

Acknowledgements

My appreciation goes to University of KwaZulu-Natal for providing the opportunity to carry out this research work. We also acknowledge the GOME and OMI satellite team for the data availability.

References

Anthón M., Cancillo M.L., Serrano A., Vaquero J.M. and Garcia A. (2007), Ozone Mini-Hole over South Western Spain During January 2004: Influence over Ultraviolet Radiation, *Geo. Res. Letter*, Vol. 34, L10808.

Arne Dahlback (2008), Global Monitoring of Atmospheric Ozone and Solar UV Radiation, *The Norwegian Academy of Science and Letters*, pp. 23-34.

Bodeker, G.E. and Scourfield, M.W.J. (1998). Estimated past and future variability in UV radiation in South Africa based on trends in total column ozone. In: *South African Journal of Science*, vol. 94, 24-32.

Bekker B. (2007), Irradiation and PV Array Energy Output Cost and Optimal Positioning Estimation for South Africa, *Journal of Energy*, Vol. 18, NO. 2.

Brooks M.J, du Clou S., van Niekerk W.L., Gauche P., Leonard C., Mouzouris M.J., Meyer R., van der Westhuizen N., van Dyk E.E., Vorster F.J. (2015), SAURAN: A new resource for solar radiometric data in Southern Africa, *Journal of Energy in Southern Africa*, Vol. 26, pp. 2-10.

Charles F. Musil, Greg E. Bodeker, Malcolm W.J. Scourfield and Leslie W. Powrie (2003), Geographical and temporal trends in Southern African Clear-sky, Solar Ultraviolet –B Flux 1979 to 2001, *South*

- African Journal of Science, Vol. 99, pp. 477-483.*
- Duigan, B.L., Scourfield, M.W.J. and Stefanski B. jr, (1995). Surface UVB irradiance measurements at Durban during 1993. In: South African Journal of Science, vol. 91, 394-398.
- Power H.C and Mills D.M. (2005), Solar Radiation Climate Change over Southern Africa, An Assessment of the Radiative Impact of Volcanic Eruptions, *Int. J. Climatol Vol. 25 pp.295-318.*
- Ramkumar Jayaraman and Douglas Maskell (2012), Temporal and Spatial Variations of the Solar Radiation Observed in Singapore, *Energy Procedia Vol. 25, pp. 108-117.*
- Ren Li, Lin Zhao, Tonghua Wu, Yongjian Dian, Yufei Xin, Defu Zou, Yao Xiao, Yongliang Jiao, Yanhui Qui and Linchan Sun (2013), Temporal and Spatial Variations of Global AND Solar Radiation over Qinghai-Tibetan Plateau During the past 40 years. *Theor APPL Climatol, Vol. 113, pp. 573-58.*
- Thompson A.M., Diab R.D., Bodeker G.E., Zunckel M., Coetzee G.J.R, Archer C.B., McNamara D.P., Pickering K.E., Combrink J., Fishman J. and Nganga D. (1996), Ozone over Southern Africa During SAFARI-92/TRACE, *J. Geores. Vol. 101, pp. 793-807*
- United Nations Environmental Programme (UNEP), (1998), Environmental Effects of Ozone Depletion: 1998 Assessment, Technical Report, U.N. Environ. Programme, Nairobi, pp. 160-171.

## FIVE YEAR CLIMATOLOGICAL TRENDS OF AOD OVER COSTAL AND INLAND TOWNS OF SOUTH AFRICA RETRIEVED BY MODIS

Lerato Shikwambana<sup>1\*</sup> and Venkataraman Sivakumar<sup>1</sup>

<sup>1</sup>School of Chemistry and Physics, University of KwaZulu-Natal, Durban 4000, South Africa

In this study, we have intended to compare the AOD trends for inland towns and coastal towns in South Africa, using MODIS. The identified three inland towns were Johannesburg (26.20° S, 28.04° E), Secunda (26.51° S, 29.20° E) and Witbank (25.87° S, 29.20° E) and the three coastal towns were Cape Town (33.92° S, 18.42° E), Durban (29.88° S, 31.05° E) and Port Elizabeth (33.95° S, 25.60° E). Inland towns showed higher values of AOD compared to those of coastal towns. Port Elizabeth (PE) has an average AOD value of 0.05 in August, however, a higher value of AOD (0.104) in August 2014 was observed. This value was the same as that of Durban for the same period. Biomass burning aerosols could be the major contributor during this period as this is when they are most prevalent. Moreover, the HYSPLIT model also revealed the possible transport of dust aerosols from the Kalahari Desert to PE.

*Keywords:* AOD, Biomass burning, Aerosols, MODIS

### 1. Introduction

Aerosol Optical Depth (AOD) is the measure of aerosols distributed within a column of air from the instrument to the top of the atmosphere. AOD is an important physical parameter for indicating atmospheric turbidity and aerosol content, and it is also a crucial factor in determining the aerosol radiance climatic effect.

AOD has been studied in various parts of the world such as China (Lin et al., 2014; Jiang et al., 2007), North Eastern regions of India (Kumar, 2013), Spain (Lyamani et al., 2006) and South Africa (Tesfaye et al., 2014; Sivakumar 2008). Kumar et al. (2014) recently reported on the decadal negative trend observed in the annual mean AOD in three cities (Pretoria, Bloemfontein and Cape Town) of South Africa. Other AOD measurements around South Africa have been reported in Sutherland (Formenti et al, 2002) and De Aar (Winkler et al., 2008).

South Africa is situated in the southern tip of Africa and has both coastal and inland regions. The east side of the country has the Indian ocean while the west side has the Atlantic Ocean. The country could be divided into three climatic regions; the subtropical wet, the subtropical dry and the arid. The subtropical wet region is characterised by hot summer temperatures and fully humid conditions, this is observed on the eastern parts of South Africa. The subtropical dry regions are observed on the northern parts of South Africa and are characterised by warm temperatures during dry summers. The arid region is observed on the west part of South Africa and are characterised by high temperatures (Kanike and Sivakumar, 2015).

For this study six towns/cities were identified and chosen according to their climate, anthropogenic activities and location. Three inland towns chosen were Johannesburg (26.20° S, 28.04° E), Secunda (26.51° S,

29.20° E) and Witbank (25.87° S, 29.20° E). Johannesburg is an urban polluted area with significant anthropogenic and industrial activities and mineral dust. Secunda and Witbank are predominately mining and industrial areas with a large volume of anthropogenic activities. Three coastal towns chosen were Cape Town (33.92° S, 18.42° E), Durban (29.88° S, 31.05° E) and Port Elizabeth (33.95° S, 25.60° E). All three cities are urban with Cape Town located close to the Atlantic Ocean while Durban and Port Elizabeth are located close to the Indian Ocean.

There are two main objectives to this study; the first objective is to compare the AOD trends for inland towns and coastal towns. The second objective is to compare the AOD trends in each town using the Multispectral Imaging Radiometer (MSIR) and Moderate Resolution Imaging Spectroradiometer (MODIS).

### 2. Experimental site and Instrumentation

#### 2.1 SITE

The measurements for this study were carried out in six towns around South Africa, see Figure 1. The measurement site comprise of coastal and inland towns. The 1x1 degree boxes around each of the cities studied (not shown here) has an impact on the averaged AOD as there is influence from the surrounding areas. For coastal towns like DUR which are close to the ocean, sea salt aerosols would contribute to the total averaged aerosols measured. For inland towns like JHB, dust aerosols from the mining activities from the surroundings will also contribute to the total averaged aerosols.

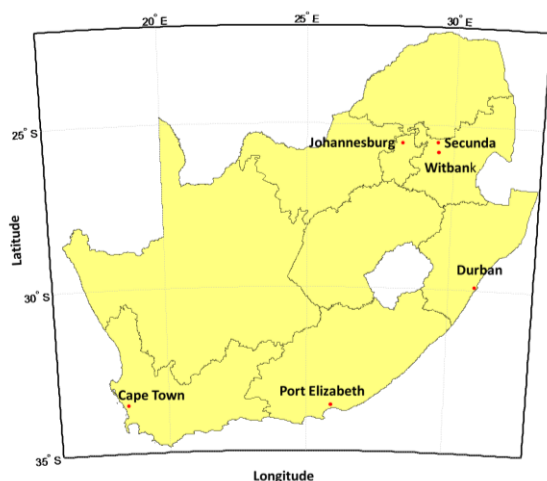


Figure 1: A map of South Africa showing the towns where measurements were carried out.

## 2.2 MODIS

The Moderate Resolution Imaging Spectroradiometer (MODIS) is an instrument aboard the Terra Earth observation system (EOS AM) and Aqua (EOS PM) satellites. The Terra's orbit around the earth is timed so that it passes over the equator from north to south in the morning. The Aqua's orbit is timed so that it passes over the equator from north to south in the afternoon. MODIS satellite provides radiance measurements in 36 spectral bands ranging between 0.44 and 15  $\mu\text{m}$ , with different spatial resolution: 250 m (bands 1 and 2), 500 m (bands 3 - 7) and 1 km (bands 8 - 36) (Bennouna et al, 2013). MODIS aerosol retrievals are done separately over land and ocean using two independent algorithms (Bennouna et al, 2013). The MODIS technical specifications are summarised in Table 1. In this study, we have used the monthly MODIS (Terra) Level - 3 data that are quality checked and globally gridded over 1X1 grid resolution for the period from May 2011 to May 2015. Expected error over land in MODIS AOD is characterised as  $\Delta\sigma = \pm 0.05 \pm 0.15\sigma$ , where  $\sigma$  is aerosol optical depth at 550 nm (suman et al, 2014).

Table 1: MODIS technical specifications (<http://wamis.meraka.org.za/modis-basics>)

Feature	Specification
Orbit	705 km, 10:30 a.m. descending node or 1:30 p.m. ascending node, sun synchronous, near-polar, circular
Scan rate	20.3 rpm, cross track
Swath dimensions	2330 km (across track) by 10 km (along track at nadir)
Size	1.0 x 1.6 x 1.0 m
Power	225 W
Data rate	11 Mbps (peak daytime)

## 2.3 HYSPLIT Model

In this study, the HYSPLIT (Hybrid Single-Particle Lagrangian Integrated Trajectory) model Version 4 was used to generate air mass backward trajectories. It is a complete system for computing simple air parcel trajectories to complex dispersion and deposition simulations (Draxler et al, 2015). The model can be run interactively on the NOAA website (<http://ready.arl.noaa.gov/HYSPLIT.php>). The air mass trajectories is useful to address various aspects related to atmosphere and environment and can be applied in various fields such as climatology, meteorology, transport of pollutants, residence time analysis, air quality, source apportionment, aerosol measurements, precipitation chemistry, and policies (Kulshrestha and Kumar, 2014). In our case the air masses trajectories were used to find out the source region of aerosols.

## 3. Results and discussion

The retrieval of AOD using MODIS for the six towns showed high aerosol loading in the towns situated in the inland regions; Secunda (SEC), Johannesburg (JHB) and Witbank (WTB), compared to those in the coastal regions; Cape Town (CPT), Durban (DUR) and Port Elizabeth (PE), see Figure 2. However, there is a period in August 2014 where a slightly higher AOD ( $\sim 0.104$ ) was observed in DUR and PE. This AOD value was higher than that of the inland towns. This indicated that high levels of aerosols were present during that time.

A comparison of AOD between the coastal towns reveals that DUR has high AOD levels during the period of August, see Figure 3. Biomass burning aerosols could be the biggest contributor to the high AOD in August. Tesfaye et al. (2014) conducted a study in South Africa to show how biomass burning aerosol travel. He showed that seasonal high levels of biomass burning aerosols are found between July and October for the Durban region. Moreover in this five year trend study the highest AOD value of 0.129 was observed in August 2012. What is of more interest is that on average PE has an AOD of ( $\sim 0.05$ ) in August. However, on August 2014 an AOD value of 0.104 was observed in PE which was the same as that of DUR. The HYSPLIT model, shown in Figure 4, was run on the ninth of August 2014 for DUR and PE. The backward trajectory suggest that the aerosols detected at DUR and PE were from the same source. The 5000 m (green) and 2000 m (blue) air masses travelled through Namibia and Botswana respectively for both DUR and PE carrying these aerosols. However, the 500 m (red line) air mass showed a different path for the two towns. The air mass from DUR came from the Indian Ocean whereas the air mass from PE originated from Botswana. Since some of these air masses travelled through the Kalahari Desert (in Botswana) it is likely that there was transport of dust aerosols which could have landed in DUR and PE. In general the different air masses origin at different altitudes revealed that most of

the AOD were from the north of South Africa. The impact of this was an increase in the AOD level in these areas.

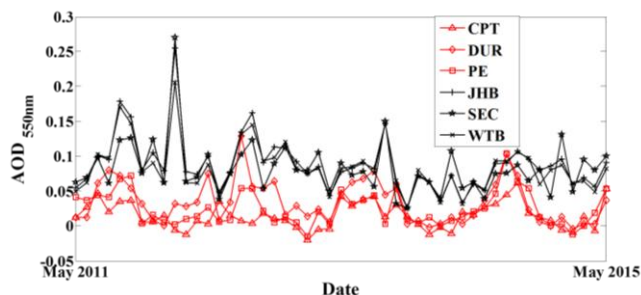


Figure 2: Five year trends of aerosol optical depths derived from Terra MODIS between May 2011 and May 2015 for inland and coastal towns.

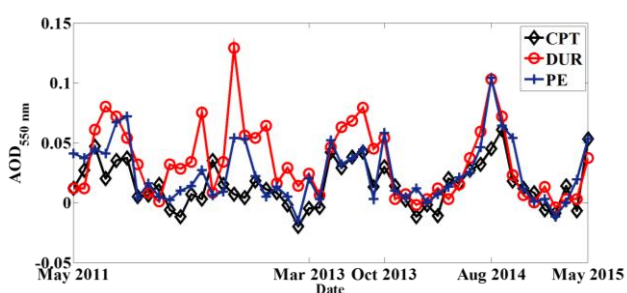


Figure 3: Five year trend of aerosol optical depth obtained by MODIS for coastal towns.

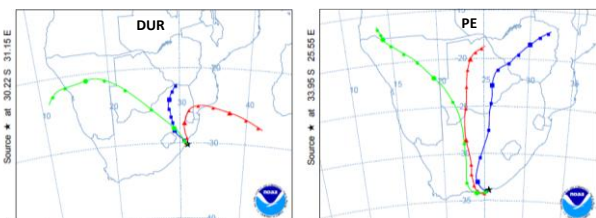


Figure 4: Backward trajectory ending at the DUR and PE sites

The AOD values for inland towns are relatively close to each other and show a decreasing AOD trend, see Figure 5. However, in February 2012 there was a sharp increase in AOD for all the towns. SEC and JHB showed the highest AOD value of 0.27. A three day backward trajectory ending on 09 February 2012 for JHB and SEC show that the aerosols originated from within South Africa, see Figure 6. The 5000 m (Green line) air mass for both towns show that the aerosols originated from Lesotho. However, the 500 m (red line) air mass suggest that the aerosols originated locally for SEC and JHB. Air masses at 2000 m showed that the aerosols originated at the north east parts of South Africa whereas in SEC the aerosols originated from the Highveld region (JHB, WTB and SEC) of South Africa.

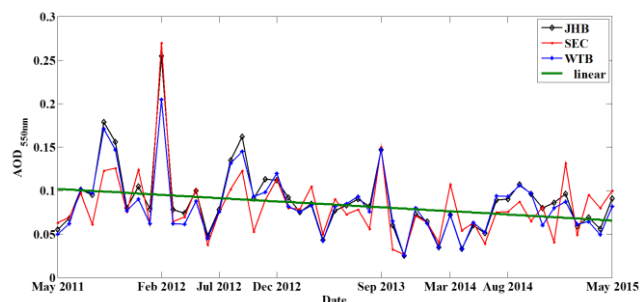


Figure 5: Five year trend of aerosol optical depth obtained by MODIS for inland towns.

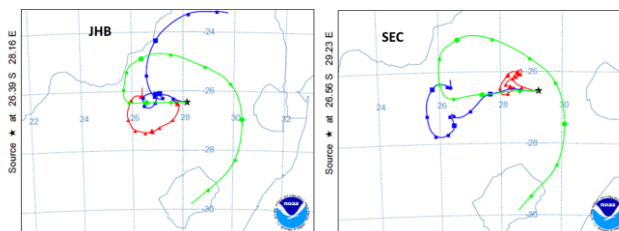


Figure 6: Backward trajectory ending at the JHB and SEC sites.

The Monthly datasets of aerosol optical depth have been averaged to make climatology for each season during each year. Seasonal mean values obtained in each year have been averaged in corresponding seasons from 2011 to 2015 to make climatological values for individual seasons, see Figure 7. JHB showed the highest AOD value (0.11) for the spring season (September – November), while the lowest AOD (0.07) was observed in the Autumn season (March – May). The main contributor to this high AOD is the biomass burning aerosols that occurs during the spring season. These aerosols are known to travel through the Highveld region (WTB, SEC and JHB) of South Africa (Tesfaye et al. 2014). DUR showed the highest AOD in the winter and spring season because of the sugar cane burning that occurs during the dry season. For DUR the lowest AOD are observed in the summer season. The major type of aerosols likely to be found in this season are the sea salt aerosols from the ocean as the biomass burning aerosols are fewer in this season. PE is the only coastal town which has a high aerosol loading in the summer season. The lowest AOD is observed in the autumn (March – May) season. CPT generally displayed a low AOD, however, the highest AOD value of about 0.03 was observed in the winter season while the lowest AOD value (0.01) was observed in the summer season.

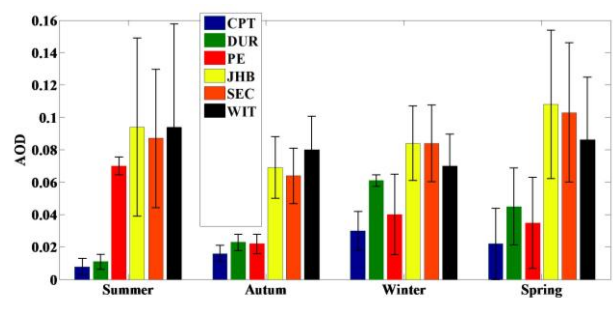


Figure 7: Seasonal variations of mean AOD obtained from Terra MODIS for the six towns.

#### 4. Conclusion

Inland towns have a much higher AOD compared to those at coastal regions. The main reason for this is that aerosol at the coastal regions are usually blown away by the winds coming from the sea. However, on August 2014 a high value of AOD was observed in PE which was the first in the five year study. The air masses from the HYSPLIT model indicate that the aerosols originated from neighbouring countries of South Africa. The air masses (500, 2000, 5000 m) conducted on nine August 2014 all passed through the Kalahari Desert indicating that there is a strong possibility that dust aerosols were transported to PE. For JHB and SEC the highest AOD is in the spring season when biomass burning is at its prime. The lowest AOD was observed in CPT during the summer season. DUR has the highest AOD in the winter season which is mostly from biomass burning from sugar cane burning in the KwaZulu Natal region in the dry season.

#### 5. References

- Bennouna Y.S., Cachorro V.E., Torres B., Toledano C., Berjón A., de Frutos A.M., Alonso Fernández Coppel I., 2013. Atmospheric turbidity determined by the annual cycle of the aerosol optical depth over north-center Spain from ground (AERONET) and satellite (MODIS), *Atmospheric Environment* 67, 352-364.
- Draxler, R.R. and Rolph, G.D., 2015. *HYSPLIT (HYbrid Single-Particle Lagrangian Integrated Trajectory) Model* access via NOAA ARL READY Website (<http://ready.arl.noaa.gov/HYSPLIT.php>). NOAA Air Resources Laboratory, Silver Spring, MD.
- Formenti P., Winkler H., Fourie P., Piketh S., Makgopa B., Helas G., Andreae M. O., 2002. *Aerosol optical depth over a remote semi-arid region of South Africa from spectral measurements of the daytime solar extinction and the night time stellar extinction*. *Atmospheric Research*, 62, 11– 32.
- Jinhuan Q., Liquean Y., (2000). *Variation characteristics of atmospheric aerosol optical depths and visibility in North China during 1980-1994*. *Atmospheric Environment*, 34, 603-609.
- Kanike R. K, Sivakumar V., (2015). *Remote sensing of Aerosol using a sunphotometer*, ISBN 978-3-659-70622-6
- Kulshrestha U., Kumar B., 2014. *Airmass Trajectories and Long Range Transport of Pollutants: Review of Wet Deposition Scenario in South Asia*. *Advances in Meteorology* 2014, 14pp. <http://dx.doi.org/10.1155/2014/596041>
- Kumar K. R., Sivakumar V., Reddy R. R., Gopal K. R., Adesina A. J., (2013). *Inferring wavelength dependence of AOD and Ångström exponent over a sub-tropical station in South Africa using AERONET data: Influence of meteorology, long-range transport and curvature effect*. *Science of the Total Environment*, 461–462, 397–408.
- Kumar K. R, Sivakumar V., Yin Y., Reddy R. R., Kang N., Diao Y., Adesina J. A., Yu X., 2014. *Long-term (2003-2013) climatological trends and variations in aerosol optical parameters retrieved from MODIS over three stations in South Africa*. *Atmospheric Environment*, 95, 400-408.
- Lin J., van Donkelaar A., Xin J., Che H., Wang Y., 2014. *Clear-sky aerosol optical depth over East China estimated from visibility measurements and chemical transport modelling*. *Atmospheric Environment*, 95, 258-267.
- Lyamani H., Olmo F. J., Alcantara A., Alados-Arboledas L., (2006). *Atmospheric aerosols during the 2003 heat wave in south eastern Spain I: Spectral optical depth*. *Atmospheric Environment*, 40, 6453–6464.
- Sivakumar V, Tesfaye M., Alemu W., Sharma A., Bollig C., Mengistu G., (2008), *Aerosol measurements over South Africa using satellite, sun-photometer and LIDAR*, *Advances in Geosciences*, vol 16, 253-262.
- Suman M. N. S., Gadhavi H., Kiran V. R., Jayaraman A., S. V. B. Rao (2014), *Role of Coarse and Fine Mode Aerosols in MODIS AOD Retrieval: a case study over southern India*. *Atmospheric Measurement Techniques*, 7, 907–917.
- Tesfaye M., Botai J., Sivakumar V., M. G. Tsidu, (2014). *Simulation of biomass burning aerosols mass distributions and their direct and semi-direct effects over South Africa using a regional climate model*. *Meteorology and Atmospheric Physics* 125, 177–195.
- Winkler H., Formenti P., Esterhuyse D. J., Swap R. J., Helas G., Annegarn H. J., Andreae M. O., (2008). *Evidence for large-scale transport of biomass burning aerosols from sunphotometry at a remote South African site*. *Atmospheric Environment*, 42, 5569–5578.

# Simulations of the Meridional Overturning Circulation using the parallel cubic ocean model (PCOM): The Spin-Up phase.

M.V. Sovara<sup>a,b</sup>, F.A. Engelbrecht<sup>a</sup>, C.J.C. Reason<sup>b</sup>, J. Deshayes<sup>c</sup>, J. Hermes<sup>d</sup>

<sup>a</sup> Council for Scientific and Industrial Research, Climate Studies, Modelling and Environmental Health, Pretoria, South Africa

<sup>b</sup> Department of Oceanography, University of Cape Town, Cape Town, South Africa

<sup>c</sup> Laboratoire de Physique des Océans, UMR 6523, CNRS/IFREMER/IRD/UBO, Brest, France

<sup>d</sup> Egagasini Node, SAEON, Cape Town, South Africa

## Abstract

This paper describes the implementation of an ocean global circulation model (OGCM) formulated on a non-orthogonal quasi-homogeneous cubic grid, at the Centre for High Performance Computing (CHPC) for the purpose of studying decadal variability of the Meridional Overturning Circulation (MOC) and related fields. The MOC plays a key role in determining the global climate and recent studies have suggested that global warming may lead to a weakening of the MOC. Results from a 10-year model spin-up are presented in this paper as an effort to evaluate of the models performance and it is shown that the model produces plausible results.

Key words: Meridional Overturning Circulation, Ocean General Circulation Model, Model Spin-Up, Multi-decadal variability.

## INTRODUCTION

The MOC comprises of surface and deep currents that encompass all of our planets ocean basins. It is the main mechanism by which the oceans globally distribute heat and salt, thus making it an important component of the global climate system, with links also to the timing and extent of past glaciation events (Manabe and Stouffer, 1999; Beal et al. 2011; Ganopolski and Rahmstorf, 2001). In the North Atlantic the MOC manifests as the Atlantic Meridional Overturning Circulation (AMOC), which transports equatorial waters northward through the Gulf Stream and North Atlantic Current efficiently contributing to the warming of Northern Europe (Broecker, 1997). Thus far, direct measurements of the AMOC have been rare and as a result it has been difficult to describe its decadal variability. Trans-Atlantic hydrographic sections at 25°N have been analyzed in 1957 (Fuglister, 1960), 1981 (Roemmich and Wunsch, 1985), 1992 (Parilla et al. 1994), 1998 (Baringer et al. 1999) & 2004 (Bryden et al. 2005).

Results obtained from the first three cruises suggested that the AMOC has been constant with only small changes in thermocline, intermediate and deep water transport. A model study by Bryden et al. (2005) showed a slowing of the AMOC under climate change. In addition, the 2001 International Panel on Climate Change (IPCC) report showed a weakening of the AMOC over the 21<sup>st</sup> century. However, previous studies have shown that the MOC has varied throughout millennia, with the perception that Ice Ages had a smaller overturning circulation (Broecker, 1999). Ongoing monitoring of the AMOC at 26.5°N by the RAPID/MOCHA/WBS mooring

array has reached 10 years of measurements and is starting to paint the big picture of AMOC variability. These measurements are showing that the range  $\pm 4\text{-}35$  Sv ( $1 \text{ Sv} = 10^6 \text{ m}^3/\text{s}$ ) of AMOC variability found in the first year was larger than that of ship-based observations over the past 50 years ( $\pm 15\text{-}23$  Sv). The RAPID array has also revealed that the amplitude of the seasonal cycle, with a minimum in spring and maximum in autumn, was much larger than anticipated ( $\pm 6.7$  Sv). Furthermore, the driving mechanism of the wind stress in the east was also unexpected. Above all, these observations suggest that over the last decade the AMOC has been declining at a rate of  $\pm 0.5$  Sv per year (Srokosz and Bryden, 2015). The long term aim of this study is to identify the internal modes of variability of the MOC as simulated by the OGCM.

## MODEL AND METHODS

The OGCM used in this study is based on a cubic grid and has been developed by the Japanese Agency for Marine and Earth Science and Technology (JAMSTEC) (Tsugawa et al. 2008). The parallel cubic ocean model (PCOM) is designed to carry out global ocean simulations but can also be used like a regional model owing to its grid-stretching capabilities. PCOM is the ocean component of the variable resolution earth system model (VRESM) under development at the CSIR. Except for the horizontal grid system the model is a typical Bryan-Cox-Semtner type dynamic OGCM. PCOM is a free surface model which solves the complete set of primitive equations rewritten on general curvilinear

coordinates, on the Arakawa B grid, and assumes the Boussinesq & Hydrostatic Approximations. The vertical is discretized in the z-coordinate system with 32 vertical layers of gradually increasing thickness from the surface to the bottom.

Bottom topography is generated from 2-minute gridded bathymetry for the world (ETOPO2) and implemented with the partial bottom cell for improving the solutions at bottom. At the surface, PCOM is forced with Hellerman and Rosenstein (1983) monthly climatological wind stress fields in the simulations presented here. At the surface the heat and salinity fluxes are added through restoring the top layer to World Ocean Atlas 1998 (WOA98) (Antonov et al. 1998) climatology using a 30 day time average. The Bryan and Lewis's (1998) vertical mixing scheme is employed because it is known to reproduce a realistic MOC. Time integration in PCOM is performed separately for external and internal modes. The external mode is integrated with a smaller time-step than that of internal modes. Finite difference methods are used to discretize the momentum equations. The prognostic equations of the momentum of the internal mode and tracer equations are integrated through the leapfrog method.

The prognostic equations of the momentum and tracers of the external mode are integrated by a forward-backward method. The Matsuno scheme (Matsuno, 1966) is inserted once every 15 steps to remove computational modes. In this time marching, the velocity equations are calculated first and then the free surface equations. Implicit time stepping is employed for the Coriolis terms. The multi-decadal variability of the MOC in the OGCM will be investigated using  $2^\circ$  horizontal resolution runs. The intention is to extend the simulation eventually to a 4000 year period, which will allow the model to reach a fully balanced state given its start from the initial condition of a motionless and homogeneous ocean with constant potential temperature and salinity. This type of simulation, driven by climatological atmospheric forcing, will allow for the identification of the internal modes of variability of the MOC as simulated by the ocean model. This may include one or more decadal to multi-decadal modes of variability.

## SPIN-UP RESULTS AND DISCUSSION

The most important oceanic variable for interaction with the atmosphere is the sea surface temperature (SST). SST is warmest in the tropics because solar input is highest there and temperatures approach freezing in the higher latitudes (as seen in Fig.1). The strongest SST gradient is found at the mid-latitudes. Interestingly, SST is non-symmetric about the equator even though solar input is symmetric at that location. The eastern Pacific is relatively cold whereas the western Pacific is warm in all seasons and these relatively cold waters extend can be observed along the equator in what is known as the "equatorial cold tongue". This cold tongue is maintained by upwelling and plays an important role in the dynamics of El Niño. The model temperature and salinity fields have been restored at the surface towards WOA climatology.

The sea surface salinity (SSS) spatial pattern reflects the climate belts associated with general atmospheric circulation. Global salinity patterns are linked to rainfall and evaporation, thus, the great subtropical deserts at the pole-ward edges of the atmosphere's Hadley cells are apparent over the ocean as a SSS maximum in the  $15^\circ$  to  $30^\circ$  latitude band (Fig. 2). Tropical rain lowers the SSS along the Inter-tropical Convergence Zone (ITCZ) and also from the mid-latitudes to the Polar Regions excess precipitation lowers SSS. Net evaporation leads to a relatively salty Atlantic; net input of freshwater generates low salinity in the Pacific Ocean.

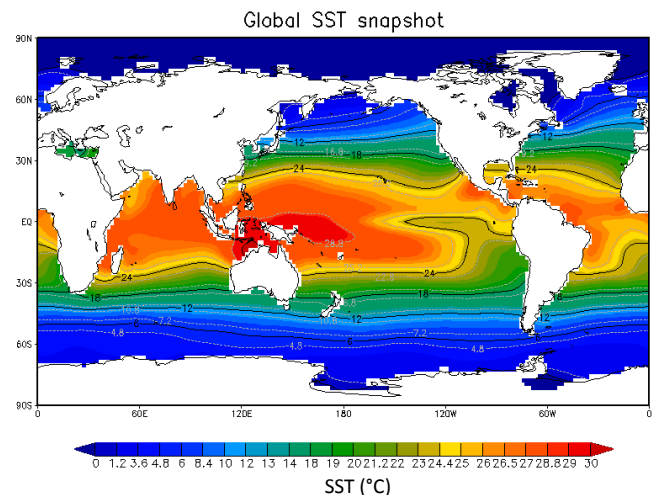


Figure 1. SST field after ten years of integration

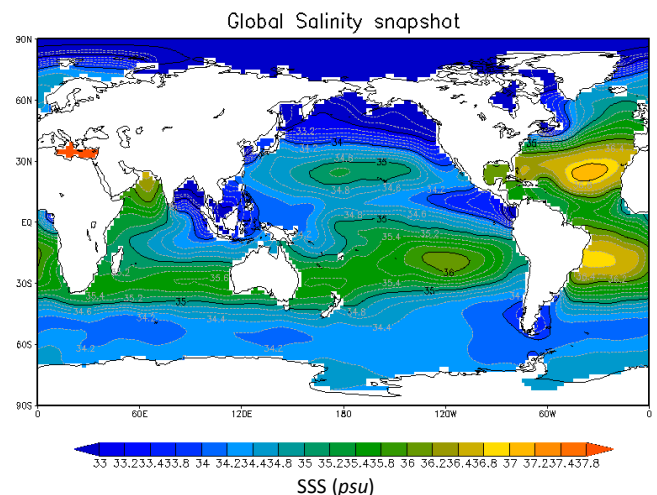


Figure 2. Salinity field after ten years of integration.

Surface currents are primarily driven by the surface wind. Along the equator the currents along the direction of the winds (i.e. easterly winds) drive the currents westward. In the interior of the ocean the currents are strongly influenced by the rate of change on the zonal wind and Coriolis force with latitude. There are also strong currents along western boundaries of the ocean basins in both hemispheres and these include the Gulf Stream, the Kuroshio, the Brazil Current and the Agulhas Current. The Agulhas Current (AC) is the western boundary current of the South Indian Ocean (Fig.3).

In the first order its pole-ward flow balances the equatorial transport of the subtropical gyre and with regard to its source regions, the AC is supplied by contributions from the Mozambique Channel, the East Madagascar Current and a re-circulated South West Indian Ocean subgyre. The currents mean flow is shown here as the flow along the coast of southern Africa from 27°S to 35°S. AC waters are subsequently leaked into the South Atlantic and the retained waters are re-calculated back into the South West Indian Ocean subgyre. The meridional section of the zonal temperature is shown in Fig. 4 with special focus on the temperature signature of the water masses after 10 model simulation years. The pink and green shades indicate the surface and intermediate water respectively.

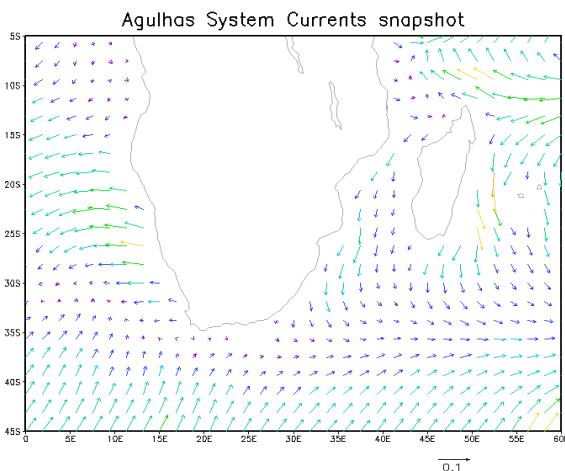


Figure. 3 Greater Agulhas System Currents ( $\text{m/s}^2$ ) after ten years of integration

These water masses are identifiable by their signature temperature range of  $\pm 25$ – $10^\circ\text{C}$  and  $10$ – $5^\circ\text{C}$ , respectively. The turquoise shade identifies the Deep and Bottom water masses. The blue shade identifies Antarctic Bottom Water (ABW) with its signature temperature range of  $\pm 0.5^\circ\text{C}$ . It must be noted that for this simulation period the model has not yet reached equilibrium state therefore the water masses shown are not completely matching observations. This is not surprising because the MOC will take several decades to adjust as it is a multi-decadal process.

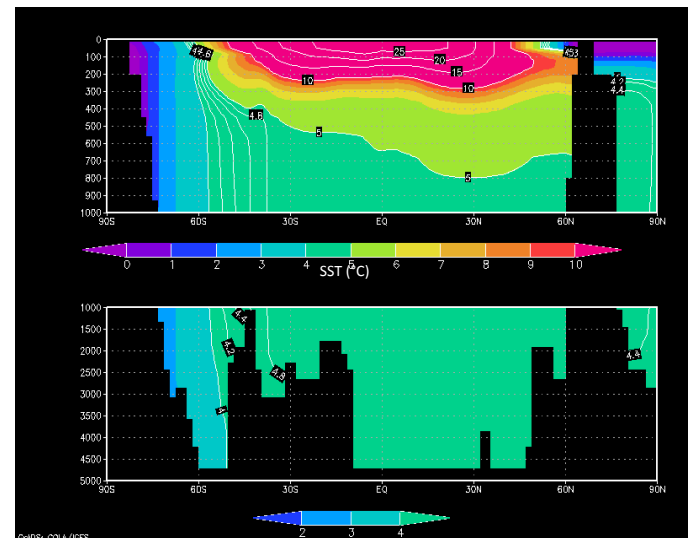


Figure. 4 Meridional section of the zonal temperature after ten years of integration.

## CONCLUSIONS

Ocean model simulations forced with realistic inter-annually varying atmospheric fields have the disadvantage that the forcing may induce multi-decadal cycles with periods equal to the length of the period for which the realistic forcing-data is available. Thus, such experiments may not be ideal for identifying internal modes of decadal variability which this study seeks to identify. However, we do intend to perform multi-century long simulations forced by realistic inter-annually varying atmospheric fields to investigate the role of inter-annual variability in the existence of multi-decadal cycles of the MOC. The 10-year results presented here demonstrate that PCOM under the prevailing configuration produces plausible SST, SSS and surface currents.

## ACKNOWLEDGEMENT

We thank the anonymous reviewer/s for carefully reviewing this manuscript. We wish to express our gratitude to the co-authors for their invaluable comments and suggestions. We also want to thank the CHPC from which the calculations have been performed.

## REFERENCES:

- Antonov, J.I., Levitus, S., Boyer, T.P., Conkright, M.E., O.F., Brien, T.D., Stephens, C., 1998: World Ocean Atlas 1998, Temperature of the Atlantic Ocean, vol. 1, NOAA Atlas NESDIS 27, US Government Printing Office, Washington DC.
- Baringer, M.O'N., & Molinari, R., 1999: Atlantic Ocean Baroclinic heat flux at 24 to 28°N. *Geophys. Res. Lett.* 353-356.
- Beal, L. M., W. P. M. de Ruijter, A. Biastoch, R. Zahn, and SCOR/IAPSO/WCRP Working Group 136 (2011): On the role of the Agulhas System in Ocean Circulation

and Climate, Nature, 472, 429-436, doi:10.1038/nature09983.

Broecker, W.S., 1997: Thermohaline Circulation, the Archilles heel of our climate system: Will man-made CO<sub>2</sub> upset the climate balance? Science, 278, 1582-1588.

Broecker, W.S., 1999: What If the Conveyor Were to Shut Down? Reflections on a Possible Outcome of the Great Global Experiment, GSA Today 9(1):1-7.

Bryden, H.L., Longworth, H.R., Cunningham, S.A., 2005: Slowing of the Atlantic Meridional Overturning Circulation at 25°N. Nature 438, 655-657.

Fuglister, F.C., 1960: Atlantic Ocean Atlas of Temperature and Salinity Profile and Data from the International Geophysical Year of 1957-1958. Woods Hole Oceanographic Institution Atlas Series 1, 1-209.

Ganopolski, A., Rahmstorf, S., 2001: Rapid changes of climate simulated in a coupled climate model. Nature, 49.

Hellerman, S., & Rosenstein, M., 1983: Normal monthly wind stress over the world ocean with error estimates. JPO 13, 1862-1104.

Lutjerharms, J.R.E., 2006: The Agulhas Current. Springer-Verlag, Heldeberg.

Manabe, S., & Stouffer, M.J., 1999: The role of thermohaline circulation in climate. Tellus, 51: 91-109.

Matsuno, T., 1966: Numerical integration of the primitive equations by a simulated backward difference method. J Meteorol. Soc. Jpn. 44, 76-84.

Parilla, G., Lavin, A., Bryden, H., Garcia, M., & Millard, R., 1994: Rising temperatures in the subtropical North Atlantic Ocean over the past 35 years. Nature 369, 48-51.

Roemmich, D., & Wunsch, C., 1985: Two transatlantic sections: meridional circulation and heat flux in the Subtropical North Ocean. Deep-Sea Res. 32, 619-664.

Srokosz, M.A., & Bryden, H.L., 2015: Observing the Atlantic Meridional Overturning Circulation yields a decade of inevitable surprises. Science. Vol, 348 Issue, 6241.

Tsugawa, M., Tanaka, Y., & Matsuno, T., 2008: An ocean general circulation model on a quasi-homogeneous cubic grid. Ocean Modell., 22, 66-86.

# The Effect of the Agulhas Current on SAR derived wind fields

Daniel Schilperoort<sup>1,2</sup>, Marjolaine Krug<sup>1,2,3</sup>, Mathieu Rouault<sup>1,2</sup>, Morten Hansen<sup>4</sup>, Alexis Mouche<sup>5</sup>

<sup>1</sup> Department of Oceanography, University of Cape Town

<sup>2</sup> Nansen-Tutu Centre for Marine Environmental Research, University of Cape Town

<sup>3</sup> Ecosystem Earth Observation, Council for Scientific and Industrial Research

<sup>4</sup> Nansen Environmental and Remote Sensing Centre, Bergen, Norway

<sup>5</sup> Institut français de recherche pour l'exploitation de la mer, Brest, France

## Abstract

987 Synthetic Aperture Radar (SAR) swaths of individual wind events were derived using the CMOD5.n, geophysical model function (GMF). The data were processed and investigated in order to determine the effect of the surface roughness of the Agulhas Current on the Normalized Radar Cross-Section (NRCS) and, ultimately, the derived wind signature error. The data were refined into 6 zones of interest and standardized into 4 direction regimes in order to eliminate time variability and ambiguity and to facilitate a better intercomparison. Preliminary results show a marked increase in along-current mean wind speeds, with a greater than expected effect occurring in the up-current direction regime and the down-current direction regime exhibiting an effect which opposes that of conventional theory. This suggests that there are other, non-negligible geophysical roughness modifying effects which need to be considered. Secondly, it was found that the degree of influence of the ocean current on the derived wind speed is relative to the initial wind speed itself. The greatest effect was found to occur between 5 and 15 m/s

## Introduction:

Synthetic Aperture Radar (SAR) is a satellite based, active radar imaging system that measures the change between emitted and returning microwave properties (i.e., magnitude, polarization, return time) in order to ascertain the surface roughness of the ocean below. The surface roughness of the ocean is predominantly driven by the boundary layer friction between the ocean and the wind above it. Thus, it is possible to relate the surface roughness signal to a wind speed and direction using empirically derived, geophysical model functions (GMFs) (Dagestad et al., 2012; Verhoef et al., 2008). However, as the wind speeds that are derived from SAR use the surface roughness resulting from the friction induced by the relative wind speed over the ocean, there is an inherent error which occurs due to the motion of the ocean relative to the wind (i.e., an ocean current) (Dagestad et al., 2012). It has been shown before, using much lower resolution Scatterometry data and slower moving currents, that any wind derived from surface roughness will contain a component error which will overestimate any up-current component of the wind speed by as much as 20% (Plagge et al., 2012). There has, as yet, been little to no research conducted on strong, fast flowing boundary currents such as the Agulhas Current at the much higher resolutions which can be achieved by SAR.

The aim of this investigation is thus, to investigate the effects of the relative motion of the Agulhas Current versus the different wind direction regimes on the, SAR measured, Normalized Radar Cross Section (NRCS) and the resulting wind derivation errors that may occur. Also to identify any other external roughness modifying factors which may influence the NRCS but have not yet been catered for in derivation models such as CMOD5.n.

## Data and Methods:

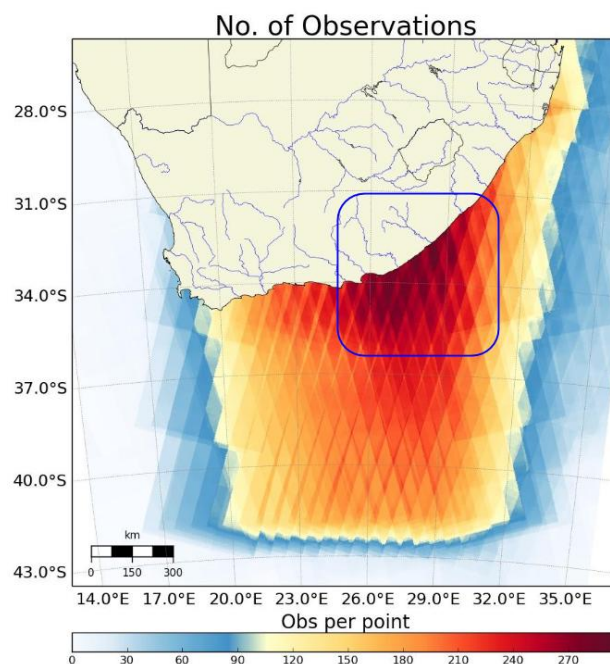


**Figure 1** Data density plot showing the availability and reliability of Envisat ASAR data over the Southern African region. In total, 987 swaths were analyzed over the period 2007-2012 which results in a maximum data density of 297 data points per grid point.

## Envisat ASAR

The Envisat ASAR has a sample rate of 1 orbit per day which leads to repeat coverage approximately every 3-5 days. A total of 987 swaths of data were collected over the 5 years from 2007 to 2012 (Figure 1). Wide swath (Approx. 400 km) coverage was used as it provided the greatest coverage at an acceptable high resolution. The resolution of 150 m × 150 m was re-gridded to 1 km × 1 km before applying the CMOD5.n GMF for wind speed derivation Verhoef et al. (2008). The resolution combined with repeat coverage resulted in a maximum data density of 297 readings per grid point. In order to maximize the reliability of the study it was decided to only select an area of

high density data coverage, thus the area demarcated by the blue square in figure 1 was selected.

## Climate Forecast System (CFS)

### Winds

The NCEP Climate Forecast System Reanalysis (CFSR) and Reanalysis: version 2 (CFSv2), available from the CFSR archive for 2007 to 2010 and 2010 to present day respectively, were used as the direction input in the CMOD5.n GMF to derive the wind speed from the Envisat ASAR data. Both model datasets were used as they were the best quality, highest resolution, hourly datasets freely available and thus allowed for a better co-location of observational and model winds. The CFSR dataset has a gridded resolution of 0.3 of a degree and the CFSv2 is 0.2 of a degree. The data were interpolated and re-gridded to a 1km spatial resolution.

### Sea Surface Temperature (SST)

SST data were used as a proxy for the location of the Agulhas Current in the investigation.

For the initial location of the 6 zones of interest (see figure 2), the MODIS 5km resolution data, averaged for the period 2000 to 2010 was used as a general indicator of the location of the core of the Agulhas Current

For further analysis the OSI-SAF hourly dataset were used as they provided repeat acquisitions of acceptably high resolution temperature data (EUMETSAT, 2015). Hourly data were averaged and interpolated into a daily, full coverage product which is preferable to other merged datasets as they are interpolated both spatially and temporally and thus tend to smooth gradients (Krug et al. 2014).

### Method of Analysis

Four zones of interest (zones B to E) were selected along the east coast in order to eliminate the huge variability in direction of both the wind and the underlying current in space and time (Figure 2). Each zone was specified at  $2\frac{1}{2}^{\circ}\text{Lat} \times 2\frac{1}{2}^{\circ}\text{Lon}$ . It was necessary to select the specific zones of interest over regions of the Agulhas which had both the strongest current signature and the highest volume of reliable SAR data with which to work.

The individual swaths were then spatially averaged within each zone and each swath was grouped in to one of 4 regimes according to its mean direction (Up-current, Down-current, Crosscurrent-West and Crosscurrent-East), within a range of accuracy of  $\pm 15^{\circ}$ . Any swath which did not fit within a direction regime was discarded as unclassified as the dominant wind direction was too ambiguous to be investigated. Once grouped into their direction regimes, the influence of the  $\pm 15^{\circ}$  variation was eliminated by extracting the component parallel to the regime. For each zone of interest, transects were then

extrapolated from the coast, through the zone of interest and out to sea, perpendicularly intercepting the core of the Agulhas Current. Each direction regime was then investigated along the transect for each zone of interest.

Initially a mean plot of scalar wind speed for each transect was plotted over mean SST data for the same period, in order to ascertain if there was a correlation between the wind speed and the Agulhas core location as well as to discern if there were any mean differences between the direction regimes for each zone of interest.

Further analysis was then needed in to the impact of variability in wind speed on the influence of the current. The mean wind speed was calculated along each swath and then grouped in to 4 wind speed regimes ( $< 5$ ;  $5 - 10$ ;  $10 - 15$ ;  $> 15\text{m/s}$ ). The mean transect was then overlaid over SEVIRI SST as a means of geolocating any changes in wind speed with the boundaries of the current.

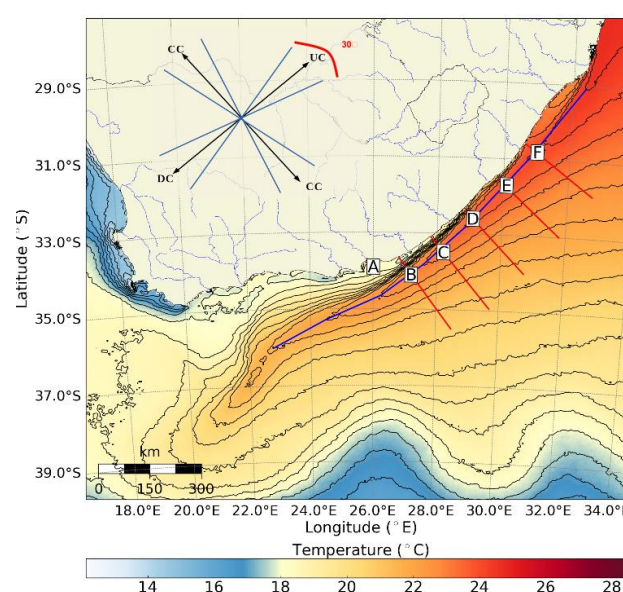


**Figure 2** Mean MODIS SST over the greater Agulhas region for the period 2000-2010. The SST data were used as a general indication of the location of the core of the Agulhas Current in order for the zones of interest to be optimally located. The Black lettered squares (A to F) mark the zones of interest. The red lines indicate the location of the transects. All data within each zone of interest was spatially averaged and grouped into a regime according to the four directions in the figure.

## Results and Discussion:

### Along current influences

For all zones of interest, the greatest indication of influence by the Agulhas current on the derived wind speed appears in the up-current regime. This is in agreement with the current theory of current relative wind speeds as first described by Kelly et al. (2001). The effect was common through all zones of interest; however, the zone with the most intense increase was zone C, the zone where the Agulhas Current is strongest and most defined (Rouault et al.

2010). the mean increase in zone C is  $7 \pm 5 \text{ m/s}$  (Nearly 100%), a far greater percentage increase than noted ever before.

In zone C (Figure 3), the sharpest increase appears between the coast and approximately  $30 \text{ km}$  off shore. The wind speed then peaks and begins to decrease more gradually, further offshore until it flattens out around  $120 \text{ km}$ . The fastest wind speeds do not occur over the core of the current as would be expected, according to the current relative wind effect as postulated by Plagge et al. (2012), but rather over the sharp temperature gradient which denotes the inshore front of the Agulhas Current. This is a region of high ocean atmosphere interaction dynamics as the rapid change in temperature could cause boundary layer instabilities. The increase in coastal friction closer to shore may result in the increase of surface roughness due to the shear in the current.

Although a similar increase in wind speed is evident in all study zones, wind speed increase at the Agulhas Current's inshore front is not as substantial further north. This is where the temperature fronts become less intense and wider.

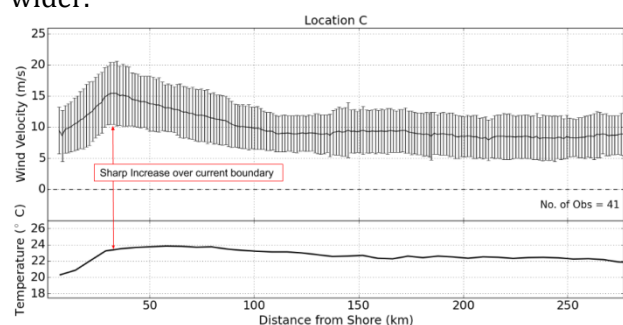


**Figure 3** Mean up-current wind speed component over zone C co-plotted with the underlying SEVIRI SST. Error bars show the mean variance of wind speed along the transect. Red arrow shows the region of greatest mean wind speed increase co-located with the SST gradient

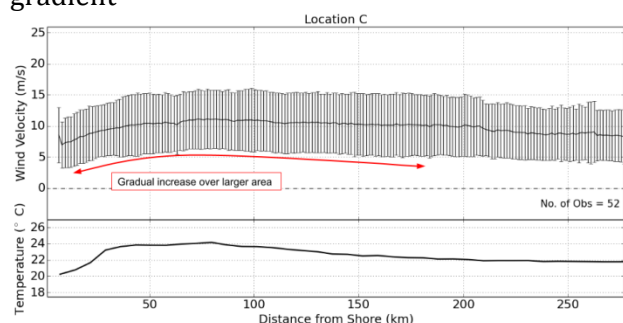


**Figure 4** Mean down-current wind speed component over zone C co-plotted with the underlying SEVIRI SST. Error bars show the mean variance of wind speed along the transect. Red curve shows the gradual increase in wind speed over the core of the current.

## Down-current decrease

The regime of secondary interest was the down-current regime, where the predominant wind vector direction was parallel with and in the same direction as the flow of the current (Figure 4). The expected impact as dictated by

the theory is that there should be a net decrease in wind speed over the width of the Agulhas current (Dagestad et al., 2012). Instead, there appears to be a mean increase in wind speed. The wind speed increase is, however, not as intense as the up-current effect. In fact, the down-current wind shows an increase in speed that starts off moderately steep close to the coast but gradually flattens further out to sea until it peaks over the core of the current around  $90 \text{ km}$  offshore. The wind speed then decreases further out to sea. The increase in wind speed is different from the up-current regime in that the increase in wind speed is only  $3 \pm 5 \text{ m/s}$  and there is no distinct peak. This effect is evident in all of the zones of interest; however it becomes less distinct further north where, again, the Agulhas is less intense and wider.

## Influence of variable wind speeds

In all zones and for both the up and down-current regimes, the increase in wind speed over the Agulhas Current is highly variable, with standard deviation in the range of  $5 \text{ m/s}$ . Interestingly, the high variability is evident throughout the entire length of the transects and not merely over the areas of wind increase. This suggests that a majority of the variability does not stem from varying surface roughness effects, but rather from the high variability in overall wind speeds between individual events. Thus, it was necessary to further categorize the data into 4 different mean wind speed regimes in order to determine the influence of wind intensity on the current relative effect.

Figure 5 shows the up-current wind speeds grouped by mean speed intensity in to 4 brackets. ( $< 5$ ;  $5 - 10$ ;  $10 - 15$ ;  $> 15 \text{ m/s}$ ). Noticeably it is evident that the greatest increase in wind speed occurs between  $5 \text{ m/s}$  and  $15 \text{ m/s}$ . Above  $15 \text{ m/s}$  the intensity of the wind becomes too great and the signature of the current is no longer evident in the wind speed. Similarly, below  $5 \text{ m/s}$  the signature of the current is no longer evident. This is primarily because the CMOD5.n model fails below  $3 \text{ m/s}$  due to the lack of sufficient boundary friction for creating detectable surface roughness (Portabella and Stoffelen, 2006).

## Conclusions:

Although it is possible to use GMF's such as CMOD5.n to derive a wind speed from the NRCS from satellite based SAR, there is a known effect which results from the relative motion of wind over a large scale ocean current which causes an error in the derived wind speeds. To date, however, no high resolution study has been conducted over such a strong western boundary current as the Agulhas Current.

This study used wind speed measurements derived from Envisat ASAR in conjunction with CFSR and CFSv2 reanalysis model data and satellite SST data to investigate

the net effect of the Agulhas current on the dominant derived wind velocity signatures.

It was found that the influence of current relative wind is a major contributing factor to the error in derivation. Particularly in the up-current wind direction regime. However there were other possible geophysical influences which contributed to an increased wind speed signature over the Agulhas region over and above the current relative effect.

It is necessary to further investigate the current relative wind increase effect in order to properly identify and isolate the key influencing factors in the wind speed derivation errors. Future research needs to incorporate much higher resolution; ocean-atmosphere coupled numerical models for incorporation in to the wind derivation process as well as for comparisons between wind products. Other, non-numerical model based techniques for SAR wind direction retrieval are also vital in increasing the accuracy of the measurements. Future satellites such as the Sentinel 1 and 2 programs will aid in this respect.

Efforts in removing the signature of ocean currents using the Doppler shift will also prove vital in isolating the different effects on the wind speed (Rouault et al., 2010).

In situ wind, surface roughness and atmospheric stability measurements are also needed for better validation of the satellite products.

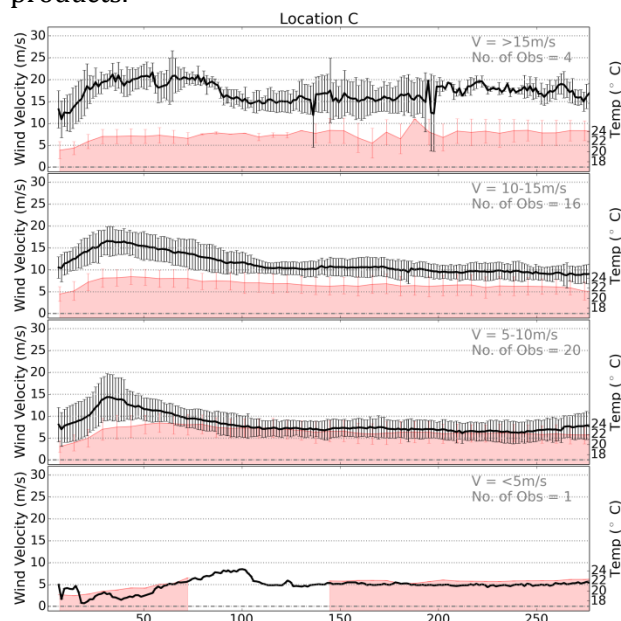


**Figure 5** Individual up-current wind speed components over zone C, grouped into 4 brackets of wind speed. Brackets are:  $< 5$ ;  $5 - 10$ ;  $10 - 15$ ;  $> 15$  m / s. Data is co-plotted with the underlying SEVIRI SST. Black line represents the mean wind speeds and error bars show the variance of wind speed along the transect. Red filled line represents the corresponding averaged daily SEVIRI SST data.

## Acknowledgements:

Nansen-Tutu Centre from Marine Environmental Research, University of Cape Town, Ma-Re, ACCESS, The ACE lab from the Centre for High Performance Computing for technical support. Finally to the SCAMPI-NRF bilateral agreement for the funding to attend the conference.

## References:

- [1] The data from the EUMETSAT Satellite Application Facility on Ocean & Sea Ice used in this study are accessible through the SAF's homepage <http://www.osi-saf.org>
- [2] Dagestad, K. et al., 2013. Wind Retrieval From Synthetic Aperture Radar – an Overview. Seasar 2012 Oceanography Workshop, 4th.
- [3] Kelly, K.A. et al., 2001. Ocean currents evident in satellite wind data. *Geophysical Research Letters*, 28(12), pp.2469–2472.
- [4] Marjolaine, K., Paolo, C. & Francois, D., 2014. Remote Sensing of the African Seas Illustrate. V. Barale & M. Gade, eds., Springer. Available at: <https://books.google.co.za/books?id=7qvIAwAAQBAJ>.
- [5] Plagge, A.M., Vandemark, D. & Chapron, B., 2012. Examining the impact of surface currents on satellite scatterometer and altimeter ocean winds. *Journal of Atmospheric and Oceanic Technology*, 29(12), pp.1776–1793.
- [6] Portabella, M. & Stoffelen, A., 2006. Scatterometer backscatter uncertainty due to wind variability. *Geoscience and Remote Sensing, IEEE Transactions on*, 44(11), pp.3356–3362.
- [7] Rouault, M.J. et al., 2010. Mapping the Agulhas Current from space: An assessment of ASAR surface current velocities. *Journal of Geophysical Research: Oceans*, 115(10), pp.1–14.
- [8] Saha, S. et al., 2010. The NCEP climate forecast system reanalysis. *Bulletin of the American Meteorological Society*, 91(8), pp.1015–1057.
- [9] Verhoef, A. et al., 2008. CMOD5. n-the CMOD5 GMF for neutral winds. EUMETSAT Ocean and Sea Ice SAF Tech.Note SAF/OSI/CDOP/KNMI/TEC/TN/165.

## Towards impact-based early warning services: Forecasting the risk of adverse societal impacts of flash floods

**Eugene Poolman\***  
South African Weather Service

### Abstract

Flash floods are some of the most devastating hazards in South Africa, causing significant adverse impacts to people and their livelihoods. Traditional weather warnings do not take into account the vulnerability of communities and the consequential socio-economic impact of severe weather hazards. This paper describes the development of an objective impact forecasting system that combines the forecasts of the likelihood of flash floods with the socio-economic vulnerability associated with flash floods to predict the risk of adverse impacts on communities. Operational application of the impact forecasting system within the Severe Weather Warning System will also be described.

**Keywords:** disasters, early warnings, impact forecasting

### Introduction

Severe weather events each year lead to significant impact to human livelihood around the world. Casualties and damage to property and infrastructure occur that adversely affect communities for many years (Auld, 2008; ISDR, 2005; Parry *et al.*, 2008; Pelling, 2011; Poolman *et al.*, 2014). This occurs despite the improvement of forecasting of these severe weather events by National Meteorological Services (NMSs), and timely dissemination of warnings to disaster management structures and the general public (WMO, 2015). There is clearly a gap between the forecast of severe weather by NMSs and the appreciation of the related socio-economic impact of the hazard by disaster management structures and general population. Against this background, there is a need to move away from predicting the weather towards predicting the risk and impacts associated with weather (Auld, 2008; Poolman *et al.*, 2014). WMO (2015) advocates an *impact forecasting* approach, which is a step beyond forecasting weather conditions to forecasting the risk of consequential adverse impact of these weather conditions on people and their livelihoods. Risk prediction of hazardous weather, however,

requires a multi-disciplinary approach combining sophisticated weather forecasting systems with specialized socio-economic vulnerability information at local levels relating to the impact of the specific hazard on local communities.

This paper describes the development of a prototype Severe Weather Impact Forecasting System (SWIFS), which is an objective impact forecasting concept that combines a probabilistic forecast of potential flash floods with event specific societal and infrastructure vulnerability information to produce a forecast of the impact risk associated with the expected flash floods.

### Modelling systems and methodology

SWIFS consists of two main components, namely a probabilistic forecast of flash flood hazards, and an impact model that models the risk of adverse impacts associated with flash floods.

#### *Probabilistic forecasting of flash floods*

The basis of the first component of SWIFS (the probabilistic forecasting component) was a combination of probabilistic precipitation forecasts from a numerical weather prediction system for the next 18 hours with Flash Flood Guidance (FFG) information. FFG is a product of the South African

---

\* Corresponding author:

Tel: +27 12 367 6001;

E-mail: eugene.poolman@weathersa.co.za

Flash Flood Guidance (SAFFG<sup>1</sup>) model, and is defined as the average amount of rain required over a small basin over a specified time to produce minor flooding at the basin outlet. This combination produced an 18-hour probabilistic outlook of the potential occurrence of flash floods in small river basins (approximately 50 km<sup>2</sup> in size). The combination process was done in three steps as discussed in detail in Poolman *et al.* (2014) and summarized here:

Step 1 required every 6 hours probabilistic rainfall forecasts for the following 18 hours for each small river basin to allow for the spatial and temporal uncertainties associated with precipitation forecasts from numerical weather prediction models. Since no high resolution ensemble forecasts were available to calculate average rainfall for the small river basins, a hybrid ensemble system was developed from the output of the deterministic 12-km South African version of the Unified Model (UM-SA12) of the United Kingdom Met Office run at the South African Weather Service (SAWS). Through this hybrid ensemble prediction scheme each small river basin had a set of 30 basin-averaged, bias-corrected, rainfall ensemble members derived from the 30 basins in its neighbourhood covering a period of 18 hours.

In Step 2 FFG values for the next 18 hours were derived for each basin. The SAFFG model produces every hour FFG values for the next 6-hours for 5366 small river basins (approximately 50 km<sup>2</sup> in size), based on the hydro-meteorological modelling of the state of the soil moisture due to recent observed rain, and the hydrological properties of each specific basin (Georgakakos, 2006). Since the SAFFG is essentially a diagnostic system with a limited predictive capability of at most 6 hours, FFG values for the next 18 hours were derived by extrapolating, or persisting, the latest available 6-hour FFG values for the next 18 hours.

Finally, in Step 3 an 18-hour probabilistic outlook of the

potential occurrence of flash floods in small river basins were prepared. This was done by comparing all the ensemble rainfall forecasts associated with a specific small river basin (i.e. how much rain is predicted for the basin by each of the associated 30 members) with the extrapolated basin-specific FFG value (i.e. how much rain is required to produce flooding) and determine the percentage of ensemble members that would exceed the FFG value. This provided an indication of the likelihood of basins to experience flash flooding by receiving more rain than required based on the soil moisture complement and other basin characteristics.

### *Modelling risk of adverse impacts*

The second component of SWIFS is the Impact Model which links hazard-specific societal and structural vulnerability with the potential flash floods, identified by the probabilistic forecasting component in the first component. The Impact Model determines the impact risk level and identifies hotspots of potential enhanced adverse impact.

The methodology used in the Impact Model to identify the impacts and link them with the predicted hazard is based on an adaptation of the well-known disaster risk expression described by Wisner *et al.* (2004):

$$Risk = Hazards \times Vulnerability$$

The adapted expression takes into account the likelihood of the hazard (flash flooding in this case) to occur, and the magnitude of the relevant vulnerability indicators.

In this study the social and structural dimensions of vulnerability relevant to flash flooding was considered. The various vulnerability indicators (such as population numbers, age, poverty index, schools, hospitals, etc.) were mapped on a spatial-scale using the mesozone approach of the CSIR (Naude, *et al.*, 2007) which divided the country into 25,000 mesozones of on average 50 km<sup>2</sup>. Through an appropriate weighting function the relevant indicators were combined and categorized to express the vulnerability on 5 levels, 1 the lowest and 5 the highest vulnerability for the specific mesozone.

In the final step this indicative vulnerability profile was

---

<sup>1</sup> The SAFFG is the intellectual property of the Hydrologic Research Center (HRC), a non-profit public-benefit corporation based in San Diego, USA. SAFFG was developed and implemented by HRC.

combined with the likelihood of imminent flash flooding for these mesozones to produce an indication of the risk of adverse impacts within each mesozone due to the expected hazard.

## Results and Discussion

Some case studies produced mixed results, largely due to the spatial and temporal uncertainties associated with rainfall forecasts from numerical weather prediction models. Nevertheless, the case studies presented encouraging indications that the hybrid ensemble prediction scheme adds significant value to the traditional deterministic rainfall forecasting of the UM-SA12 model, particularly for the small river basins used in the SAFFG system. The hybrid ensemble prediction scheme provided a relatively cheap option in producing probabilistic forecasts to cater for the spatial and temporal uncertainties associated with rainfall forecasts from UM-SA12.

The case studies provided evidence that the concept of SWIFS can produce useful information to disaster managers to identify areas most likely to be adversely affected in advance of a hazardous event and to decide on appropriate distribution of their resources between the various hotspots where the largest impacts would be. Furthermore, the additional 18 hours lead-time beyond the current 6 hours provided by SAFFG would have facilitated earlier decision making by disaster managers. The mesozone data proved to be quite useful to determine the potential impact of flash flooding on a regional spatial scale.

The main achievement of SWIFS is that it translates complex scientific forecasts of flash flooding into information that can support the decision making of disaster managers prior and during adverse weather conditions. SWIFS successfully managed to link various scientific sectors, namely meteorology (through the UM-SA12), hydrology (through SAFFG) and social sciences (through vulnerability indicators), to potentially provide benefit to decision making of disaster management structures in operational settings.

## Conclusions and future developments

SWIFS contributes to the current international research on short-term impact forecasting by focussing on forecasting the impacts of flash floods in a developing country with its limited spatial vulnerability information. It provides user-oriented information in support of disaster manager decision-making through additional lead-time of the potential of flash floods, and the likely impact of the flooding. The study provided a firm basis for future enhancement of SWIFS to other severe weather hazards in South Africa.

Future enhancements will have to include far more detailed vulnerability and impact information for specific impact hotspots to provide additional local scale information to disaster management. These datasets include detailed geo-referenced flood line information of flood prone streams and small rivers, or data relating to the temporal sensitivities such as vehicle movement per day and per hour to identify peak-hour hotspots, etc. Availability of spatial vulnerability data at these small scales, however, is a significant problem that will require major development efforts.

SWIFS will form the basis of the development of an objective decision support system for future enhancements of the Severe Weather Warning System (SWWS) of South Africa. Over the next few years the South African Weather Service will partner with the National Disaster management Centre to develop, test and implement an Impact-based SWWS in the country in line with the guidelines developed by the World Meteorological Organization (WMO, 2015). This Impact-based SWWS will utilize similar principle as discussed in the development of SWIFS to change the focus of the early warning system from *weather prediction* to people-centred *risk prediction* tailored to local conditions.

## References

- Auld, H., 2008: Disaster Risk Reduction under current and changing Climate Conditions. *WMO Bulletin*, Vol. 57(2): 118 – 125
- Georgakakos, K. P., 2006: Analytical Results for Operational Flash Flood Guidance. *Journal of Hydrology*, 317, 81-103
- ISDR, 2005: Living with Risk: A Global Review of Disaster Reduction Initiatives. *ISDR, Geneva, Switzerland*
- Naudé, A., W. Badenhorst, L. Zietsman, E. Van Huyssteen, and J. Maritz, 2007: Geospatial Analysis Platform – Version 2: Technical overview of the mesoframe methodology and South African Geospatial Analysis Platform. *CSIR Report number: CSIR/BE/PSS/IR/2007/0104/B*
- Parry, M., O. Canziani, J. Palutikof, 2008: Key IPCC Conclusions on Climate Change Impacts and Adaptations. *WMO Bulletin*, Vol. 57(2): 78-85.
- Pelling, M., 2011: Adaptation to Climate Change – from resilience to transformation. *Routledge, New York, 203 pages.*
- Poolman, E., H. Rautenbach, C. Vogel, 2014: Application of probabilistic precipitation forecasts from a deterministic model towards increasing the lead-time of flash flood forecasts in South Africa. *Water SA*, Vol. 40(4): 729-738.
- Wisner, B., P. Blaikie, T. Cannon, I. Davis, 2004: At Risk, Second Edition, Natural hazards, People's vulnerability and disasters. *Routledge, London, 471pp.*
- WMO, 2015: WMO Guidelines on Multi-hazard Impact-based Forecast and Warning Services. *WMO No. 1150, Geneva, Switzerland.*

## Decadal variability of summer Southern African rainfall

Bastien Dieppois<sup>1,2,3</sup>, Benjamin Pohl<sup>4</sup>, Mathieu Rouault<sup>2,5</sup>, Mark New<sup>2</sup>,  
Noel Keenlyside<sup>6</sup>, Damian Lawler<sup>1</sup>

<sup>1</sup> Centre for Agroecology, Water and Resilience, Coventry University, UK.

<sup>2</sup> African Climate and Development Initiative, University of Cape Town, RSA.

<sup>3</sup> Department of Oceanography, MARE Institute, University of Cape Town, RSA.

<sup>4</sup> Centre de Recherche de Climatologie, Université de Bourgogne, France

<sup>5</sup> Nansen-Tutu Center for Marine Environmental Research, University of Cape Town, RSA.

<sup>6</sup> Geophysical Institute, University of Bergen and Bjerknes Centre for Climate Research, Norway.

**Abstract** – Summer Southern African rainfall exhibit three significant timescales of variability over the 20<sup>th</sup> century: interdecadal (15–28 year), quasi-decadal (8–13 year) and interannual (2–8 year). Teleconnections with global sea-surface temperature and atmospheric circulation anomalies are different for each timescale. Interdecadal fluctuations in summer rainfall are associated with the Pacific Decadal Oscillation (PDO), while quasi-decadal and interannual fluctuations are related to decadal ENSO-like, often described as the Interdecadal Pacific Oscillation (IPO), and ENSO. Annular geopotential anomalies related the Pacific SST influence strongly interact with those driven by the Southern Annular Mode (SAM). Shifts in the westerlies thus lead to anomalous low-level easterly moisture fluxes from the Mascarene region even though decadal timescales, which are not significantly expressed in the SAM.

### 1. Introduction

Year-to-year variations in rainfall across Southern Africa have major consequences for human livelihoods and ecosystems through their impact on drought, temperature, water supply, vegetation and agriculture. Interannual variability of summer Southern African rainfall is known to be primarily influenced by El Niño Southern Oscillation (ENSO), with dry/wet anomalies during El Niño/La Niña (e.g., Ropelewski and Halpert, 1987, Mason & Jury, 1997; Rouault & Richard, 2005).

Decadal fluctuations have also been found in summer Southern African rainfall (e.g., Dyer & Tyson, 1977; Mason & Jury, 1997; Jury, 2014). Of particular importance is the interdecadal Dyer-Tyson cycle, which has been recently related to the SAM, and thus to changes in the meridional circulations (Malherbe *et al.*, 2014). Also, a quasi-decadal cycle has been described as a chaotic resonance of high-frequency variability (Reason and Rouault, 2002). However, until now, discussions about potential mechanisms of these decadal fluctuations have been limited. For instance, most of the studies are based on comparisons between two periods of approximately 10-years, which are too short to capture the decadal signals (*i.e.*, roughly two ½ cycles). They are thus likely to describe changes in interannual variability between two decades that are not necessarily related to decadal signals. Using a time-scale approach based on spectral analysis, this study aims to address these gaps, by defining the changing characteristics of summer South African rainfall, and their specific teleconnections for the main timescale of climate variability.

### 2. Data

The Climatic Research Unit data set (CRU TS 3.22) is used to estimate Southern African rainfall

from 1901 to 2013. The Summer Rainfall Index (SRI) has been defined by averaging the values over the regions where the wettest months occur between November and February (NDJF; red in Fig. 1a). We also used the multi-proxy summer Southern African rainfall reconstruction back to 1796 (Neukom *et al.*, 2014).

To examine teleconnections with global SSTs, we used the monthly Sea-Surface Temperature (SST) data from the extended reconstructed SST (ERSST.v4) of the National Climatic Data Centre. To infer monthly atmospheric dynamics, the Twentieth Century Reanalysis version 2 (20CR.v2) is used.

### 3. Timescale of Summer Southern African rainfall variability

Timescales of summer Southern African rainfall variability are identified according to the global wavelet spectra (Fig. 1a). In observation, interannual (*i.e.*, 2–8 years), quasi-decadal (8–13 years; QDV) and interdecadal (15–28 year; IDV) timescales are significant and fairly spatially coherent (Fig. 1a). This is not true at the multidecadal scale (>30 year), where observations are constrained by edge, wrap-around and zero-padding effects. However, multidecadal fluctuations are significantly identified in the reconstruction from Neukom *et al.* (2014; Fig. 1a). At the first glance, a distinct separation (*i.e.*, spectral gap) between the interdecadal and quasi-decadal signals does not seem to be clear in the bicentennial reconstruction. But, according to the continuous wavelet spectra, these two timescales are only separated over the 20<sup>th</sup> century in the observed and reconstructed SRI (Fig. 1b-c). The SRIs display significant increasing variance since the 1930s at the interdecadal timescale, and since the late 1960s at the quasi-decadal timescale (Fig. 1b-c).

#### 4. Multi-scale relationship with global SSTs

The teleconnections between the SRI and the global SSTs are examined using composite analysis (Fig. 2a-c). The time-series are subjected to a FFT filtering before to construct typical states of SSTs during periods of high-amplitude (*i.e.*,  $\geq 1$  standard deviation of interannual to interdecadal fluctuations) and for the successive timescales analyzed.

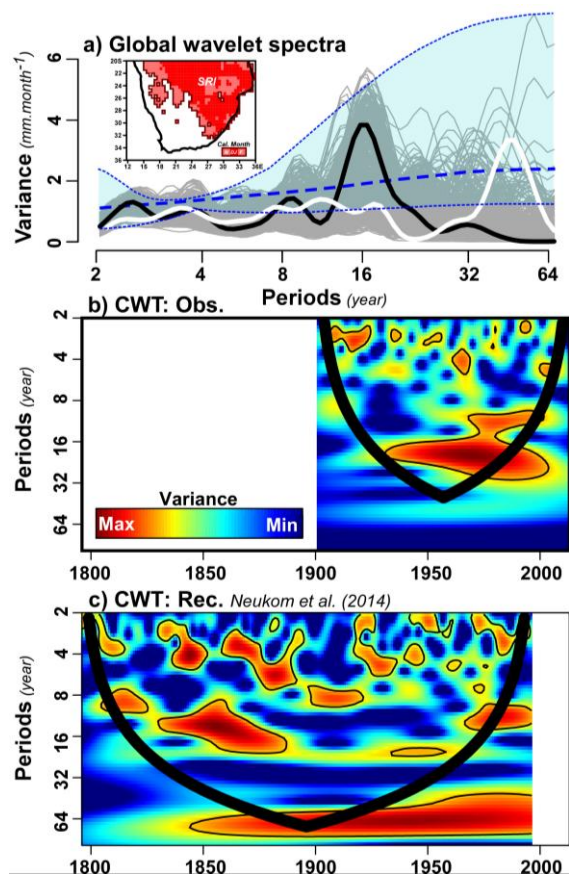


Figure 1. Timescale pattern of SRI variability (a) Global wavelet spectra of the observed SRI (black), of each grid-points used for its calculation (grey), and of the reconstructed SRI (white). The dashed blue lines indicate the red noise spectra with regard to the first order autoregressive of the observed SRI and its potential spatial drifts (b-c) Continuous wavelet spectrum of the observed and reconstructed SRI. Bold lines delineate the area under which power can be underestimated as a consequence of zero padding; thin contour lines show the 95% confidence limits based on Monte-Carlo simulations of the red noise background spectrum.

At the interdecadal timescale (15–28 year; IDV), Pacific SST anomalies associated with positive SRI display a horseshoe pattern, with cold anomalies in the central North Pacific surrounded by anomalies of opposite sign east of Asia, off California, in the Alaska gyre and in Southern Hemisphere extratropical regions (Fig. 2a). This SST pattern is consistent with the interdecadal signals described by Tourre *et al.* (2001), and it is also reminiscent of the

Pacific Decadal Oscillation (PDO) during its negative phase (Mantua *et al.*, 1997).

At the quasi-decadal timescales (8–13 year; QDV), Pacific SST anomalies associated with positive SRI fluctuations show cold anomalies in the tropical Pacific flanked by a horseshoe pattern of opposite sign, with marked anomalies in both North and South Pacific (Fig. 2b). This SST pattern is consistent with the quasi-decadal signals described by Tourre *et al.* (2001), and is reminiscent of the Interdecadal Pacific Oscillation (IPO), which is a wide-basin pattern of ENSO, during its negative life-cycles (Power *et al.*, 1999). This negative IPO occurs concomitantly with cold anomalies in the tropical Indian Ocean, while the South Atlantic SST dipole is identified (Fig. 2b). However, note that the physical independence between the IPO and ENSO remains controversial (*e.g.*, Power *et al.*, 1999; Tourre *et al.*, 2001). The IPO might thus be viewed as a decadal ENSO-like.

At the interannual scale (2–8 year), Klein *et al.* (1999) suggest that La Niña SST anomalies, which are associated with a cooler tropical Indian Ocean SST, are related to positive SRI anomalies (Fig. 2c).

#### 5. Atmospheric circulation

Figure 2d-f displays composite anomalies of geopotential ( $z$ ) and moisture fluxes at 1000 hPa based on significant timescales of SRI variability.

At the interdecadal timescale (15–28 year; IDV), low-tropospheric circulations associated with positive SRI display a quasi-annular mode, with low-pressure anomalies between the Polar Regions and 36°S and high-pressure anomalies in the subtropical and tropical regions (Fig. 2d). A southward shift of subtropical westerly moisture fluxes is identified for a large part of the Southern Hemisphere, which acts to weaken westerly moisture flows toward South Africa (Fig. 2d). This leads to an anomalous anticyclonic circulation in the Mascarene high-pressure region driving an anomalous low-level easterly flux along 10–20°S towards Southern Africa, which is favored by low-pressure anomalies over the continent (Fig. 2d). Such anomalies have some similarities with those driven by the Southern Annular Mode (SAM; spatial correlation = 0.51), but there is no significant interdecadal signal in the summer SAM index (not shown). These geopotential anomalies are therefore unrelated to the SAM.

At the quasi-decadal timescale (15–28 year; QDV), positive SRI anomalies are associated with an annular signal in the Southern Hemisphere, with weak low-pressure anomalies over Antarctica and in the tropics over the Atlantic and Indian basins, as well as high-pressure anomalies in the mid-latitudes and tropical Pacific (Fig. 2e). Due to zonally asymmetric patterns in the annual geopotential anomalies between the Atlantic and the Indian Ocean, high-pressure anomalies are northward in the Indian Ocean up to Madagascar (Fig. 2e). An

anomalous low-level easterly moisture flux reaching southeastern Africa is generated from enhancing the Mascarene High. These anomalies are partly reminiscent of those driven by the SAM and ENSO (spatial correlation = 0.48 and 0.53, respectively). However, there is significant quasi-decadal signal in different ENSO and IPO indices, but not in the SAM (not shown). Summer rainfall variability would thus be predominantly driven by the tropical dynamic linked to ENSO, the IPO or decadal ENSO-like.

At the interannual timescale (2-8 year), similar annular geopotential anomalies to those observed at the quasi-decadal scale are linked to positive SRI. Low-pressure anomalies in the Polar Regions and asymmetric enhancing of the St Helena and

Mascarene High indicate a southward shift of the westerly wind belt (Fig. 2f). Meanwhile, anomalous low-level easterly moisture flux into South Africa, which is favored by low-pressure anomalies over the continent, is generated from anticyclonic circulation in the South Indian Ocean (Fig. 2f). These anomalies, even though they are weak over Antarctica and reveal some zonal asymmetries in the mid-latitudes, show some similarities with the SAM (spatial correlation = 0.58), but also with the Southern Oscillation Index (spatial correlation = 0.47). This is consistent with earlier studies (Pohl *et al.*, 2009), which show the statistical dependence between the SAM and ENSO in austral summer, and their consequences for Southern African rainfall.

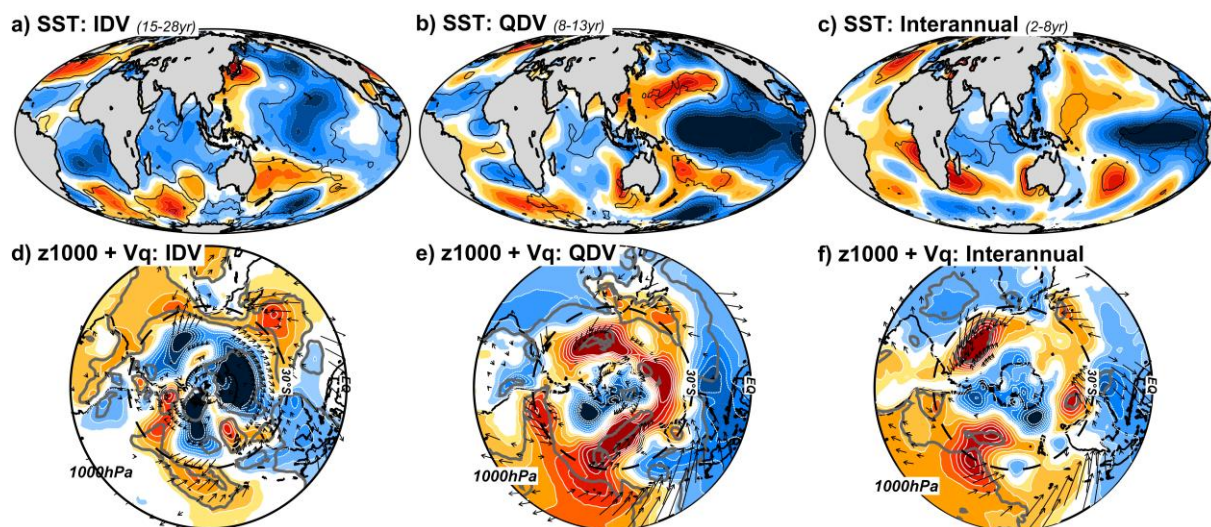


Figure 2. Summer anomalies of SSTs and low-tropospheric circulations associated with periods of high-amplitude over the dominant timescales of SRI variability. (a) Interdecadal composite anomalies of SSTs (in  $^{\circ}\text{C}$ ) during periods of enhancing interdecadal variability ( $\text{IDV} \geq 1$  standard deviation) in the SRI. (b-c) as for (a) but for the quasi-decadal and interannual timescale (QDV). (d-f) as for (a-c) but for geopotential height ( $z$  in m) and moisture fluxes (arrows,  $Vq$  in  $\text{gkg}^{-1}\text{m}\cdot\text{s}^{-1}$ ) at 1000 hPa. The statistical significance (contours) has been estimated by testing the difference in mean between geopotential height anomalies during periods of rainfall variability greater and lower than 1 SD, through a modified  $t$ -test accounting for pseudo-replication in the series at  $p=0.05$ . Only significant zonal and meridional moisture flux anomalies at  $p = 0.05$  are shown by arrows.

## 6. Conclusion

This study analyses the changing characteristics of winter rainfall, and their teleconnections with large-scale climate through the dominant timescale of variability. As determined by wavelet analysis, observed and reconstructed summer rainfall exhibit three significant timescales of variability since the end of the 19<sup>th</sup> century: interdecadal, quasi-decadal and interannual. Summer Southern African rainfall displays significant increasing variance since the 1930s at the interdecadal timescale, and since the late 1960s at the quasi-decadal timescale. Multidecadal fluctuations can also be detected based on the reconstruction back to 1796, but, due to the shortness of the instrumental records, any study of multidecadal teleconnections is limited.

Teleconnections with global SST and atmospheric circulation anomalies are different on all three timescales considered here. As proposed by Dieppois *et al.* (2015), the PDO can drive interdecadal fluctuations in summer South African rainfall in shifting the Walker circulation and, at the regional scale, the South Indian Convergence Zone. Decadal ENSO-like (or the IPO) and ENSO also drive such anomalies, but at the quasi-decadal and interannual timescale. Annular geopotential anomalies, which could be related to the SAM or ENSO-like anomalies in the Southern Hemisphere (Pohl *et al.*, 2009), influence interdecadal to interannual variability in summer rainfall through shifts in the westerlies, which generate an anomalous low-level easterly moisture flux from the Mascarene region. At the decadal timescales, the influence of the IPO or decadal ENSO-like could result from the generation

of atmospheric Rossby waves. This is consistent with Tourre *et al.* (2001), which proposed that interannual to quasi-decadal fluctuations in the equatorial Pacific require coupled Rossby wave dynamics.

These results present, for the first time, analyses of atmospheric dynamics associated with global ocean-atmosphere modes of variability which influence, seasonally and regionally, vital Southern African rainfall receipts at the decadal timescales. Such analyses will help to understand recurrent space-time evolution of rainfall and drought patterns across this dry region.

## References

- Dieppois, B., Pohl, B., Rouault, M., New, M., Lawler, D., Keenlyside, N. (Submitted). Interannual to Interdecadal variability of winter and summer Southern African rainfall, and their teleconnections. *Clim Dyn.*
- Dyer, T.G.T, Tyson, P.D. (1977). Estimating above and below normal rainfall periods over South Africa, 1972–2000. *J. Appl. Meteor.* **16**:145–147.
- Jury, M.K. (2014). Factors contributing to a decadal oscillation in South African rainfall. *Theor. Appl. Climatol.* Published online:doi.10.1007/s00704-014-1165-4.
- Klein, S.A., Soden, B.J., Lau, N.C. (1999). Remote sea surface variations during ENSO: evidence for a tropical atmospheric bridge. *J. Clim.* **12**:917–932.
- Malherbe, J., Landman, W.A., Engelbrecht, F.A. (2014). The bi-decadal rainfall cycle, Southern Annular Mode and tropical cyclones over the Limpopo River Basin, southern Africa. *Clim. Dyn.* **42**:3121–3138.
- Mantua, N.J., Hare, S.R., Zhang, Y., Wallace, J.M., Francis, R.C. (1997). A Pacific Interdecadal Climate Oscillation with Impacts on Salmon Production. *Bull. Amer. Meteor. Soc.* **78**:1069–1079.
- Mason, S.J., and Jury, M. (1997). Climatic variability and change over the Southern Africa: a reflection on underlying processes. *Prog. Phys. Geo.* **21**:23–50.
- Neukom, R., Nash, D.J., Endfield, G.H., Grab, S.W., Grove, C.A., Kelso, C., Vogel, C.H., Zinke, J. (2014). Multi-proxy summer and winter precipitation reconstruction for southern Africa over the last 200 years. *Clim. Dyn.* **42**:2713–2726.
- Pohl, B., Fauchereau, N., Richard, Y., Rouault, M., Reason, C.J.C. (2009). Interactions between synoptic, intraseasonal and Interannual convective variability over Southern Africa. *Clim. Dyn.* **33**:1033–1050.
- Power, S., Casey, T., Folland, C.K., Colman, A., Mehta, V. (1999) Inter-decadal modulation of the impact of ENSO on Australia. *Clim. Dyn.* **15**:319–323.
- Reason, C.J.C, Rouault, M. (2002). ENSO-like decadal patterns and South Africa rainfall. *Geophys. Res. Lett.* **29**:161–164.
- Ropelewski, C.F., and Halpert, M.S. (1987). Global and regional scale precipitation patterns associated with the El Niño/Southern Oscillation. *Mon. Wea. Rev.* **115**:1606–1626.
- Rouault, M., and Richard, Y. (2005). Intensity and spatial extent of droughts in Southern Africa. *Geophys. Res. Lett.* **32**:L15702.
- Tourre, Y.M., Rajagopalan, B., Kushnir, Y., Barlow, M., White, W.B. (2001) Patterns of coherent ocean decadal and interdecadal climate signals in the Pacific basin during the 20<sup>th</sup> century. *Geophys. Res. Lett.* **28**:2069–2072.

## *Observing the atmospheric boundary layer structure over the Highveld using a ceilometer*

Rosa T. Gierens\*<sup>1</sup>, Svante Henriksson<sup>2,3</sup>, Ville Vakkari<sup>2</sup>, Miroslav. Josipovic<sup>3</sup>, Kerneels Jaars<sup>3</sup>, Andrew D. Venter<sup>3</sup>,  
Johan P. Beukes<sup>3</sup>, Pieter G. Van Zyl<sup>3</sup>, and Ewan J. O'Connor<sup>2,4</sup>

<sup>1</sup>Department of Physics, University of Helsinki, P.O. Box 64, Helsinki, 00014, Finland

<sup>2</sup>Research and Development, Finnish Meteorological Institute, P.O. Box 503, Helsinki, 00101, Finland

<sup>3</sup>Unit for Environmental Sciences and Management, North-West University, Private Bag X6001, Potchefstroom, 2520,  
South Africa

<sup>4</sup>Meteorology Department, University of Reading, Reading, UK

A semi-automatic method for detecting the tops of the mixed layer in day time and the stable and residual layers in night time has been developed. The observations were carried out at Welgegund, a regional background site on the South African savannah, and results from the first year of observations are presented. Despite having some limitations, the method provides notably high data coverage. The frequency at which each layer was detected showed an annual cycle being lowest in the summer and highest in the winter for all the three layers studied.

Keywords: Mixed layer, Stable layer, Residual layer, Ceilometer

### *Introduction*

The atmospheric boundary layer (ABL) is the lowest part of the troposphere that directly interacts with the Earth's surface, defined as the layer that responds to surface forcing in a time scale of an hour or less (Stull, 1988). The continental boundary layer has a distinct structure and diurnal variation pattern, especially in high pressure regions (Stull, 1988), characterized with a well-mixed layer during the day, and a residual layer on top of a stable layer at night. The depth of the ABL varies from some tens or hundreds of meters to a couple of kilometres. As people live their lives in the boundary layer, its properties form a large part of what is experienced as weather (e. g. temperature, humidity and wind speed near the surface). In unstable conditions the volume of air being mixed is defined by the depth of the ABL making it also an important length scale for the mixing of pollutants. Since the ABL responds to the changes in surface conditions rapidly, small scale heterogeneities cause local variations that are challenging to reproduce in numerical weather prediction and models developed for research. Due to limited spatial resolution and the high computational cost of simulating the properties of turbulent flows, these models must rely on rather simple parametrisations when describing the properties of the ABL. Publications of observations related to the

ABL depth in South Africa are scarce (Korhonen *et al.* 2014, Tyson *et al.* 1976), limiting the possibilities for understanding the evolution of the ABL and model validation in this region.

In this work observations made at Welgegund, Highveld ([www.welgegund.org](http://www.welgegund.org)), were used to estimate the depth of the ABL using a ceilometer and surface flux measurements. The ceilometer is an eye-safe remote sensing instrument using LIDAR (light detection and ranging) technology, and requires very little maintenance. It has been successfully used for detecting the ABL depth at various locations (e.g. Munkel *et al.* 2007); here we demonstrate how the ceilometer can be used in studying the boundary layer structure at the Highveld, and present preliminary results from the first year of observations.

### *Methods*

A Vaisala CT25K ceilometer has been operating at the Welgegund measurement station continuously since September 2012. Auxiliary measurements at Welgegund include turbulent fluxes of sensible and latent heat, momentum and CO<sub>2</sub> obtained with the eddy covariance method, temperature profile at the surface (2.5m and 7.5m above surface) and soil heat flux.

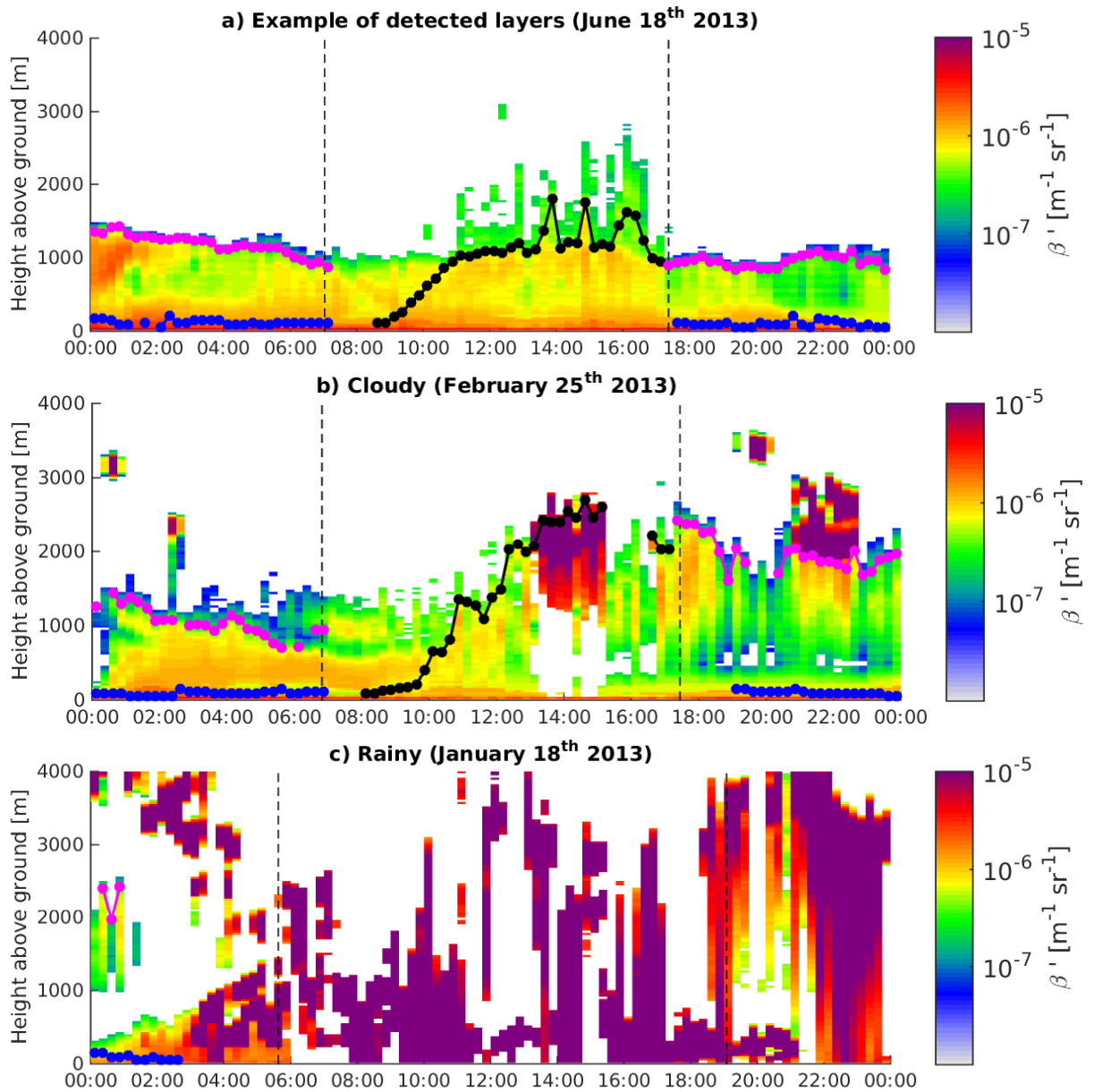


Figure 1: Time-height plot of attenuated backscatter showing the diurnal evolution over 24 hours on 3 days at Welgegund. Time is local time (UTC+2). Sunrise, sunset and the identified residual, stable and mixed layers are also indicated.

The process of detecting the ABL from the observed backscattering coefficient profiles included automated algorithms as well as manual data processing. The method is described in detail by Gierens (2015), and here a short summary is given. Firstly, three different algorithms for detecting the ABL depth were individually applied on the ceilometer data (Brooks 2003, Steyn *et al.* 1999). These ABL depths were combined using the guidance of stability conditions (the Monin-Oboukhov stability parameter) in the surface layer retrieved from an eddy covariance system to identify stable, residual and mixed layers. From sunrise to sunset only the mixed layer is considered, and is calculated as the average of all the available data when the surface layer was unstable or near neutral. In the night time, from sunset to sunrise, under stable conditions the stable layer was retrieved using a modified version of the gradient method (Steyn

*et al.* 1999). The residual layer was estimated by averaging the results acquired by the wavelet fitting (Brooks 2003) and the so called signal-to-noise ratio limited layer methods (Gierens, 2015). No stability criteria were applied for the residual layer. Manual cleaning and checking of the data was performed at several steps of the process to ensure the quality of the results.

### Results

Diurnal evolution of the vertical profile of observed attenuated backscatter coefficient ( $\beta$ ), as well as the identified residual, stable and mixed layers, is presented in Fig. 1 for three days. The selected days were chosen to describe the performance of the method under different kind of weather conditions. To illustrate the method firstly an ideal case is chosen; the day is a cloudless winter day with a clearly distinguishable

boundary layer (Fig. 1a). Approximately one hour after sunrise the convective layer starts growing, reaching above 1 km by midday. When the sun sets the heat flux

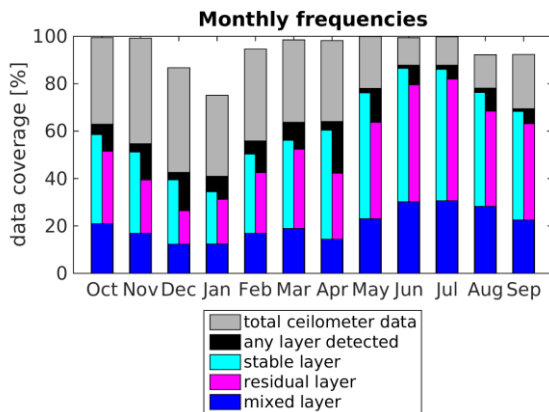


Figure 2: Monthly data coverage for the ceilometer, together with the frequencies at which the mixed, stable and residual layers as well as any layer were detected for one year starting from October 2012.

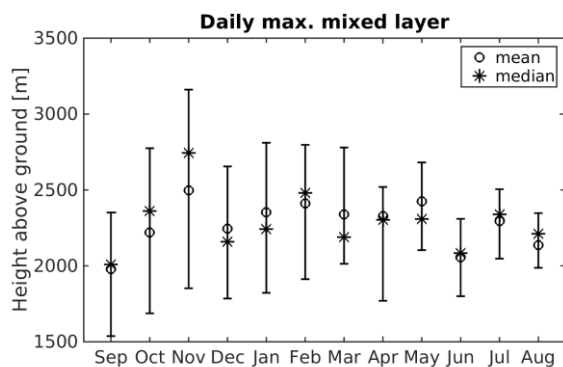


Figure 3: Monthly mean, median, and 25 and 75 percentiles of maximum daily mixed layer depth.

from the surface, which drives the convective mixing, diminishes. The surface starts to cool, and a surface inversion develops. Here the layer with the strongest  $\beta$ -gradient is assumed to be representative for the stable layer at night. Above the stable layer lies the residual layer from the previous days' mixed layer.

The second example is a summer day with some clouds present near the top of the boundary layer in the afternoon and night time (visible as the purple colour in Fig. 1b). The mixed layer reaches slightly higher than in the winter day shown in Fig. 1a, and a stable layer is again detected for most of the night.

The third example is a rainy day in the middle of the summer (Fig. 1c), illustrating the challenges in both defining and detecting the ABL when precipitation occurs.

The frequency at which the mixed, residual and stable layers were detected exhibits a clear annual cycle (Fig. 2), with lower frequencies in the summer

and higher in the winter. The challenging weather conditions such as rain, clouds, frontal activity and storms, which make defining the ABL difficult, are more common in the summer causing the observed annual variation in the detection frequencies. The longest gap in the observations occurred in December-January, which lowered the frequencies during these months even further but does not change the fact that the frequency of detecting the ABL relative to available ceilometer data is lowest in the summer. Fig. 2 further illustrates the remarkably high data coverage achieved by the ceilometer, which can be attributed to the easy maintenance of the instrument. The value of this quality should not be underestimated, as the results presented here show a higher temporal coverage of ABL layer depth observations in South Africa than in any other study known to the authors to have been published to date.

Evaluating the daily maximum of the mixed layer depth showed that on average the seasonal characteristics were not well-distinguished: the means and medians of the daily maximum mixed layer depth vary from month to month but overall the annual cycle is weak (Fig. 3). A notable difference between the seasons can be found in the spread of the observed values, which is much larger in summer than in winter.

### Conclusions

We presented examples of how the ceilometer observations combined with other measurements at the Welgegund measurement station can be utilised to study the diurnal evolution of mixed, stable and residual layers. Weather conditions at which ABL definition is challenging is the main obstacle in reaching higher temporal data coverage. The long time series of ceilometer observations at Welgegund (since September 2012) provides a reasonably good basis to study the diurnal and annual variations of the ABL together with the controlling factors at South African Highveld. The data coverage for the first year of observations shows strong annual variation in the frequencies at which the mixed, stable and residual layers could be detected. The maximum daily mixed layer depth showed on average only a weak seasonality, however the spread of the values had clear seasonal characteristics. Further studies are undertaken to both extend the time series and the analysis of the data presented here.

### Acknowledgements

This work was supported by the Academy of Finland Center of Excellence (project no 1118615). Matti Räsänen, Mika Aurela and their colleagues at the Finnish Meteorological Institute are acknowledged for the processing and guidance for using the eddy covariance data.

### References

Brooks, I. M. (2003). Finding boundary layer top: Application of a wavelet covariance transform to

- lidar backscatter profiles. *Journal of Atmospheric and Oceanic Technology*. 20(8): 1092 – 1105.
- Gierens, R.T. (2015) Understanding the evolution of the boundary layer over the Highveld, South Africa. Masters Thesis, University of Helsinki.
- Korhonen, K., Giannakaki, E., Mielonen, T., Pfüller, A., Laakso, L., Vakkari, V., Baars, H., Engelmann, R., Beukes, J. , Van Zyl, P., Ramandh, A., Ntsangwane, L. , Josipovic, M., Tiitta, P., Fourie, G., Ngwana, I., Chiloane, K. and Komppula M. (2014). Atmospheric boundary layer top height in South Africa: measurements with lidar and radiosonde compared to three atmospheric models. *Atmospheric Chemistry and Physics*. 14(8): 4263 – 4278.
- Münkel, C., Eresmaa, N., Räsänen, J. and Karppinen, A. (2007). Retrieval of mixing height and dust concentration with lidar ceilometer. *Boundary-layer meteorology*. 124(1): 117 – 128.
- Steyn, D. G., Baldi, M. and Ho, R. (1999) The detection of mixed layer depth and entrainment zone thickness from lidar backscatter profiles. *Journal of Atmospheric and Oceanic Technology*. 16(7): 953 – 959.
- Tyson, P.D., Preston-Whyte, R.A. and Diab, R.D. (1976). Towards An Inversion Climatology Of Southern Africa: Part I, Surface Inversions. *South African Geographical Journal*. 58(2): 151 – 163.

## ***Acknowledging decadal to intraseasonal variability in support of agriculture – the 2014/15 maize production season***

Johan Malherbe, Wiltrud Durand and Christien Engelbrecht – Agricultural Research Council – Institute for Soil, Climate and Water

e-mail:johan@arc.agric.za

The maize yield of the 2014/15 summer was negatively affected by a mid-summer drought lasting from early January well into February. In order to understand the reasons for the negative impacts, we evaluate the season in terms of specific weather events in the main maize production regions. A crop model is used to quantify negative impacts by specific events through the season and to understand how planting date may have been adjusted to manage potential impacts. The seasonal rainfall profile is then evaluated in terms of decadal variability in South Africa – to ascertain whether any useful information, apart from the seasonal forecast, may potentially have been available prior to the summer. Using an existing understanding of lunar tidal influence on South Africa’s weather, relatively low rainfall through the 2014/15 season together with the intensity of the mid-summer dry period and wet conditions by late summer may be identified years in advance.

**KEYWORDS:** Decadal variability, Intraseasonal variability, Maize production, Lunar tidal potential

### *Introduction*

The decadal and intraseasonal time scales are both important for practical decision-making purposes in agriculture (e.g., Mehta et al. 2013, Vogel and O’Brien, 2006). Extremes and variability is expected to have large impacts under a changing climate, underlining the importance of being able to resolve decadal variability (Goddard et al. 2012). One of the drivers of decadal variability is variability in the lunar tide (e.g. Tanaka *et al.* 2012). On intraseasonal time scale, large-scale circulation regimes (such as the SAM and MJO) provides the opportunity to improve forecast skill (e.g. Bladwin et al. 2003). Lunar tidal variability have also been shown to be associated with the SAM on both decadal and intra-seasonal time scales (Malherbe et al. 2014), and may therefore present a future opportunity to increase skill at both time scales.

Extreme conditions during part of the 2014/15 summer highlighted the importance of information regarding intraseasonal variation to the maize industry, including individual farmers. Latest estimates are for both white and yellow maize to be the lowest since 2007, with the total maize yield expected to be down 30% from the final estimates for the previous summer.

In this presentation, we evaluate the impacts of the seasonal rainfall and temperature profile on the yields in the western and eastern maize production regions of South Africa. Additionally, we consider the main characteristics of the season in terms of lunar tidal variation, as one of the possible drivers of decadal variability though intraseasonal impacts.

### *Instrumentation and Method*

To understand the influence of intraseasonal characteristics on the 2014/15 maize crop in the 2 main maize production regions, daily weather data and soil profile information from the ARC-ISCW climate and soil databanks respectively were used as input data to a crop model to test for the sensitivity or potential yields to a change in the planting date. Adjusting the planting date, within the normal bounds, is a management practice that may be applied to reduce the risk of negative impacts by changing the timing, in terms of plant physiology, of projected extreme events anomalies.

The DSSAT Crop System Model (previously known as CERES-maize) (Jones et al., 2003 and Hooigeboom et al , 2010) (was used to simulate the effect of eight different planting dates on yield at two sites representing the cooler eastern (Middelburg) and warmer western (Hertzogville) maize production regions of South Africa. Table 1 represents the crop management systems of which all combinations were simulated for each of 8 planting dates within the normal planting window. Fertilization was assumed to be at optimum rates.

<b>Planting dates</b>	<b>Soils</b>	<b>Row width (m)</b>	<b>Plant population (plants/m<sup>2</sup>)</b>
15 September	Middelburg		
30 September	Glencoe appam	0.75	2.5
15 October	Avalon normandien	0.90	3.0
31 October		1.20	3.5
15 November	Hertzogville		
30 November	Covelly annandale	1.5	1.0
15 December	Hutton shorrocks	2.0	1.5

31 December		2.5	2.0
-------------	--	-----	-----

The seasonal rainfall profile is considered within the context of decadal variability, as represented by the component driven by lunar tidal variation (Malherbe et al. 2014). While research into the mechanisms and effect of external drivers on the climate system at various time scales are being pursued, integration of lunar tidal variation within current seasonal and short-range forecasts are largely absent. For this reason, previous summers with similar tidal variation as the 2014/15 summer, based on lunar trajectory, are used as a prediction for the 2014/15 summer. The main characteristics investigated are seasonal total rainfall, the variation in the Southern Annular Mode (SAM) and wet versus dry periods. For rainfall, 5 analogue years were available for use since the start of the daily climate record whilst 2 analogue years were available for considering possible tidal associations with the SAM since 1979.

#### Results and Discussion

Even though total summer rainfall during 2014/15 was near normal over most of the summer rainfall region, conditions during February had a particularly negative impact on maize.

An intense hot and dry spell by early to mid-February resulted in large negative impacts on the summer maize crop due to the critical part of the growing season during which it occurred.

Due to the developing El Niño conditions by late 2014, the official message, based on seasonal forecast model output, was to use the wetness during the middle and early summer and try to avoid sensitive activity by the dry part of the season (late summer). This would translate, for dryland maize farmers, to use the earliest date within the normal planting window, following the first significant rain. Fig. 1 shows the yields (kg/ha) for 8 different planting dates as simulated for the western (Hertzogville) and eastern (Middelburg) maize production regions.

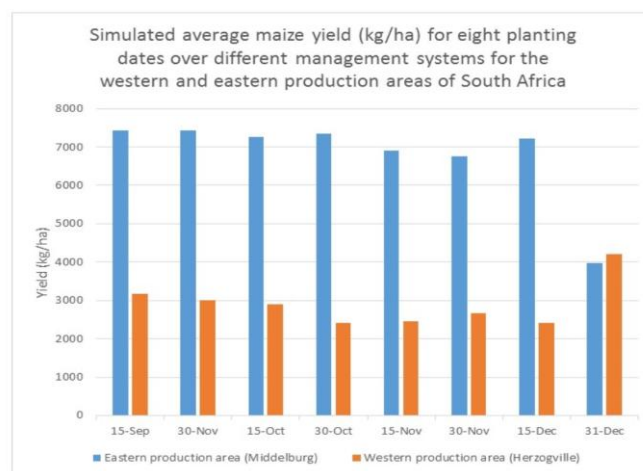


Figure 1 Simulated average maize yield (kg/ha) for eight planting dates over different management systems for the western and eastern production areas of South Africa.

In the eastern production region there was very little variation in the yields over the first seven planting dates (mid-September to mid-December) with an average yield of 7200 kg/ha. However, simulations of the very late plantings at the end of the year indicate a 45% drop in yield (3980 kg/ha) from the average over the first seven planting dates that can be ascribed to the cooler temperatures experience during the grain filling phase (not shown).

Interestingly, the last planting date in western production areas had highest simulated yield (4200 kg/ha), with the yield 54% higher than the average of the first seven planting dates of 2716 kg/ha. This pattern would be in stark contrast to the recommendation for an El Niño season. The simulations for the western region indicated decrease in yield especially around the traditional planting dates of mid-November. This can possibly be ascribed to the extreme high temperatures that concurred with grain filling phase of these planting dates (Fig. 2).

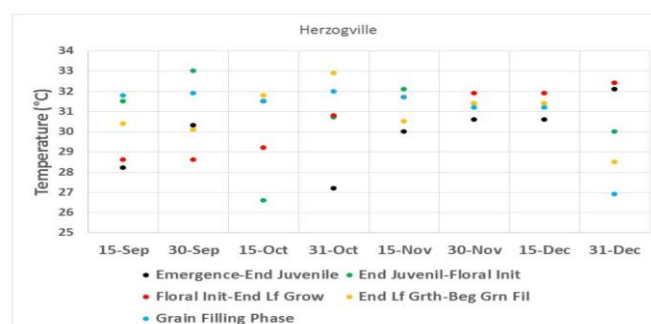


Figure 2 Average maximum temperature during various growth stages of maize as simulated for maize at Hertzogville during the 2014/15 summer, for 8 plant dates as indicated

During the period of mid-January to mid-February, maximum daily temperatures were well above 30°C. Highest maximum temperatures, together with minimal rainfall, occurred during early February. Given the fact that the optimum temperature during grain filling is 27°C the extreme high temperatures experience during 2014/15 production season in the western areas had a damaging effect on the yield potential especially in the earlier plantings (1 November to 15 November) whilst the later plantings (15 November to 30 November) were marginally better. The latest planting date (31 December) yielded the most positive results as the sensitive grain filling stage occurred after the hot period, during a cooler, wetter period that started from mid-February (Fig.2 and Fig.3).

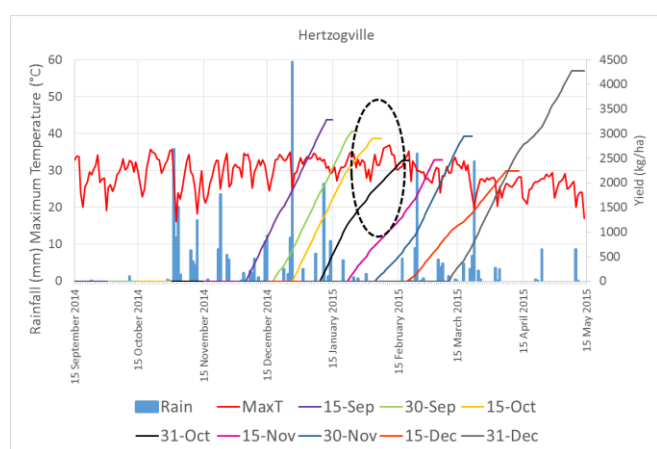


Figure 3 Rainfall (blue bars), maximum temperature (red line) and grain filling rate of maize planted over eight different planting dates (diagonal lines) in the western maize production region of South Africa.

While maize yields in the eastern areas were, according to simulations, largely insensitive to planting date, the conditions in the west may have been managed to some degree by alternate planting date. The wetter and cooler conditions from mid-February represented a possible management option that may have led to a better yield, had it been foreseen.

Based on the relationship between lunar tidal potential, the Southern Annular Mode (SAM) and rainfall over the South African summer rainfall region (Malherbe et al. 2014), previous years analogous to 2014/15 had been characterized by near-normal to below-normal rainfall over the summer rainfall region despite occurring close to the lunar nodal minimum which is associated, broadly speaking, to the maximum in the quasi-18-year cycle over the northeastern parts of South Africa (primarily Limpopo). Moreover, Fig. 4 shows that the predicted seasonal rainfall profile, based on rainfall distribution during 5 analogue years since 1920, as well as that observed during 2014/15,

indicate relatively dry conditions around mid-summer, followed by wetter conditions towards March. The tendency for drier conditions specifically around late December to middle February. These conditions were observed at Hertzogville (and the rest of the summer rainfall region in general), responsible for the crop failures over many areas. The profile for the predicted rainfall distribution has been created from the data of analogue years, based on tidal potential similar to 2014/15.

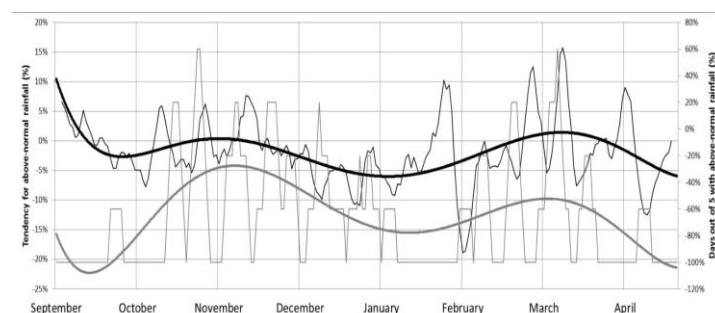


Figure 4 Seasonal profile of tendency for above-normal rainfall for analogue years across the summer rainfall region (black line) and tendency for above-normal rainfall at Hertzogville during 2014/15 (grey line).

At decadal timescale, periods with higher rainfall over the summer rainfall region and a higher SAM have been associated with higher near-equatorial tidal potential (Malherbe et al. 2014). On intraseasonal time scale, during years such as 2015, periods of high near-equatorial potential occur near the date of new moon, followed by prolonged periods of low equatorial potential (with a much smaller increase in potential around full moon). New moon and full moon define the period of maximum tidal potential according to the 29-day lunar synodic month. These prolonged periods of lower potential are associated with little movement in the SAM (based on 3 analogue years since 1948), also tending to be somewhat lower than during the time on or before maximum tidal potential. (Fig. 5).

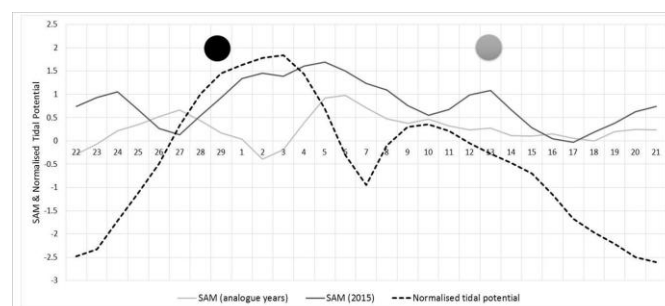


Figure 5 Normalised near-equatorial tidal potential (broken line), the SAM in JFM relative to tidal potential in (3) analogue years (light grey line) and the SAM during JFM 2015. Days of the lunar synodic month are indicated on the x-axis.

While rainfall during the mid-summers of analogue years have been below average over most of the summer rainfall

region (not shown), the distribution of rainfall events are strongly un-even. During the times with a larger movement on the SAM (around maximum tidal potential), rainfall tends to be increased for a short period (about 5 days out of the synodic half-month of +/-15 days) relative to the rest (10 days) across the summer rainfall region in JFM of analogue years as well as in 2015, thus remaining relatively low for a much longer period (Fig. 6).

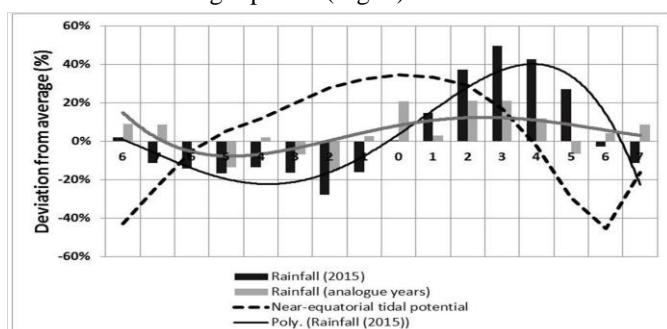


Figure 6 Percentage deviation from the average rainfall distribution of rainfall, around new and full moon, during analogue years (grey bars) and during JFM 2015 (black bars). Near-equatorial tidal potential (broken black line) is also indicated.

### Conclusions

Hot and dry conditions during January and early February had a strong negative impact on maize production over especially the western maize production region. Prior knowledge of dry mid-summer conditions followed by wetter weather since middle February may have informed management decisions before the summer over and above expected drier conditions during JFM, related to the weak El Niño of 2014/15. Evidence have been presented to show that further study of the effect of lunar tidal potential on the climate system may increase the ability to predict and understand intra-seasonal variation, in context with other influences in the climate system. Understanding of intra-seasonal variation, culminating in total seasonal rainfall, will contribute to the understanding of decadal variability. These two aspects can play a major role in agricultural management practices.

### References

- Baldwin MP, Stephenson DB, Thompson DWJ, Dunkerton TJ, Charlton AJ, O'Neill A. (2003) Stratospheric memory and extended-range weather forecasts. *Science*. **301**: 636-640.
- Goddard L, Kirtman B, Hurrell J, Murphy J, Stockdale T and Vera C. (2012) Two Timescales for the Price of One (almost). *Bulletin of the American Meteorological Society*. **93**: 621–629. Doi: 10.1175/BAMS-D-11-00220.1.
- Hoogenboom G, Jones JW, Wilkens PW, Porter CH., Boote KJ,

Hunt LA, Singh U, Lizaso JL, White JW, Urusev O, Royce FS, Ogoshi R, Gijsman AJ, and Tsuji GY. (2010) Decision Support System for Agrotechnology Transfer (DSSAT) Version 4.5 [CD-ROM]. University of Hawaii, Honolulu, Hawaii.

- Jones JW, Hoogenboom G, Porter CH, Boote KJ, Batchelor WD, Hunt LA, Wilkens PW, Singh U, Gijsman AJ, and Ritchie JT. (2003) DSSAT Cropping System Model. *European Journal of Agronomy*. **18**:235-265.
- Malherbe J, Engelbrecht FA and Landman WA. (2014) Response of the Southern Annular Mode to tidal forcing and the bidecadal rainfall cycle over subtropical southern Africa. *Journal of Geophysical Research (Atmospheres)*. **119**:2032–2049. Doi:10.1002/2013JD021138.
- Mehta VM, Knutson CL, Rosenberg NJ, Olsen JR, Wall NA, Bernadt TK and Hayes MJ. (2013) Decadal Climate Information Needs of Stakeholders for Decision Support in Water and Agriculture Production Sectors: A Case Study in the Missouri River Basin. *Weather, Climate and Society*. **5**:27–42.
- Tanaka YI, Yasuda H, Hasumi H, Tatebe H and Osafune S. (2012) Effects of the 18.6-yr Modulation of Tidal Mixing on the North Pacific Bidecadal Climate Variability in a Coupled Climate Model. *Journal of Climate*. **25**:7625-7642.
- Vogel C and O'Brien K. (2003) Climate forecasts in southern Africa. Chapter 1. In coping with climate variability: The use of seasonal forecasts in southern Africa, O'Brien K and Vogel C. (eds). Ashgate: Aldershot.

## Variability of Aerosol Optical Depth over Richard's Bay (South Africa) based on MODIS, OMI satellite and GOCART model measurements

Joseph A. Adesina<sup>1,\*</sup>, Stuart J. Piketh<sup>1</sup>, Kanike R. Kumar<sup>2</sup>

<sup>1</sup>School of Geo- and Spatial Science, Unit for Env. Sc. and Management, North-West University, Potchefstroom

<sup>2</sup>Key Laboratory for Aerosol-Cloud-Precipitation of China Meteorological Administration, School of Atmospheric Physics, Nanjing University of Information Science and Technology, Nanjing 210044, Jiangsu Province, China

\*corresponding author: [jadesina173@gmail.com](mailto:jadesina173@gmail.com)

### Abstract

Anthropogenic aerosols are multicomponent and include sulfate, black carbon, dust and sea salt. The present study reports the aerosol optical depth (AOD) and its components over a coastal area, Richards Bay in South Africa using observations from multiple satellite sensors. Using the monthly average values from Moderate resolution Imaging Spectrometer (MODIS), AOD<sub>550</sub> varies between 0.12±0.07 (May) and 0.30±0.13 (September) from Aqua, while it varies from 0.13±0.08 (June) to 0.33±0.16 (September) from Terra. Using Goddard global Ozone Chemistry, Aerosol, Radiation, and Transport (GOCART) model, Sulfate was the dominant aerosol component, and aerosol index from Ozone Monitoring Instrument (OMI) indicated the presence of absorbing aerosol characteristics over the study region throughout the year.

Key words: Aerosol optical depth, Sea salt, Black carbon, sulfate, Dust, MODIS, GOCART, OMI

### I. Introduction

Aerosols from natural and anthropogenic sources affect climate significantly through their various effects. The effects are simply grouped into three; direct, indirect and semi-direct. Aerosol optical thickness/depth (AOD) is a key parameter by which aerosol burden can be inferred and it is made available through satellite retrievals and other field instruments (Cheng et al., 2012). It has been found that different aerosol retrievals reports somewhat different values of AOD even when time and space remain the same because the algorithms of the instruments are not generally the same (Mishchenko et al., 2009). In this study, we have used different instruments to study the variability of AOD over Richards Bay. The year 2007 was selected because in a different study (paper under review), aerosol loading was exceptionally high and we decided to do further work particularly, on the various types of aerosols dominant over the location.

### II. Study region and Dataset

#### a. Area of study

Richards Bay (28.8°S, 32.1°E) is the country's largest port and its coal terminal is the single largest export coal terminal in the world and also a world leader in sand mining and

mineral processing operations. It produces high purity iron, titanium, and zircon. Richards Bay's is considered to have a warm temperate climate (Cfa) according to the Köppen-Geiger climate classification with the average annual temperature and rainfall of 21.9 °C and 1123 mm, respectively.

#### b. Datasets

The study was carried out based on the datasets from MODIS (Terra/Aqua) and (OMI) satellites with GOCART model retrievals. AOD spectral dependence is given by the Ångström's formula

$$\tau(\lambda) = \beta\lambda^{-\alpha} \quad (1)$$

where  $\tau(\lambda)$  is the estimated AOD at the wavelength  $\lambda$ ,  $\beta$  is the Ångström's turbidity coefficient which equals AOD at  $\lambda = 1 \mu\text{m}$ , and the wavelength exponent  $\alpha$ , is the Ångström's exponent which is a good indicator of the fraction of accumulation-mode particles ( $r < 1 \mu\text{m}$ ) to coarse-mode particles ( $r > 1 \mu\text{m}$ ). The AOD data was retrieved from MODIS satellite for the period of January - December, 2007. The OMI satellite was used to study the aerosol index (AI) while, the GOCART provided the types of aerosol in the total column AOD for the same study period. MODIS, which has been flying aboard Terra since December, 1999 and Aqua since May, 2002 provides a lot of aerosol products from over both land and sea. Details about MODIS has been dealt with by several earlier researchers (Misra et al., 2008; Remer et al.,

2005) and hence not repeated. The GOCART model is used to simulate the AOD for major types of tropospheric aerosols including sulfate, dust, black carbon, and sea salt. GOCART fields have model assimilated global analysis constrained by meteorological observations including wind, temperature, pressure, specific humidity, convective cloud, mass flux, cloud friction, precipitation, boundary layer depth, surface wind and surface wetness that are used in aerosol simulations. Due to its low resolution ( $2^\circ \times 2.5^\circ$ ), its total column AOD is of lower values and about two to five times smaller than satellite data in this region except in burning season when it is about 35% (Cheng et al., 2012; Chin et al., 2002). AI is provided by the OMI and is, mathematically defined as:

$$AI = 100[\log_{10}(I_{360}/I_{331})_{\text{measured}} - \log_{10}(I_{360}/I_{331})_{\text{calculated}}] \quad (2)$$

Positive values of AI are associated with absorbing aerosols whereas, small or negative AI values are associated with non-absorbing aerosols (Torres et al., 2007). The data were downloaded in ASCII format and time series from NASA GIOVANNI interactive website and filtered from NAN and outlier's data.

### III. Results and Discussion

#### a. Variation of AOD

Figure 1 shows the monthly variation of AOD<sub>550</sub> values during the study period for MODIS (Terra/Aqua). The AOD<sub>550</sub> values vary between  $0.12 \pm 0.07$  in May and  $0.30 \pm 0.13$  in September for Aqua, and for Terra MODIS, the AOD<sub>550</sub> vary from  $0.13 \pm 0.08$  in June to  $0.33 \pm 0.16$  in September. Both Terra and Aqua showed low aerosol loading from December to June except, with a small increase in March. It then gradually increased from July, attaining peak in September and then decreased again to December. Both sensors measured AOD<sub>550</sub> values as generally above 0.2 during August-October. Many authors have found that the months from August-October have a high aerosol loading in South Africa (Adesina et al., 2014; Kumar et al., 2013) and this period is generally known as the biomass burning season. It can also be seen that MODIS Terra AOD<sub>550</sub> has lower values than Aqua AOD<sub>550</sub> in some months especially when AOD<sub>550</sub> is high. This is likely due to higher AOD<sub>550</sub> in the afternoon when there are more anthropogenic activities coinciding with the Aqua overpass time (Kumar et al., 2014).

#### b. Aerosol Types

The GOCART model contains the following modules in

aerosol simulation: emissions which include sulfate, dust, black carbon, organic carbon, and sea salt. In Fig. 2, the sulfate aerosol is seen to be dominant in all the months. Sulfate is mainly formed in the atmosphere from the oxidation

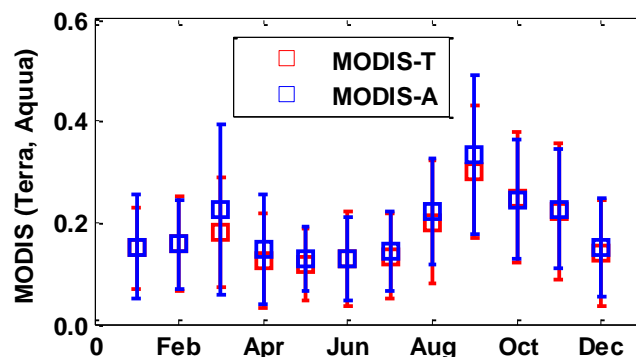


Fig 1: Monthly mean variations of aerosol optical depth over Richards Bay from MODIS (Terra, Aqua) with plus or minus one standard deviation for the year 2007

of SO<sub>2</sub>, which is emitted dominantly from fuel combustions and industrial activities. A fraction of SO<sub>2</sub> is also released from biomass burning and volcanic eruptions (Chin et al., 2002). Hence, this component may be dominant over the study region due to the heavy presence of industries at Richards Bay. Next in concentration is the sea salt aerosol which seems to have higher values from January to March and October to December. Sea salt emissions are highly dependent on wind speed. Richards Bay being a coastal city must enjoy this off shore winds. The black carbon has its most important sources from biomass burning and forest fires and in-house cooking from organic materials. Although this component is present throughout the year, its presence is mostly felt from July to October coinciding with biomass burning season as discussed earlier.

Dust aerosol is the least in the column. This ought to be so as Richards Bay is not close to desert and vegetation hinders the uplifting of sand dust when there is wind hence, not much is blown into the atmosphere. Main source of dust may then come from long range transport.

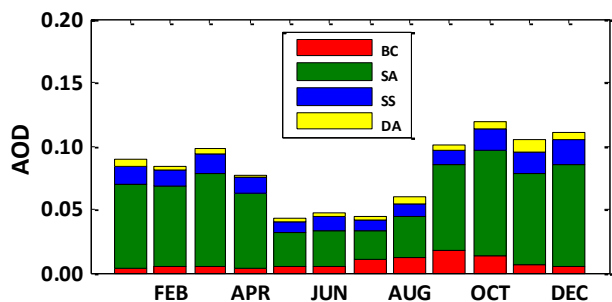


FIG 2: Modelled monthly mean contribution of different types of aerosol - black carbon (BC), sulfate aerosol (SA), sea salt (SS), and dust aerosol (DA) to the total AOD during January - December 2007

### c. Aerosol Index

AI is a qualitative parameter that indicates the presence of UV absorbing aerosols like carbonaceous particles, desert dust, and volcanic ash. The detection of AI covers all aerosols types over lands, oceans and even over ice or snow covered surfaces and mixed with or above clouds. The AI is, particularly, sensitive to large scale aerosol events of UV absorbing aerosols such as desert dust and biomass burning. When absorbing aerosol is detected, AI is observed to be positive but negative when aerosol is non-absorbing. The ability to detect this is based on the measurement of the spectral changes that takes place as aerosol undergoes UV absorption (Torres et al., 2007).

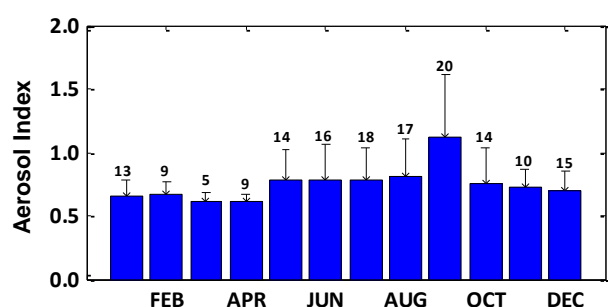


FIG 3: Monthly mean aerosol index with the available number of data over Richards Bay for the year 2007

According to Fig 3, AI is positive throughout the study period and is above 0.6. Though there was an increase in May

through to August, a major increase occurred in September.

The increased value in September can be traced to long term transport of smoke particles emitted from biomass burning or forest fires in and surrounding regions of South Africa (Hersey et al., 2014)

### IV. Conclusion

From the present study, MODIS products captured similar values of AOD over the location except for some few months when Aqua values were a bit higher than Terra values. This being a coastal location, one might expect that Aqua should perform better than Terra. Generally there was a low AOD in May – July and high AOD from August – October. The region was dominated by sulphate aerosols perhaps due to the presence of industries. The presence of absorbing aerosols was felt more in September, a period coinciding with the peak of biomass burning.

### V. Acknowledgements

The data used for this work is obtained from GIOVANNI interactive surface <http://disc.sci.gsfc.nasa.gov/giovanni> operated by NASA and we wish to thank them. We also thank the reviewer of this paper for the insightful comments.

### References

- Adesina, A. J., Kumar, K. R., Sivakumar, V. and Griffith, D. (2014). Direct radiative forcing of urban aerosols over Pretoria (25.75° S, 28.28° E) using AERONET Sunphotometer data: First scientific results and environmental impact. *Journal of Environmental Sciences*.
- Cheng, T., Chen, H., Gu, X., Yu, T., Guo, J. and Guo, H. (2012). The inter-comparison of MODIS, MISR and GOCART aerosol products against AERONET data over China. *Journal of Quantitative Spectroscopy and Radiative Transfer*, 113(16), 2135-2145.
- Chin, M., Ginoux, P., Kinne, S., Torres, O., Holben, B. N., Duncan, B. N., Martin, R. V., Logan, J. A., Higurashi, A. and Nakajima, T. (2002). Tropospheric aerosol optical thickness from the GOCART model and comparisons with satellite and Sun photometer

- measurements. *Journal of the atmospheric sciences*, 59(3), 461-483.
- Hersey, S., Garland, R., Crosbie, E., Shingler, T., Sorooshian, A., Piketh, S. and Burger, R. (2014). An overview of regional and local characteristics of aerosols in South Africa using satellite, ground, and modeling data. *Atmospheric chemistry and physics discussions*, 14(17), 24701-24752.
- Kumar, K. R., Sivakumar, V., Reddy, R., Gopal, K. R. and Adesina, A. J. (2013). Inferring wavelength dependence of AOD and Ångström exponent over a sub-tropical station in South Africa using AERONET data: Influence of meteorology, long-range transport and curvature effect. *Science of The Total Environment*, 461, 397-408.
- Kumar, K. R., Sivakumar, V., Yin, Y., Reddy, R., Kang, N., Diao, Y., Adesina, A. J. and Yu, X. (2014). Long-term (2003–2013) climatological trends and variations in aerosol optical parameters retrieved from MODIS over three stations in South Africa. *Atmospheric Environment*, 95, 400-408.
- Mishchenko, M. I., Geogdzhayev, I. V., Liu, L., Laci, A. A., Cairns, B. and Travis, L. D. (2009). Toward unified satellite climatology of aerosol properties: What do fully compatible MODIS and MISR aerosol pixels tell us? *Journal of Quantitative Spectroscopy and Radiative Transfer*, 110(6), 402-408.
- Misra, A., Jayaraman, A. and Ganguly, D. (2008). Validation of MODIS derived aerosol optical depth over Western India. *Journal of Geophysical Research: Atmospheres (1984–2012)*, 113(D4).
- Remer, L. A., Kaufman, Y., Tanré, D., Mattoo, S., Chu, D., Martins, J. V., Li, R.-R., Ichoku, C., Levy, R. and Kleidman, R. (2005). The MODIS aerosol algorithm, products, and validation. *Journal of the atmospheric sciences*, 62(4), 947-973.
- Torres, O., Tanskanen, A., Veihelmann, B., Ahn, C., Braak, R., Bhartia, P. K., Veeffkind, P. and Levelt, P. (2007). Aerosols and surface UV products from Ozone Monitoring Instrument observations: An overview. *Journal of Geophysical Research: Atmospheres (1984–2012)*, 112(D24).

## **Toward better understanding of interannual rainfall variability over central Africa and its relation with its surrounding tropical Oceans.**

Georges-Noel T. Longandjo<sup>a, b</sup> and Mathieu Rouault<sup>a, b</sup>

<sup>a</sup>Nansen-Tutu Center for Environmental Marine Research, Rondebosch, South Africa

<sup>b</sup>Oceanography Department, University of Cape Town, South Africa

**Abstract** The main objectives of this paper are to advance our understanding of the relationships between central Africa rainfall and its surrounding tropical Ocean basins and to unravel how atmospheric circulation over central Africa respond to the inter-basin SST gradient ( $\Delta$ SST) between tropical Atlantic and Indian Oceans. Using observational and reanalysis datasets from the postsatellite era, we have shown that second leading variability mode (EOF2) of austral spring central Africa rainfall could be associated with  $\Delta$ SST, which in other hand, is well correlated to ENSO and IOD. The atmospheric circulation associated with  $\Delta$ SST is Gill-Matsuno type, but a strong anomalous cyclone pattern has been highlighted over southern Atlantic. Further, we found that the modification of Walker circulation anomalies and the associated atmospheric teleconnections might be triggered mainly by ENSO and thus, play an indirect key role in the distribution of rainfall over central Africa.

*Keywords:* Central Africa; Walker circulation; Sea surface temperature; Tropical Atlantic; Tropical Indian.

### ***Introduction***

Recent studies have found that central Africa rainfall is modulated by tropical Indian (Seidel et al. 2008; Washington et Preston et al. 2009) and tropical Atlantic Oceans (Pokam et al. 2011; Nicholson and Dezfuli, 2013; Dezfuli and Nicholson, 2013; Lutz et al, 2015). Longandjo and Rouault (2014) have argued that central Africa rainfall (7-32°E; 10°N-15°S) is also influenced by the inter-basin sea surface temperature (SST) gradient between tropical Atlantic and Indian Oceans. Nevertheless, the relationships between central Africa rainfall and its surrounding tropical ocean basins remain complex and seasonally dependent (Balas et al. 2007; Dezfuli and Nicholson, 2013). But it is still unclear how atmospheric circulation over central Africa responds to the inter-basin SST gradient between the both surrounding tropical Oceans. So the main objectives of this study are (i) to advance our understanding of the relationships between central Africa rainfall and its surrounding tropical ocean basins and (ii) to unravel how atmospheric circulation over central Africa respond to this inter-basin SST gradient.

### ***Datasets***

For this paper, we used monthly Global Precipitation Climatology Project (GPCP) version 2.2 (Huffman et al., 2009) and NOAA Optimum interpolated (OI) SST version 2.2 (Reynolds et al., 2002). In order to analyze atmospheric

circulations that link the inter-basin SST gradient with climate variability over Central Africa, horizontal wind, vertical velocities as well as the geopotential heights have been obtained from ERA-Interim reanalysis (Dee et al., 2011). Stream functions ( $\Psi$ ) and velocity potential ( $\Phi$ ) are calculated respectively at 200- hPa and 850- hPa in order to describe the Walker circulation over our area of interest. But because of the limited period covered by NOAA (OI) SST, we will focus on 1982 to 2013 period where reanalysis are also more reliable, unless otherwise stated. Monthly anomalies are departures from their respective mean values averaged over the study period. The monthly anomaly data are detrended linearly and averaged over the seasonal months to get the seasonal anomalies data. So, in this paper, all calculations are based on austral spring (September to November), unless explicitly noted.

### ***Results***

#### **a. Central Africa rainfall variability**

To capture the essential feature of central Africa rainfall variability, we apply empirical orthogonal functions (EOF) analysis to explore the spatio-temporal rainfall distribution. The first leading mode (EOF1, 18.68% of total variance) of rainfall anomaly is characterized by a quite homogeneous pattern over central Africa and depicted above normal conditions over central Africa (Fig. 1a).

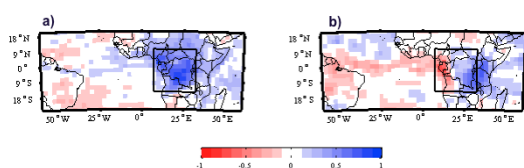


Figure 1: The first two leading modes of EOF analysis of central Africa rainfall (7-32E; 10N-15S) performing on GPCP data (Huffmann et al., 2008, 1979-2013). The patterns are regression coefficients between PCs and rainfall anomalies at each grid point. (a) EOF1 (18.68%) (b) EOF2 (11.50%). Black box in (a) and (b) delineates central Africa.

The second mode (EOF2, 11.50% of total variance) features an east-west dipole pattern that distinguishes two areas: the west central Africa (Atlantic coasts, 7°-15°E) and the east central Africa (15-32°E) over similar latitude (10°N-15°S) (Fig 1b). The Atlantic coast exhibits less rainfall that extends along the ITCZ in tropical Atlantic, whereas the east central Africa experienced above normal conditions. The rainfall indices have been extracted by area-averaging rainfall anomalies over central Africa (7°-32°E), Atlantic coasts (7°-15°E) and eastern (15°-32°E) part of central Africa over similar latitudes (10°N-15°S) (cfr box in Fig. 1). We have noticed the positive trend of rainfall over eastern central Africa while over Atlantic Coasts there is no significant trend. Figure 2 shows the teleconnections between the first two principal components of central Africa rainfall and the adjacent tropical SST anomalies. We found that for PC2 (Fig. 2b), over tropical Atlantic, the SST correlation pattern resembles to the Atlantic zonal mode (Keenlyside and Latif, 2007; Lübbecke et al., 2010; Burls et al., 2012) while over Indian Ocean, the pattern is a reminiscent of IOD (Saji et al, 1999), which exhibit the SST gradient between tropical Atlantic and Indian Oceans. Thus, we have defined the inter-basin SST gradient index ( $\Delta$ SST) as the difference of detrended normalized SST anomalies averaged over tropical Atlantic (tropical Atlantic index, 20°W-10°E, 6°N-6°S) and over western tropical Indian (western tropical Indian index, 45°-80°E, 5°N-15°S) (Cfr. Fig 2b).

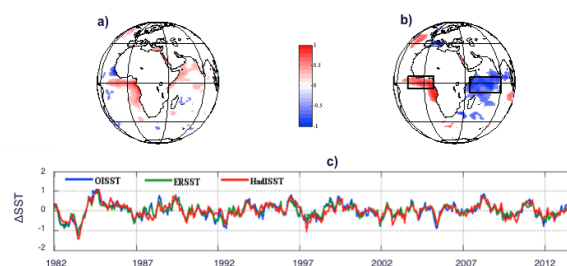


Figure 2: Simultaneous correlation between principal components (PC) of the two first leading modes of central Africa rainfall (7-32E; 10N-15S) performing on GPCP data and NOAA OI SST anomalies (1982-2013). From left to right: (a) PC1; (b) PC2; (c)  $\Delta$ SST (the inter-basin SST gradient time series, 1982-2013). Only correlation coefficients exceeding 95% confidence level based on student-t test ( $\sim 0.24$ ) are displayed. In (c) blue, green and red lines represent respectively, NOAA OI SST (Reynolds et al, 2002), Extended Reconstructed Sea Surface Temperature (ERSST, Smith et al. 2008) and Hadley Centre's sea ice and SST (HadISST1, Rayner et al. 2003). The black boxes in (b) delineate regions where  $\Delta$ SST has been defined. Correlation between OISST and ERSST (HadISST) is 98.22% (96.45%).

Therefore, in relation to the observed correlations, east central Africa rainfall decreased with  $\Delta$ SST (-0.35) and increased with tropical Indian (0.34) and IOD (0.28). No significant correlations have been found between central Africa and Atlantic coast rainfall anomalies with remote (ENSO, IOD) or local (tropical Atlantic and Indian and  $\Delta$ SST) teleconnections. These findings suggest that  $\Delta$ SST could play more important role than any remote or local teleconnections in modulating central Africa rainfall.

#### **b. Atmospheric circulations anomalies associated with $\Delta$ SST**

To highlight the atmospheric circulation associated with  $\Delta$ SST, adjacent Oceans and major climate modes (ENSO and IOD), we have investigated the changes in Walker circulation over central Africa through the anomalies of stream functions and velocity potential in lower- and upper- troposphere (not shown). Nevertheless, the tropospheric responses to oceanic variables have shown that the divergence (convergence) in lower troposphere corresponds relatively to convergence

(divergence) in upper troposphere. The sequential evolution of the atmospheric teleconnections at 850- hPa is illustrated in Figure 3. We have to notice that cyclonic (anticyclonic) features describe anticyclonic (cyclonic) anomalies over central Africa. Thus at low-level, the cyclonic anomalies prevailed over tropics for Atlantic SST anomaly and  $\Delta$ SST, while anomalous anticyclonic flow dominate for Indian SST anomaly, ENSO and IOD.

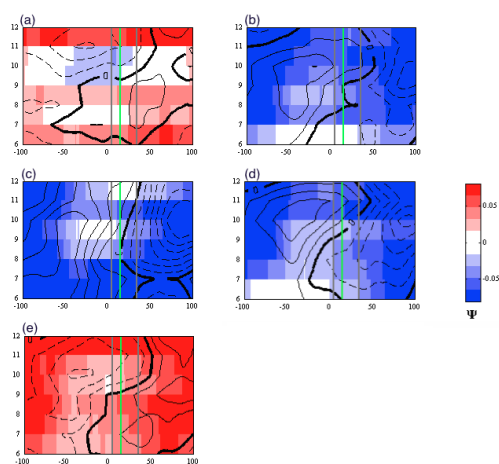


Figure 3: Lagged regressions of austral spring (SON) oceanic variables and sliding 3-month- averaged on  $10^{\circ}\text{N}$ – $15^{\circ}\text{S}$  of stream functions ( $\Psi$ , shaded. Unit:  $\text{m}^2\text{s}^{-1}$ ) and velocity potential ( $\Phi$ , contours. Unit:  $\text{m}^2\text{s}^{-1}$ ) anomalies: (a) tropical Atlantic index, (b) tropical Indian index, (c) Nino3 SST index, (d) DMI and (e)  $\Delta$ SST from June to February. Contour interval is  $5 \times 10^{-6} \text{m}^2\text{s}^{-1}$ . Solid (dashed) contours indicate positive (negative) values. The thick black contours represent the zero line. The Nino3 SST index is extracted by area averaging SST anomalies over ( $5^{\circ}\text{N}$ – $5^{\circ}\text{S}$ ,  $90^{\circ}$ – $150^{\circ}\text{W}$ ) in equatorial Pacific (Trenberth, 1997) and the dipole mode index (DMI) was calculated as difference between SST anomalies in the western ( $10^{\circ}\text{N}$ – $10^{\circ}\text{S}$ ,  $50^{\circ}$ – $70^{\circ}\text{E}$ ) and eastern ( $0$ – $10^{\circ}\text{S}$ ,  $90$ – $110^{\circ}\text{E}$ ) tropical Indian Ocean (Saji et al., 1999). The gray lines delineates central Africa and the green line is located at  $15^{\circ}\text{E}$ .

For Atlantic SST anomaly (Fig. 3a), the anomalous convergence flow is predominant over tropical Pacific, Amazon and tropical Atlantic from June to October, while over tropical Indian the flow remains convergent during all seasons. But from spring (SON) and for 2 months, the shrinking of convergence cell over tropical Atlantic and Atlantic coasts, allowed a build up of anomalous anticyclonic and divergence cell. On the other side, for ENSO, the anomalous convergence flow is predominant over central Africa, except from July to January over east central Africa where the anomalous flow is divergent while over Atlantic coasts, the flow remained convergent. These seasons are

characterized by an atmospheric bump that reached the western boundary of east central Africa ( $\sim 15^{\circ}\text{E}$ ) in SON – when ENSO is highly correlated with IOD (Fig. 3c). Whereas For IOD and Indian SST anomaly, the patterns are similar so that the anomalous flow is divergent over central Africa before JAS for Indian SST anomaly and SON for IOD, but the intensification of convergence cell swept Atlantic coasts region for respectively two months or one month before the east central Africa (Fig. 3b and d). For  $\Delta$ SST (Fig. 3e), an anomalous convergence is predominant in the austral winter (JJA) over central Africa, but 3months later (in SON and onward), the divergence branch cell stirs eastward from tropical Atlantic coasts ( $\sim 7^{\circ}\text{E}$ ) to western tropical Indian ( $\sim 50^{\circ}\text{E}$ ), when the IOD peaks, meanwhile the anomalous motion remained cyclonic over central Africa.

### Discussion and conclusions

The main objectives of this paper were to shed more light to the relation between central Africa rainfall and its adjacent Ocean basins and to unravel how atmospheric circulation over central Africa responds to  $\Delta$ SST. Using observational and reanalysis datasets, we have characterized various features of the austral spring rainfall anomalies by EOF analysis. The first leading mode (EOF1) is characterized by a homogeneous pattern over central Africa whereas the second mode (EOF2) features an east-west dipole pattern that distinguishes two areas: West central Africa (or Atlantic coasts,  $7^{\circ}$ – $15^{\circ}\text{E}$ ) and Eastern central Africa ( $15^{\circ}$ – $32^{\circ}\text{E}$ ) over similar latitude ( $10^{\circ}\text{N}$ – $15^{\circ}\text{S}$ ). We have noticed a positive trend of rainfall over Eastern central Africa since 1979 while over Atlantic Coasts there is no significant trend. Also, we have shown that  $\Delta$ SST play a key role in modulating central Africa rainfall and it induces at low-level zonal wind anomalies that link the two surrounding Oceans. The intensification of divergence cell associated with  $\Delta$ SST (Fig. 3e) is occurred during spring when the IOD matures and strongly correlates with ENSO, so that it propagates eastward but remains confined around  $50^{\circ}\text{E}$  two months later (Fig. 3e). However, the atmospheric circulation associated with  $\Delta$ SST can be explained by a Gill-Matsuno mechanism – consistent with Kurcharski et al. (2008; 2009) and Barimalala et al. (2012) – but we have also

highlighted a strong anomalous cyclone over southern Atlantic. Significant negative correlations have been found between  $\Delta$ SST and IOD (0.54) and ENSO (0.65). These findings suggest the modification of Walker circulation anomalies and the associated atmospheric teleconnections over central Africa might be triggered mainly by ENSO.

#### Acknowledgements

ERA-Interim reanalysis data were obtained from ECMWF through their website at <http://ecmwf.int/>. NOAA OI v2 SSTs data are provided by the NOAA CIRES Climate Diagnostics Center, Boulder, Colorado, from their web site (available online at <http://www.cdc.noaa.gov>). The first author would like to acknowledge the AfDB/ISACIP Project through SADC-CSC that partly supported his work. The research leading to these results received funding from EU FP7/2007-2013 under grant agreement no. 603521.

#### References

- Balas N, Nicholson SE, Klotter D. 2007. The relationship of rainfall variability in West Central Africa to sea-surface temperature fluctuations. *Int. J. Climatol.* **27**: 1335-1349.
- Barimalala R., Bracco, A. and Kucharski, F. (2012), The representation of the South Tropical Atlantic teleconnection to the Indian Ocean in AR5 coupled models, *Clim Dyn*, doi:10.1007/s00382-011-1082-5.
- Burls, N. J., C. J. C. Reason, P. Penven, and S. G. Philander (2012), Energetics of the tropical Atlantic zonal mode, *J. Clim.* **25**(21), 7442–7466.
- Dezfuli, A. K., and S. E. Nicholson, 2013: The relationship of interannual variability in western equatorial Africa to the tropical oceans and atmospheric circulation. Part II: The boreal autumn. *J.Clim.*, *26*, 66–84
- Dee D, Uppala S, Simmons A, Berrisford P, Poli P, Kobayashi S, Andrae U, Balsamada M, Balsamo G, Bauer P (2011) The ERA-Interim reanalysis: configuration and performance of the data assimilation system. *Q.J.R.M.S.* **137**(656): 553–597
- Huffman, G. J., R. F. Adler, D. T. Bolvin, and G. Gu, 2009: Improving the global precipitation record: GPCP version 2.2. *Geophys. Res. Lett.* **36** (17).
- Keenlyside, N. S., and M. Latif (2007): Understanding equatorial Atlantic interannual variability, *J. Clim.*, *20*(1), 131–142.
- Kucharski, F. Bracco, A., Yoo, J. H., Tompkins, A., Feudale, L., Ruti, P., Dell'Aquila, A., (2009): A Gill-Matsun-type mechanism explains the Tropical Atlantic influence on African and Indian Monsoon Rainfall. *Q.J.R.M.S.*, *135*, 569-579.
- Kucharski, F., Bracco, A., Yoo, J. H., Molteni, F. (2008): Atlantic forced component of the Indian monsoon interannual variability. *Geophys. Res. Lett.*, *35*, L04706, doi:10.1029/2007GL033037.
- Longandjo G-NT and Rouault M. 2014: The annual cycle of Central Africa rainfall and its relationship with the surrounding tropical oceans. *Proc. of 30th Annual Conf. of SASAS 01-02 October 2014, Potchefstroom, SA*. ISBN 978-0-620-62777-1
- Lübbecke, J. F., C. W. Böning, N. S. Keenlyside, and S.-P. Xie (2010), On the connection between Benguela and equatorial Atlantic Niños and the role of the South Atlantic anticyclone, *J. Geophys. Res.*, *115*, C09015.
- Lutz K., Jacobeit J., Rathman J. 2014: Atlantic warm and cold water events and impact on African west coast precipitation. *Int. J. Climatol.* *35*: 128–141 (2015). doi: 10.1002/joc.3969.
- Nicholson S. E., and A. K. Dezfuli, 2013: The relationship of interannual variability in western equatorial Africa to the tropical oceans and atmospheric circulation. Part I: The boreal spring. *J. Clim.*, *26*, 45–65
- Pokam WM, Djotang LAT, Mkankam FK. (2011) Atmospheric water vapor transport and recycling in equatorial Central Africa through NCEP/NCAR reanalysis data. *Clim. Dyn.* **38**, 1715– 1729.
- Rayner, N. A., D. E. Parker, E. B. Horton, C. K. Folland, L. V. Alexander, D. P. Rowell, E. C. Kent, and A. Kaplan (2003), Global analyses of sea surface temperature, sea ice, and night marine air temperature since the late nineteenth century, *J. Geophys. Res.*, **108**(D14), 4407.
- Reynolds, R. W., N. A. Rayner, T. M. Smith, D. C. Stokes, and W. Wang (2002), An improved in situ and satellite SST analysis for climate, *J.Clim.* **15**, 1609– 1625
- Saji, N. H., B. N. Goswami, P. N. Vinayachandran, and T. Yamagata (1999), A dipole mode in the tropical Indian Ocean, *Nature*, **401**(6751), 360–382.
- Smith, T.M., Reynolds, R.W., Peterson, T.C., Lawrimore, J., 2008. Improvements to NOAA's historical merged land–ocean surface temperature analysis (1880–2006). *J. Clim.* **21** (10), 2283–2296.

## ***Downscaled climate change projections over northeastern South Africa: Implications for streamflow***

Musa Mkhwanazi<sup>1</sup>, Willem A. Landman<sup>2,3</sup>, Francois A. Engelbrecht<sup>2</sup>, Cobus Olivier<sup>1</sup>

<sup>1</sup>South African Weather Service, Pretoria, South Africa

<sup>2</sup>Council for Scientific and Industrial Research, Pretoria, South Africa

<sup>3</sup>Department of Geography, Geoinformatics and Meteorology, University of Pretoria, Pretoria, South Africa.

### ***Abstract***

The study assesses the impacts of anthropogenic forcing on seasonal streamflows over northeastern South Africa by using both dynamically and statistically downscaled multi-decadal climate change projections. The statistical model approach is to build linear links between observed present-day climate of flows and mid-tropospheric atmospheric circulation and then use the developed relationships to provide guidance on future-climate streamflows. Both CCAM raw runoff (as a proxy for streamflows) and statistically downscaled streamflows indicate a decreasing trend over northeastern South Africa. Statistical analysis on simulated data is done based on four 30-year periods (1981-2010, 2011-2040, 2041-2070, 2071-2100) from which parametric distributions are calculated and interpreted.

Key words: Streamflow, Perfect prognosis, Climate change, Statistical downscaling

### **1. Introduction**

Climate change impacts on a number of human and natural systems. One of the most fundamental sectors impacted by climate change is water resources. Water in turn has an impact on several systems such as human health, agriculture and biodiversity. A comprehensive assessment and understanding of the long-term impacts of climate change on water resources is therefore vital. This information, if applied in planning processes and decision making can potentially minimize the adverse impacts of climate change on several interlinked sectors. The observed changing climate over southern Africa (Hughes and Balling 1996; Kruger and Shongwe 2004; New et al. 2006; Kruger 2006) continues to raise concerns on the future climate change and impacts over the region.

### **2. Data and method**

The study makes use of the six-hourly output from a Regional Climate Model (RCM) run at a resolution of about 0.5° x 0.5° lon/lat, covering both historical (1979-2010) and future periods (up to 2100). Observed streamflow data obtained from the Department of Water and Sanitation's Hydrological Information System (HIS), are for the Limpopo Water Management Area (WMA), Olifants WMA, Levuvhu/Letaba WMA and Inkomati WMA. The RCM used in this study is the conformal-cubic atmospheric model (CCAM), whose simulations are available at a C64 stretched

grid (approximately 60km) within South Africa and has 18 vertical levels. From the CCAM simulations, 500 hPa geopotential height fields are used. Both control (driven by the NCEP-based CCAM reanalysis) and future (forced using the CMIP4 GCMs) simulations are considered. The control run of the CCAM is performed by applying a multiple-nudging approach with low-resolution NCEP reanalysis data as the boundary forcing in order to produce "reanalysis" data at a resolution of about 60 km over southern Africa. The runs forced with the CMIP4 data are produced over the period 1951 to 2100, subsequently creating an ensemble of 6 projections. More details on the CCAM RCM configuration can be obtained from Engelbrecht et al. (2011). Additional RCM output for some of the aforementioned climate variables may be obtained for the Coordinated Regional Downscaling Experiment (CORDEX) data (Nikulin et al. 2012).

The approach is to first identify the high flow season over the area and then to assess the potential climate change impact on these flows. The peak season of streamflow over the area is identified as January-February-March (JFM) as shown in Fig. 1.

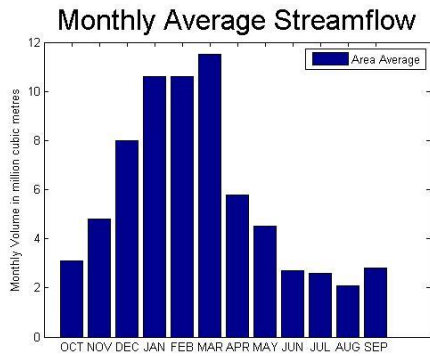


Figure 1: Monthly average streamflow data for northeastern South Africa (observed data from 31 stations)

After identifying JFM as the peak season for streamflow over the area model output statistics (MOS; Wilks 2011) is applied to estimate the statistical relationship between climate model simulations and the observed streamflow through a perfect prognosis approach (Landman and Goddard 2005). The perfect prognosis equations are created by canonical correlation analysis (CCA) of the Climate Predictability Tool (CPT). These statistical equations are developed for the JFM season, and the sets of equations form the basis for the statistical downscaled climate change projections (Landman et al 2013). The downscaling is done by first using CCAM Reanalysis for the 500 hPa as the predictor and station streamflow data as the predictand. This statistical model’s validation is performed to test model skill and hindcast analysis (Fig. 2) to further test the developed statistical relationship.

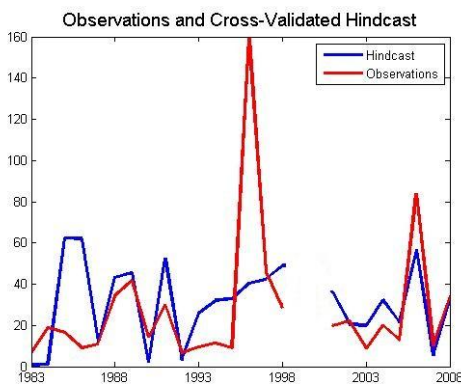


Figure 2: Observations and cross-validated hindcast, area average for northeastern South Africa.

CCAM multi-decadal projections from six climate models (CSIRO, GFDL20, GFDL21, MIROC, MPI & UKMO) are available from 1961 to 2100. These

projections are then included into the statistical developed equations for downscaling. The downscaled data is then compared with CCAM raw model data to test if datasets are showing similar trends (Figs. 3 and 4). After verification, outputs are produced and data are analysed based on four periods namely; Present Day Climate (PDC) 1981-2010, Climate Change period 1 (CC1) 2011-2040, Climate Change period 2 (CC2) 2041-2070 and Climate Change period 3 (CC3) 2071-2100. The output is analysed and the analysis is based on area averages.

### 3. Results and Discussion

The statistically downscaled streamflow data shows a similar decreasing trend as the CCAM raw runoff trend (Figs 3 & 4). Rainfall is the main driver of streamflow over the area and the decreasing trends are in line with projected decreases of rainfall over the some parts of the sub-continent (Niang et al. 2014).

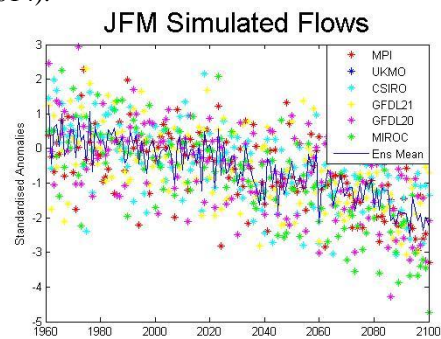


Figure 3: Area-averaged perfect prognosis stream flow from six models and ensemble mean for JFM (standardised anomalies).

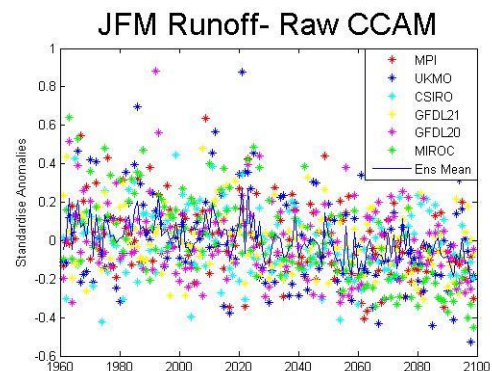


Figure 4: Area-averaged raw CCAM runoff from six models and ensemble mean for JFM (standardised anomalies).

Four theoretical distributions are fitted to the statistically downscaled data and they are the Gamma, Lognormal, Normal and Weibull distributions (Fig 5). These distributions are often used for analyzing rainfall and are subsequently developed here for streamflow. Negative log-likelihood estimates as well as the Kolmogorov-Smirnov test have found these distributions to adequately represent the statistically downscaled flows. All four distributions are subsequently fitted to the projected flows and all of them shift to the left for subsequently 30-year periods into the future (Fig 5).

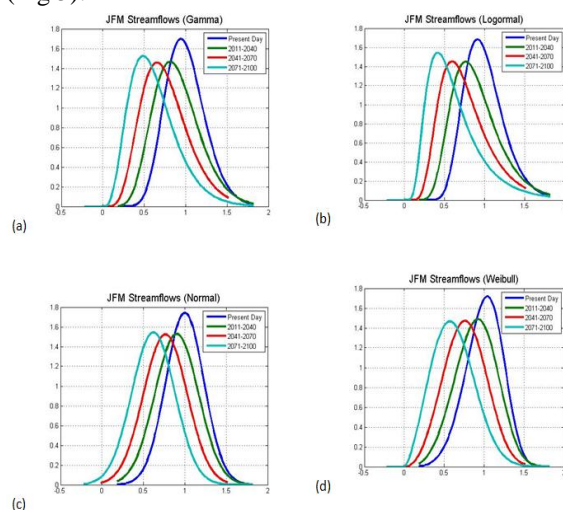


Figure 5: Gamma (a), Lognormal (b), Normal (c) & Weibull (d) Distributions for period 1981-2010, 2011-2040, 2041-2070 & 2071-2100.

#### 4. Conclusion

The statistical downscaling procedure described here has been successfully applied in simulating streamflow by using mid-tropospheric atmospheric circulation as predictor in a perfect prognosis model. Both CCAM raw runoff and statistically downscaled streamflows indicate a decreasing trend over northeastern South Africa. The projected decreasing flows are in line with the expected consequence of projected decreases in rainfall over the catchment. Although rainfall is the main influence on streamflow, there are other factors such as ground water levels and the geology of the area, to name but two factors, which might affect the direct relationship between rainfall and streamflow. Such factors may have to be included for future downscaling studies.

#### 5. References

- Engelbrecht, F.A., Landman, W.A., Engelbrecht, C.J., Landman, S., Bopape, M.M., Roux, B., McGregor, J.L. and Thatcher, M. (2011). Multi-scale climate modelling over Southern Africa using a variable-resolution global model. *Water S.A.*, **37**, 647-658
- Hughes, W.S. and Balling, R.C. (1996). Urban influences on South African temperature trends. *Int. J. Climatol.* **16**: 935-940
- Kruger, A. C. and Shongwe, S. (2004). Temperature trends in South Africa: 1960-2003. *Int. J. Climatol.* **24**: 1929-1945
- Kruger, A. C. (1999). The influence of the decadal-scale variability of summer rainfall on the impact of El Niño and La Niña events in South Africa. *Int. J. Climatol.* **19**: 59-68.
- Landman, W.A, Engelbrecht, F.A, Malherbe, J and Van der Merwe, J. (2013). Statistical downscaling of multi-decadal climate change projections: Bridging the gap between climate models and the end-user. In: 29th Annual Conference of South African Society for Atmospheric Sciences, Durban, South Africa, 26-27 September 2013
- Landman W.A. and Goddard L. (2005). Predicting Southern African summer rainfall using a combination of MOS and perfect prognosis. *Geophysical Research Letters* **32**: L15809, DOI:10.1029/2005GL022910.
- New, M., Hewitson, B., Stephenson, D.B., Tsiga, A., Kruger, A., Manhique, A., Gomez, B., Coelho, C.A.S., Masisi, D.N., Kululanga, E., Mbambalala, E., Adensina, F., Saleh, H., Kanyanga, j., Adosi, J., Bulane, L., Fortunate, L., Mdoka, M.L. and Lajoie, R. (2006). Evidence of trends in daily climate extremes over southern and west Africa, *J. Geophys. Res.*, **111**, D14102, doi: 1029/2005JD006289.
- Niang, I., Ruppel, O.C., Abdrabo, M.A., Essel, A., Lennard, C., Padgham, J., and Urquhart, P. (2014). Africa. In: *Climate Change 2014: Impacts, Adaptation, and Vulnerability. Part B: Regional Aspects. Contribution of Working Group II to the Fifth Assessment Report of the Intergovernmental Panel on Climate Change* [Barros, V.R., Field, C.B., Dokken, D.J., Mastrandrea, M.D., Mach, K.J., Bilir, T.E., Chatterjee, M., Ebi, K.L., Estrada, Y.O., Genova, R.C., Girma, B., Kissel, E.S., Levy, A.N., MacCracken, S., Mastrandrea, P.R., and White L.L. (eds.)]. *Cambridge University Press*, Cambridge, United Kingdom and New York, NY, USA, pp. 1199-1265.
- Nikulin, G., Jones, C., Samuelsson, P., Giorgi, F.,

- Sylla, M. B., Asrar, G., B"uchner, M., Cerezo-Mota, R., Christensen, O. B., D'equ' e, M., Fernandez, J., H"ansler, A., van Meijgaard, E., and Sushama, L. (2012): Precipitation Climatology in An Ensemble of CORDEX-Africa Regional Climate Simulations, *J. Climate*, **25**, 6057-6078
- Wilks, D. S. (2011). *Statistical Methods in the Atmospheric Sciences*, Third Edition, International Geophysics Series. Elsevier Academic Press. Oxford, UK

## Predictability of synoptic types over southern Africa

Isaac Ngwana<sup>1</sup>, Francois Engelbrecht<sup>2,3</sup> and Christien Engelbrecht<sup>4</sup>

<sup>1</sup> South African Weather Service, 442 Rigel South Avenue, Erasmus rand, 1882

<sup>2</sup> CSIR Natural Resources and the Environment – Climate Studies, Modelling and Environmental Health, Pretoria, South Africa

<sup>3</sup>School of Geography, Archaeology & Environmental Studies, University of the Witwatersrand, Johannesburg, South Africa

4. Institute for Soil, Climate and Water, Agricultural Research Council, Pretoria, South Africa

### Abstract

Synoptic weather types over South Africa are clustered using a Self-Organizing Maps (SOMs). The clustering is obtained using daily NCEP reanalysis data of geopotential heights at 850 hPa, for the period 1979-2014. Predictability of the prevailing synoptic types that occurred over South Africa during the period 2006-2014 are analysed, using short-range weather forecasts obtained from the Unified Model (UM). The 24-hr and 48-hr forecasts of 850 hPa geopotential heights are verified against observations. Preliminary results show that large-scale anti-cyclonic circulation is more predictable than large-scale cyclonic circulation.

Key words: Unified Model, Predictability, Tropical Temperate Troughs, Self-Organizing Maps

### INTRODUCTION

Weather hazards pose threats to socioeconomic development worldwide and southern Africa is one of the regions that are highly negatively affected. Knowledge of forthcoming weather conditions well ahead of time enables communities to minimise the impacts of weather hazards and is useful to the public, construction companies, farming activities, sports, manufacturing industries, mining and commercial operations. Most meteorological centres are vested with the responsibility to minimize the adversity associated with weather and climatic variations by providing weather forecast to the public and clients. As a result, weather forecasts issued by designated institutions should be skilful and accurate, if possible at temporal scales of several days, weeks or months ahead. However, this is not entirely possible due to the chaotic nature of the atmosphere, limited and erroneous atmospheric observations, and limitations in Numerical Weather Prediction (NWP) models which are used to produce weather forecasts.

The extent of weather forecast or prediction accuracy varies according to the weather type, variables to be predicted and spatial locations affected by the weather type. For example, large-scale well-resolved (by models) winter weather systems in the southern hemisphere are generally more predictable than smaller length-scale systems in the tropics during summer.

Predictability of weather systems have been extensively studied. However there is still a gap to objectively understand the predictability of weather systems that occur in southern Africa. Synoptic types that normally dominate weather in southern Africa are subtropical high-pressure systems, tropical cyclones, cut-off lows, midlatitude cyclones and tropical-temperate

troughs. The relative predictability of these systems have not been quantified as yet over southern Africa. Consequently, this study aims to objectively identify the prevailing synoptic weather types that dominate circulation over southern Africa during the summer half-year. This is the season during which the country receives the bulk of its annual rainfall. The value of this research is in the objective quantification of the predictability of a large range of synoptic types.

### DATA AND METHODS

#### *Observed data (NCEP)*

Self-Organizing Maps (SOMs) software is used to identify or cluster 35 (7x5) nodes from 850 hPa 00Z geopotential fields (Figure 1), obtained from National Centers for Environmental Prediction /National Center for Atmospheric Research (NCEP/NCAR) reanalysis fields (Kalnay et al., 1996) for the period 1979-2014. These 35 nodes provide an objective description of the frequency of occurrence of synoptic weather types that are dominant over southern Africa during the summer half-year. Synoptic weather systems that occurred prior to 1979 have been excluded from the analysis because before that period, observations in our area of interest were poor and had adverse effect on the quality of the data (Tennant, 2004). The NCEP/NCAR reanalysis data are available on a horizontal latitude-longitude grid of 2.5° x 2.5° resolution. This is adequate for the identification of synoptic-scale systems.

#### *Unified Model (UM) forecast data*

The Unified Model (UM) of the United Kingdom (UK) Met Office has been used by the South African Weather Service (SAWS) since 2006, to forecast weather systems over southern Africa. The UM is the name given to the suite of numerical modelling software developed

and used at the Met Office. It is a seamless modelling system that can be used for the prediction of atmospheric evolution across a wide range of timescales, and is applied in regional model mode at SAWS. The UM, from version 5.2 onwards, solves the non-hydrostatic deep-atmosphere equations using a semi-implicit, semi-Lagrangian numerical scheme (Lean et al, 2008).

At SAWS, the UM is configured to run at a horizontal resolution of 12 km and the domain covers the southern part of Africa (45° S to 0° and 10° W to 55° E). It is initialised at 00Z SAST to produce a two-day forecast. Forecast data from the period 2006/2007 to 2014/15 is used in this research.

### Self-Organizing Maps (SOM)

SOMs are used to cluster the prevailing synoptic weather patterns objectively. The SOM is a technique for pattern recognition in large datasets and is becoming increasingly important as datasets grow in size and complexity (Kohonen, 2001). When applied to meteorological data (e.g. Engelbrecht et al, 2014), it can identify weather patterns and categorise them. The technique is well suited for weather pattern identification where the daily transitions between weather patterns are important (Hewitson and Crane 2002). SOMs are increasingly being employed in atmospheric studies (Tennant and Hewitson 2002; Engelbrecht et al, 2014). The technique is based on a non-human intervention nonlinear clustering algorithm that organizes the input data into a user-specified number of nodes that span the range of the input data.

Each daily synoptic analysis field obtained from the UM forecast is mapped to one of the nodes obtained from the NCEP/NCAR derived SOM. The pattern correlation between the UM analysis field and the synoptic types are used for this purpose.

#### Predictability of synoptic types

The model forecast skill associated with each node is determined using by calculating the Root Mean Square Error (RMSE), Brier Skill Score (BSS) and Pattern Correlation between the 24-hr and 48-hr forecast fields associated with each node, and the corresponding observed fields (from NCEP reanalysis data). We subsequently calculate the median of these scores obtained for each synoptic type, thereby quantifying the relative predictability of each type.

## 3. RESULTS AND DISCUSSION

Figure 1 shows 35 identified weather patterns (nodes) for the 1979-2014 summer half-years, as determined by the SOM. From the identified nodes, the dominating weather patterns are extra-tropical troughs, TTTs, ridging high-pressure systems from the Atlantic and Indian Oceans and tropical weather systems. The verifications performed

quantify objectively that the high-pressure systems dominating over the region are more predictable than any other synoptic weather type. Final results are expected to quantify the relative degree of predictability of each identified synoptic weather type.

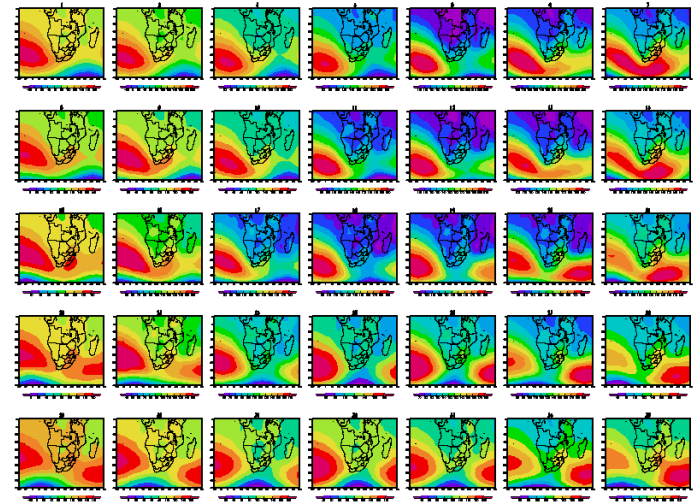


**Figure 1: Prevailing weather patterns over southern Africa for the summer half-year over the period 1979-2014.**

The skill of the model deteriorates as the forecast lead time increases, however, the forecasts remain skilful over 24-hr persistence forecasts.

## 4. ACKNOWLEDGEMENTS

The study is supported by the Applied Centre for Climate and Earth System Science (ACCESS), CSIR South Africa and South African Weather Service, 442 Rigel South Avenue, Erasmus rand, 1882

## 5. REFERENCES

- D'Abreton PC, Tyson PD. (1995). Divergent and non-divergent water vapour transport over southern Africa during wet and dry conditions. *Meteorology and Atmospheric Physics* **55**: 47–59.
- Engelbrecht CJ, Landman WA, Engelbrecht FA, and Malherbe J. (2014). A synoptic decomposition of rainfall over the Cape south coast of South Africa: *Clim. Dyn.* **44**: 2589-2602
- Engelbrecht CJ, Engelbrecht FA, Dyson LL. (2013). High-resolution model-projected changes in mid-tropospheric closed-lows and extreme rainfall events over southern Africa. *Int J Climatol* **33**:173–187
- Engelbrecht FA, Rautenbach CJdeW, McGregor JL, Katzfey JJ. (2002). January and July climate simulations over the SADC region using the limited-area model DARLAM. *Water SA* **28**: 361–374.
- Harrison MSJ. (1984). A generalized classification of South African summer rain-bearing synoptic systems. *J. of Climatol.* **4**:547–560.

Hewitson, B. C., and R. G. Crane. (2002). Self-organizing maps: Applications to synoptic climatology. *Climate Res.* **22**, 13–26

Kalnay E, Kanamitsu M, Kistler R, Collins W, Deaven D, Gandin L, Iredell M, Saha S, White G, Woolen J, Zhu Y, Chelliah M, Ebisuzaki W, Higgins W, Janowiak J, Mo KC, Ropelewski C, Wang J, Leetma A, Reynolds R, Jenne R, Joseph D. (1996). The NCEP/NCAR reanalysis 40 year project. *Bulletin of the American Meteorological Society.* **77**: 437–471.

Kohonen T. (2001). *Self Organizing Maps*, Third Edition. Springer

Lean HW, Clark PA, Dixon M, Roberts MN, Fitch A, Forbes R, and Falliwell C. (2008). Characteristics of High-Resolution Versions of the Met Office Unified Model for Forecasting Convection over the United Kingdom. *Mon. Wea. Rev. Vol.* **136**: 3408 -3424

Lyon B and Mason SJ. (2009). The 1997/98 Summer Rainfall Season in Southern Africa. Part II: Model Simulations and Coupled Model Forecasts. *J. Climate*, **22**, 3802–3818.

Reason CJC, Landman W., Tennant W. (2004). Seasonal to Decadal Prediction of Southern African Climate and Its Links with Variability of the Atlantic Ocean. *Amer. Met. Soc.* 941-955

Tennant, W.J. and C.J.C. Reason, (2005) Associations between the Global Energy Cycle and Regional Rainfall in South Africa and Southwest Australia. *J. Clim. Vol.* **18**, 3032 -3047.

Tyson PD. (1986). *Climate Change and Variability in Southern Africa*. Oxford University Press: Cape Town; 220. Walsh K, McGregor JL. 1995. January and July

Shingeo, O., (2007). Atmospheric Predictability. *J. Met. Soc. of Japan*, Vol. 85B, 77-102

Tennant WJ, Hewitson BC. (2002). Intra-seasonal rainfall characteristics and their importance to the seasonal prediction problem. *Int J Climatol* **22**:1033–1048

Vigaud, N., Pohl B. and Cre´tat J. (2012). Tropical-temperate interactions over Southern Africa simulated by a regional climate model. *Clim Dyn* **39**, 2895–2916

Walker, N. D. (1990). Links between South African summer rainfall and temperature variability of the Agulhas and Benguela Current systems. *J. Geophys.Res.*, **95**, 3297–3319.

# Last Glacial Maximum simulations over southern Africa using a variable-resolution global model: synoptic-scale verification

R. Nkoana<sup>1,2</sup>, F.A. Engelbrecht<sup>1,3</sup> and <sup>2,4</sup> C.W. Marean

<sup>1</sup> Council for Scientific and Industrial Research, Climate Studies, Modelling and Environmental Health, Pretoria, South Africa

<sup>2</sup> Centre for Coastal Palaeosciences, Nelson Mandela Metropolitan University, South Africa

<sup>3</sup> Schools of Geography, Archaeology and Environmental Studies (GAES), University of the Witwatersrand, South Africa

<sup>4</sup> Institute of Human Origins, School of Human Evolution and Social Change Arizona State University, Tempe, USA

## Abstract

Reconstructing the glacial maximum climates of the Cape south coast region of South Africa is important within the context of understanding the evolution of modern humans in this region. Simulating the Last Glacial Maximum (LGM) climate was also a focal period of the Paleoclimate Intercomparison Project Phase 3 (PMIP3), in order to test the ability of climate models to produce realistic simulations under radiative forcings very different to today's. The purpose of this research is to reconstruct the paleoclimate of the Cape south coast region of South Africa using high resolution regional climate modelling. The model used for this purpose is a variable-resolution global atmospheric model, the conformal-cubic atmospheric model (CCAM), which has been developed by the Commonwealth Scientific and Industrial Research Organization (CSIRO) in Australia. An ensemble of LGM simulations was constructed, through the downscaling of PMIP3 coupled model simulations over southern Africa. A multiple nudging was performed, where CCAM was first integrated globally at a quasi-uniform resolution, with subsequent high-resolution downscaling to southern Africa. This paper describes the global CCAM simulations. The simulations provide new insights into the LGM climate over southern Africa, including evidence that winters during the LGM were significantly wetter than in the present-day climate.

Key words: Last Glacial Maximum, Cape south coast, regional climate model

## INTRODUCTION

This paper focuses on simulations of the Last Glacial Maximum (LGM) climate over southern Africa. The research forms part of a larger project SACP4 (South African Coastal Paleoclimate, Paleoenvironment, Paleoecology, and Paleoanthropology), which explores the paleoscape of the Cape south coast during the latter part of the Quaternary. This region is thought to be of primary importance within the context of the evolution of modern humans. More specifically, the cyclic changes in climate from glacial to interglacial periods is known to have caused dramatic shifts in regional species distributions over the millenia [e.g. Marean et al 2014]. However, there is evidence that early humans thrived along the Cape south coast, under both interglacial and glacial maximums. It is therefore critical to gain insight into the glacial maximum climate of the Cape south coast, to better understand the stresses and opportunities that early humans faced in this region during this critical period in the evolution of our species.

Our focus within the larger SACP4 project is to provide high-resolution simulations of LGM climate over the Cape south coast, which in turn involves the application of dynamic regional climate model (RCM).

The output of the model will be verified against the available paleoarchive evidence, and in a preceding step, the model simulations of the present-day Cape south coast climate are also verified against observations. It may be noted that simulating the LGM is a focal period of the Paleoclimate Intercomparison Project Phase 3 (PMIP3) of the World Climate Research Program (WCRP). PMIP3 provides us with the global simulations of LGM climate, which we need to force the regional simulations. It may be noted that simulating LGM climate is also important from the perspective of testing the ability of climate models to simulate climate under very different radiative forcings. For the LGM, we have relatively good constraints on the main forcing (solar radiative forcing and atmospheric greenhouse gas concentrations). On the other hand, there are limits to which proxy records can reveal information about the state of the climate system during the LGM. In fact, for some of the questions on paleo-climates that cannot be answered using proxy data alone, climate models may be extremely useful to reconstruct the climate of the period in question. The main objective of this paper is to report on simulations of the LGM climate of southern Africa, with the purpose of gaining new insights into the associated Southern Hemisphere circulation dynamics and surface climate of the Cape south coast.

**EXPERIMENTAL DESIGN**

The model used in this paper is the conformal-cubic atmospheric model (CCAM), a variable-resolution global model which has been developed by the Commonwealth Scientific and Industrial Research Organization (CSIRO) Marine and Atmospheric Research in Australia [McGregor, 2005]. To obtain high-resolution simulations over the Cape south coast, the model is first applied in quasi-uniform resolution globally and subsequently in stretched-grid mode over southern Africa. The model's ability to realistically simulate present-day southern African climate has been extensively demonstrated (e.g. Engelbrecht et al., 2009; Engelbrecht et al., 2011; Engelbrecht et al., 2013; Malherbe et al., 2013; Winsemius et al., 2014; Engelbrecht et al., 2015).

CCAM is used to perform LGM simulations forced by the sea-surface temperature (SST) and sea-ice concentration (SIC) simulations of six coupled global climate models (CGCMs) of PMIP3. The same sets of models are also used to drive CCAM simulations of present-day climate.

As illustrated in Fig.1, all simulations of present-day climate were obtained for the period 1979-2009. A multiple nudging strategy was followed in order to obtain 8 km resolution simulations of present-day climate over the Cape south coast in South Africa from the initial set of 200 km resolution global simulations. Similarly, 100 years long simulations of LGM climate were obtained, first at 200 km resolution and subsequently at 8 km resolution over southern Africa. In this paper, we present results from the first phase of the downscaling's, namely results from the first ensemble member of the 200 km resolution global simulations.

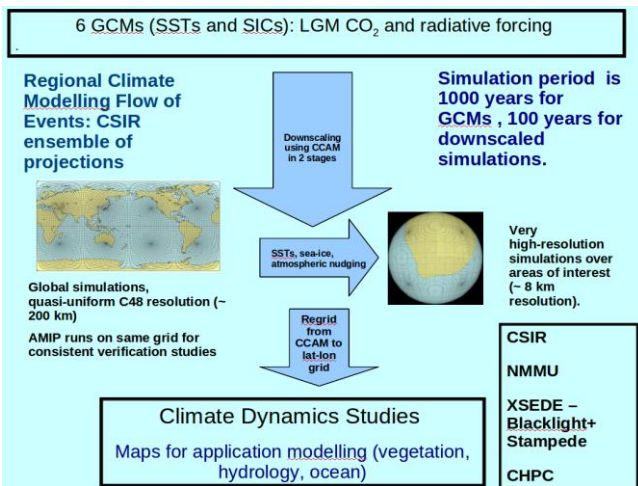
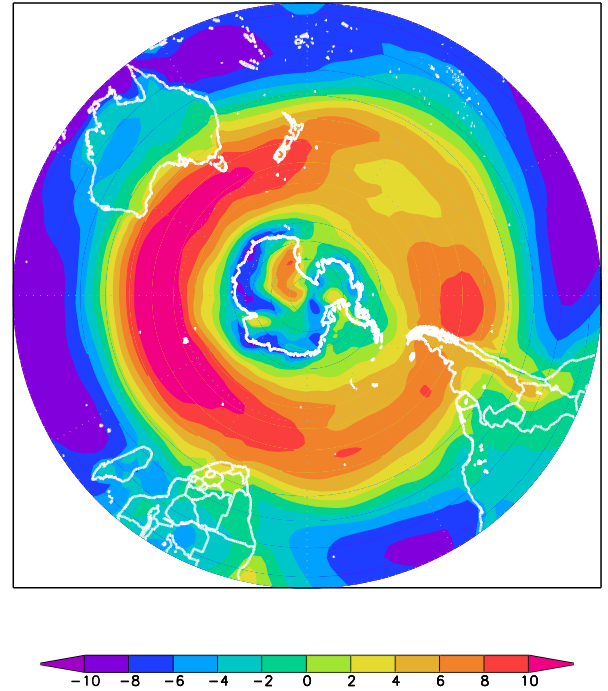


**Figure 1: Schematic representation of the experimental design of the paleo-climate simulations over southern Africa.**

**Model simulations of present-day climate**

A first requirement for confidence in a model projection of climate change is that the model should be able to adequately simulate the present-day climate, since the ability to predict past or future climate depends partly on the model's ability to simulate current climate.

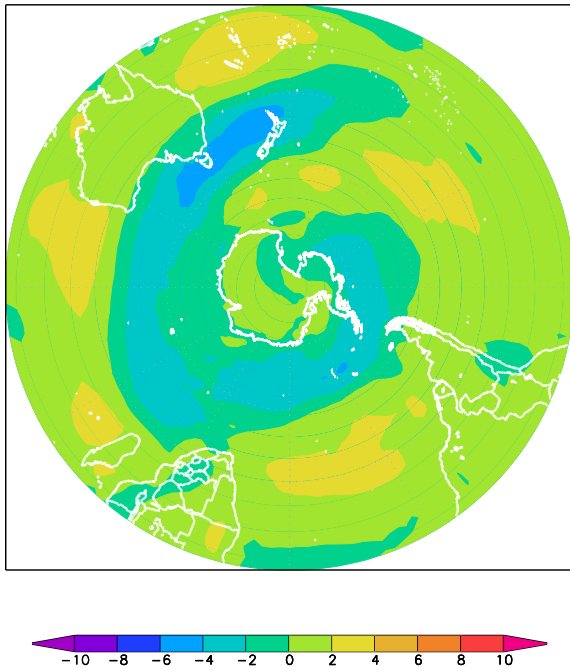
Fig 2 shows the simulated 1000 hPa zonal winds in the southern hemisphere for winter (June - August, JJA) during the period 1979-2009. The values illustrate that the westerlies reach well into southern Africa during the winter of the present-day climate.



**Figure 2: CCAM simulated 1000 hPa zonal winds for the period 1979-2009.**

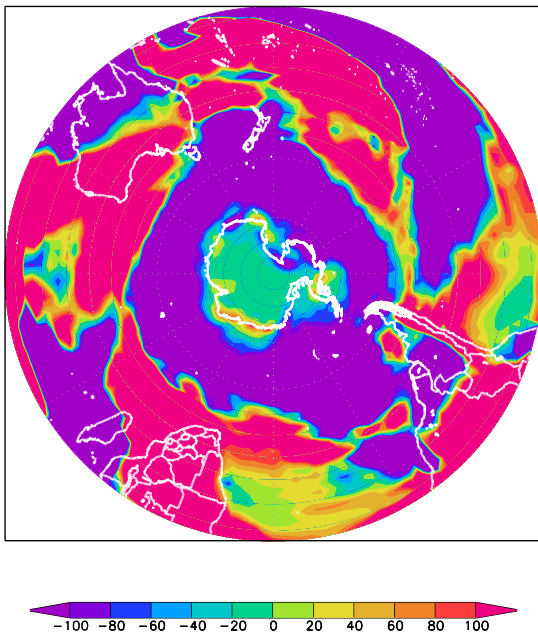
**Model simulations of Last Glacial Maximum climate**

Fig. 3 illustrates the changes projected by the model in the westerlies, for the LGM climate as compared to present-day climate. The results are indicative of a clear northwards shift in the westerlies. This would imply more frontal systems reaching the Cape south coast, in association with increased rainfall and a generally cooler climate.



**Figure 3: CCAM simulated 1000 hPa zonal-wind anomalies, for the LGM vs present-day conditions.**

In Fig. 4, we illustrate the model simulated changes in rainfall over the Cape south coast region, for LGM climate compared to present-day climate. The model simulation of present-day rainfall realistically represents the all-year nature of rainfall along the Cape south coast. The results demonstrate that as the westerlies shifted towards the equator, cold front tracks and frontal rain also shifted to the north. Therefore, the model simulates a much wetter winter climate in the southern part of South Africa for LGM than for present-day winters.



**Figure 4: CCAM simulated anomalies winter precipitation, for the LGM vs present-day conditions.**

**Simulated monthly precipitation for Pinnacle Point (Mossel Bay)**

Fig. 5 shows the CCAM simulated annual rainfall cycle for the grid box including Pinnacle Point, Mossel Bay (a location of great archeological importance in terms of the evolution of early humans). The x-axis of the graph represents months, whereas the y-axis represents the precipitation. The green line indicates the LGM and the black line indicate the present-day climate (here the model simulations have been bias-corrected using observed data from the Climatic Research Unit). CCAM projects a pronounced increase in winter rainfall over the location, consistent with the projected northward displacement of the westerlies and frontal rain bands. However, the simulations contradict the interpretation of some paleo-proxy data for the Cape south coast. More specifically, the speleothem record for the glacial maximum before the LGM, known as MIS4 (dating to ~74-60 ka), has been interpreted as indicating the occurrence of more summer rain during the LGM [Bar-Matthews (2010)]. Possible explanation for this discrepancy are (1) that the paleoarchive evidence has not interpreted correctly; (2) that conditions differed for the LGM compared to MIS4 and (3) that the LGM simulations performed here are not realistic..

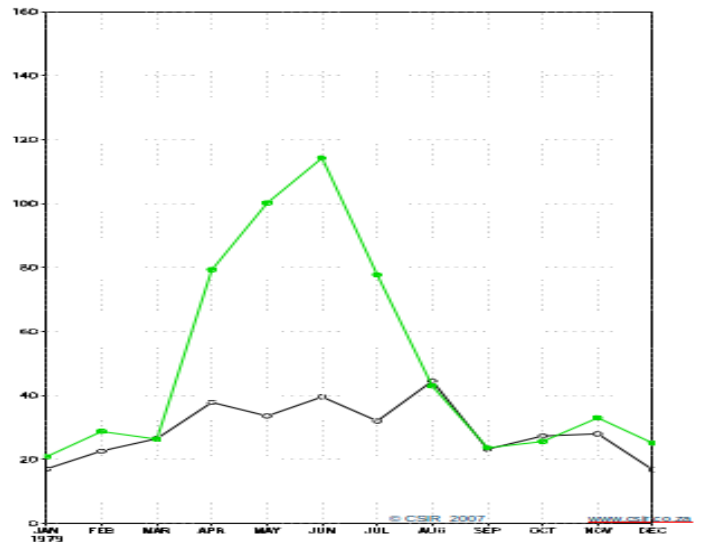


**Figure 5: CCAM simulated annual rainfall cycle at Pinnacle Point, Mossel Bay, for the LGM (green) and present-day climate (black).**

**DISCUSSION AND CONCLUSIONS**

The CCAM atmospheric model has been used to obtain global simulations of LGM climate, through the downscaling of PMIP3 CGCM simulations. The single ensemble member analysed here indicates that the LGM precipitation along the Cape south coast may have exhibited a pronounced winter rainfall peak. This result contradicts to some extent the interpretation of the paleoarchive record. The speleothem record of glacial maximum before the LGM has been interpreted as

indicating more summer rain rather than more winter rain [Bar-Matthews (2010)]. The simulations indicate that the paleoarchive evidence may have been interpreted incorrectly since an increase in winter rainfall is highly plausible given the northward displacement of the westerlies during the LGM.

## ACKNOWLEDGEMENTS

The simulations were performed on the supercomputers of the Center for High Performance Computing (CHPC) in South Africa and the XSEDE supercomputing facility in the USA.

## REFERENCES

Engelbrecht, C.J., Landman, W.A., Engelbrecht, F.A., and Malherbe, J. (2015). A synoptic decomposition of rainfall over the Cape south coast of South Africa. *Climate Dynamics*. 44: 2589-2607. DOI: 10.1007/s00382-014-2230-5.

Akasofu, S. (2013). On the Present Halting of Global Warming. *Climate*, 1, 4-11. Available: [www.mdpi.com/225-1154/1/1/4](http://www.mdpi.com/225-1154/1/1/4)

Engelbrecht, F.A., Landman, W.A., Landman, S., Bopape, M.M., Roux, B., McGregor, J.L., and Thatcher, M. (2011). Multi-scale climate modelling over Southern Africa using a variable-resolution global model.

Malherbe, J., Engelbrecht, F.A., and Landman, W.A. (2012). Projected changes in tropical cyclone climatology and landfall in the Southwest Indian Ocean region under enhanced anthropogenic forcing. *Clim Dyn*.

Engelbrecht, F.A., McGregor, J.L., and Engelbrecht, C.J. (2009). The dynamic of the Conformal-Cubic Atmospheric Model projected climate-change signal over southern Africa. *International Journal of Climatology*. 1013-1033.

National Research Council. (2010). *Understanding Climate's influences on Human Evolution*. Washington, DC: National Academies Press. Available: <http://www.nap.edu/catalog/12825/understanding-climate-s-influence-on-human-evolution>

Marean, C. W., et al. (2014). Stone Age People in a Changing South African Greater Cape Floristic Region. *Fynbos: Ecology, Evolution, and Conservation of a Megadiverse Region*. N. Allsopp, J. F. Colville and T. Verboom. Oxford, Oxford University Press: 164-199.

Bar-Matthews, M., Marean, C.W, Jacobs, Z., Karkanas, P., Fisher, E.C., Herries, A.I.R., Brown, K., Williams, M.H., Bernatchez, J., Ayalon, A., and Nilssen, P.J. (2010). A high resolution and continuous isotopic speleothem record of paleoclimate and paleoenvironment from 90 to 53 ka Pinnacle Point on the south coast of South Africa. *Quaternary Science Reviews*. (29) 2131-2145.

# Seasonal forecasting of synoptic type variability: potential intraseasonal predictability relevant to the Cape south coast of South Africa

Christien J Engelbrecht<sup>1,2</sup> and Willem A Landman<sup>2,3</sup>

<sup>1</sup>Agricultural Research Council, Institute for Soil, Climate and Water, Pretoria, South Africa

<sup>2</sup>Department of Geography, Geo-informatics and Meteorology, University of Pretoria, Pretoria, South Africa

<sup>3</sup>Council for Scientific and Industrial Research, Climate Studies, Modelling and Environmental Health, Pretoria, South Africa

## Abstract

An ensemble of 12 sea-level pressure (SLP) simulations from the United Kingdom Meteorological Office (UKMO) Global Seasonal Forecast System 5 (GloSea5) is used to investigate the potential predictability of synoptic types within 14 austral spring seasons (September–November, (SON)) for the 14 yr period from 1996 to 2009. Daily SLP model fields for the 14 SON seasons are mapped to the corresponding observed synoptic types, using self-organising maps (SOMs). Predictability of intraseasonal synoptic type characteristics is evaluated by comparing the frequency of synoptic types as simulated by GloSea5 against the observed synoptic type occurrence. Intraseasonal circulation variability for the Cape south coast of South Africa at interannual time scales is found to be predictable, although poorly.

Key words: Cape south coast, synoptic types, intraseasonal predictability

## INTRODUCTION

The Cape south coast region of South Africa (Fig. 1) receives all-year rainfall. In fact, the pronounced rainfall seasonality as observed over the summer and winter rainfall regions of the country is absent over this region. Notwithstanding, along the Cape south coast SON is the season that receives the most rainfall. It is in particular the months of October and November that contributes to SON rainfall. October receives slightly more rain than November on average and is the month with the highest mean rainfall over the Cape south coast. It is in particular ridging high pressure systems and cut-off lows that are the main contributors to rainfall (Engelbrecht et al., 2015). Seasonal forecasting research in South Africa has focused mostly on summer rainfall (e.g. Landman et al., 2012) and in particular for the December to February period (e.g. Landman and Beraki, 2012) when the strongest association between rainfall totals and the El-Niño Southern Oscillation (ENSO) has been shown to exist. The highest skill seasonal forecasts are found over the northeastern interior of South Africa (Landman et al., 2012) and forecasts work best during ENSO seasons (Landman and Beraki, 2012). Often these seasonal forecasts are produced by statistically downscaling the ensemble mean low-level circulation (e.g. 850 hPa geopotential height) from global model forecasts to rainfall stations or districts. Unfortunately the relatively high levels of skill found over the northeast are not reflected over the Cape south coast. In this paper, we aim to assess the within-SON-season predictability by considering the predicted frequencies of different synoptic types affecting seasonal climate variations over

the Cape south coast. If it can be shown that this intraseasonal variation in circulation over the Cape south coast can be predicted skillfully at interannual time scales, it will imply that skillful rainfall forecasts can be generated through the use of predicted daily circulation statistics.

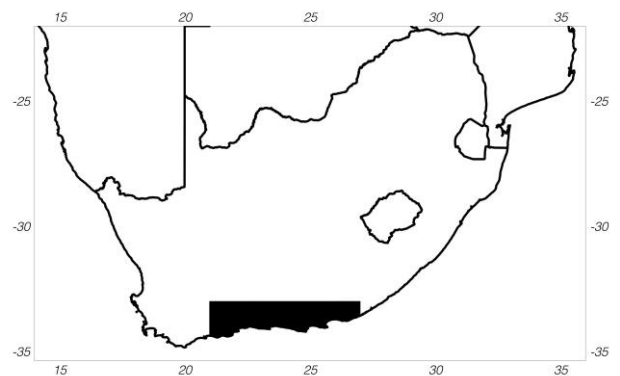


Fig. 1. Geographical location of the Cape south coast.

## DATA AND METHOD

Hindcasts (1-month lead) of a fully coupled model administered by the UKMO, the GloSea5, are used in this study. Daily SLP fields for 14 SON seasons from 1996–2009 for 12 ensemble members are used to study the frequencies of synoptic types. A full description of GloSea5 can be found in MacLachlan et al. 2014. National Centers for Environmental Prediction (NCEP) daily SLP data is used to calculate the observed synoptic type frequencies for the corresponding SON seasons to

that of the model simulations. The SOM method is used for identification of 9 synoptic types during SON of which the frequencies are determined. The choice of 9 synoptic types is based upon the average mapping of about 10 days to a specific synoptic type during a season of approximately 90 days, translating to 10 degrees of freedom (e.g. Tennant, 2003). Before the GloSea5 daily SLP fields are mapped to the SOM, model output was converted to the horizontal resolution of the NCEP SLP fields by application of a bicubic interpolation function. The SOM method requires for the model data mapped to the SOM to have a common grid as the SLP fields used to develop the SOM. Also, to account for model biases, the long term mean is subtracted from the observed daily SLP fields before subjected to development of the SOM. Similarly, the long term mean of each ensemble member is subtracted from the corresponding model daily SLP fields before these fields are mapped to the SOM in order to determine the model simulated synoptic type frequencies for each of the 12 ensemble members.

The atmospheric circulation that influences weather along the Cape south coast is mostly located over the surrounding oceanic region. Therefore, the domain used to develop the SOM are bounded by 10°E-40°E and 32.5°S-45°S. The selected region allows for capturing the progression of high pressure systems and troughs, advancing from west to east, to the south of the Cape south coast. Tropical-temperature troughs are also captured by this domain since the axis of tropical-temperate troughs passes through it.

This study includes both deterministic and probabilistic verification of the frequency of synoptic types over the region as produced by the GloSea5. Deterministic verification is included to determine whether interannual variability of the frequency of synoptic types is captured. The anomaly correlation is used for this purpose. The anomaly correlation is not sensitive to biases and quantifies the spatial correlation between forecast and observed deviations from climatology (Wilks, 2011). The different synoptic types, represented by the nodes on the SOM, are regarded similar as grid points in a spatial field. The frequency distribution of synoptic types across the SOM space is therefore assessed by the anomaly correlation.

Seasonal forecasts are inherent probabilistic in nature. Synoptic type occurrences are probabilistic assessed by introducing tercile categories. Resolution and reliability of the forecasting system is assessed by application of the relative operating characteristic (ROC) and the reliability diagram (Wilks, 2011). In this study, probability bins of 20% are used, to accommodate the sparseness of occurrences found for the traditional probability bins of 10%.

**DISCUSSION**

Fig. 2 shows the anomaly correlation of the model forecast of the frequency of synoptic types (solid line) as well as the persistence forecasts (dotted line) for the 14 SON seasons from 1996 to 2009. The forecasts were

obtained from the ensemble average and can therefore be regarded as deterministic. Positive anomaly correlation coefficients are indicative of corresponding forecast and observed anomalies across the SOM, while negative anomaly correlation coefficients indicate disagreement between the forecast and observed anomalies. Over this 14-year hindcast period, 9 of the seasons are associated with positive anomaly correlation coefficients. Compared to persistence (dotted line), 11 out of the 14 SON seasons exhibit skillful deterministic forecasts of the synoptic type frequency distribution within the SOM space. The 3 seasons that had no forecast skill relative to persistence are all below-normal rainfall seasons (1998, 2006 and 2009).

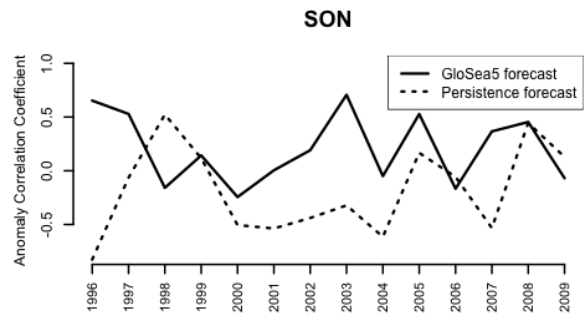


**Fig. 2. Anomaly correlation coefficient for GloSea5 (solid lines) and persistence (dotted lines) for SON deterministic forecasts of synoptic type frequencies across the SOM.**

Figs. 3 and 4 show the ROC curves for the lower and upper tercile probabilistic forecasts of synoptic type frequencies. ROC curves are a measure of resolution and address the question whether the forecast system can discriminate between the occurrence and non-occurrence of an event. The ROC areas for both categories are above 0.5, indicative that the GloSea5 system is able to discriminate between the occurrence and non-occurrence of events for the lower and upper tercile categories. Although the ROC areas seem small the above-normal ROC area is significant above the 90% level.

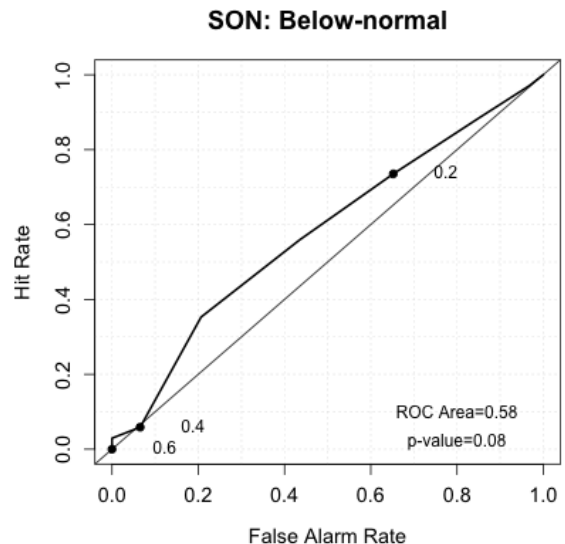


**Fig. 3. ROC diagram of the probability that the frequency of the 9 synoptic types over the 14 SON seasons is in the lower tercile.**

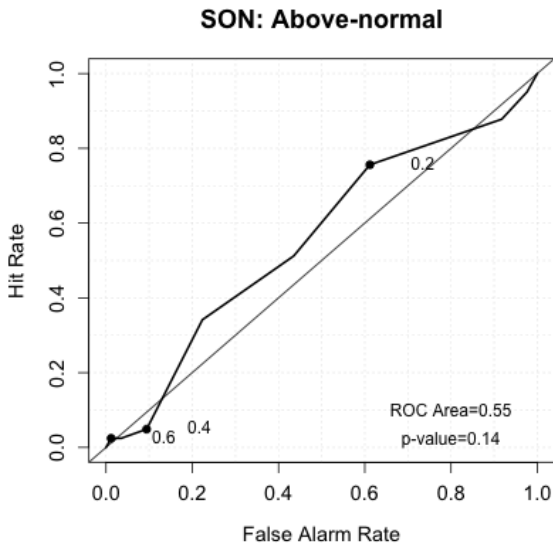


**Fig. 4. ROC diagram of the probability that the frequency of the 9 synoptic types over the 14 SON seasons is in the upper tercile.**

Figs. 5 and 6 show the reliability diagrams for the lower and upper tercile categories of synoptic type frequency forecasts during the 14 SON seasons. A perfect reliable forecast would coincide with the diagonal. Forecasts for both categories falling within the probability bin of 0.4-0.6 and higher are overconfident while forecasts indicating probabilities within the 0.0-0.2 probability bin are generally underconfident. Forecasts within the probability bin 0.2-0.4 are reliable. The frequency histograms for both categories indicate a peak in forecast probability similar to the corresponding climatological probability. This feature indicates that the forecasts lack sharpness.

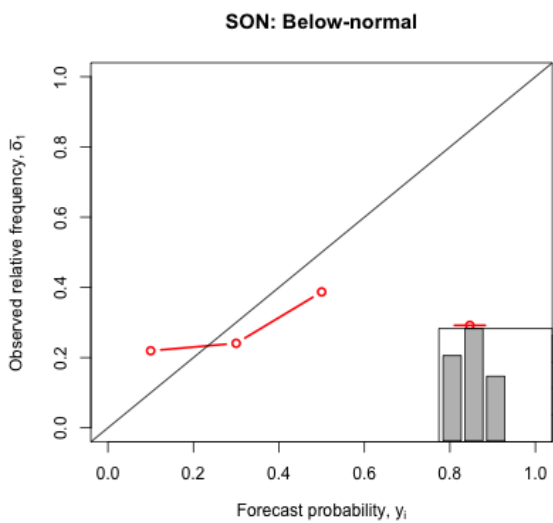


**Fig. 5. Reliability diagram of the probability that the frequency of the 9 synoptic types over the 14 SON seasons is in the lower tercile.**

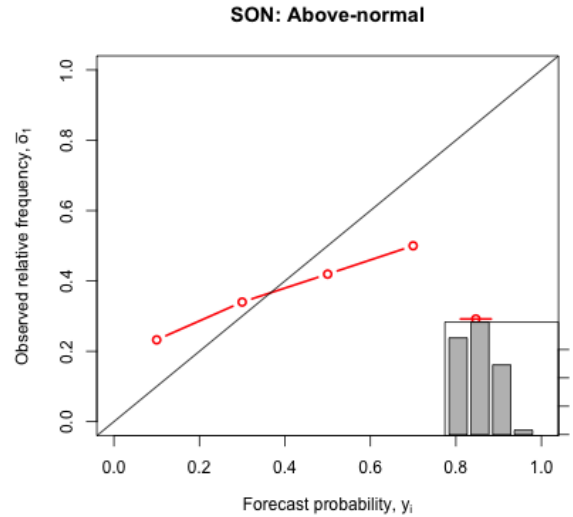


**Fig. 6. Reliability diagram of the probability that the frequency of the 9 synoptic types over the 14 SON seasons is in the upper tercile.**

**CONCLUSION**

The intraseasonal circulation variability over the Cape south coast is predictable, although poorly, by the GloSea5 coupled model for SON seasons. It may be noted that a similar analysis performed over a domain that include southern Africa yielded similar results of poor to marginal predictability of synoptic type frequencies for SON seasons, highlighting the challenge of the seasonal prediction problem.

**REFERENCES**

Engelbrecht, C.J., Landman, W.A., Engelbrecht, F.A. and Malherbe, J. (2015). A synoptic decomposition of rainfall over the Cape south coast of South Africa. *Climate Dynamics*. 44: 2589-2607. DOI: 10.1007/s00382-014-2230-5.

Landman, W.A. and Beraki, A. (2012). Multi-model forecast skill for mid-summer over southern Africa. *International Journal of Climatology*. 32: 303-314.

Landman, W.A., DeWitt, D., Lee, D.E., Beraki, A. and Lotter, D. (2012). Seasonal rainfall prediction skill over South Africa: one- versus two-tiered forecasting systems. *Weather and Forecasting*. 27: 489-501. DOI: 10.1175/WAF-D-11-00078.1

MacLachlan, C., Arribas, A., Peterson, K.A., Maidens, A., Fereday, D., Scaife, A.A., Gordan, M., Vellinga, M., Williams, A., Comer, R.E., Camp, J., Xavier, P. and Madec, G. (2014). Global Seasonal forecast system version 5 (GloSea5): a high-resolution seasonal forecast system. *Quarterly Journal of the Royal Meteorological Society*. DOI: 10.1002/qj.2396

Tennant, W. (2003). An assessment of intraseasonal variability from 13-Yr GCM Simulations. *Monthly Weather Review*. 131: 1975-1991.

Wilks, D.S. (2011). *Statistical Methods in the Atmospheric Sciences*. 3<sup>rd</sup> ed. Academic Press, p. 676.

## Predicting the extreme 2015/16 El Niño event

Lerato E. Mphesha<sup>1,2</sup> and Willem A. Landman<sup>1,2</sup>

<sup>1</sup>Council for Scientific and Industrial Research, Natural Resources and the Environment, Pretoria, South Africa

<sup>2</sup>Department of Geography, Geoinformatics and Meteorology, University of Pretoria, Pretoria, South Africa

### *Abstract*

A strong El Niño event is expected to develop during the coming austral summer. This study seeks to address the two main questions. 1) How strong will the 2015/16 event be? 2) With how much skill and confidence can a really strong event be predicted? A state-of-the-art coupled ocean-atmosphere model's Niño3.4 SST forecast for January 2016 is presented, followed by an evaluation of the model's ability to have predicted events of similar magnitude in the past. The January forecast, initialized in July 2015, shows a Niño3.4 SST anomaly larger than the 75th percentile of the observed climatological record. Verification over 19 years of Niño3.4 SST hindcasts suggest that such forecasts may be made with high confidence even at several months lead-time.

Key words: El Niño, coupled model, verification

### **Introduction**

The anomalous fluctuations of sea-surface temperatures (SSTs) in the tropical Pacific Ocean have considerable global impact on inter-annual climate variability (e.g. Ropelewski and Halpert, 1987). In southern Africa, anomalously warm (cold) SSTs in the tropical eastern Pacific Ocean are strongly linked to drier (wetter) than normal seasons (Lindesay et al., 1988; Lindesay and Vogel, 1990; Rouault and Richard, 2003). In an event of a dry season, agricultural production tends to be impacted negatively and water scarcity tends to be exacerbated especially in the rural areas. Since the 1990's when seasonal forecasting became operational in South Africa, decision makers are informed ahead of time whether the coming season is likely to be drier, near-normal or wetter (Landman, 2014). Such forecasts, however, work best in the presence of an El Niño or a La Niña event (Landman and Beraki, 2012). The July El Niño advisory issued by the USA's Climate Prediction Center states that the "consensus is in favour of a significant El Niño in excess of +1.5°C in the Niño-3.4 region." The aim of this study is to analyse the ability of a state-of-the-art coupled ocean-atmosphere model to predict such extreme El Niño events at lead-times up to 6

months. Our analysis indicates an exceptionally strong El Niño to occur and since such predictions have skill southern Africans may have to brace themselves for a summer drought in 2015/16.

### **Data and Method**

#### *Verification data*

The monthly Optimal Interpolation Sea Surface Temperature (OISST) data (Reynolds, et al., 2007) are used for verification. The months considered are November, December, January, February and March from 1981 to 2015 in order to capture the mature phase of ENSO.

#### *Model validation*

The model used is the GFDL-CM2.5-FLOR-B01 fully coupled model of the North American Multi-model Ensemble (Kirtman et al., 2014). Monthly hindcast global data from March 1980 to the present are available at a 1°x1° latitude-longitude resolution for 12 ensemble members and for lead-times up to 11 months. We consider only lead-times up to 6 months which is typical for seasonal forecasting in South Africa. The model validation methods applied in this study are achieved by

using the Climate Prediction Tool (CPT) statistical software of the International Research Institute for Climate and Society. To assess model performance, a retroactive forecast procedure is employed so as to obtain realistic estimation of its prediction skill (Mason & Mimmack, 2002). The training period is initially set as 15 years (1980-1995) with a training period update interval of one year. We do not do a recalibration or downscaling of model output to the OISST grid, but rather only correct for the mean and biases of the model while interpolating to the nearest gridpoint of the OISST. These settings allow the optimal model to produce a set of 19-year retroactive predictions (hindcasts). The above- and below-normal events are defined at the 25% extreme tails of the climatological distribution of SSTs. Relative operating characteristic (ROC) areas (Mason, 1982; Mason and Graham, 1999) are computed to evaluate the discrimination in the hindcasts more specifically. For the purpose of assessing the reliability the resolution slope is computed. The verification results presented in the following section are only for the upper 25% tail. This threshold represents extreme El Niño events in terms of Niño3.4 SST anomalies.

## Results and Discussion

Fig. 1a shows a time series of the hindcasts and the observed SSTs for the Niño3.4 region. These series represent area averages. Hindcasts have a bias of about 1°C which is subsequently removed. These hindcasts compare well with the observations. The 2002/03 and 2009/10 events resulted in the wide spread dry conditions in southern Africa (Rojas, et al., 2014). The impact of the 1997/98 event on the rainfall over southern Africa was much less than anticipated (Rojas, et al., 2014). Many studies attribute the modification of ENSO/rainfall to the variability SSTs in the South Indian Ocean (e.g. Reason, 2001). In general, El Niño events are associated with dry summers. If the hindcast appears

to satisfactorily agree with the observed data as seen in Fig. 1a, it is plausible to have confidence in the forecast system to predict future events. In this case, the upcoming season is predicted to be amongst the most intense El Niño events. The hindcast and forecast anomalies are presented in Fig. 1b. The January forecast of the SSTs in the Niño3.4 domain lies above the 75<sup>th</sup> percentile of the observed climatological data (see fig. 1a). The probabilistic forecast issued in July 2015 for each of the three outcomes (La Niña, Neutral and El Niño) for January 2016 Niño3.4 SST is shown in Fig. 2. The figure shows a 92% chance of an extreme El Niño condition (in terms of SST) to occur. So not only is the prediction for a strong event to occur, the likelihood of this happening is also large.

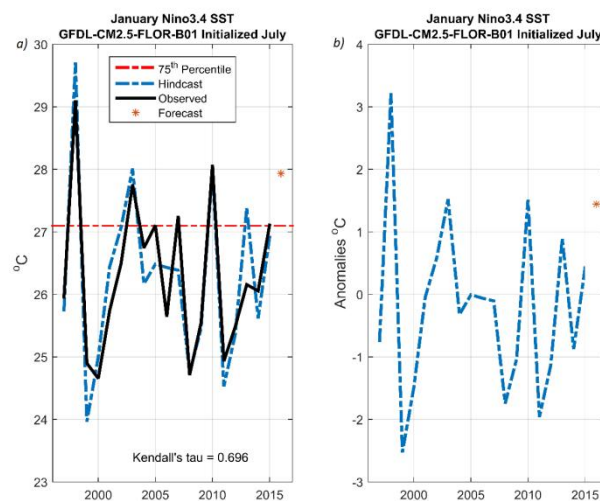


Figure 1: a) Area averaged hindcast and observed SSTs in the Niño3.4 region [ $5^{\circ}$  N-  $5^{\circ}$  S;  $120^{\circ}$  W –  $170^{\circ}$  W] presented in blue and black respectively. The SST forecast for January 2016 is represented by an asterisk. The red dashed line marks the 75<sup>th</sup> percentile of the observed climatological record. b) Shows the anomalies of the SST hindcasts (dashed line) and forecast for January 2016 (asterisk) in the Niño3.4 domain.

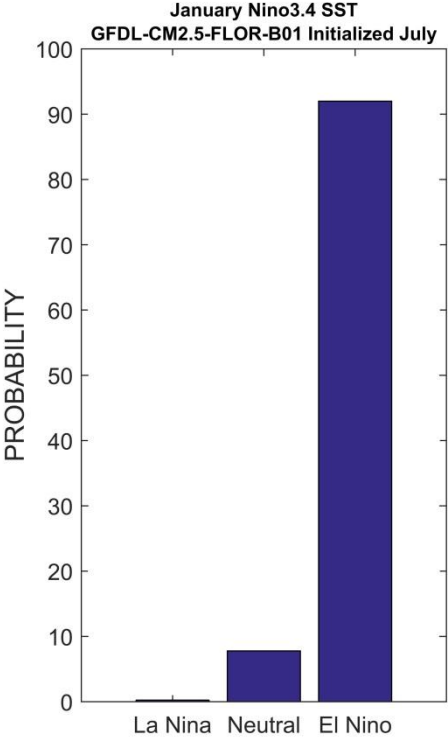


Figure 2: Probabilistic forecast of January 2016 Niño3.4 SST in terms of La Niña (0.2%), Neutral (7.8%) and El Niño (92%) occurrence.

Fig. 3 shows the ROC area scores for the model to discriminate above-normal SST events (El Niño) from the near- and below-normal (La Niña) events in the tropical eastern Pacific Ocean. At all months considered here (i.e. Nov-Mar), from 1-month to 6-months lead, the forecast system demonstrates a strong ability to differentiate El Niño events from neutral and La Niña events. ROC values are relatively higher for the Dec-Jan period and lower for March. This skill pattern also resembles the typical ENSO cycle – development in April to June, reaches its maximum peak in December to January and then dissipates around March. Although the spring predictability barrier is a known feature in ENSO prediction, our analysis does not include this period. A skill pattern similar to Fig. 3 is evident in the analysis of the hindcasts’ reliability as represented by the resolution slopes of attributes diagrams (Fig. 4). For perfect reliability slopes will be exactly one. Resolution slopes

close to one are observed mainly for November and December hindcasts issued a month and two months prior to the event, respectively. For instance, let us consider the case of an extreme El Niño event occurring in December, say such event is predicted in October (2-month lead) we can be confident enough say that the event will occur based on the fact that the forecast system is good at predicting the occurrence of such events with probabilities that are substantially different from climatological frequencies (see Fig.4) and that the system has an ability to distinguish this event from all other possible events (see Fig.3).

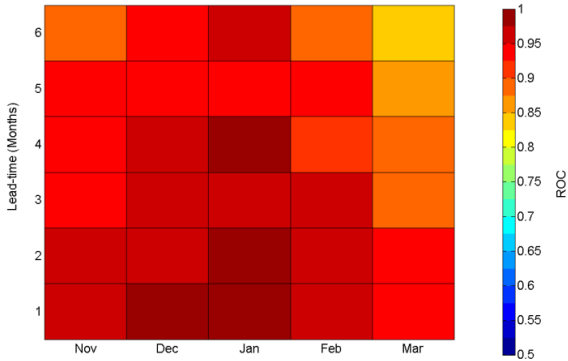


Figure 3: ROC scores for the probabilistic forecast of above-normal SST events in the Niño3.4 domain. The scores are presented for November to March at lead-times of 1 to 6 months.

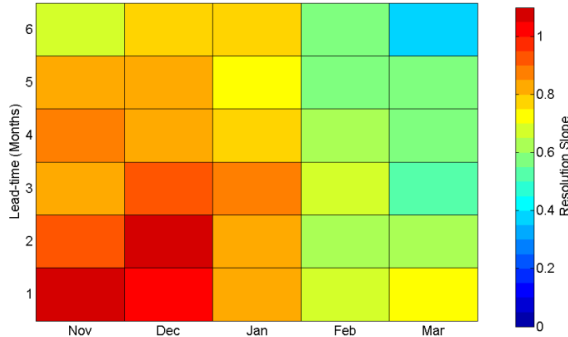


Figure 4: Resolution slopes for hindcasts of above-normal SST events in the Niño3.4 region for the target months of November to March for lead-times from 1 to 6 months.

## Conclusion

The coupled model, initialized in July 2015, predicts very strong El Niño type SST anomalies for January 2016. This 2016 anomaly is similar to the 2<sup>nd</sup> and 3<sup>rd</sup> largest positive anomalies (El Niño events) of the 18-year verification period. In fact, the anomaly is likely to be larger than the 75<sup>th</sup> percentile of the observed climatological record. Verification of the hindcasts shows that such strong El Niño events can be discriminated successfully from other (Neutral and La Niña) events and can be predicted reliably. We should expect southern Africa's coming summer season's rainfall and temperatures to be influenced by a strong El Niño event and that often means droughts and associated high temperatures over the subcontinent.

## References

- Kirtman, B. P. et al., 2014. The North American Multimodel Ensemble: Phase-1 Seasonal-to-Interannual Prediction; Phase-2 toward Developing Intraseasonal Prediction. *Bulletin of the American Meteorological Society*, pp. 585-601.
- Landman, W. A., 2014. How the International Research Institute for Climate and Society has contributed towards seasonal climate forecast modelling and operations in South Africa. *Earth Perspectives*, 1(22).
- Landman, W. A. & Beraki, A., 2012. Multi-model forecast skill for midsummer rainfall over southern Africa. *International Journal of Climatology*, Volume 32, pp. 303-314.
- Lindesay, J. A., 1988. Southern African rainfall, southern oscillation and southern hemisphere semi-annual cycle. *Journal of Climatology*, Volume 8, pp. 17-30.
- Lindesay, J. A. & Vogel, C. H., 1990. Historical evidence for southern oscillation- southern African rainfall relationships. *International Journal of Climatology*, Volume 10, pp. 679-689.
- Mason, I., 1982. A model for assessment of weather forecasts.. *Australian Meteorological Magazine*, Volume 30, pp. 291-303.
- Mason, S. & Graham, N. E., 1999. Conditional probabilities, relative operating characteristics, and relative operating levels. *Weather Forecasting*, Volume 14, pp. 713-725.
- Mason, S. J. & Mimmack, G. M., 2002. Comparison of some statistical methods of probabilistic forecasting of ENSO. *Journal of Climate*, Volume 15, pp. 8-29.
- Reason, C. J. C., 2001. Subtropical Indian Ocean SST dipole events and southern African rainfall. *Geophysical Research Letters*, 28(11), pp. 2225-2227.
- Reynolds, R. W. et al., 2007. Daily High-Resolution-Blended Analyses for Sea Surface Temperature. *Journal of Climate*, Volume 20, p. 5473-5496.
- Rojas, O., Li, Y. & Cumani, R., 2014. The influence of El Niño on the global agricultural areas. In: *Understanding the drought impact of El Niño on the global agricultural areas: An assessment using FAO's Agricultural Stress Index (ASI)*. Rome: Food and Agriculture Organization of the United Nations, pp. 9-13.
- Ropelewski, C. F. & Halpert, M. S., 1989. Precipitation patterns associated with high index phase of the southern oscillation. *Journal of Climate*, Volume 2, pp. 268-284.
- Rouault, M. & Richard, Y., 2003. *Intensity and spatial extension of drought in South Africa at different time scales*. [Online]  
Available at: <http://www.wrc.org.za>

# Ranking seasonal rainfall forecast skill of emerging and developing economies

Willem A Landman<sup>1,2</sup>, Anthony G Barnston<sup>3</sup> and Coleen Vogel<sup>4</sup>

<sup>1</sup>Council for Scientific and Industrial Research, Natural Resources and the Environment, Pretoria, South Africa

<sup>2</sup>Department of Geography, Geoinformatics and Meteorology, University of Pretoria, Pretoria, South Africa

<sup>3</sup>International Research Institute for Climate and Society, The Earth Institute of Columbia University, New York, USA

<sup>4</sup>Global Change and Sustainability Research Institute, University of the Witwatersrand, Johannesburg, South Africa

## *Abstract*

Some of the biggest emerging markets economies include countries in South America, Asia and Africa. In the global south, political and developmental similarities (e.g. climate variability occurring in conjunction with marked developmental challenges) offer opportunities for comparative research and thereby possible societal benefits (e.g. enhanced disaster risk reduction). In fact, countries or geographical regions of the world significantly affected by climate extremes may consider collaboration on issues such as understanding and modelling of the climate system, especially if there is a common dominant and somewhat predictable climate mode such as the El Niño-Southern Oscillation (ENSO) affecting the climate variability over these regions. Notwithstanding the value of enhanced understanding and preparedness for ENSO, better predictions are not enough to reduce the risks associated with such events. The socio-economic and political context in which forecasts are located also needs to be understood. Here we present seasonal forecast skill over a large number of regions including emerging or developing countries, but also for a small number of developed regions, in order to rank their ENSO-related seasonal rainfall predictability in an attempt to cluster regions of similar predictability.

Key words: Emerging economies, ENSO, seasonal climate modelling, skill

## INTRODUCTION

The El Niño-Southern Oscillation (ENSO) has long been known to have global impact on seasonal-to-interannual climate variability (Ropelewski and Halpert, 1987, 1989). For example, during most of the strongest El Niño events (e.g. 1982/83, 1991/92 and 2006/07) drought conditions occurred over parts of southern Africa, Australia and southern USA, while La Niña events caused excessive seasonal flooding over these parts (e.g. 1999/2000 and 2010/11). The reliability with which most ENSO events can be predicted several months before they reach maturity (Stockdale et al., 1998) and the skill in predicting seasonal extremes over parts of the globe linked to ENSO (e.g. Landman and Beraki, 2012) may result in effective uptake of seasonal forecasts in order to minimize such impacts (Braman et al., 2013). Evidence of existing international collaboration, such as that of IBSA (India-Brazil-South Africa), has already led to scientific agreements on addressing research and modelling questions on oceanography, meteorology and the Antarctic. In addition to successful politically-based frameworks such as IBSA, collaboration motivated more directly by common scientific questions is also warranted, especially if such questions can lead to further societal improvement and development, including economic development.

The level of uptake of seasonal forecasts and applying these forecasts for the benefit of users,

commercial or otherwise, across regions differs widely. For example, in Uruguay (a nation whose economy is based upon agriculture) the government is currently working with the International Research Institute for Climate and Society (IRI) to create one of the most sophisticated agricultural information networks in the world that can provide reliable seasonal climate forecasts for temperature and rainfall patterns up to three months in advance. Countries or geographical regions with political and socio-economic challenges similar to Uruguay's may benefit from learning about how they have put to use seasonal forecasts to improve on their agricultural practices and decision making. However, regions where seasonal forecasts are not skillful enough may not benefit from learning about the Uruguayan experience.

In South Africa, where it has been suggested that the uptake of seasonal forecasts for the region may have stagnated notwithstanding proof that forecasts have improved (Landman, 2014), may benefit from learning from the Uruguayans since southern Africa has, like Uruguay, ENSO-forced seasonal predictability and has a large agricultural sector sensitive to climatic fluctuations. Moreover, climate models applied to South African agriculture and rivers have also been successfully applied to Uruguayan and Chilean river flows over multiple decades (Landman et al., 2014). Such South-South collaboration is made in part possible owing to the regions' teleconnections to ENSO and subsequent

seasonal predictability. However, there are a number of regions similarly linked to ENSO and whose modelling and forecast application efforts may also co-benefit through multi-national collaboration with southern African modellers and social scientists.

Complex socio-economic and political drivers that shape the vulnerability context in which ENSO operates also need to be understood when preparing seasonal climate forecasts (e.g. Eakin, 2000, Davis, 2002; Lemos et al. 2002; ODI, 2011, Ziervogel and Downing, 2004). The social and human dimensions require detailed attention (as the recent interest in the focus on ‘Climate knowledge for action’ and the ‘Global Framework for Climate Services’ is planning to address). Several investigations on the use and uptake of seasonal forecasts in southern Africa have been undertaken and key elements can be profiled further.

This paper attempts to find out where southern Africa seasonal rainfall predictability ranks with a good number of other countries or regions linked to ENSO so that collaboration may be sought and established.

## DATA AND METHOD

Two data sets are considered: hindcasts from a coupled model and a gridded rainfall product against which the model hindcasts are verified. The model used is the GFDL-CM2.5-FLOR-B01 fully coupled model of the North American Multi-model Ensemble (Kirtman et al., 2014). Monthly global hindcast data from March 1980 to the present are available at a  $1^{\circ} \times 1^{\circ}$  latitude-longitude resolution for 12 ensemble members and for lead-times up to 11 months. We are using only 1-month lead-time hindcasts. The gridded data is the Climatic Research Unit (CRU) TS3.21 (Harris et al., 2014) from which seasonal total rainfall is derived. Table 1 shows the regions and their latitude-longitude description together with their respective ENSO related rainfall seasons used in the analysis.

**Table 1. The regions, their latitude-longitude areas and their seasons used in the analysis.**

Region	Lat-Long	ENSO responses season
Central Chile	28°-38°S; 70°-75°W°	JJAS
Central SW Asia	34°-44°N; 62°-77°E	FMA
Coastal Equador,Northern Peru	8°S-0°; 79°-82°W	JFMA
Eastern Australia	20°-40°S; 140°-154°E°	ASOND
Eastern Equatorial Africa	7°N-7°S; 31°-48°E	OND
Europe	36°-60°N; 10°W-4°E	SON
India	13°-30°N; 70°-88°E	JAS
Indonesia	10°S-10°N; 95°-127°E	JASOND
Nordeste	2°-8°; 34°-45°W	MAM
Northern South America	0°-12°N; 52°-82°W	JASOND
Philippines	5°-20°N; 118°-128°E	ONDJF
Sahel	8°-16°N; 18°W-40°E	JAS
Southeast Asia	10°-20°N; 97°-110°E	JJAS
Southeast China	20°-30°N; 110°-123°E	AMJ
Southeast South America	29°-39°S; 48°-63°W	SOND
South-central, SW Canada	49°-55°N; 88°-132°W	DJFM
Southern Africa	14°-36°S; 11°-41°E	NDJFM
Southern USA	25°-34°N; 75°-120°W	NDJFM

Seasonal total precipitation gridded ensemble mean hindcasts are interpolated to the nearest CRU gridpoint after which the mean and variance biases of the model data are corrected with the IRI’s Climate Predictability Tool (CPT). There are 31 years of matching model and CRU data available from 1981 to 2011 of which the first 15 years are used to calculate error variances through cross-validation. Probabilistic and deterministic model hindcasts for year 16 are subsequently obtained by the CPT. A new cross-validation is then performed over 16 years of hindcasts in order to produce probabilistic and deterministic hindcasts for year 17. The process is continued until 15 years of hindcasts are obtained from 1997 to 2011. These hindcasts are subsequently verified.

## RESULTS

The 15-year hindcasts are verified both deterministically and probabilistically. For the former Spearman’s rank correlations between model and CRU data are calculated, and for the latter the model’s discrimination and reliability attributes are evaluated. Relative operating characteristics (ROC) are used to determine discrimination and the least squares weighted regression lines of attributes diagrams are used for reliability. In fact, the difference between these resolution slopes and the slope for perfect reliability is used as a measure of reliability at each gridpoint. For both ROC and reliability the upper and lower thresholds of the hindcast categories are determined from respectively the 75<sup>th</sup> and 25<sup>th</sup> percentile values of the climatological record.

The deterministic verification results are shown in Fig. 1. All CRU gridpoints per region are evaluated by calculating the 25<sup>th</sup>, 50<sup>th</sup> (median) and 75<sup>th</sup> percentile values of the correlations. The results are ranked according to the median values for each region and shown on the figure in a descending manner. The Philippines is ranked highest and southern Africa only 13<sup>th</sup>. All three IBSA regions (Southeast South America, Nordeste and India) are ranked higher than southern Africa. Surprisingly coastal Ecuador and northern Peru are ranked lowest, but this result may be a function of the model used and so the evaluation of additional models may be warranted.

ROC scores (for the three percentile values mentioned above) for the upper quartile (the “above-normal” category used here) of Fig. 2 rank southern Africa even lower in the 16<sup>th</sup> position. This lower position is partly a consequence of a large number of southern African gridpoints associated with very low ROC scores (the 25<sup>th</sup> percentile is near 10) even though the 75<sup>th</sup> percentile ROC scores for this region is ranked slightly higher at 15<sup>th</sup>. However, certain regions of southern Africa, such as the Limpopo Province and the adjacent areas from neighbouring countries, have been found to have much higher skill (Landman et al., 2012). For the lower quartile (the “below-normal” category) presented in Fig. 3 southern Africa ranks higher than before and even competes with the ranks of some of the IBSA regions. Take note that for Figs. 1 to 3 that the Philippines rank highest.

The reliability results of Figs. 4 and 5 are shown in an opposite orientation than the previous results, i.e., the highest ranked region are associated with the smallest distances from perfect reliability. As with the correlations and ROC scores, southern Africa ranks in the lower half of the regions. Take note that for the way in which reliability is portrayed here, some regions that have been ranked high before may rank more poorly now (e.g. Philippines). We may have to revisit the reliability estimates since with the current approach under-confident forecasts get penalized more severely than over-confident ones since under-confident slopes can go very high, such as 3 or 4, while under-confident slopes can only deviate from 1 by 1 at the most (unless they have negative slopes, which may be possible).

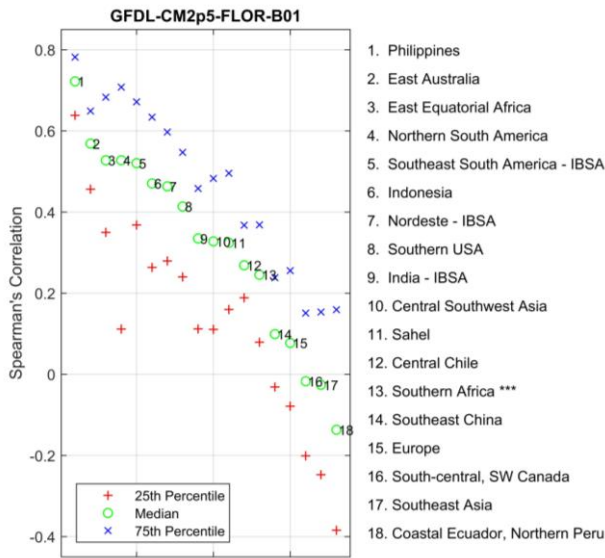


**Fig. 1.** Percentile values (25<sup>th</sup>, 50<sup>th</sup> and 75<sup>th</sup>) of the Spearman's rank correlation over all gridpoints obtained over the 15-year test period from 1997 to 2011.

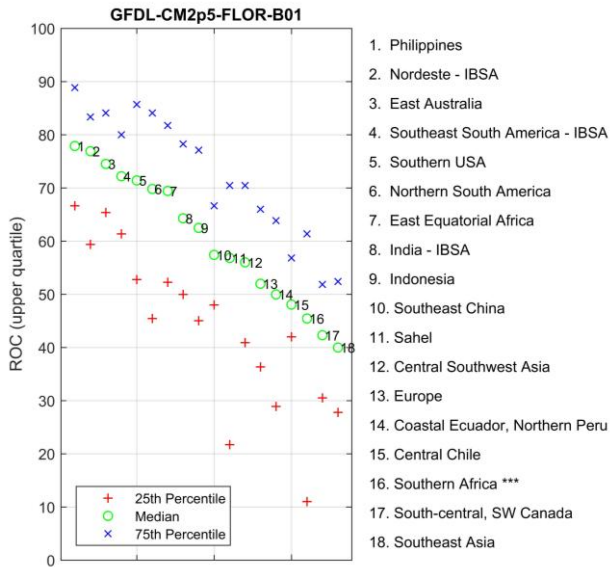


**Fig. 2.** As for Fig. 1, but for wet season discrimination (ROC for upper quartile).

**DISCUSSION AND CONCLUSION**

We wanted to determine how seasonal rainfall predictability over a number of regions compares with each other and in particular where southern Africa as an emerging economy ranks globally. Since ENSO is a strong forcing for climate variability over many parts of the globe and found often to be the main source of seasonal predictability, only seasons of the regions with ENSO responses are considered. For the analysis we used the output of a state-of-the-art coupled model of the North American Multi-model Ensemble that has been corrected for mean and variance biases. Only 15 years of verification data are considered from only one model.

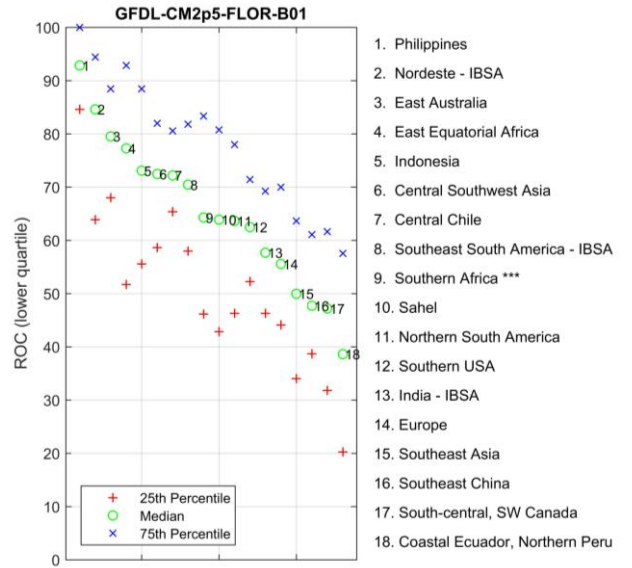


**Fig. 3.** As for Fig. 1, but for dry season discrimination (ROC for lower quartile).

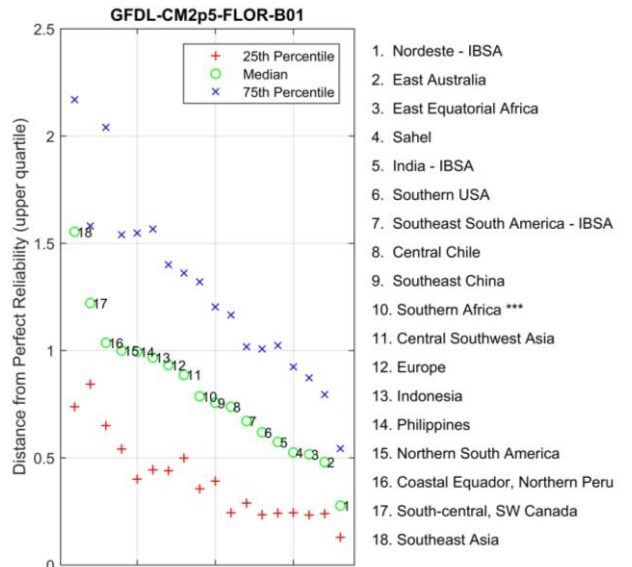


**Fig. 4.** As for Fig. 1, but for wet season reliability.

The verification results are presented in terms of deterministic predictability and how probabilistic forecasts are able to discriminate extreme seasons and how reliable these are. In general, predictability varies quite substantially across the selected regions, and perhaps rather disappointingly, southern Africa ranks

poorly against the majority of regions. However, we only tested how a single model's rainfall forecasts performed and as is certainly the case with southern Africa, statistically downscaling of low-level circulation instead can significantly improve skill. Perhaps through downscaling, southern African seasonal rainfall predictability can be brought up to par with more of these regions even if their forecasts are also similarly corrected.

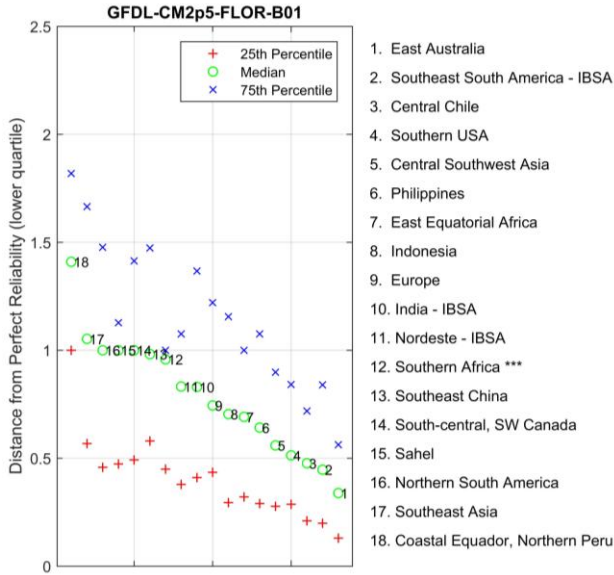


Fig. 5. As for Fig. 1, but for dry season reliability.

Based on the results of this work, southern African predictability ranks lower with developing regions or countries with which formal collaboration already exists (e.g. Brazil, India, Uruguay and Chile). Notwithstanding, in South Africa in particular, the more than 20 years of experience to model and predict seasonal climate variations and how such forecast can be applied to decision-making (Landman, 2014) may be of interest to these regions, in spite of their superior forecast skill. For example, South African modelling experience and expertise have already benefitted predictability studies over the Middle East (Shirvani and Landman, 2015). However, southern Africa modellers should also expand their network of collaborators to regions with similar limits of predictability such as Western Europe but where advanced modelling has been taking place over a sustained time (e.g., Doblas-Reyes et al., 2013).

The use and uptake of such forecasts, as indicated earlier, is another field of endeavor that requires intensive research. The use and co-design of what information may be required is an area that would have to be carefully considered when trying to use such information. Careful collaboration of what users require, how such information should be communicated and shared and also used would need careful articulation and further research.

**ACKNOWLEDGEMENT**

The work is a result of collaboration between South Africa and the IRI, supported by the National Research Foundation through their financial support of rated researchers.

**REFERENCES**

Braman, L.M.1., van Aalst, M.K., Mason, S.J., Suarez, P., Ait-Chellouche, Y. and Tall, A. (2013). Climate forecasts in disaster management: Red Cross flood operations in West Africa, 2008. *Disasters*. 37(1): 144-64. doi: 10.1111/j.1467-7717.2012.01297.x.

Davis, M. (2002). *Late Victorian Holocausts, El Nino famines and the making of the Third World*. Verso, San Francisco, California.

Doblas-Reyes, F.J., García-Serrano, J., Lienert, F. Biescas, A.P. and Rodrigues, L.R.L. (2013). Seasonal climate predictability and forecasting: status and prospects. *WIREs Climate Change*. 4: 245–268. doi: 10.1002/wcc.217.

Eakin, H. 2000: Smallholder maize production and climatic risk: a case study from Mexico. *Climatic Change*. 45:19-36.

Harris, I., Jones, P. D., Osborn, T. J., and Lister, D. H. (2014). Updated high-resolution grids of monthly climatic observations - the CRU TS3.10 Dataset. *International Journal of Climatology*. 34: 623-642. doi: 10.1002/joc.3711

Kirtman, B.P., and Coauthors. (2014). The North American Multimodel Ensemble: Phase-1 seasonal-to-interannual prediction; Phase-2 toward developing intraseasonal prediction. *Bulletin of the American Meteorological Society*. 95: 585–601. doi: <http://dx.doi.org/10.1175/BAMS-D-12-00050.1>

Lamos, M.C., Finan, T.J., Fox, R.W., Nelson, D.R. and Tucker, J. (2002). The use of seasonal climate forecasting in policymaking: lessons from NorthEast Brazil. *Climatic Change*. 55: 479-507.

Landman, W.A. (2014). How the International Research Institute for Climate and Society has contributed towards seasonal climate forecast modelling and operations in South Africa. *Earth Perspectives*. 1: 22.

Landman, W. A. and Beraki, A. (2012). Multi-model forecast skill for midsummer rainfall over southern Africa. *International Journal of Climatology*. 32 303-314.

Landman, W.A., DeWitt, D. Lee, D.-E., Beraki, A. and Lötter, D. (2012). Seasonal rainfall prediction skill over South Africa: 1- vs. 2-tiered forecasting systems. *Weather and Forecasting*, 27: 489-501. DOI: 10.1175/WAF-D-11-00078.1.

Landman W.A., Diaz, A., Montecinos, A., Engelbrecht, F. (2014). Climate change estimates of South American riverflow through statistical downscaling. *WCRP conference for Latin America and Caribbean: Developing, linking and applying climate knowledge*. Montevideo, Uruguay, 17-21 March 2014.

ODI, Blench, R. (1999) Seasonal climate forecasting: Who can use it and how should it be disseminated? *Overseas Development Institute*. 47: 1-8.

Ropelewski, C.F. and Halpert, M.S. (1987). Global and regional scale precipitation patterns associated with the El Niño–Southern Oscillation. *Monthly Weather Review*. 115: 1606–1626.

Ropelewski, C.F. and Halpert, M.S. (1989). Precipitation patterns associated with the high index of the Southern Oscillation. *Journal of Climate*. 2: 268–284.

Shirvani, A. and Landman, W.A. (2015). Seasonal precipitation forecast skill over Iran. *International Journal of Climatology*. In press.

Stockdale, T.N., Anderson, D.L.T., Alves, J.O.S. and Balmaseda, M.A. (1998). Global seasonal rainfall forecasts using a coupled ocean-atmosphere model. *Nature*. 392: 370-373.

Ziervogel, G. and Downing, T.E. (2004) Stakeholder networks: Improving seasonal forecasts. *Climatic Change*. 65: 1-2, 73-101.

# Comparing interpolated daily gauge rainfall over RSA with TRMM to determine possible bias correction for hydrological applications

Geoffrey GS Pegram<sup>1,2</sup>, Scott Sinclair<sup>1,2</sup> and Simon Ngoepe<sup>2,3</sup>

<sup>1</sup>Pegram and Associates (Pty) Ltd, Umhlanga

<sup>2</sup>Civil Engineering, UKZN, Durban

<sup>3</sup>Department of Water and Sanitation, Pretoria

## Abstract

TRMM rainfall data are available at 3-hourly intervals globally, in near real time, therefore the product promises to be a useful data source for operational hydrological applications, as well as many others. Comparisons over RSA between 24 hour accumulated TRMM rainfall estimates, matching the timing of SAWS daily rainfall catch, show that there are unfortunately some mismatches. The work reported here is taken from an ongoing Water Research Commission study and illustrates the links between these two data sources based on comparisons over a 10-year period, highlighting both the limitations and benefits of the TRMM product.

## Introduction

Rainfall is a fundamental forcing variable required for hydrological modelling. Satellite derived rainfall products offer the advantage of being both freely and easily available in a timeous manner for such modelling efforts, however the indirect connection between the measurements recorded by the satellite borne instruments and rainfall necessitates care in the use of these data.

In this paper we present some initial results of a comparison between rainfall derived from the TRMM 3B42RT product and block averaged rainfall from daily rain gauges. We show that while there are some similarities in the gross behaviour of the two rainfall estimates, there are also some significant differences which require a careful treatment of the TRMM data before using it.

## Methodology and results

To obtain spatial daily rainfall averages matching the TRMM footprint, an estimate of the gauge rainfall on each TRMM block (0.25° square) was determined over RSA where raingauge daily data were recorded, using the Multiquadric interpolation code developed by Pegram and Pegram (1993). This FORTRAN code was wrapped in a Python package interface to make it more convenient to use in conjunction with the Python based workflow. At the core of the Multiquadric approach is the calculation of weights to multiply each gauge value in a given block and thereby obtain the block average rainfall. The configuration of gauges on a day within a given block may change from day to day (depending on missing records). Since the gauge configuration defines the weights, it was necessary to compute the weights for each wetted TRMM block on each day of the 10 year analysis period over RSA.

The product of the Multiquadric analysis was a NetCDF file containing a three dimensional array of block averaged daily rainfall totals for each TRMM block on all 3682 days in the analysis period running from 2000-03-01 until 2010-03-31. This overlap period was chosen because the TRMM dataset runs from 2000-03-01 until April 2015, while the gauge dataset spans the period 1850-01-01 until 2010-03-31.

A similar dataset of daily rainfall accumulations was developed for the TRMM data, being careful to match the accumulation times of the TRMM in UTC to those of the gauge reporting periods in SAST (a 2 hour shift). It was important to ensure that the TRMM accumulations represented the 24 hour accumulation reported at 08:00 SAST.

Once all weights were calculated for each block, they were arranged in a matrix relating gauge weights in each block with individual gauges. This matrix ensures that the correct information is collected in each column of block averages.

If the gauge population of a particular block changes, then its gauge weights were recalculated for that day, as mentioned above. Figure 1 shows TRMM blocks populated by gauges over part of the Western Cape region, 32°S to 35°S by 17.5°E to 20°E, to give an idea of the variation of gauge density in TRMM blocks.

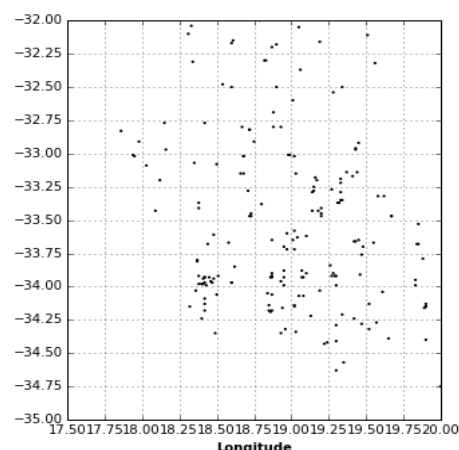


Figure 1. TRMM grid and rain gauge sites over the Western Cape region 32°S to 35°S by 17.5°E to 20°E.

The TRMM product comes in 2 forms: uncalibrated and post-calibrated. Figure 2 gives a comparison of daily totals from block-averaged gauges and TRMM on 3 March 2000. Panel (a) shows the rainfall amount estimated by the uncalibrated TRMM algorithm -

uncalibrated means the rainfall estimates are made using only satellite data and retrieval algorithms. Panel (b) shows the block averaged gauge rainfall, with those grid blocks containing no data coloured grey. Panel (c) shows the post-calibrated TRMM estimate. This is the uncalibrated estimate of panel (a) adjusted by NASA via a quantile transform of relatively sparse gauges to match the gridded GPCP rainfall product (Huffman et al., 2010). Note the general agreement on raining areas indicated by gauges, but with many more zeros in the gauge estimates. Panel (c) differs from (a) in the lower left part, where very heavy rainfall in (a) has been reduced in (c). Comparisons of these with panel (b) shows that the TRMM rainfall was largely mythical, as only 4 blocks recorded gauge rainfall in this area on that day. Not all days are as bad as this, but it is a cause for concern.

The total rainfall accumulations for the 10 year analysis period as estimated by each product are shown in Figure 3. The general patterns and amounts in the Summer rainfall region show good agreement, but the gauge values show considerably more noisy variation. This variation is explained by the inequality of available record lengths which strongly affects the total. In addition, note the artefacts in panel (c) from the NASA post-calibration process, particularly in the Southern and Eastern parts, which are very 'blocky'. This suggests that it might be wise to rescale the uncalibrated rather than the post-calibrated TRMM product. However, even with this correction, the region surrounding the Cape Peninsula are markedly underestimated by both TRMM products.

Figure 4 shows the mean rainfall values for the 10 year analysis period as estimated by each product. The general patterns and amounts show good agreement, as in Figure 3. The values in (b) are mostly low due to the large proportion of zeros in the dataset (missing values have been accounted for). The gauge estimates are smoother than the totals shown in figure 3 since the length of record has a much smaller effect in this case. Particularly noticeable in panel 4(a) are three isolated very high counts in small areas in Gauteng. They appear to be associated with large water-bodies.

Figure 5 gives a comparison of time series for a single grid block in the Eastern Cape centred on (30.875 S, 27.625 E). The figure shows the time series for TRMM, gauge-block average and rescaled TRMM over a single year of data. There is good agreement on the longer wet and dry periods and the magnitudes of rainfall. However, there are many mismatches evident in the detail which reduce the correlation between the Gauge Block averages and TRMM time series to about 0.5.

The reason for providing Figures 5 is illustrated by comparing the three different Empirical Cumulative Distribution Functions (ECDFs) in Figure 6. The dry probabilities of the gauge estimates are much higher than the dry probabilities of the TRMM estimates and

there is also a marked difference between the gauge and TRMM distributions for the higher rainfall amounts.

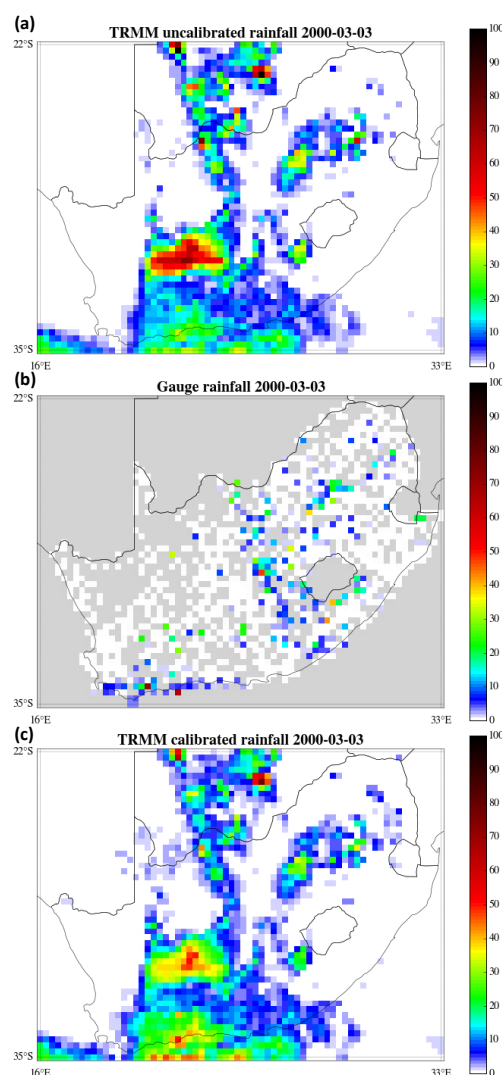


Figure 2. Comparing TRMM and gauge estimates on 3 March 2000. (a) raw TRMM (b) spatially averaged gauge catch (c) post-calibrated TRMM

It is interesting to check the cross-correlations between the uncalibrated TRMM and the block-averaged gauges. In 4 provinces, areas with different climates were chosen - Gauteng, Kwazulu-Natal, Western Cape and Limpopo - to compare the TRMM and block averaged precipitation.

The sites are shown in Figure 7, where the darkness of the circles centred in the  $0.25^\circ$  blocks indicates the number of gauges available to be averaged.

It was found that  $R^2$  values between TRMM and Block Averaged Gauge Data (BAGD) ranged from 0.06 to 0.46 for daily totals, a disappointingly low result. In contrast the accumulations into pentads and monthly totals move the  $R^2$  values up to 0.4 and 0.7 respectively. Figure 8 shows the scatter-plot for Block 5 in Gauteng, typical of daily data.

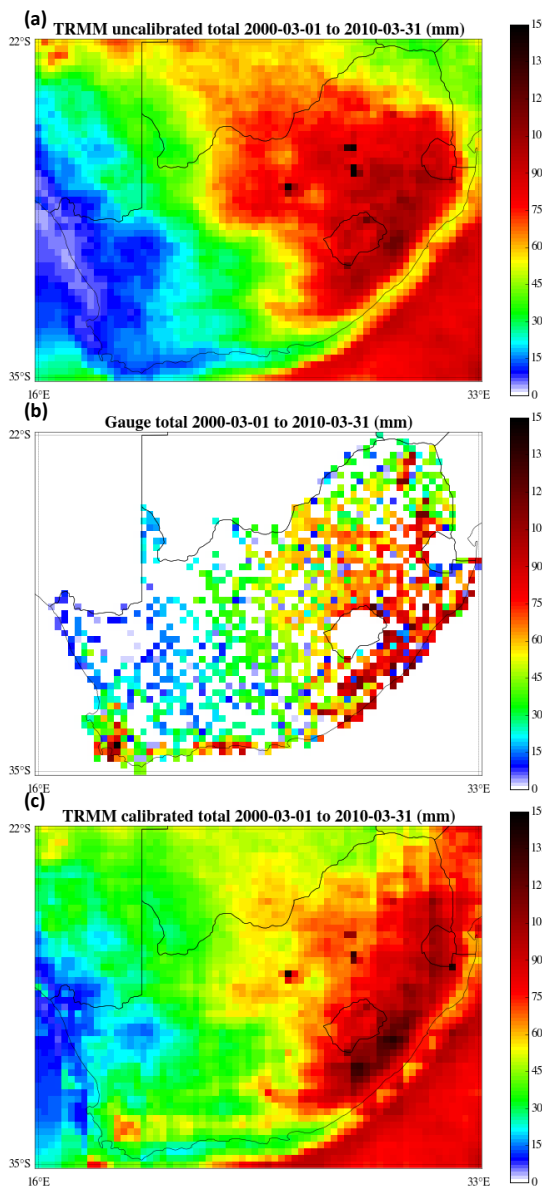


Figure 3: The total rainfall accumulations for the 10 year analysis period as estimated by each product. (a) raw TRMM, (b) spatially averaged gauge catch (c) post-calibrated TRMM

By contrast the monthly accumulations are much improved as shown in Figure 9 for the same block; the bias has reduced and the  $R^2$  increased.

Unfortunately the rest are not as good as that. For example, Figure 10 compares the monthly totals in Block 2 in the Western Cape, where TRMM seriously underestimates the rainfall, confirming the observations made about this feature in Figure 3. In Figure 10,  $R^2$  is reasonably high at 0.67, but the slope is 0.296, indicating an average bias of about 1/3. To confound the problem, Block 7 in the Western Cape (not shown) has the same  $R^2$ , but the slope is 1.41, nearly the mirror of Block 2. The relationship between TRMM and gauges is therefore very site-specific, likely due to topography and possibly the number of gauges in each block.

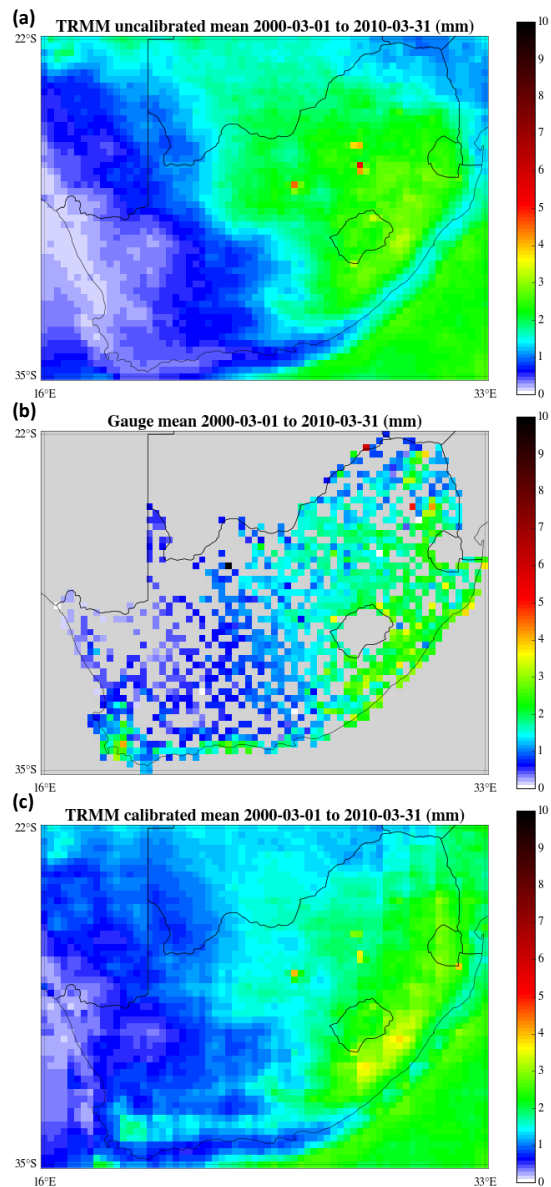


Figure 4: The mean rainfall values for the 10 year analysis period as estimated by each product (a) raw TRMM, (b) areally averaged gauge catch (c) post-calibrated TRMM.

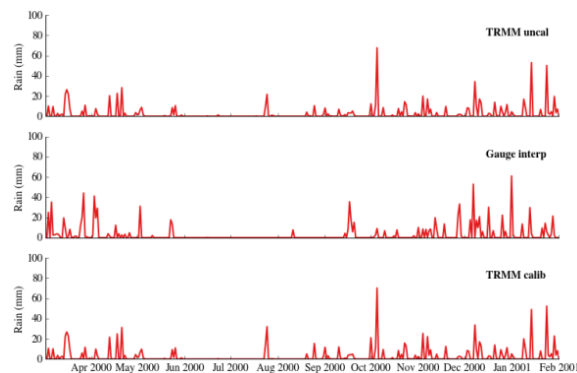


Figure 5: Comparison of time series for a single grid block centred on (30.875 S, 27.625 E).

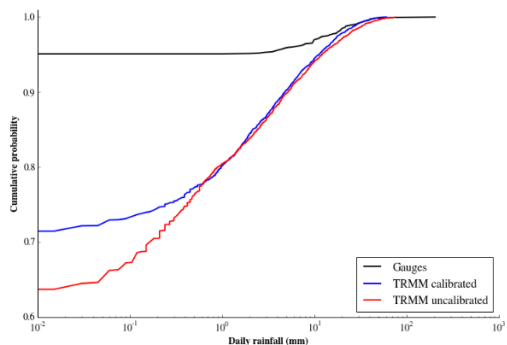


Figure 6. Empirical Cumulative Distribution Functions (ECDFs) for gauge averages over a block (black curve), uncalibrated (red curve) and post-calibrated (blue curve). Interestingly, the post-calibration increases the dry probability (but not to the level of the gauges).

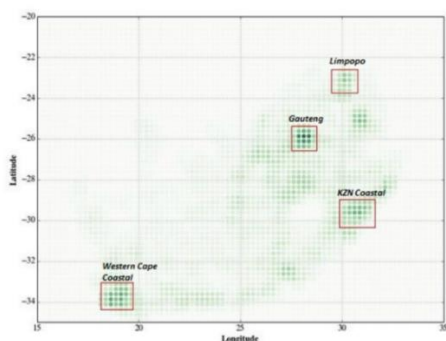


Figure 7. 4 areas in RSA with different climates in which to compare the TRMM and block averaged precipitation.

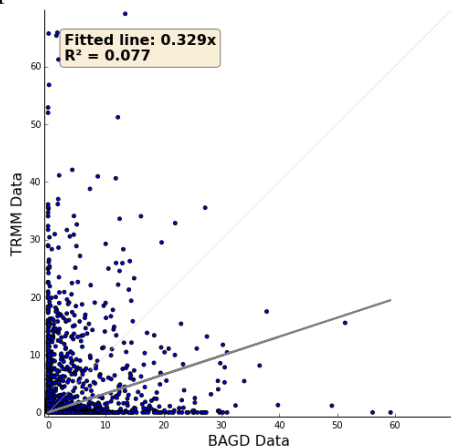


Figure 8 scatter-plot between TRMM and BAGD daily data for Block 5 in Gauteng.

**Conclusion**

In summary, the bias, as measured by the regression lines of the raw data is low for the daily values (0.3 to 0.5) and is much improved for the monthly totals (0.7 to 0.9). On the down side, the relationships are very site specific, so require great care in matching corrections to locations. In addition, the daily data do not yield helpful correction slopes (see figure 8 for example) so a plausible solution to the scaling problem is to use the monthly relationships to scale the daily values. Unfortunately, this ruse does not solve the problem on the mistiming of the daily TRMM totals

when compared to the BAGD values. In a more formal manner, in place of scaling, it is probable that quantile-quantile transforms based on curves like those in Figure 6 will be used, ensuring that besides scaling the wet days, the wet/dry proportions are correctly captured, but that is a nicety.

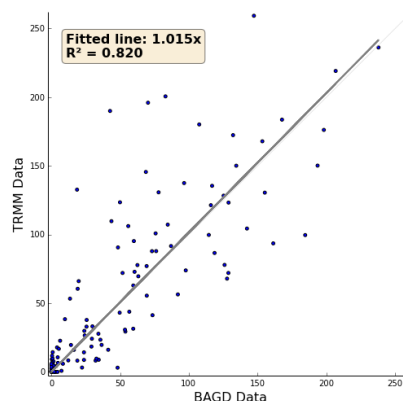


Figure 9 scatter-plot between TRMM and BAGD monthly data for Block 5 in Gauteng.

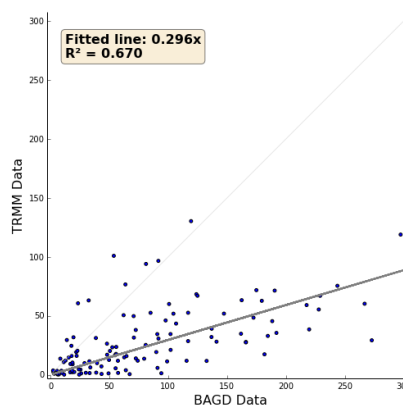


Figure 10 scatter-plot between TRMM and BAGD monthly data for Block 2 in Western Cape.

Given the above, it is likely that TRMM data (and the output of its successor GPM) will be useful for large-scale hydrology and agriculture, particularly at the monthly scale, in contrast to daily. Thus crop monitoring and reservoir storage calculations will benefit, but not Flash Floods. The short conclusion is that TRMM is useful for hydrology in a coarse way, but poor in detail.

**References**

Huffman, G J, Adler, RF, Bolvin, DT, and Nelkin, E J (2010). *Satellite Rainfall Applications for Surface Hydrology – The TRMM Multi-Satellite Precipitation Analysis (TMPA)*. Springer Science+Business Media B.V.  
 Pegram, GC and Pegram, GGS (1993). Integration of rainfall via multiquadric surfaces over polygons. *J. Hydraul. Eng.*, ASCE, 119(2):151–163  
 Pegram, GGS and DS Sinclair (2014) Report to WRC on Deliverable 4 of project K5/2241, "Revision of the Mean Annual Precipitation (MAP) estimates over Southern Africa"

## Weather effects on maize production in the eastern Free State: Case study of 2013/14 and 2014/15 agricultural seasons

Moeletsi, ME<sup>1</sup>, Nape M·Tongwane MI, Mazibuko S, Masupha T

Agricultural Research Council - Institute for Soil, Climate and Water, Private Bag X79, Pretoria, 0001, South Africa

### Abstract

The study investigated the agroclimatological suitability of maize in the eastern Free State during the 2013/14 and 2014/15 agricultural seasons. Climate data for these two summer rainy seasons was sourced and missing values were patched. A series of plantings of maize was carried out on farmers' fields from the start of the rains until the mid-December each year. The drought during the second season resulted in significantly lower yields than in the 2013/14 year. The other climate hazard of concern was first frost date which had a negative impact on production from the late planted trials hence the need for early planting in the region.

Keywords: Cessation of frost/rains, onset of frost/rains, frost-free/rainy season, drought

### Introduction

Climate variability and climate change are affecting ecosystems and threatening South Africa's food security, economic system, livelihoods, socio-economic development and the availability of natural resources (FAO, 2010). Climate has always varied from one season to another, but in more recent times the magnitude of inter-seasonal and intra-seasonal variability has been increasing. Crop yield varies from one season to another due to variation in climate during the growing season (Kumar *et al.*, 2004). There are also many non-climatic factors that influence yield like the cultivation techniques, fertilization practices, cultivars and farm management practices (Zhang, 2004). Understanding how climate influences the yields can be helpful in designing policies that aim at reducing climate vulnerability and improving food security (Sun *et al.*, 2006). The aim of the study was to analyse the weather that influenced the growth and development of maize during the two agricultural seasons (2013/14 and 2014/15).

### Methods

Maize (*Zea mays* PAN6479) was planted from the 1<sup>st</sup> November until the end of December during each ten days period (dekadal basis) depending on the soil moisture level. PAN6479 cultivar requires around 1330GDD from planting to maturity. Maize plots of size 5m X 5m were planted at three selected sites in the Maluti-a-Phofung Municipality of the Eastern Free State (Table 1). Weather data (rainfall, temperature and evapotranspiration) was obtained from the nearest ARC-ISCW weather stations (Hika for Farm 1 and 2; Kestell for Farm 3). Climate records for the Hika station were complete while Kestell weather station had missing values during November and December 2014. Missing data was patched using inverse distance weighting for rainfall and normal ratio for temperature data (Tang *et al.*, 1996).

Onset of rainfall was determined as the day on which 25mm of rainfall was obtained in ten days followed by 20mm in the next 20 days (Tadross *et al.*, 2005).

**Table 1: Weather stations and farms geographical information**

Farm / Station #	Latitude	Longitude	Altitude (m)	Seasonal Rainfall (mm)	
				2013/14	2014/15
Farm 1	28.30270	28.89167	1715		
Farm 2	28.27796	28.83449	1641		
Farm 3	28.43120	28.89669	1746		
Hika	28.27796	28.83449	1641	494	480
Kestell	-28.3142	28.70859	1693	519	504

<sup>1</sup> Corresponding author: Tel: +27 12 310 2537. Fax: +27 12 323 1157. E-mail: [moeletsim@arc.agric.za](mailto:moeletsim@arc.agric.za)

To determine the frost incidence, a temperature threshold of 0°C was used (Tait & Zhang, 2003). Agricultural drought for each of the planting dates was determined using Water Requirement Satisfaction Index (WRSI) which requires dekadal rainfall, dekadal evapotranspiration, profile water holding capacity, crop coefficients and growing period (Senay & Verdin, 2000). Maize was harvested in June in both seasons and grain yield was determined in tonnes per hectare at a moisture content of 12.5%.

## Results and Discussion

The onset of rains occurred during 1<sup>st</sup> dekad of October during 2013/14 season while in 2014/15 season it occurred in the 1<sup>st</sup> dekad of November, a month later, and with a higher amount of rainfall. WRSI index ranged from 60 to 100 for the 2013/14 agricultural season with corresponding yield values

of 1.4 to 6.5 t ha<sup>-1</sup> at Farm 1, 2 and 3. The rate of accumulation of degree units did not show any major variances in the two seasons with maize growing periods not differing significantly (Fig. 1). Early (< 10 November) and mid (> 10 December) planted maize trials matured later (longer growing period) than maize trials planted from mid-November to early December due to relatively lower temperatures during the growing period. Planting periods with high WRSI (low drought occurrences) corresponding to relatively higher production per area. During the 2014/15 agricultural season, agricultural production in most of the planting periods was relatively low from all the trial sites with values ranging from 0.3 tha<sup>-1</sup> to 2.5 tha<sup>-1</sup>. Maize planted in mid-December and later experienced frost damage (end March 2014 and mid-April 2015) contributing to low production and poor quality grain.

**Table 2: Yields for different planting dates**

Farm	Yield(tons/ha) for 2013/14 planting dates						Yield(tons/ha) for 2014/15 planting dates					
	23/10	04/11	14/11	26/11	02/12	11/12	05/11	18/11	26/11	03/12	10/12	18/12
1	4.2	4.8	4.5	3.7	2.5	3.2	2.5	1.3	2.2	1.6	0.6	0.8
2	5.4	5.1	3.4	2.2	2.1	1.4	1.5	2.4	0.3	1.4	1.1	0.9
3	4.7	6.5	3.1	2.8	2.2	1.7	n/a	n/a	2.5	1.78	1.6	1.0

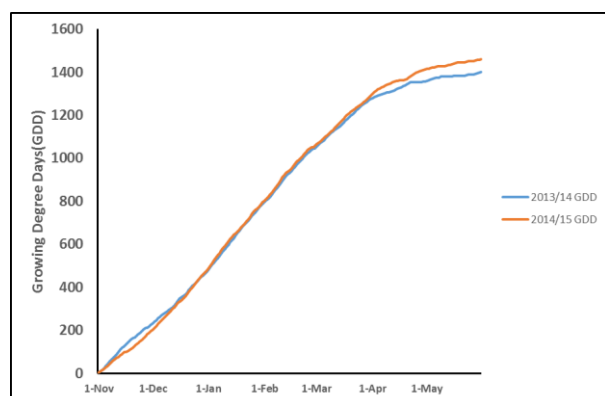


**Figure 2: Cumulative heat units accumulation from November to May**

## Conclusions

Weather conditions experienced during the growing period play a vital role in determining the maize crop production for rainfed regions. In the eastern Free State, the timing of planting of maize is important due to extreme weather events like frost which are hazardous to optimum crop production.

## Acknowledgements

The work was funded by the Department of Agriculture, Fisheries and Forestry (DAFF)-GW57/011. Gratitude to farmers in the Maulti-a-

Phofung Municipality for their cooperation while undertaking trials on their farms.

## References

- FAO, 2010. Global survey of agricultural mitigation projects. Mitigation of Climate Change in Agriculture Series 1. United Nations Food and Agricultural Organisation, Rome, Available at <http://www.fao.org/> last viewed 20/08/2015
- Kumar, K.K., Kumar, K.R., Ashrit, R.G., Deshpande, N.R., Hansen, J.W., 2004. Climate impacts on Indian agriculture. *International Journal of Climatology* 24: 1375-1393.
- Tadross, M.A., Hewitson, B.C., Usman, M.T., 2005. The interannual variability of the onset of the maize growing season over South Africa and Zimbabwe. *Journal of Climate* 18:3356-3372.
- Tait, A., Zheng, X., 2003. Mapping frost occurrence using satellite data. *Journal of Applied Meteorology* 42: 193-203.
- Tang, W.Y., Kassim, A.H.M. & Abubakar, S.H., 1996. Comparative studies of various missing data treatment methods - Malaysian experience. *Atmospheric Research* 42(1-4): 247-262.

Senay, G.B. & Verdin, J., 2003. Characterization of yield reduction in Ethiopia using a GIS-based crop water balance model. *Canadian Journal of Remote Sensing* 29 (6): 687 - 692.

Sun, L., Li, H., Ward, M.N., 2006. Climate variability and corn yields in semiarid Ceará, Brazil.

*Journal of Applied Meteorology and Climatology* 46: 226-240.

Zhang, J., 2004. Risk assessment of drought disaster in the maize-growing region of Songliao Plain, China. *Agriculture Ecosystems & Environment* 102: 133-153.

## Solar UVR instrument inter-comparison focussing on measurement interval recording setting and solar zenith angle as important factors

Caradee Y. Wright<sup>a,b\*</sup> and Derek Griffith<sup>c</sup>

<sup>a</sup>Environment & Health Research Unit, South African Medical Research Council, Pretoria, South Africa.

<sup>b</sup>Department of Geography, Geoinformatics and Meteorology, University of Pretoria, Pretoria, South Africa.

<sup>c</sup>CSIR Defence, Peace Safety and Security, Pretoria, South Africa.

\*Corresponding author. Email: [cwright@mrc.ac.za](mailto:cwright@mrc.ac.za). Tel: +27 82 677 4037

### Abstract

Solar ultraviolet radiation (UVR) data for matching time periods between November 2014 and February 2015 were recorded by two instruments, namely a UVR biometer and a Davis UVR sensor, and their data were compared. Several checks and challenges were identified during the data preparation stage. The measurement interval of the biometer was changed from 30-minutes to 1 hour which prompted the recalculation of readings measured by the Davis UVR sensor for the periods affected. On average, the Davis UVR sensor slightly overestimated solar UVR levels when compared to the biometer data and this relationship was strongest for small solar zenith angles (SZA) when the sun was high in the sky. Further research is necessary to investigate the influence of other external factors that may influence the differences in the two instruments' solar UVR measurements, such as instrument hardware in the form of fins on the Davis UVR sensor housing.

**Keywords:** solar ultraviolet radiation, solar zenith angle, Pretoria.

### 1. Introduction

Solar ultraviolet radiation (UVR) has beneficial and harmful effects on ecosystems, animals and humans. Monitoring ambient (surface) solar UVR is important to detect trends and patterns, particularly in the context of global stratospheric ozone depletion. Various instruments are commercially available for science-grade measuring of solar UVR. Comparing measurements made by different instruments helps one understand the importance of critical factors and related considerations, to make meaningful deductions from the data.

By comparing two solar UVR instruments, namely, a UV biometer and a Davis Vantage Pro2 UVR Detector, we look at an important factor influencing ambient solar UVR, namely SZA, and its impact on solar UVR measurements and we highlight some of the important checks to make when comparing data measured by different instruments for the same time period.

### 2. Data and Methods

Data were collected from two instruments located at the South African Weather Service (SAWS) Head Office and the Council for Scientific and Industrial Research (CSIR) Defence Peace Safety and Security (DPSS) Building in Pretoria (25.7° S, 28.2° E, altitude ~ 1 340 m), respectively.

A UV Biometer (model 501), comprising a Robertson-Berger pattern UVR detector, digital recorder and control unit, is used to measure ambient solar UVR levels at the Pretoria SAWS head office. The UV Biometer spectral response closely mimics the McKinley/Diffey Erythral Action Spectrum (280-340 nm) (CIE, 1987). Calibration of the UV Biometer enables the logged values to be converted into MED (Minimal Erythral Dose, where 1 MED = 210 Jm<sup>-2</sup> for skin phototype I) per hour or per 30-minutes (see Table 1 for 1-hr versus 30 minute measurement periods). The SAWS instrument measurement interval was changed

for unknown reasons and dictated the interval period used for the inter-comparison.

Recently, the Pretoria UV Biometer was inter-compared with a travelling standard instrument calibrated against the fast scanning spectro-radiometer SPECTRO 320D NO 15 that has traceability to the International Bureau of Weights and Measures. Analysis found the difference in the instrument pre- and post-calibration was less than 4%.

The Davis Vantage Pro2 UV detector comprises a transducer which is a semiconductor photodiode with a spectral response that matches the McKinley/Diffey Erythral Action Spectrum. It includes a diffuser which provides good cosine response and multiple hard-oxide coatings that ensure that the interference filter provides the required spectral response. Each sensor is calibrated against a Yankee Environmental Systems Ultraviolet Pyranometer Model UVB-1 in natural, summer daylight. The unit's measurements are displayed in MED units (1 MED = 210 Jm<sup>-2</sup>) at 1-minute intervals. These were converted into MED per 30 minutes or per 1 hour to match the SAWS biometer recording interval based on the measurement periods outlined in Table 1.

**Table 1.** Dates and times of 1-hour and 30-minute measurements periods as determined by the SAWS UV biometer measurement periods.

	Start date	Start time	End date	End time
1-hr interval	1-11-2014	24:00	30-11-2014	24:00
30-min interval	1-12-2014	1:00	5-12-2014	10:30
1-hr interval	5-12-2014	11:00	12-01-2015	8:00
30-minute interval	13-01-2015	8:30	31-01-2015	24:00

Data from the two streams of the SAWS and Davis instruments were compared, based on identical

measurement periods and for the same durations, using linear regression. Upon observation of this initial result, it became apparent that SZA may be an important influencing factor for differences in instrument sensitivity. Hence, data were compared by SZA in three bands from small to large SZA: <35° (sun high in the sky); <70° and >35°; and < 105° and > 70° (sun low in the sky). SZA data was obtained from the Davis instrument. Linear regression was applied to determine for which SZA band correlation between the two instruments was the strongest. Analyses were carried out in Microsoft Excel 2013 and spearman correlation tests were made using STATA IC 13.1. During the analyses, notes were made about checks and challenges when making inter-instrument comparisons and these results are also presented.

**3. Results and discussion**

A total of 2 416 data points from each instrument were included in this analysis of three months’ data. Careful procedures were executed to ensure that the identical measurement period and duration were matched for both data streams. All units are in MED/30 min or MED/hour.

**3.1 All data together for both instruments**

Figure 1 depicts the correlation between all data points for the SAWS and Davis instruments for all matching time periods. A good fit was evident with tighter correlation at lower MED values and more scatter with increasing MED values. At this early stage of analysis it was evident that the fit was not perfectly linear; there was a slight bowing in the trend line, suggesting that correlation between the two instruments’ data points may vary by some external factor. Since SZA is the most obvious factor changing in a consistent manner based on the movement of the sun and thereby influencing solar UVR levels, this was identified as the factor for further analysis. Other factors such as cloud and aerosols usually cause erratic changes in solar UVR levels.

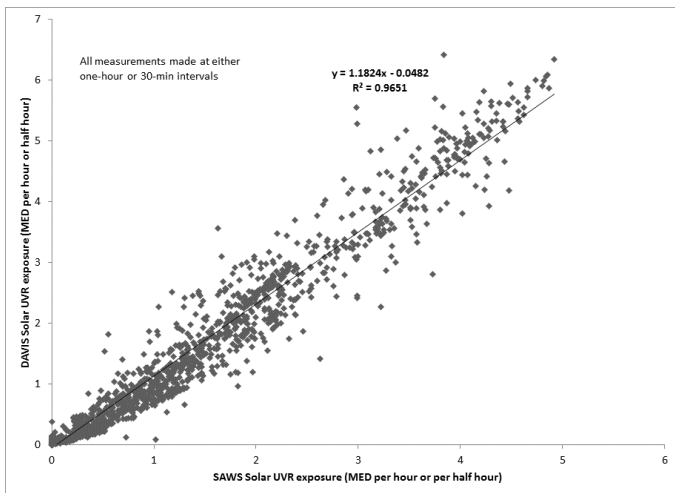


**Figure 1.** Correlation between SAWS and Davis data for all data points.

The Davis values were calculated as a percentage of the SAWS values and a mean of 107.12%, with a range of 10.75%-613.44% was found. Therefore, it seemed that the Davis instrument over-estimated solar UVR levels as

measured by the SAWS instrument by, on average, 7%. The Spearman correlation test results for the Davis versus SAWS data returned  $p = 0.9694$  ( $p < 0.001$ ).

**3.2 Differences in measurement intervals**

Before focussing on analyses using SZA, we considered the challenges of working with data derived from different measurement periods (i.e. measurement intervals set to 30 minutes versus 60 minutes). Figure 2 illustrates the challenges of trying to plot a time series using data from different measurement periods.

In general, there are more data points for the 30-minute measurement periods (two per hour) and MED values are half that of the 1-hourly measurements, as one would expect. A logical solution to this problem would be to merge MED values for 30-minute periods to create a 1-hour MED value instead and then be able to make comparisons across the whole measurement campaign. The disadvantage of doing so is that the finer resolution changes in solar UVR captured by the 30-minute measurements are then lost.

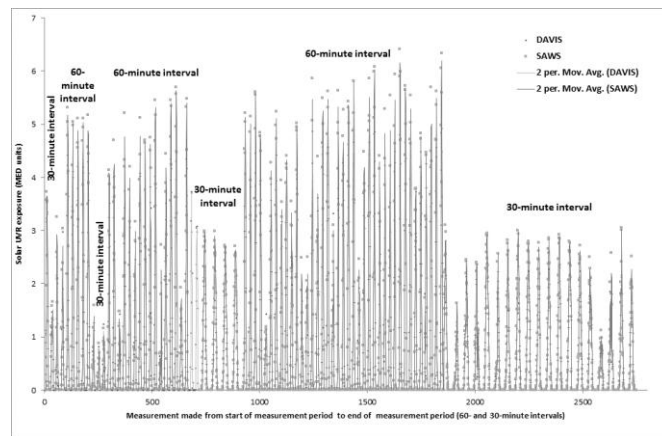


**Figure 2.** Quasi-time series plot to show changes in measurement intervals from 30- to 60-minute intervals during the measurement campaign driven by the changes made to the SAWS instrument measurement interval and with the Davis instrument data calculated to match the SAWS measurement interval.

**3.3 Hourly data by SZA**

The data sets were then split into hourly and half-hourly data sets to further investigate the role of SZA in the correlation coefficients of the two data sets. In so doing, one can see that the strength of the correlation is slightly stronger when the sun is low in the sky (large SZA) compared to when the sun is high in the sky (small SZA).

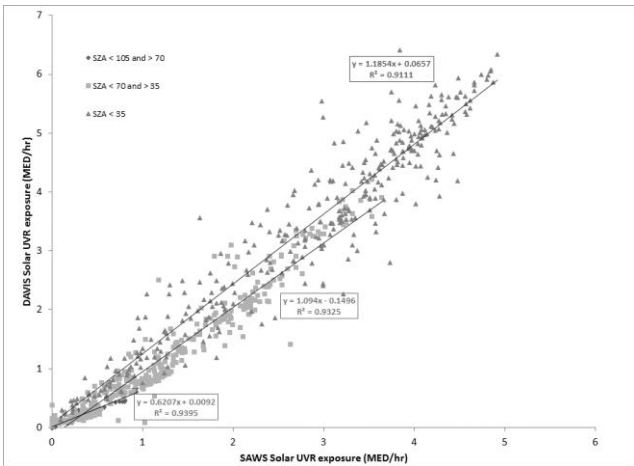


**Figure 3.** Correlation between SAWS data and Davis – hourly interval data only – by SZA band.

This may partly be explained by the location of the Davis UVR sensor on the meteorological station (Figure 4). It may be partially obscured by the rain gauge and by the pole on which the station is mounted, however, this needs further investigation as well as in relation to location of the sun’s direct rays. The SAWS biometer sits on an unobscured tray and can scan the whole sky all day (Figure 5).



**Figure 4.** Location of the DAVIS UVR sensor (white dome in the centre of a black housing with small black fins on its rim indicated by the black arrow) on the DAVIS instrument in relation to surrounding physical obstructions.



**Figure 5.** Location of the SAWS biometer on the roof of SAWS Head Office in Pretoria.

**3.4 Half-hourly data by SZA**

A similar pattern of strength in correlation by SZA using the half-hourly data was found. R-squared values were highest for SZA <70° and > 35°, so roughly when the sun is midway between the horizon and directly above. While still a fair correlation, the lowest r-squared value was for when the sun was highest in the sky; the same finding as for the hourly readings in Figure 3. A possible reason for there not being a stronger correlation would be an error in the cosine response of the Davis UVR sensor which is specified as accurate to +- 4%. Such sensors are also prone to changes in response with temperature, which would also tend to vary in a fashion well-correlated with SZA.

**3.5 Checks and challenges**

When making inter-comparisons of solar UVR readings from two different instruments, the first check was to consider the specifications of both instruments. Here, both instruments were measuring solar irradiance closely matched to the Erythemal Action Spectrum. The second check was to scrutinise the measuring unit of both instruments. In our case, both instruments were providing output in MED units where MED was fortunately defined as 210 Jm<sup>-2</sup> for both data sets. This may not have been the case, since MED is usually defined by skin phototype and, unlike SED (Standard Erythemal Dose) unit which is always 1 SED = 100 Jm<sup>-2</sup>, 1 MED may range from 210 Jm<sup>-2</sup> for skin phototype I (fair skin, light eyes and hair) to 510 Jm<sup>-2</sup> for skin phototype IV (Fitzpatrick, 1986).

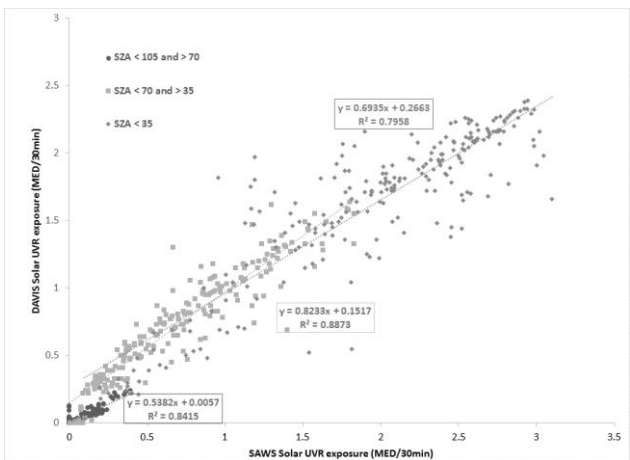


**Figure 5.** Correlation between SAWS data and DAVIS – half-hourly interval data only – by SZA band.

The first surprise arose when we plotted a time series of the raw data and noticed periods when data points were about half the amplitude of the highest data points. It became apparent that SAWS has changed the measuring interval and hence we needed to recalculate the Davis data accordingly.

The final investigation we made was a more detailed analysis of the influence of SZA on the relationship between the solar UVR data measured by the two instruments. We suspected that the two instruments’ housing, location and orientation may have contributed to a non-perfect 1:1 relationship. Specifically, we were interested in the ‘fins’ arranged on the rim of the Davis instrument.

These fins are described by the manufacturer ‘to aid in aligning the sensor with the sun’s rays’ (Davis, 2010). It therefore made sense to consider the role of SZA in the correlation of solar UVR measurements from the two instruments. Having found that the Davis instrument tended to overestimate UVR levels, and that the correlation between Davis and SAWS data was strongest for low-to-moderate solar UVR levels when the sun is not directly overhead, do not help to explain the influence of the fins. However, the relatively good r-squared values for all SZA do confirm that the Davis instrument measures solar UVR levels reasonably accurately when compared to the SAWS instrument (if we assume that the SAWS biometer is accurate).

#### 4. Conclusions

Comparing solar UVR data measured by different instruments is possible, although careful consideration must be given to instrument set-up and location, measurement unit, recording interval, exposure calculations and the plotting of meaningful data on graphs.

#### 5. Acknowledgements

The South African Weather Service is gratefully acknowledged for provision of solar UVR data. Patricia Albers (South African Medical Research Council) is thanked for assisting with drawing plots.

#### 7. References

- CIE, 1987. A reference action spectrum for ultraviolet induced erythema in human skin. *CIE Journal* 6, 17-22.
- Fitzpatrick, TB, 1986. Ultraviolet-induced pigmentary changes: Benefits and hazards. *Curr Probl Dermatol*. 1986;15:25-38.
- Davis Instruments, 2010. Vantage Pro2 Accessories UV Sensor, DS6490 (Rev. G, 29/11/2010), 1-2.

# PREDICTABILITY OF THE INTRA-SEASONAL RAINFALL CHARACTERISTICS VARIABLES OVER SOUTH AFRICA

Steven Phakula <sup>\*1,2</sup>, Willem A. Landman <sup>2,3</sup> and Asmerom F. Beraki <sup>1</sup>

<sup>1</sup> South African Weather Service, Pretoria, South Africa, [steven.phakula@weathersa.co.za](mailto:steven.phakula@weathersa.co.za)

<sup>2</sup> Department of Geography, Geo-informatics and Meteorology, University of Pretoria, Pretoria, South Africa

<sup>3</sup> Council for Scientific and Industrial Research, Pretoria, South Africa, [walandman1981@gmail.com](mailto:walandman1981@gmail.com)

## Abstract

Aspects of seasonal forecast skill of the SCM and ECHAM4.5 general circulation model (GCMs) are assessed over South Africa. The GCMs output is configured to predict low and high number of rainfall days at South African Weather Service stations exceeding different threshold values for the summer rainy seasons and to predict the onset of the rainy seasons for eight homogeneous rainfall regions of South Africa. Using canonical correlation analysis as statistical downscaling tool the forecast skill levels of both the coupled and uncoupled models are determined through retro-actively generated hindcasts. Both approaches have skill in predicting low and high number of rainfall days exceeding different threshold values for the summer rainy seasons as well as the onset of the rainy seasons for the homogeneous rainfall regions.

**Keywords:** Retro-active validation, Forecast skill, Area-averaged ROC scores, Reliability diagrams.

## Introduction

Southern Africa is a region of significant rainfall variability on a range of temporal and spacial scales and is prone to extreme droughts and floods events (Usman & Reason, 2004). Examples include, the devastating floods in northeast South Africa and southern Mozambique during February/March 2000 and severe droughts of 1991/92, 2002/03 and 2003/04 over northern South Africa and surrounding areas (Cook *et al.*, 2004). Most of African countries depend significantly on rain fed agriculture, which is highly vulnerable to the amount and distribution of rainfall (Kijazi & Reason, 2005). According to Usman and Reason (2004) the occurrence of extreme dry (wet) conditions over southern Africa during the austral summer have been associated with high dry spell frequency (wet spell frequency). Previous studies showed that seasonal rainfall totals are predictable over South Africa (e.g. Landman *et al.* 2012). Very few studies of the predictability of the intra-seasonal rainfall characteristics variables such as onset of the rainy seasons over South Africa are documented. The purpose of this study

is therefore to assess the skill of the state-of-the-art forecasting systems in predicting low and high number of summer seasons rainfall days exceeding different threshold values and the onset of the rainy seasons over South Africa.

## Data and Methodology

The observed daily rainfall data from 563 stations over South Africa obtained from the South African Weather Service (SAWS) are used to calculate monthly and seasonal rainfall totals as well as indices of the number of rainfall days exceeding the threshold values of 1mm, 5mm, 10mm, 15mm, 20mm, 30mm, 40mm and 50mm for October to November (OND), November to January (NDJ), December to February (DJF) and January to March (JFM) summer rainy seasons over South Africa from 1982 to 2009. The predicted large-scale 850hPa geopotential heights for the above mentioned summer rainy seasons, which are taken from the hindcast simulations of the SAWS Coupled Model (SCM; Beraki *et al.*, 2014) and ECHAM4.5 (Roeckner *et al.*, 1996; Beraki *et al.*, 2015) GCMs are used as predictors in a statistical downscaling system.

Using the Climate Predictability Tool (CPT) developed at the IRI the hindcast outputs of both the coupled and uncoupled GCMs are first statistically recalibrated and downscaled to seasonal rainfall totals, then to number of days exceeding different rainfall threshold values and finally to the onset of the rainy seasons over South Africa by using model output statistics (MOS). Forecast skill levels of both GCMs are evaluated using retro-actively generated hindcasts through canonical correlation analysis (CCA). Retro-active forecast validation is a robust method to assess forecast model performance and give unbiased skill levels (Landman *et al.*, 2001). Two attributes of the downscaled forecasts are to be tested, namely, discrimination and reliability. For the former relative operating characteristics (ROC) is used and for the latter the attributes or reliability diagram is used. A high ROC score ( $>0.5$ ) indicates the models' ability to discriminate event from non-events. Furthermore, to test if the hindcasts are well calibrated the reliability diagrams is used to assess the extent to which forecast probabilities match observed frequencies. ROC and reliability plots are calculated for seasonal totals, rainfall thresholds and for seasonal onsets.

## Results and Discussion

Firstly, the forecast skill of both the SCM and ECHAM4.5 GCMs are assessed in predicting the seasonal rainfall totals for OND, NDJ, DJF and JFM seasons over South Africa. The area-averaged ROC scores greater than 0.5 in Figure 2 indicate that the 850hPa geopotential height fields produced by GCM initialized at 0, 1, 2, 3 and 4 month lead-times of both forecast systems have skill in discriminating wet or dry seasons from the rest of the seasons when predicting seasonal rainfall totals for the seasons considered. The higher skill scores is mostly found during NDJ and DJF seasons and this findings are agreement with Landman *et al.* (2012).

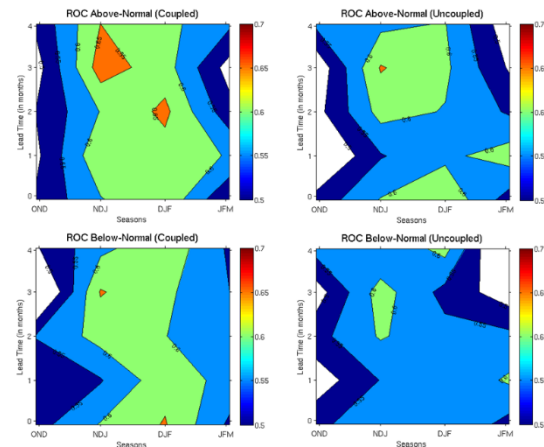


Figure 2. Area-averaged ROC scores of both the coupled and uncoupled GCMs in predicting OND, NDJ, DJF and JFM seasonal rainfall totals over South Africa from 1982 to 2009.

The forecast systems are also reliable in predicting seasonal rainfall totals. Reliability diagrams in Figure 3 shows that the 1-month lead-time hindcasts of both coupled and uncoupled forecasting systems possesses some reliability in predicting dry and wet conditions during DJF seasons. Although close to perfect reliability is obtained when the coupled system predicts wet conditions, both forecasting systems are overconfident in predicting dry seasons.

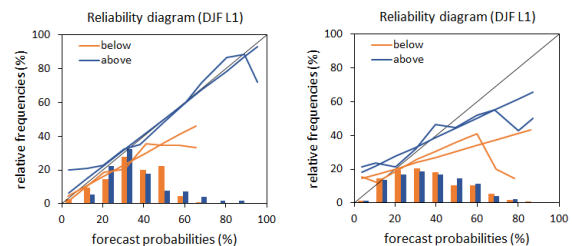


Figure 3. Reliability diagrams of both the coupled (left) and uncoupled (right) GCMs in predicting seasonal rainfall totals for DJF seasons from 1982 to 2009.

Secondly, the forecast skill of both sets (coupled and uncoupled) 850hPa geopotential heights at a 1-month lead-time is evaluated in predicting low and high number of rainfall days exceeding different threshold values for summer rainfall seasons over South Africa. The area-averaged ROC scores greater than 0.5 in Figure 4 indicate the models' ability to discriminate between a low

and a high number of rainfall days exceeding the different threshold values for the OND, NDJ, DJF and JFM summer seasons. The forecast skill of predicting low (high) number of rainfall days is however increasing (decreasing) with the higher rainfall threshold values.

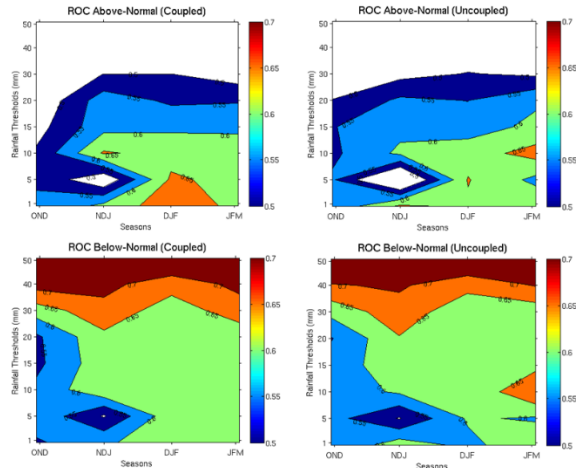


Figure 4. Area-averaged ROC scores of both the coupled and uncoupled GCMs in predicting high (Above-Normal) and low (Below-Normal) number of days exceeding different rainfall threshold values for the OND, NDJ, DJF and JFM seasons over South Africa from 1982 to 2009.

The forecast systems of both GCMs have some degree of reliability in predicting high and low numbers of rainfall days exceeding certain thresholds. The reliability diagrams in Figure 5 show good reliability for both systems, especially for the coupled model. However, for both models forecasts tend to be over-confident for high probability forecasts.

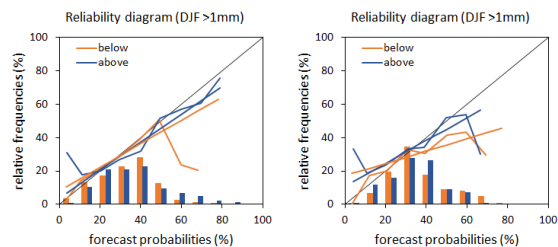


Figure 5. Reliability diagrams of both the coupled (left) and uncoupled (right) GCMs in predicting number of rainfall days exceeding 1mm for DJF seasons from 1982 to 2009.

Lastly, the skill of the 850hPa geopotential heights (1-month lead-time) of both coupled and uncoupled GCMs is tested in predicting the onset of the rainy seasons for all of the eight homogeneous rainfall regions of South Africa. The onset is defined here as the first month of a three month season on condition that the season consists of the wettest consecutive three months of the year as calculated over several decades (climatological values). According to our definition of onset, the onset month for region 1 is May, October for region 2 and 3, November for region 4, 5 and 6, December and January for region 7 and 8, respectively and are indicated with black arrows on the climatological annual rainfall circles in Figure 6.

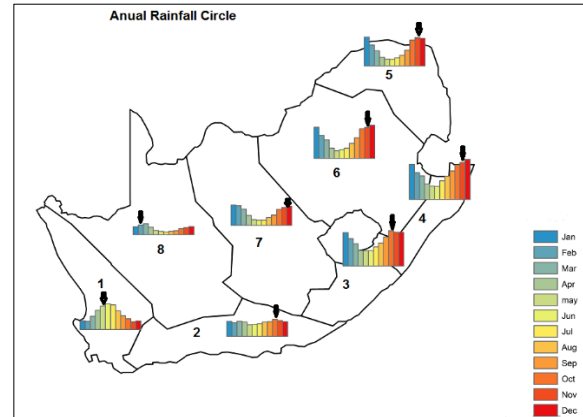


Figure 6. The eight homogeneous rainfall regions with their annual rainfall circle from 1982 to 2009.

Area-averaged ROC scores for both coupled and uncoupled GCMs have the skill scores above 0.5 for all the rainfall region's onset months (Figure 7), indicating the models ability to successfully discriminate between a good start (above-normal ) and a poor start (below-normal) rainfall totals for the first month of the 3-month season. The skill level is however different from region to region.

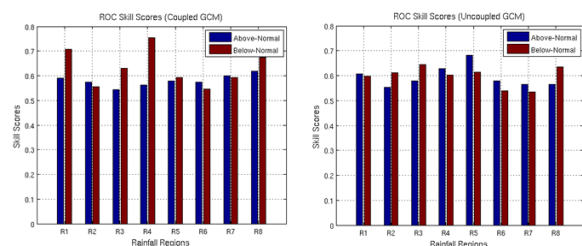


Figure 7. Area-averaged ROC scores of both coupled and uncoupled GCMs in predicting the onset of the rainy seasons for the 8 homogeneous rainfall regions of South Africa from 1982 to 2009.

The reliability diagrams in Figure 8 shows that the 850hPa geopotential height fields of both coupled and uncoupled forecasting systems are producing reliable downscaled onset forecasts for Region 1. As was found before, the below-normal cases are over-confident mostly for high probability forecasts.

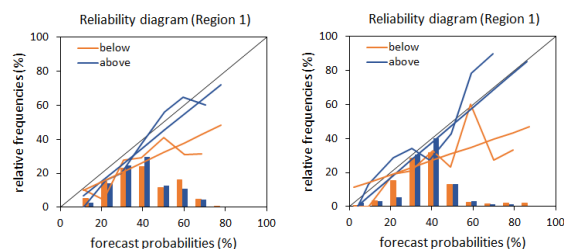


Figure 8. Reliability diagrams of both the coupled (left) and uncoupled (right) GCMs in predicting the onset of the rainy seasons for Region 1 from 1982 to 2009.

## Conclusions

The forecast systems considered have the skill in terms of discrimination and reliability to predict for a range of seasonal rainfall characteristics over South Africa. These characteristics include seasonal rainfall totals, number of rainfall days exceeding certain thresholds, and seasonal onset of the rainy seasons as defined here.

## Acknowledgements

The Applied Centre for Climate and Earth Systems Science (ACCESS) is acknowledged for funding this study. The South African Weather Service (SAWS) is acknowledged for providing both the rainfall and model data as well as computing facilities. Lastly the International

Research Institute for Climate and Society (IRI) for making available the CPT software package free.

## References

- Beraki A.F., D.G. DeWitt, W.A. Landman and C. Olivier. 2014, Dynamical climate prediction using an ocean-atmosphere coupled model developed in partnership between South Africa and the IRI, *Journal of Climate*, **27**, 1719-1741.
- Beraki A. F., W.A. Landman, D. DeWitt and C. Olivier. 2015, Global dynamical forecasting system conditioned to robust initial and boundary forcings: Seasonal Context, *Int. J. Climatol.*, Submitted.
- Cook C., C.J.C. Reason and B.C. Hewitson. 2004, Wet and dry spells within particularly wet and dry summers in the South African summer rainfall region, *Climate Research*, **26**: 17-31.
- Kijazi A.L. and C.J.C. Reason. 2005, Relationships between intraseasonal rainfall variability of Coastal Tanzania and ENSO, *Theoretical and Applied Climatology*, **82**: 153-176.
- Kijazi A.L. and C.J.C. Reason. 2011, Intra-seasonal variability over the northeastern highlands of Tanzania, *International Journal of Climatology*, DOI: 10.1002/joc.2315.
- Landman W.A., S.J. Mason, P.D. Tyson and W.J. Tennant. 2001, Retro-active skill of multi-tiered forecasts of summer rainfall over southern Africa, *Int. J. Climatology*, **21**: 1-19.
- Landman W.A., D. DeWitts, D.E. Lee, A. Beraki and D. Lotter. 2012, Seasonal rainfall prediction skill over South Africa: One- versus two-tiered forecasting systems, *Weather and Forecasting*, **27**: 489-501.
- Usman M.T. and C.J.C. Reason. 2004, Dry spell frequencies and their variability over southern Africa, *Climate Research*, **26**: 199-211.

# High Resolution Rainfall Modelling over the Eastern Escarpment of South Africa

Zane Dedekind<sup>1,2</sup> and Francois A. Engelbrecht<sup>1,2</sup>

1. CSIR Natural Resources and the Environment – Climate Studies, Modelling and Environmental Health, Pretoria, 0001, South Africa

2. Department of Environmental Sciences and Management, North West University, South Africa

## Abstract

Steep topography has an adverse effect on the realistic representation of the spatial and temporal distribution of rainfall totals within regional climate model (RCM) simulations, and even when measuring rainfall via satellite instrumentation. The conformal-cubic atmospheric model (CCAM) is used for present-day climate simulations (8 km horizontally) over the region. The model simulations are verified against TRMM satellite and SAWS station rainfall data. There exist large biases in the CCAM simulations, but the model is able to capture the west-east rainfall gradient and diurnal cycle remarkably well, as well as an undetected feature, by the weather station network, that is independently verified through NDVI data.

**Keywords:** Dynamical downscaling, Conformal-Cubic Atmospheric Model, Diurnal Cycle, West-east Rainfall Gradient, Lesotho

## Introduction

Steep gradients in orography are known to induce steep gradients in climate, and the realistic representation of these gradients in climate models requires the use of high-resolution modelling (e.g. Engelbrecht et al., 2002). The orography of southern Africa exhibits some particularly steep orographic gradients, which require careful consideration in the design of climate simulations over the region.

Variations in topography often trigger meso-scale convective systems, and in addition convective systems have the potential to create meso-scale convective vortices over the eastern escarpment of South Africa and Lesotho (e.g. Blamey and Reason, 2009). More specifically, the two prominent rainfall-producing systems over the region during summer (December-January-February; DJF) are organized line thunderstorms and orographically-induced thunderstorms (Tyson et al., 1976). Stations in the Drakensberg record 16 to 18 rain days on the average during December and January and the extended summer period from November to March yield 70 % of the annual rainfall (Tyson et al., 1976). The effects of the eastern escarpment are not limited to localized rainfall effects - this region is the primary cause of the well-defined west-east gradient in rainfall totals across South Africa (e.g. Jury, 2012; Engelbrecht et al., 2009).

Of particular interest with regards to model simulations over the eastern escarpment, is the representation of the diurnal cycle in convection and convective rainfall. Generally the simulation of the amplitude and phase of the diurnal cycle provides a valuable test for model parameterizations and for the representation of

land-atmosphere feedbacks (e.g. Yang and Slingo, 2001). In the simulations of Hernandez-Diaz et al. (2012), rainfall peaks too early in the day over the eastern parts of South Africa. General overestimations of rainfall over eastern South Africa has also been reported in the modelling studies of Engelbrecht et al. (2002), Engelbrecht et al. (2009) and Engelbrecht et al. (2011). Along the eastern escarpment of South Africa the diurnal amplitude of surface moisture fluxes has been shown to be important for the diurnal cycle in rainfall as daytime surface latent heat fluxes increase steeply toward the east compared to the almost non-existent night time fluxes that exhibit little east-west gradient (Jury, 2012). Tadross et al. (2006) analyzed the diurnal cycle for 2 seasons and found that the amplitudes are roughly comparable to observations, but the noticeable differences are found in the model's timing of the rainfall peaks. It was also found that the difference in the diurnal cycle is largely as a result of the type of convection scheme used, with the sensitivity to the planetary boundary layer scheme being smaller (Tadross et al., 2006). Correctly simulating all the variables that contribute to the diurnal cycle is of utmost importance, because it influences rainfall on a variety of time scales such as monthly, seasonal, annual, intra-annual and inter-annual.

With the strong advance in super-computing technologies, which enables simulating the weather at high spatial resolutions, simulations resolving convections to some extent have become a reality (e.g. Engelbrecht et al., 2007; Pearson et al., 2014). Only a few studies where regional climate models have been applied beyond the hydrostatic limit (~ 10 km resolution in the horizontal, see Engelbrecht et al., (2007)) have been performed for the southern African region to date (e.g. Engelbrecht et al.,

2011). At the Council for Scientific and Industrial Research, the conformal-cubic atmospheric model has recently been applied at resolutions of 1 km to simulate the transport of carbon dioxide over the Cape Peninsula (Nickless et al., 2015), but these simulations were performed over a rather small area. In the research presented here CCAM will be tested at resolutions beyond the hydrostatic limit over a relatively large region, to investigate whether the model is capable to produce better high-resolution simulations over the eastern escarpment.

## Methodology

The dynamic regional climate model applied in this research is the conformal-cubic atmospheric model (CCAM) of the Commonwealth Scientific and Industrial Research Organization (CSIRO) in Australia (McGregor and Dix, 2008). Towards obtaining the high resolution (8 km resolution in the horizontal) simulations over Lesotho CCAM was applied in stretched-grid mode using a Schmidt transformation factor of 0.133. Each panel of the cube projected onto the sphere contained 160 x 160 grid points. In these simulations the model employed 27  $\sigma$ -coordinate levels in the vertical. Horizontal pressure-gradient calculations are performed after interpolation to the pressure-coordinate following the method of McGregor (2005b). The 8 km resolution simulations were nudged within ERA reanalysis, using a digital filter technique to preserve large-scale patterns of the ERA data (Thatcher and McGregor, 2010). The model simulations were performed for the period 1979-2005. At its lower boundary, the model was forced with sea-surface temperatures and sea-ice from the ERA reanalysis data.

Rainfall station data from around in South Africa surrounding Lesotho were selected based on completeness of the records. The rainfall stations acquired from the South African Weather Service (SAWS) were required to have more than 80 % of their entries to be complete (hourly and daily data, for the case of automatic stations (data record from 1993-2012) and manual stations (data record for 1979-2012)). The hourly stations are used to create the 6-hourly datasets ranging from 02-08 h, 08-14 h, 14-20 h and 20-02 h.

The MODerate-resolution Imaging Spectroradiometer on board NASA's Terra satellite is used to capture the Normalized Difference Vegetation Index (NDVI) time series. The NDVI is used for 16 January 2001 to 1 February 2001. A 16 day mean is calculated for every 250 m pixel over the region of the eastern escarpment of South Africa and Lesotho (Carroll et al., 2004). The data is supplied by the University of Maryland, Department of geography and NASA.

Different metrics are used to analyze the simulations. First the simulated and observed fields are subtracted from each other to detect systematic biases. Secondly the pattern correlation is calculated. Thirdly the Root Mean Square Error (RMSE) is a measure of the accuracy between a specific forecasted variable from a model and the same observed variable (Hyndman and Koehler, 2006). Fourthly the South African Weather Service (SAWS) station rainfall is analyzed against the simulations as a direct measure of rainfall at a particular point on a monthly, seasonal and annual time-scale. Fifthly the diurnal cycle is calculated and verified on a 6-hour basis against SAWS rainfall stations that measured hourly rainfall. Lastly the monthly rainfall fields are compared to the NDVI dataset to confirm validity of the simulated rainfall.

## Results

The steep topography of the eastern escarpment of South Africa and Lesotho can induce very large differences in rainfall occurrence over relatively small areas as a weather system moves over the region. Stations to the east have seasonal (DJF) rainfall totals well above 500 mm, which are severely over estimated by CCAM showing totals above 1000 mm. At the Cathedral Peak and Royal National Park Hotels locations rainfall totals are over estimated by factors of almost 4 times and 2.5 times, respectively (Table not shown). Over this region, the lower tropospheric flow is upslope and surface moisture is advected from the east when ridging anti-cyclones are present to the east of South Africa (Joubert et al., 1999). It is possible that orographic lift and related rainfall are overestimated in the CCAM simulations.

The lower rainfall totals in the south and west of Lesotho is partially due to the rain-shadow effect - the ridging high-pressure cloud bands moving in from the east often do not move over the higher eastern escarpment due to the steep topography. Convective clouds that occur in association with the easterly winds in the presence of an upper-air disturbance also largely rain out to the east of the Lesotho escarpment. This situation is reflected in the lower rainfall amounts, between 250-350 mm (station data), recorded over the eastern Free State showing a strong west-east rainfall gradient over the domain. CCAM correctly simulates the west-east gradient in rainfall, but also overestimates rainfall totals in the west, by a factor of two at some locations.

The simulated rainfall correlates well with that with CRU in space (Fig. 1), more so than in the case of the TRMM data. The model climate is at least twice as variable as the CRU and TRMM climate.

The CCAM simulates a western rainfall maximum similar to TRMM at 27.5 °E, but then extends this feature to 28 °E (at 2400 m) as the topography increases on the western side of the mountain. This feature is not present in the TRMM data.

Representation of the diurnal cycle in convection is known to be problematic in dynamic climate

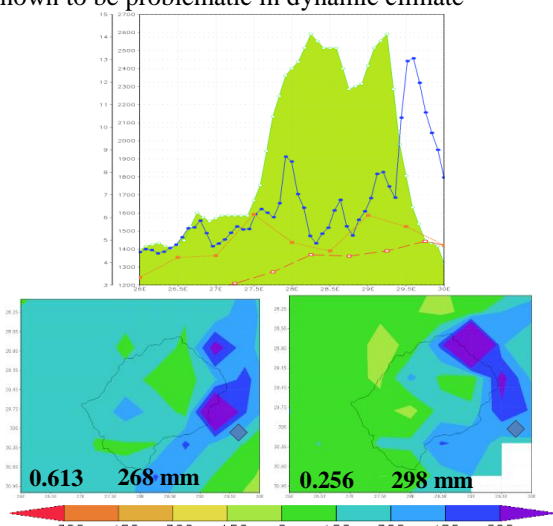


Figure 1. a) Vertical cross-section at 29.25 °S for DJF rainfall in mm/day (solid line – CCAM; long stripes – CRU; short stripes – TRMM). DJF rainfall totals (mm) for a) CCAM-CRU and b) CCAM-TRMM. Pattern correlation (bottom left) and RMSE (bottom middle).

models, with most models simulating the peak in rainfall too early in the day (see **Tadross et al., 2006**). However, these misrepresented maximum rainfall peaks are dependent on the type of convection scheme used in the model. Here the 6-hourly simulated totals of CCAM are analyzed to investigate how the model deals with changes in the daily heat balance, moisture distributions during and the influences orographic lift has on the diurnal cycle. The diurnal cycles from CCAM have a clear distinction between the time of day and the location where rainfall occurs. Rainfall on the western side of the escarpment is mostly simulated to fall in the afternoon and early evening (14h-20h) whereas rainfall on the eastern escarpment fall in the evening over a bigger area of the domain and in the early parts of the morning (Fig.2).

The TRMM data exhibits temporal and spatial biases, especially over steep topography when it is compared to either SAWS or CRU data (not shown here). Therefore, to verify the artifact in simulated rainfall as is shown in Fig. 3 is especially hard, since no station data is available to verify that the simulated feature is realistic. The artifact seen in the November, December and January climatology simulations show rainfall totals in excess of 300mm/month in the west of Lesotho. Even though it is noted that, in the presence of steep topography, CCAM usually over estimates rainfall the question

still remains whether there is truth in the simulated extremum. An independent data source, NDVI, is used to verify the existence of this artifact. In the

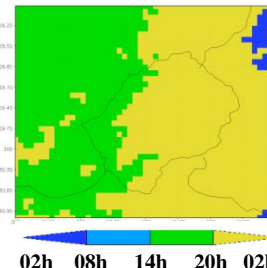


Figure 2. 6-Hourly diurnal cycle for CCAM (DJF). Intervals are 02h to 08h (dark blue), 08h-14h (light blue), 14h-20h (green) and 20h-02h (yellow)

presence of high rainfall totals there is a higher NDVI index number (denser vegetation) in the vicinity, not sensitive to rainfall above an approximate 500mm/year threshold (Nicholson and Farrar, 1994), as is the cases on the eastern side of the escarpment where forests transitions and

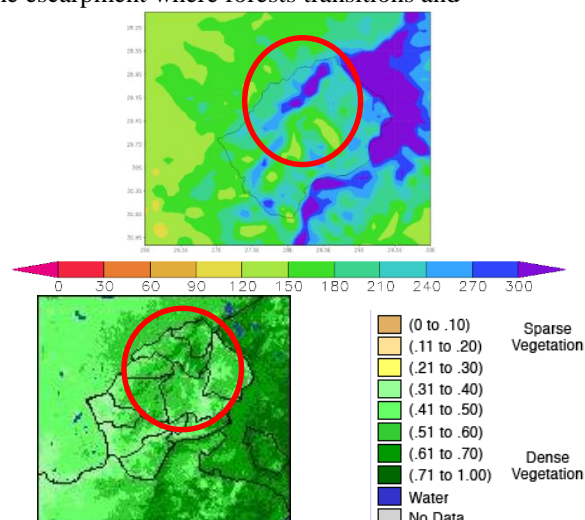


Figure 3. Top: January rainfall totals (mm) for b) CCAM (Jan 2001). Bottom: NDVI data for 17 Jan-01Feb 2001.

mosaics are found (White, 1986). In Fig. 3 the index for dense vegetation is higher (0.51 - 1.0) than for the rest of Lesotho (0.31 - 0.5) confirming the relatively higher rainfall totals simulated by CCAM are realistic.

## Conclusions

CCAM is a variable-resolution atmospheric model that is used to generate high resolution simulations (8 km in the horizontal) over the eastern escarpment of South Africa and Lesotho. These simulations are analysed against observational data sets including CRU, TRMM SAWS station rainfall and NDVI data.

A well-defined west-east gradient in rainfall is present and simulated well over the eastern escarpment of South Africa (the gradient is relatively weak in the TRMM data). CCAM does simulate the temporal and spatial pattern to closely resemble the SAWS station data pattern. However,

CCAM severely overestimates rainfall totals over the eastern side of the escarpment. It is on the same side of the escarpment where there are discrepancies between the CCAM simulations and SAWS data when analysing the diurnal cycle. Over western Lesotho CCAM simulates a rainfall maximum not resolved by either the SAWS or TRMM data, but which is detected implicitly by NDVI data. The high resolution simulations are most valuable in this regard, and demonstrate the value that RCMs can add to global circulation models, and to low-density station data (e.g. over Lesotho).

### Acknowledgements

I would like to thank SAWS for the stations data as well as the Centre for High Performance Computing for providing computational resources to perform the high resolution simulations.

### References

- Blamey, R.C. and Reason, C.J.C. (2009). Numerical simulation of a mesoscale convective system over the east coast of South Africa. *Tellus*, 61A: 17–34.
- Carroll, M.L., DiMiceli, C.M., Sohlberg, R.A. and Townshend, J.R.G. (2004). 250m MODIS Normalized Difference Vegetation Index, 250ndvi28920033435, Collection 4, University of Maryland, College Park, Maryland, Day 289, 2003.
- Engelbrecht, F.A., Landman, W.A., Engelbrecht, C.J., Landman, S., Bopape, M.M., Roux, B., McGregor, J.L. and Thatcher, M. (2011). Multi-scale climate modelling over Southern Africa using a variable-resolution global model. *Water SA*, 37: 647-658.
- Engelbrecht, F.A., McGregor, J.L., and Engelbrecht, C.J. (2009). Dynamics of the Conformal-Cubic Atmospheric Model projected climate-change signal over southern Africa. *Roy. Met. Soc.*, 29: 1013-1033
- Engelbrecht, F.A., McGregor, J.L. and Rautenbach, C.J. deW. (2007). On the development of a new nonhydrostatic atmospheric model in South Africa. *SA J. of Sci.*, 103: 127-134.
- Engelbrecht, F.A., Rautenbach, C.J. deW. and Katzfey, J.J. (2002). January and July climate simulations over the SADC region using the limitedarea model DARLAM. *Water SA*, 28: 361–374.
- Hernandez-Diaz, L., Laprise, R., Sushama, L., Martynov, Winger, K. and Dugas, B. (2013). Climate simulation over CORDEX Africa domain using the fifth-generation Canadian Regional Climate Model (CRCM5). *Clim. Dyn.*, 40: 1215-1433.
- Hynman, R.J., and Koehler, A.B. (2006). Another look at the measure of forecast accuracy. *Int. J. of Forecasting*, 679-888.
- Joubert, A. M., Katzfey, J.J., McGregor J.L. and Nguyen, K.C. (1999). Simulating mid-summer climate over southern Africa using a nested regional climate model. *J. Geophys. Res.*, 104: 19015-19025
- Jury, M.R., (2012). An intercomparison of model-simulated east-west climate gradient over South Africa. *Water S.A.*, 38: 1816-7950.
- McGregor, J.L. (2005b). C-CAM: Geometric aspects and dynamical formulation. CSIRO Atmospheric Research Tech. Paper No. 70. 43 pp.
- McGregor, J.L., and Dix, M.R. (2008). An updated description of the Conformal-Cubic Atmospheric Model. In: Hamilton K and Ohfuchi W (eds.) High Resolution Simulation of the Atmosphere and Ocean. Springer Verlag. 51-76.
- Nickless, A., Ziehn, T., Rayner, P.J., Scholes R.J. and Engelbrecht F.C., (2015). Greenhouse gas network design using backward Lagrangian particle dispersion modelling—Part 2: Sensitivity analyses and South African test case. *Atmos. Chemistry and Physics*, 15: 2051-2069.
- Nicholson, S. E., and Farrar, T. J., (2004). The influence of soil type on the relationships between NDVI, rainfall and soil moisture in semiarid Botswana. I. NDVI response to rainfall. *Remote sensing of the Environment*, 50: 107-120.
- Pearson, K. J., Lister, G.M.S., Birch, C.E., Allan, R.P., Hogan R.J. and Woolnough, S.J. (2014). Modelling the diurnal cycle of tropical convection across the ‘grey zone’. *Quarterly J. of the Royal Met. Soc.*, 140: 491-499.
- Richard, Y. and Pocard, I., (1998). A statistical study of NDVI sensitivity to seasonal and interannual rainfall variations in Southern Africa. *Int. J. of Remote Sensing*, 19: 2907-2920.
- Tadross, M.A., Gutowski Jr, W.J., Hewitson, B.C., Jack, C. and New, M. (2006). MM5 simulations of interannual change and the diurnal cycle of southern African regional climate. *Theoretical and applied clim.*, 86: 63-80.
- Thatcher, M., and McGregor, J.L. (2010). A technique for dynamically downscaling daily-averaged GCM datasets over Australia using the Conformal Cubic Atmospheric Model. *Mon. Weather Rev.*, 139: 79-95.
- Tyson, P.D., Preston-Whyte, R.A. and Schulze, R. E. (1976). The climate of the Drakensberg. Natal Town and regional planning commission: Pietermaritzburg.
- White, F, 1986: *The vegetation of Africa*. UNESCO. ISBN 92-3-201955-8.
- Yang, G.Y., and Slingo, J. (2001). The diurnal cycle in the Tropics. *Mon. Weather Rev.*, 129: 784–801.

## ***A lightning threat index for South Africa using numerical weather prediction data***

Morné Gijben<sup>\*1,2</sup>, Liesl L. Dyson<sup>1</sup>, Mattheüs T. Loots<sup>3</sup>

<sup>1</sup> Department of Geography, Geoinformatics and Meteorology, University of Pretoria

<sup>2</sup> South African Weather Service

<sup>3</sup> Department of Statistics, University of Pretoria

There is a need to forecast the threat of lightning to ensure the protection of humans and infrastructures. A new lightning threat index (LTI) was developed for SA by using numerical weather prediction data. Logistical regression techniques were utilized to determine which model parameters are best suited for lightning prediction and to design equations to predict the probability of lightning. Verification show that the LTI performs quite well with a Brier Skill score of 0.2631 for the spring and 0.1252 for the summer seasons. This new LTI can be a useful tool for operational weather forecasters.

Keywords: Regression, Rare events, Bootstrapping, Probabilities

### ***Introduction***

Lightning is a phenomenon that can cause death or injury among humans and animals (Blumenthal et al., 2012), damage to infrastructures (Lynn and Yair, 2010), and can be a hazard to various sectors like the aviation and forestry industry (Price, 2013). South Africa (SA) has between 1.5 and 8.8 lightning deaths per million people of the population each year (Jandrell et al., 2009). Bhavika (2007) stated that the number of lightning deaths in SA is about four times higher than the global average. SA also experiences great financial losses and damages due to lightning, which is evident in the insurance sector where claim amounts of more than R500 million per annum are recorded (Gill, 2008). It is also said that 24% of the electrical faults reported by the electricity provider, Eskom, is because of lightning (Peter, L. & Mokhonoana, F. 2010). There is a need to forecast the areas where lightning can cause a threat (Lynn and Yair, 2010) to ensure the protection of people and property.

Many institutions are moving away from statistical and empirical lightning prediction methods to model based techniques. The advantage of these methods is that lightning can be predicted on the very short-range (2 – 12 hours ahead) as well as short-range (12 - 72 hours ahead) forecast scale due to Numerical Weather Prediction (NWP) models being capable of providing accurate parameters related to lightning formation (McCaul et al, 2009) for several hours ahead.

The Lightning Potential Index (LPI) was proposed by Frisbie et al. (2009) and this methodology uses the NWP prognosis of most unstable Convective Available Potential Energy (muCAPE), Lifted Index (LI), Equivalent Potential Temperature lapse rate ( $\Theta_e\Gamma$ ), Temperature (T), Precipitable Water (PW) and Relative Humidity (RH) to calculate the potential of lightning. This version of the LPI, developed at The National Weather Service Forecast Office in Grand Junction, Colorado is still in the developing phase, but has shown the ability to be useful in improving lightning prediction.

The same methodology of the LPI was tested over SA (Gijben, 2013) and showed potential for lightning prediction in SA. The LPI was developed for Colorado in the USA where weather conditions differ from the conditions in SA. Furthermore, the LPI was tested on a different NWP model than the ones

available in SA. As a result, a completely new index, named the Lightning Threat Index (LTI) was developed for SA by using the Unified Model (UM). The same type of model parameters used in the LPI was considered for the LTI, but the most optimal variations from these parameters were identified for SA conditions. The LTI was trained with lightning data over SA where relationships between different model parameters and lightning could be developed.

### ***Instrumentation and Method***

In this study, lightning data from the Southern African Lightning Detection Network operated by the South African Weather Service (SAWS) were used. This network consists of 24 sensors across the country that detects cloud-to-ground lightning with a detection efficiency of 90% or more (Gijben, 2012). NWP model data was obtained from the local version of the UM which is the main operational NWP model at SAWS. The UM has a horizontal resolution of 12km.

Spring, defined as September, October and November (SON) and summer, defined as December, January and February (DJF) were considered in this study, since most lightning activity occurs during these periods (Gill, 2008). SON and DJF were considered separately for the development of the LTI since environmental conditions for lightning development can be different. Three consecutive seasons were utilized for the development of the LTI. The 2011 and 2012 SON and the 2011/12 and 2012/13 DJF months were considered for the development of the LTI while the 2013 SON and 2013/14 DJF months were used to evaluate the index.

Model and lightning data were extracted on a 0.5° X 0.5° grid. This grid is much coarser than the UM grid, but due to the long periods considered and the intensive calculations performed, the coarser grid was utilized to save on computation time. The 0.11° X 0.1112° resolution grid of the UM would have meant that all the calculations would have taken about 22 times longer than using the coarser grid. This work had to be done on a research server, and this 22 times increase in computation time of all the parameter extractions and calculations, as well as logistical regression techniques would have been unfeasible. A higher resolution would provide more detail in the LTI especially with the smaller forecast scales of thunderstorms.

The LTI equations, on the coarser grid, can however still be directly applied to a higher resolution model when the product is made operational on a supercomputer.

Lightning was the dependent variable (observation) in this study. If lightning occurred in a grid box, it was given a value of 1, and a value of 0 if no lightning occurred. This resulted in the dependent variable having a binary outcome. The model parameters were the independent variables and were used to predict the binary outcome of the dependent variable.

Six main groups of model parameters were considered for the development of the LTI, namely: 1. CAPE, 2. PW, 3. T, 4. LI, 5.  $\Theta e\Gamma$ , 6. RH. For each of the groups different variations were selected from literature that proved useful for lightning predictions. Table 1 shows 24 different parameters that were considered. Most of these variables were not available in the UM and had to be calculated.

Table 1: Different parameters considered for the LTI

<b>1</b>	Surface CAPE	muCAPE (1-6 km AGL)
	muCAPE (0-3 km AGL)	muCAPE (lowest 300 hPa)
<b>2</b>	Mean PW (850-300 hPa)	Mean PW (700-400 hPa)
	T (1.5 m AGL)	T (700 hPa)
<b>3</b>	Mean T (850-700 hPa)	Mean T (500 – 300 hPa)
	Lifted Index	Best Lifted Index
<b>5</b>	$\Theta e\Gamma$ (850-400 hPa)	$\Theta e\Gamma$ (850 - 500 hPa)
	$\Theta e\Gamma$ (700-500 hPa)	$\Theta e\Gamma$ (600 hPa)
	$\Theta e\Gamma$ (1-6 km AGL)	$\Theta e\Gamma$ (-10°C to -20°C)
	Surface $\Theta e$	
<b>6</b>	RH (at -10°C)	Ave RH (-12°C to -18°C)
	Ave RH (3-6 km AGL)	Max RH (3-6 km AGL)
	Min RH (3-6 km AGL)	

\*AGL – above ground level

The LTI was developed by making use of the logistical regression technique. Logistical regression is often utilized for predicting the probability that an event will occur by using a set of predictor variables (Kiezun *et al.*, 2009) and is given by Eq. (1):

$$p_i = \frac{1}{1 + e^{-(\hat{\alpha} + \sum \hat{\beta}_i x_i)}} \quad (1)$$

where  $p_i$  is the probability of the event as a function of  $m$  independent variables  $X$ , when  $i$  ranges from 1 to  $m$ . The regression coefficients,  $\hat{\alpha}$  and  $\hat{\beta}$ , are estimated from the data by means of the maximum likelihood method (Guns and Vanacker, 2012).

Studies by King and Zeng (2001) showed that ordinary logistical regression underestimates the probabilities of rare events (Guns and Vanacker, 2012). This is due to the logistical regression favoring the larger amount of non-events (0's) compared to the smaller amount of events (1's) when training the model. The number of grid cells with lightning compared to grid cells without lightning is not necessarily considered a rare event. Rare events are classified as dozens to thousands of times more non-events than events (King and Zeng, 2001). It was however decided to follow the rare event logistical

regression methodology proposed by King and Zeng (2001) in the development of the LTI. There are three steps in the rare event logistical regression: Firstly, to make use of endogenous stratified sampling where all the events are taken together with a random sample of non-events. Secondly, by making use of sampling, the intercept term of the regression output might be significantly biased, and thus a correction is made to avoid the sampling bias. Lastly, the underestimation of probabilities is taken into account by adding a correction term to the estimated probabilities (Guns and Vanacker, 2012). The last two corrections are available in the R software package 'Zelig' (Kosuke, *et al.*, 2009).

In the development of the LTI, the following procedure was followed for the rare event logistical regression:

1. Take all events (1's) in the dataset and select a random sample of an equal amount of non-events (0's).
2. Run the 'Zelig' package to perform a rare event logistical regression with the bias correction and addition of the correction term.
3. Repeat the process 1000 times by selecting a new sample of non-events (0's). The samples are taken with repetition, where the 0's in the previous sample is added back into the dataset where there is the possibility that they can be chosen again.

The 1000 models are then combined by averaging their output. This process is called bootstrap aggregating and aims to improve any instability found in the estimation of the regression output (Kotsiantis *et al.*, 2006).

The first step was to determine which of the 24 parameters was best for lightning prediction. The aim was to select one variable out of the six main groups (Table 1) to include in the development of the equations of the LTI. This was achieved by performing a stepwise logistical regression on the data by considering only the parameters in each of the main groups. In the stepwise logistical regression, each parameter was added one by one to the regression. In the end each variable had an Akaike information criterion (AIC) value which is a theoretic approach for variable selection as well as one of the most common variable selection techniques in statistical software (Chaurasia and Harel, 2012). The lowest AIC value indicates the best parameter, and the parameter with the lowest AIC from each group was selected for the development of the LTI.

The most suitable parameters for lightning predictions were utilized in the rare event logistical regression described above. The 1000 bootstrap samples were aggregated into one model by averaging all the results. The average regression coefficients were used to set up an equation for the LTI with the form of Eq. (1). The process was repeated for the SON as well as the DJF periods, and thus equations for each season were developed. Evaluations of the new LTI were done for the entire SON season of 2013 and DJF season of 2013/14 by making use of standard probabilistic evaluation techniques. The following techniques were considered: Relative operating characteristic (ROC) plots with associated area under curve (AUC), Reliability diagrams, Sharpness diagrams, and Brier score.

**Results and Discussion**

The most suitable parameters for lightning prediction in each of the six main groups were determined by means of the lowest AIC value of a stepwise logistical regression. Table 2 lists the parameters that proved to be the most optimal for lightning prediction for the SON and DJF periods. Most of the parameters were the same for SON and DJF, except for RH and  $\Theta_e\Gamma$ , where the minimum RH in the 3-6 km above ground level (AGL) and  $\Theta_e\Gamma$  of the 700-500 hPa were selected for SON, while the average RH in the 3-6 km AGL and  $\Theta_e\Gamma$  of the 850-400 hPa was selected for the DJF period.

Table 2: Parameters selected for the SON and DJF periods

SON	DJF
muCAPE (1-6 km AGL)	muCAPE (1-6 km AGL)
Lifted Index	Lifted Index
Mean PW (850 - 300 hPa)	Mean PW (850 - 300 hPa)
Min RH (3 - 6 km AGL)	Ave RH (3 - 6 km AGL)
$\Theta_e\Gamma$ (700 - 500 hPa level)	$\Theta_e\Gamma$ (850 - 400 hPa level)
Mean T (850 - 700 hPa)	Mean T (850 - 700 hPa)

The parameters listed in Table 2 were utilized in rare event logistical regressions by making use of 1000 bootstrap samples. The 1000 models were aggregated into a single model by taking the average for all of the models. This was performed on the SON and DJF data where the regression coefficients could be utilized to design Eq. (2) for the SON and DJF period.

$$LTI = \frac{1}{1 + e^{-(A+(B)\mu\text{CAPE}+(C)PW+(D)LI+(E)\Theta_e\Gamma+(F)RH+(G)T)}} \quad (2)$$

where muCAPE, PW, LI,  $\Theta_e\Gamma$ , RH and T are the parameters indicated in Table 2 for SON + DJF while the regression coefficients A-G for the two periods are indicated in Table 3.

Table 3: Regression coefficients for SON and DJF

SON		DJF	
<b>A</b>	81.2564450094	<b>A</b>	96.3739728597
<b>B</b>	-0.0000341603	<b>B</b>	-0.0003621305
<b>C</b>	1.8711318175	<b>C</b>	1.6498509643
<b>D</b>	-0.3075713873	<b>D</b>	-0.2744099332
<b>E</b>	-0.2004598804	<b>E</b>	-0.2538438647
<b>F</b>	0.0218575175	<b>F</b>	0.0228283828
<b>G</b>	-0.3076425065	<b>G</b>	-0.3646825175

Fig. 1a shows a typical forecast from the new LTI. The associated lightning that occurred during the forecast period of the LTI is shown in Fig. 1b. By comparing the two images it is clear that the LTI performs quite well, where most of the lightning occurred in the areas where the LTI forecasted probabilities greater than 60%.

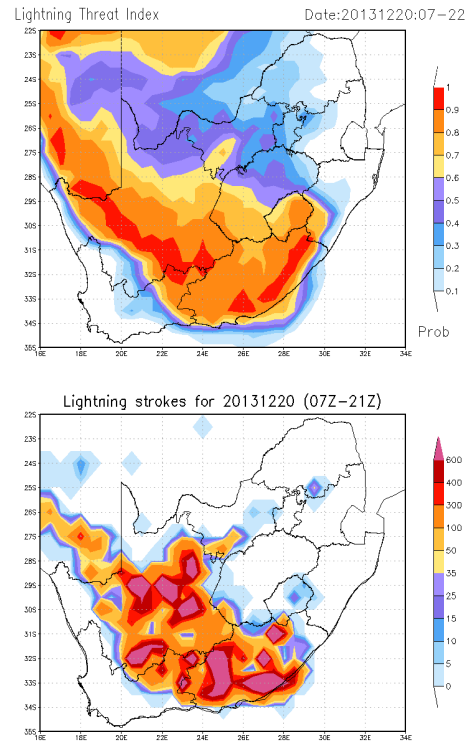


Figure 1: (a) The LTI and (b) the total amount of lightning strokes for 20 December 2013 between 07:00 and 22:00 UTC.

Fig. 2 shows the ROC plot for the evaluation of the LTI for the SON and DJF seasons. By looking at the ROC curves one can see that the LTI discriminated really well between the areas where lightning occurred and did not occur for DJF and not too bad for SON. The AUC for DJF was 0.899 while the AUC for SON was 0.758.

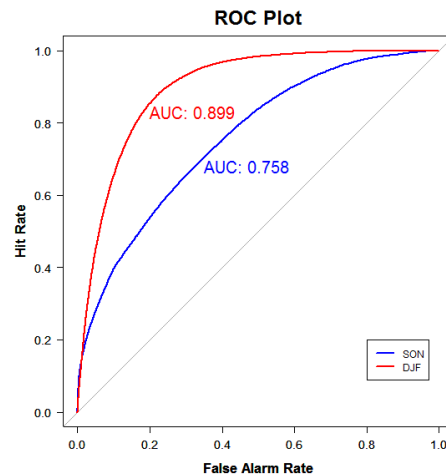


Figure 2: ROC plot for the SON and DJF periods.

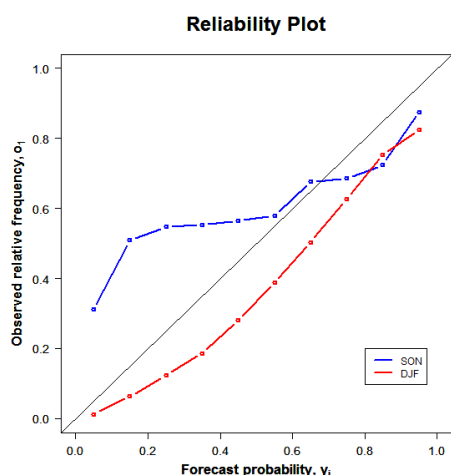


Figure 3: Reliability plot for the SON and DJF periods.

Table 4 shows the Briar score for the SON and DJF periods. The Brier score shows that the magnitude of the probability forecast error is small for SON and DJF.

Table 4: The Brier score for SON and DJF

<u>SON</u>	<u>DJF</u>
0.2631	0.1252

The evaluation results show that the LTI performs better during the DJF months than during the SON months. This can be due to the atmospheric conditions being different during SON and DJF. In early summer, the atmospheric circulation is generally extra-tropical with a conditionally unstable atmosphere over certain parts of SA, while in late summer the circulation is tropical with a convectively unstable atmosphere (Dyson *et al.*, 2015). Another possibility is that the UM model can resolve the atmospheric conditions better during DJF than during SON.

## Conclusions

A new NWP-based lightning threat index, the LTI, was developed for SA. Rare event logistical regression was used to get the relationships between different model parameters and lightning occurrence for the SON and DJF seasons. The most optimal parameters for lightning prediction was selected and used to set up new equations to predict the probability of lightning occurrence. Standard probabilistic evaluations techniques were used to evaluate the LTI against observed lightning where the results indicate that the LTI discriminates well between areas where lightning occurred and did not occur. The DJF period outperforms the SON period. For the SON period, the LTI underestimates the occurrence of lightning for lower probabilities while overestimating higher probabilities. During the DJF period, the LTI overestimates the occurrence of lightning. The LTI can be a valuable tool to implement operationally, and can be implemented on the higher resolution UM model, which runs on the supercomputer at SAWS. Future work will be to test if running the LTI on the higher resolution UM improves the lightning threat forecast.

## Acknowledgments

Thank you to the South African Weather Service for supplying the UM model and lightning data used in this study.

## References

- Bhavika, B. (2007). The influence of terrain elevation on lightning density in South Africa. MSc thesis. Johannesburg: University of Johannesburg.
- Blumenthal, R. *et al.* (2012). Lightning medicine in South Africa. *S Afr Med J.* 102: 625-626.
- Chaurasia, A. and Harel, O. (2012). Model selection rates of information based criteria. *Electron. J. Statist.* 7:2762-2793
- Dyson, L.L. *et al.* (2015). A baseline climatology of sounding-derived parameters associated with heavy rainfall over Gauteng, South Africa. *Int. J. Climatol.* 35:114-127
- Frisbie, P.R. *et al.* 2009. Lightning prediction by WFO Grand Junction using model data and graphical forecast editor smart tools, viewed 2 May 2013, <https://ams.confex.com/ams/pdfpapers/149101.pdf>
- Gijben, M. (2012). The lightning climatology of South Africa. *S Afr J Sci.* 108: 44-53.
- Gijben M. (2013). Verification of a Unified Model based Lightning Risk Indicator for Southern Africa, 29th Annual Conference of South African Society for Atmospheric Sciences, September 2013, Durban. ISBN 978-0-620-56626-1
- Gill, T. (2008). Initial steps in the development of a comprehensive lightning climatology of South Africa. MSc thesis. Johannesburg: University of the Witwatersrand.
- Guns, M. and Vanacker, V., (2012). Logistic regression applied to natural hazards: rare event logistic regression with replications. *Nat. Hazards Earth Syst. Sci.* 12: 1937-1947
- Jandrell I.R. *et al.* Recent lightning research in South Africa with a special focus on Keraunopathology, Proc. International Symposium on High Voltage Engineering. Cape Town, South Africa, 2009.
- Kiezun, A. *et al.*, (2009). Evaluation of optimization techniques for variable selection in logistic regression applied to diagnosis of myocardial infarction. *Bioinformatics.* 3:311-313
- Kosuke, I. *et al.* (2009). Zelig: Everyone's Statistical Software. <http://gking.harvard.edu/zelig>
- Kotsiantis, S.B. *et al.*, (2006). Machine learning: a review of classification and combining techniques. *Artif Intell Rev.* 26:159-190
- Lynn, B. and Yair, Y. (2010). Prediction of lightning flash density with the WRF model. *Adv Geosci.* 23: 11-16.
- McCaul, Jr. E.W. *et al.* (2009). Forecasting lightning threat using cloud-resolving model simulations. *Wea Forecasting.* 24: 709-729
- Peter, L. and Mokhonoana, F. Lightning detection improvement FALLS brought to Eskom's transmission line design and fault analysis, Proc. International Lightning Detection Conference, Orlando, USA, 2010
- Price, C.G. (2013). Lightning applications in weather and climate research. *Surv Geophys.* online: 24 January 2013, DOI:10.1007/s10712-012-9218-7

## Application of a Commercial Lidar-Ceilometer to Studies of Aerosols in the Atmospheric Boundary Layer

Arshath Ramkilowan<sup>a,\*</sup> and Derek J. Griffith<sup>a</sup>

<sup>a</sup>CSIR Defence, Peace Safety and Security

Optronics Sensor Systems, Pretoria, South Africa.

\*Corresponding author. Email: [aramkilowan@csir.co.za](mailto:aramkilowan@csir.co.za). Tel: +27 12 841 4859

### Abstract

Ceilometers operating on several optical principles have been extensively applied to vertical visibility and cloud base measurements relating to aviation safety. The latest generation of laser time-of-flight backscatter ceilometers use the same optical sounding principle as more powerful and costly research lidar systems. Ceilometers in persistent and unattended operation have become ubiquitous for aviation safety, particularly in Europe and the USA and their potential for use in aerosol studies has therefore become of great interest. CSIR/DPSS has acquired and deployed a Vaisala CL51 ceilometer chiefly for the purpose of investigating the vertical distribution of aerosols in the Atmospheric Boundary Layer (ABL) and cloud base height for application in the modelling of optical surveillance through the ABL. We show some results from ABL analysis of CL51 backscatter data and explore the potential for retrieval of more quantitative aerosol properties such as the lidar ratio. The latter retrievals can be either compared to or calibrated using complementary measurements such as those from AERONET sun-photometers. We conclude that commercial lidar/ceilometers such as the Vaisala CL51 offer cost-effective and long-term potential for aerosol studies in the optical surveillance and atmospheric radiative transfer applications.

**Keywords:** Lidar, ceilometer, aerosol studies, atmospheric boundary layer

### 1. Introduction

Backscatter lidar systems are powerful remote-sensing tools for investigation of the structure and composition of the atmosphere. Research-grade lidars are high cost systems that are typically only operated in a supervised mode. Compact, robust, eye-safe and cost-effective laser ceilometers operating on the lidar principle have become an essential tool in aviation safety. While less capable than research lidars, the widespread and long-term deployment [1] of such ceilometers in unsupervised operation has led to strong interest in the application of these instruments to atmospheric research [2,3,4,5]. This is particularly the case in relation to the spatial distribution, transport and optical properties of aerosol particles in the atmospheric boundary layer (ABL).

CSIR/DPSS has been operating a Vaisala CL51 lidar-ceilometer since late 2014 in order to investigate applicability to establishing a local climatology for the vertical distribution of aerosols and clouds. In our case, such a climatology is important for statistical modelling of the effectiveness of optical surveillance systems viewing targets through the ABL, particularly from airborne platforms.

Potential application of lidar-ceilometer systems could also be found in ABL studies for climate, meteorology and air quality.

### 2. Instrumentation

The Vaisala CL51 is a commercial lidar ceilometer that measures laser backscatter at a wavelength of 910 nm as a function of height above ground up to a maximum height of 15 km and with a range resolution of 10 m. The optical design is monostatic, meaning that the same optical

aperture is used for laser transmission and detection. The monostatic design has full optical overlap to ground level, which is a useful feature for aerosol studies.

The instrument is primarily stationed in a peri-urban environment atop a building at the CSIR, Pretoria campus (25.757°S, 27.280°E) 25 m above ground level at an altitude of 1449 m. Data from a temporary installation of the instrument in Simon's Town is also considered. This setup, also on the roof of a building is 22 m above ground level, 25 m above sea level and in a coastal environment.

Other instrumentation used in this study includes the Cimel CE318 robotic sun-photometer, which is the standard instrument used in the AEROSOL ROBOTIC NETWORK (AERONET) [6] for measurement of Aerosol Optical Depth (AOD) and other aerosol optical properties.

### 3. Theory and Methods

The elastically backscattered optical power  $P$  received by a lidar system from a vertical range (height)  $z$  can be expressed as [7]

$$P(z) = C_L \frac{\beta(z)}{z^2} \exp\{-2 \int_0^z \alpha(z') dz'\},$$

where  $\beta(z)$  is the volume backscatter coefficient as a function of height,  $\alpha(z)$  is the extinction (attenuation) coefficient and  $C_L$  is a lidar system calibration constant. The backscatter and extinction coefficients can be separated into that from aerosol particles and that from molecules. In the near-infrared (910 nm wavelength in the case of the CL51), the backscatter due to molecules will be neglected and is usually below the noise floor in the case of low-power ceilometers. It is further assumed that the received signal is

single-scattered (not valid at high optical depth, such as in clouds).

The Vaisala CL51 reports the two-way attenuated backscatter profile [8]

$$\beta'(z) = \beta(z) \exp\{-2 \int_0^z \alpha(z') dz'\} = \frac{P(z)z^2}{c_L}$$

This means that the instrument constant has been determined by the manufacturer. There is currently little information available on the accuracy and stability of the instrument constant so we assume reliability and cannot yet perform a credible uncertainty analysis.

The backscatter and extinction coefficients are related through the lidar ratio  $S_p$  as

$$\alpha(z) = S_p(z)\beta(z).$$

The lidar ratio is often assumed constant with height in aerosol layers and then written simply as  $S_p$ .

The argument of the exponential function above is twice the optical depth  $\tau(z)$  from ground level to height  $z$  i.e.

$$\beta'(z) = \beta(z)e^{-2\tau(z)}$$

The differential increase in optical depth at height  $z$  can be expressed as

$$d\tau = \alpha(z)dz = S_p(z)\beta(z)dz.$$

Following the calibration argument presented by Vande Hey [7], integrating the attenuated backscatter profile over the full atmospheric column yields

$$B = \int_0^\infty \beta'(z)dz = \int_0^\infty \beta(z)e^{-2\tau(z)}dz.$$

Assuming the lidar ratio constant with height in a cloudless scenario and changing the integration variable to  $\tau$  provides

$$B = \frac{1}{S_p} \int_0^{\tau_{top}} e^{-2\tau} d\tau = \frac{1 - e^{-2\tau_{top}}}{2S_p},$$

where  $\tau_{top}$  is the full vertical aerosol optical depth from ground to top-of-atmosphere. If  $\tau_{top}$  is available from a sun-photometer measurement, it is possible to estimate the height-independent lidar ratio from the CL51 output profile as

$$S_p = \frac{1 - e^{-2\tau_{top}}}{2B}.$$

The total vertical aerosol optical depth (AOD) at 910 nm can be interpolated from data reported by the AERONET sun-photometer which is located at DPSS in close proximity to the ceilometer.

Conversely, if a reasonable estimate of the lidar ratio is available it is possible to estimate the vertical AOD from the ceilometer profile as

$$\tau_{top} = \frac{-\ln(1 - 2BS_p)}{2}$$

The latter approximation is potentially useful in our work to estimate the AOD at night using CL51 backscatter data when the sun-photometer is inoperable.

If the extinction coefficient  $\alpha$  can be considered uniform in the aerosol layer, the simple model for  $\tau(z)$  up to the top of the layer  $z_{top}$  is

$$\tau(z) = \alpha z,$$

so that

$$\tau_{top} = \alpha z_{top}$$

and

$$\alpha = \frac{-\ln(1 - 2B_{top}S_p)}{2z_{top}}.$$

This last expression is potentially useful in our optical surveillance application for providing an estimate of the aerosol extinction coefficient at 910 nm using a reasonable estimate of the lidar ratio when dealing with a cloudy scenario by performing integration of the ceilometer backscatter profile up to the first cloud base. It can also form the basis of estimating horizontal visibility near the surface by integrating only over the first few height bins. For example, visibility (surface meteorological range) in km is computed in the MODTRAN<sup>®</sup> radiative transfer code using [9]

$$VIS = \frac{\ln(50)}{\alpha_{550} + 0.01159},$$

where  $\alpha_{550}$  is the extinction coefficient at 550 nm in units of  $\text{km}^{-1}$ .

#### 4. Results and discussion

Four clear days have been selected for computation of the lidar ratio according to the above procedure.

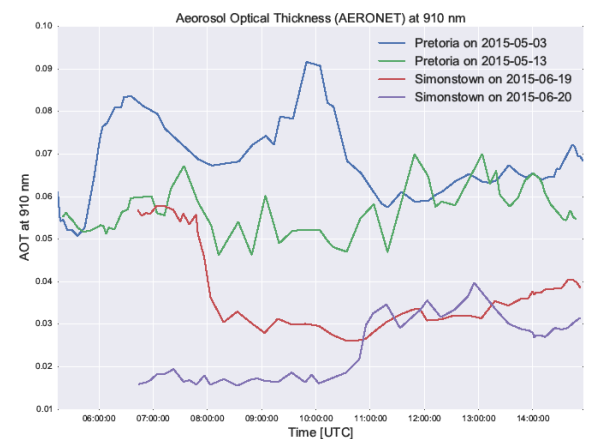


Figure 1: Aerosol Optical Depth from AERONET Cimel CE318 sun-photometers at CSIR/Pretoria and IMT/Simon's Town.

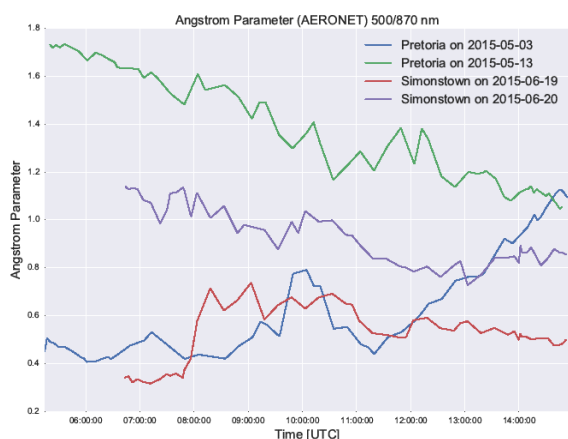


Figure 2 Angstrom parameter from AERONET Cimel CE318 sun-photometers at CSIR/Pretoria and IMT/Simon's Town

Two days were taken from the ceilometer operational period in Pretoria and another two days from the period in Simon's Town.

The four days in question were chosen in order to cover both inland and maritime aerosol characters, as well as a variety of AOD and Angstrom parameter values.

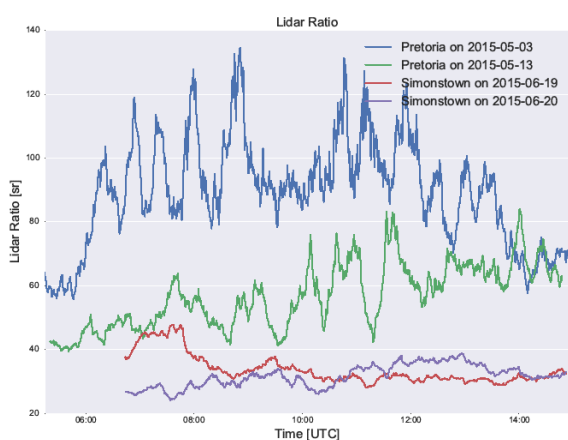


Figure 3: Lidar Ratios computed from ceilometer backscatter profiles in conjunction with AERONET sun-photometer AOD.

Figure 1 provides the AOD from AERONET for all four days, while the Angstrom parameter (spanning wavelengths 500 nm to 870 nm) is shown in Figure 2. Higher Angstrom parameter and lower lidar ratio are both generally associated with smaller particle size and would therefore be expected to show an inverse correlation. For example, 2015-05-13 at Pretoria shows relatively constant AOD, but declining Angstrom parameter, whereas the lidar ratio is clearly increasing in inverse correlation with the Angstrom parameter.

The magnitudes of the computed lidar ratios are generally plausible, but the strong variations at the Pretoria station do require explanation. Current reasoning attributes such

variations partially to the difference in temporal sampling, 15 s for the ceilometer compared to the  $\pm 15$  minute sampling resolution of the AERONET node. Additionally, the CL51 samples an air mass volume extending 15 km directly upwards from the instrument whereas the sun-photometer collects data integrated along the node-sun path.

Computation of the lidar ratio from a combination of ceilometer and sun-photometer data makes numerous assumptions and approximations and the uncertainty is impossible to quantify without an independent calibration of the CL51. A further factor which has been neglected is that the operating wavelength of the CL51 (910 nm) lies just within the wing of a water-vapour absorption band. The backscatter profile is therefore impacted by the water vapour vertical profile and total column. Corrections for this are potentially required depending on the level of accuracy that is needed. Wiegner and Gasteiger [10] provide a methodology for correcting ceilometer data for water vapour absorption in such instances. The rapid fluctuations of the ceilometer backscatter profiles are thought to be a manifestation of uncharacterised hygroscopic growth of the aerosol particles as well as particle quantity. An investigation of humidity and wind profiles is required to confirm this hypothesis.

## 5. Boundary Layer Analysis

Vaisala offers a software package for boundary layer analysis called BL-VIEW [11]. This package uses a negative gradient algorithm with vertical and temporal averaging procedures on backscatter profiles passed through cloud and precipitation filters to identify candidate heights for the tops of aerosol layers and cloud bases. BL-VIEW is set up by default to report up to 3 candidate aerosol ceilings and up to 3 cloud base candidates. This data can be used, for instance, to gather statistics on diurnal and seasonal variation in ABL height.

### 5.1 Diurnal ABL Height

Typical results from BL-VIEW for a cloudless day in which the height of the ABL (broadly identified with the mixing layer for air quality purposes) is strongly driven by convection are shown in Figure 4.

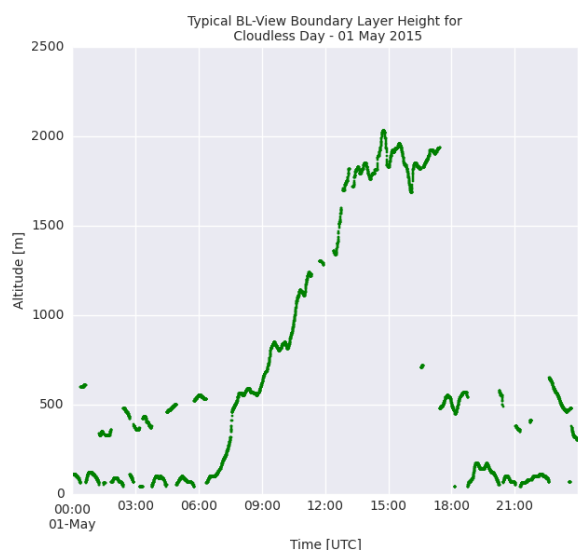


Figure 4: Boundary layer height candidates identified by BL-VIEW at Pretoria on 2015-05-01

## 5.2 Seasonal ABL Height

A seasonal trend in ABL height is also to be expected. For days meeting a low-cloud criterion of 80% (meaning that 80% of BL-VIEW measurements detected no cloud base), the first BL-VIEW height candidate for the ABL ceiling has been aggregated for the period around local noon, over the 8 months for which the CL51 was operational in Pretoria. The results are shown in Figure 5.

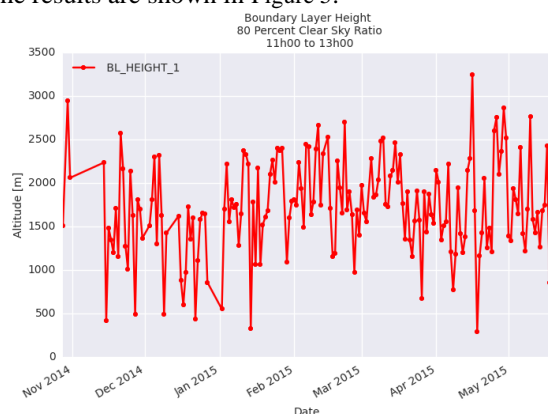


Figure 5: Daily mean ABL height candidates from BL-VIEW on days with less than 20% ceilometer cloud hits at Pretoria

Figure 5 clearly shows how the convective boundary layer becomes more compact in winter. For all data, including all data with cloud hits, this seasonal trend is partially masked by high prevalence of low level cloud hits in summer. This is seen in Figure 6.

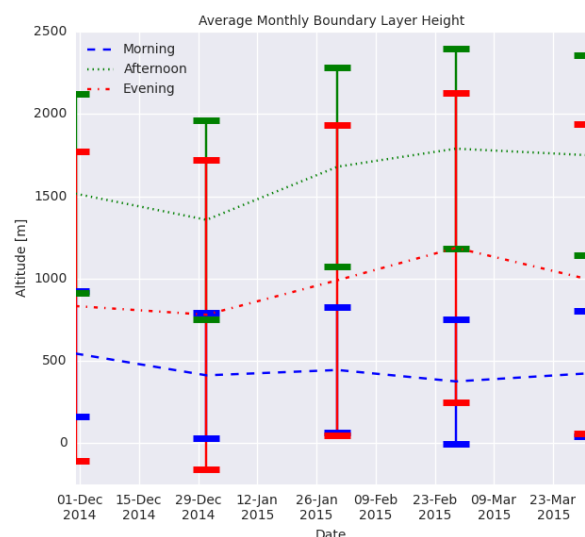


Figure 6: Monthly averages of all BL-VIEW ABL height candidates, including measurements with cloud hits (Pretoria site).

## 6. Conclusions

In general, lidar-ceilometers do not have sufficient laser power to allow absolute calibration from Rayleigh backscatter in clear air (free troposphere) which is a common calibration method for higher power research lidars. In the absence of additional data, this restricts the use of such ceilometers to determination of ABL and cloud base height with less reliable quantitative determination of the vertical distribution or optical properties. With a total aerosol optical depth obtained from a sun-photometer (e.g. AERONET), it becomes possible to estimate the lidar ratio and conversely, with a reasonable estimate of the lidar ratio it becomes possible to estimate total AOD and the extinction coefficient in simple situations.

The data yielded by the CL51 in conjunction with AERONET data will provide climatologies for ABL height and cloud base to be used in statistical models of optical surveillance system effectiveness. Extrapolations of aerosol optical depth and optical extinction to cloudy scenarios and night scenarios will be possible but with increased uncertainty. Methods for independent calibration (e.g. Jin [12]) and uncertainty assessment will have to be adopted or developed.

## 7. References

- [1] Deutscher Wetterdienst (2015), 'DWD Ceilometer Viewer', DWD, <http://www.dwd.de/ceilomap>. Accessed 2015-07-20.
- [2] Flentje, H.; Heese, B.; Reichardt, J. & Thomas, W. (2010), 'Aerosol profiling using the ceilometer network of the German Meteorological Service', Atmospheric Measurement Techniques Discussions 3(4), 3643--3673.
- [3] Jin, Y.; Kai, K.; Kawai, K.; Nagai, T.; Sakai, T.; Yamazaki, A.; Uchiyama, A.; Batdorj, D.; Sugimoto, N. & Nishizawa, T. (2015), 'Ceilometer calibration for retrieval of aerosol optical properties', Journal of Quantitative Spectroscopy and Radiative Transfer 153, 49 - 56.

[4] Wiegner, M.; Madonna, F.; Biniotoglou, I.; Forkel, R.; Gasteiger, J.; Geiß, A.; Pappalardo, G.; Schädler, K. & Thomas, W. (2014), 'What is the benefit of ceilometers for aerosol remote sensing? An answer from EARLINET', *Atmospheric Measurement Techniques* 7(7), 1979--1997.

[5] Wiegner, M. & Geiß, A. (2012), 'Aerosol profiling with the Jenoptik ceilometer CHM15kx', *Atmospheric Measurement Techniques* 5(8), 1953--1964.

[6] NASA Goddard Space Flight Center (2015), 'The AEROSOL ROBOTIC NETWORK (AERONET)', National Aeronautics and Space Administration (USA), <http://aeronet.gsfc.nasa.gov/>. Accessed 2015-07-20.

[7] Vande Hey, J. (2014), *A Novel Lidar Ceilometer: Design, Implementation and Characterisation*, Springer International Publishing.

[8] Vaisala Oyj (2010), 'User's Guide : Vaisala Ceilometer CL51', <http://www.vaisala.com>.

[9] Berk, A.; Anderson, G.; Acharya, P. & Shettle, E. (2008), 'MODTRAN 5.2.0.0 User's Manual', Spectral Sciences, Inc. and Air Force Research Laboratory (AFRL), <http://www.modtran5.com/>.

[10] Wiegner, M. & Gasteiger, J. (2015), 'Correction of water vapor absorption for aerosol remote sensing with ceilometers', *Atmospheric Measurement Techniques Discussions* 8(6), 6395--6438.

[11] Vaisala Oyj (2010), 'User's Guide : Vaisala Boundary Layer View Software BL-VIEW', <http://www.vaisala.com>.

[12] Jin, Y.; Kai, K.; Kawai, K.; Nagai, T.; Sakai, T.; Yamazaki, A.; Uchiyama, A.; Batdorj, D.; Sugimoto, N. & Nishizawa, T. (2015), 'Ceilometer calibration for retrieval of aerosol optical properties', *Journal of Quantitative Spectroscopy and Radiative Transfer* 153, 49 - 56.

## *A local diagnosis of the Hadley circulation over South Africa*

Dawn Mahlobo<sup>1</sup>, Thando Ndarana<sup>2</sup>

<sup>1</sup>South African Weather Service, Private Bag X097, 0001 South Africa

<sup>2</sup>Council for Scientific and Industrial Research, Pretoria, South Africa

### **ABSTRACT**

This study attempts to provide the local diagnostics of the Hadley circulation over South Africa. The zonally averaged mass stream function have been calculated using the NCEP reanalysis data for the period 1979 to 2013. Preliminary results from the mass stream function indicate regional differences of the local Hadley circulation, South Africa in particular is characterized by a downward mass stream function for both the DJF and JJA seasons

**Key words:** Hadley cell, Mass stream function, Circulation, Mass flux

### **1. Introduction**

In its Integrated Resource Plan (IRP) 2010, the South African government has identified a number of renewable energy options to inform the country's energy mix on the 2030 horizon and beyond. One of these options is solar energy, which depends on the ability of incoming short wave radiation to penetrate through the atmosphere to the ground, where solar energy conversion technologies are located. One of the major phenomena that influence solar power generation is large scale cloud formation. As the former might be impacted by climate change (Crook et al., 2011), increasing greenhouse gasses might present opportunities or threats to South Africa's renewable energy industry since this would influence the country's ability to generate electricity from the solar energy resource.

Large scale cloud formation requires two things to occur; the large scale ascent of atmospheric air mass and enough moisture content for adiabatic cooling to lead to condensation. Over South Africa, this large scale ascent is, to a very large extent, informed by the subtropical branch of the Hadley cell, and so climate change induced changes in this branch might have a knock on effect that eventually ends up enhancing or threatening solar power generation.

A detailed analysis over South Africa of this causal knock on effect is dependent on the ability to properly diagnose Hadley cell motions over the country. The necessity of such diagnostics is clearly indicated by the zonal gradient of rainfall during the summer and the domi-

nance of the winter high pressure system over the country (van Heerden and Taljaard, 1998). The Hadley cell is defined by Wallace and Hobbs (2006), and many other systematic reviews of atmospheric processes, as a large scale atmospheric circulation that is caused by differential heating of the earth's surface. On average, the subsiding branch of the Hadley cell is dry, warm and cloud free. This causes arid and semi-arid climates in the subtropical regions. As will be noted further below, this has important implications for the solar energy resource along the subtropical belts, and over South Africa in particular.

The Hadley cell plays an integral role in the context of climate change and associated changes in the atmospheric circulation. Several studies have shown that the Hadley cell has progressively been widening (Johanson and Fu, 2009; Choi et al., 2014; Hu and Fu, 2007; Lu et al., 2007) and strengthening (Engelbrecht et al., 2011; Loeb et al., 2014; Grenfell, 2003) and will continue to do so in future, as greenhouse gas concentrations increase.

As it is well known in meteorology and climatology, in as far as atmospheric motion is concerned, clouds form as a result of rising air parcels which cool adiabatically and moisture condenses. Descending motion leads to less cloud formation. Therefore, the broadening and strengthening of the descending branch of the Hadley cell will lead to broader subtropical regions of cloudless skies and higher frequencies of cloudless days.

<sup>1</sup> Email: dawn.mahlobo@weathersa.co.za

Whilst these might be undesirable developments in far as sectors such as water and agriculture are concerned, they might have good implications and might present opportunities for the solar energy industry.

## 2. Data and Methods

The National Centre for Environmental Prediction reanalysis (NCEP1, Kinamitsu et al., 2002) for the period 1979-2013 was used in this study.

The first step is to calculate the zonally averaged mass stream function using the NCEP reanalysis data. Most studies have used the mass stream function to portray the local Hadley cell (e.g. Hartman, 1990).

The mass stream function is defined as

$$\Psi = \frac{2\pi a \cos\phi}{g} \int_0^p \bar{v} dp$$

Where  $\Psi$  is the mass stream function,  $\bar{v}$  is the zonally-averaged meridional velocity,  $a$  is the radius of the earth,  $g$  is gravity,  $\phi$  is latitude and  $p$  pressure level.

The second step will be to produce local Hadley cell diagnostics using the method of Reeder et al. (2012), whereby the psi-vector method of Keyser et al. (1989) is used to partition the irrotational part of the three dimensional flow into a pair of orthogonal two-dimensional circulations.

Given  $\omega$  the vertical motion from the NCEP reanalysis data. The potential function  $\mu$  was obtained by solving the Poisson's partial differential equation using FORTRAN 77 subroutines of Swarztrauber (1974) as in Chen (1985) and D'Abreton and Tyson (1995) and hence the vector stream function.

$$\nabla_p \cdot \psi = -\nabla_p^2 \mu = \omega$$

Where  $\nabla_p$  is the gradient operator in isobaric coordinates.

The divergent wind is written as the velocity stream function:

$$u_{div} = (u_\lambda, u_\phi) = -\frac{\partial \psi}{\partial p} = -\left(\frac{\partial \psi_\lambda}{\partial p}, \frac{\partial \psi_\phi}{\partial p}\right)$$

Where  $u_\lambda$  and  $u_\phi$  are the zonal and meridional components of the divergent part of the wind and  $\psi_\lambda$  and  $\psi_\phi$  are the components of  $\psi$  in the zonal and meridional directions respectively. The vertical motion was then partitioned into zonal and meridional planes

$$\omega_\lambda \cos\phi = \frac{1}{a} \frac{\partial \psi_\lambda}{\partial \lambda} = \frac{1}{a^2} \frac{\partial^2 \mu}{\cos\phi \partial \lambda^2}$$

$$\omega_\phi \cos\phi = \frac{1}{a} \frac{\partial}{\partial \phi} (\omega_\phi \cos\phi) = \frac{1}{a^2} \frac{\partial}{\partial \phi} \left(\frac{\partial \mu}{\partial \phi}\right)$$

Where  $a$  is the radius of the earth.

The vertical motion is defined as the sum of the vertical motion in two orthogonal directions

$$\omega = \omega_\lambda + \omega_\phi$$

The upward mass fluxes associated with the zonal and meridional parts of the circulation are

$$m_\lambda = -\omega_\lambda \cos\phi / g \quad \text{and}$$

$$m_\phi = -\omega_\phi \cos\phi / g$$

respectively, and they denote the local Hadley and local Walker circulations respectively where  $g$  is the gravitational acceleration.

## 3. Preliminary Results

The time-mean local Hadley circulation is defined by the mass stream function at 500hPa. The local Hadley circulation is characterized by zonal elongated bands of vertical mass stream function with marked ascent in the tropics and subsidence in the subtropics (FIG 1).

For both the southern and the northern hemisphere the mass stream function subsidence is more pronounced during December to February (DJF) than in June to August (JJA). During DJF the ascent is more prominent in the Southern Hemisphere while subsidence is more significant in the Northern Hemisphere. The situation is reversed during JJA.

South Africa's position in the subtropics, which is the descending branch of the Hadley cell might be the reason for the downward mass stream function for both DJF and JJA.

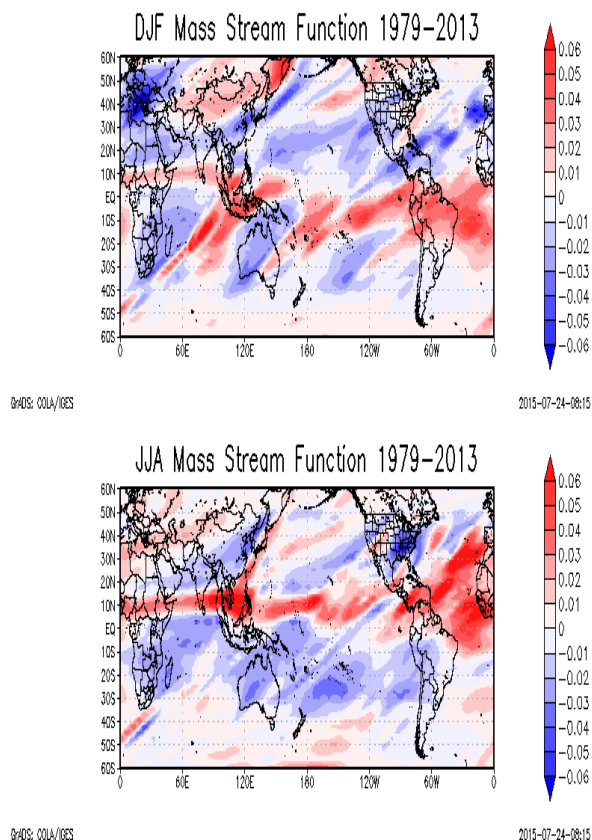


FIG. 1. Mass stream function of the Hadley Cell

#### 4. Conclusions

This study is an attempt to preliminary diagnose the local Hadley based on the NCEP Reanalysis data. The approach is to calculate zonal average mass stream function by (e.g. Liu et al., 2012; Ngunyen et al., 2013) and psi-vector method of Keyser et al. (1989) to partition the irrotational part of the three dimensional flow into a pair of orthogonal two-dimensional circulations. Preliminary results from the mass stream function indicate regional differences of the local Hadley circulation, South Africa in particular is characterized by a downward mass stream function for both the DJF and JJA seasons. Going forward a comparison between the mass stream function calculations as well as the mass flux calculations will be made to check areas of similarities and differences of the local Hadley diagnostics over South Africa.

#### 5. References

Chen TC, 1985: Global water vapour flux and maintenance during FGGE, *Mon.Wea.Rev.*, 113, 1801-1819

Choi J, Sun S-W, Lu J and Min S-K, 2014: Further observational evidence of Hadley cell widening in the Southern Hemisphere, *Geo.Phy.Res.Let.*, 41, 2590-2597

Crook JA, LA Jones, Forster PM and R Crook, 2011: Climate change impacts on future photovoltaic and concentrated solar power energy output, *Energy Environ.Sci.*, 4, 3101-3109

D'Abreton PC and Tyson PD, 1995: Divergent and non-divergent water vapour transport over Southern Africa during wet and dry conditions. *Meteorol.Atmos.Phys.* 55, 47-59

Engelbrecht F.A, W.A Landman, CJ Engelbrecht, S. Landman, M.M Bopape, B. Roux, J.L McGregor and M Thatcher, 2011: Multi-scale climate modelling over Southern Africa - using a variable-resolution global model. *Water S.A.*, 37, 647-658.

Grenfell JI, DT Shindell and V Grewe, 2003: Sensitivity studies of oxidative changes in the troposphere in 2100 using the GISS GCM, *Atmos.Chem.Phys.*, 3, 1267-1283

Hartmann, H.C. 1990. Climate Change Impacts on Laurentian Great Lakes Levels. *Climatic Change*, 17: 49-67.

Hu Y and Q Fu, 2007: Observed poleward expansion of the Hadley circulation since 1979. *Atmos. Chem.Phys.*, 7, 5229-5236.

Johanson CM and Q Fu, 2009: Hadley Cell Widening: Model Simulations versus Observations. *Journal of Climate*, 2713-2725.

Keyser, D., B. D. Schmidt, and D. G. Duffy, A technique for representing three-dimensional vertical circulations in baroclinic disturbance, *Mon. Wea. Rev.*, 117, 2463-2494, 1989.

Liu J, M. Song, Y. Hu and X. Ren, 2012, Changes in the strength and width of the Hadley Circulation since 1871, *Clim. Past*, 8, 1169-1175.

Loeb NG, DA Rutan, S Seiji and Wang w, 2014: Observing intrannual variations in

Hadley circulation atmospheric heating and circulation strength, *J.Clim*, 27, 4139 - 4158

Lu J, GA Vecchi and T Reichler, 2007; Expansion of the Hadley Cell under global warming. *Geophysics Research Letter*, L06805, doi:10.1029/2006GL028443.

Nguyen H, Evans A, Lucas C, Smith I, and Timbal B, 2013: The Hadley circulation in reanalysis: *Climatology, variability and Change. J.Clim*, 26, 3357 - 3376

Reeder M, Govekar P and R Wardle, 2012, Partitioning of the overturning circulation in the tropics and the connection to the Hadley and Walker circulations, School of Mathematical Science, Monash University

Schwendike, J., P. Govekar, M. J. Reeder, R. Wardle, G. J. Berry, and C. Jakob, 2014: Local Partitioning of the overturning circulation in the tropics and the connection to the Hadley and Walker circulations, *J. Geophys. Res. Atmos.*, 119.

Swarztrauber PN, 1974. The direct solution of the discrete Poisson Equation on the Surface of a Sphere, *J.Comp.Phys.* 15, 46 -54.

Van Heerden J and Taljaard JJ, 1998: Africa and Surrounding Waters, *Meteorological monographs*, 27, 141-174

Wallace JM and PV Hobbs, 2006: *Atmospheric Science: An Introductory Survey*. 2<sup>nd</sup> ed. Academic Press, 483pp.

# Atmospheric anomalies during the 2012/13 extreme hail seasons over Gauteng.

Nita Pienaar, Liesl L Dyson and Emsie Klopper

Department of Geography, Geoinformatics and Meteorology, University of Pretoria.

## Abstract

The Gauteng Province, South Africa, experienced severe hailstorms during 2012 and 2013. This led to the disruption of lives and large financial losses which were reflected in dramatically higher hail related insurance claims. This paper explored the anomalies in the circulation patterns of the years associated with damaging hail over Gauteng. The synoptic circulation patterns over Southern Africa for the hail months, September to December, were compared to the climatological mean. Similarly the thermodynamic properties of the atmosphere over Gauteng were analysed and compared. During 2012 and 2013 a temperature trough was present at 500 hPa level west of Gauteng. At 850 hPa the temperatures were warmer over the southern interior and the surface trough was deeper and more developed. The 2012/13 sounding parameters which deal with temperature and temperature lapse rates, moisture and cloud properties differed significantly from the long term mean. The mid troposphere was unstable with warmer surface temperatures and colder upper air inflow. It was found that the anomalies in circulation patterns together with lower freezing levels, shallower cloud depth below freezing level and lower cloud base pressure can thus be indicators of higher than normal hail seasons. It is recommended that the study be expanded to include other years that significant hail events occurred over Gauteng and the rest of South Africa.

Keywords: hail season, atmospheric anomalies, circulation patterns, atmospheric properties, Gauteng

## Introduction

Hail is precipitation in ice format with a diameter of at least 5mm and is associated with thunderstorms. Typically hail stone sizes vary from 5mm to 10cm and in exceptional cases it may even be larger. Hail stones fall towards the earth under gravity at velocities that depend upon their size and the larger stones will reach the ground first during a hail storm (Rinehart, 2004).

In the highly populated Gauteng province hail regularly causes extensive damage to vehicles and property, which leads to the disruption of lives and to large financial losses. The 2012 and 2013 hail seasons were particularly disruptive and made headline news on several occasions. Figure 1 indicates the large number of Santam hail claims in 2012/13 (Melville, 2014) compared to period 2001 to 2011.

This paper aims to identify anomalies in atmospheric properties during the 2012 and 2013 hail seasons in comparison to the climatology of the preceding 33 years. First, the synoptic scale circulation climatology was compared to the circulation patterns of 2012 and 2013 over Southern Africa for the months September to December. Secondly a quantitative analysis of the thermodynamic conditions of days when thunderstorms were present over Gauteng was carried out by comparing the sounding data and sounding-derived indices associated with hail over Gauteng. Significant anomalies were identified through comparing the hail seasons of 2012 and 2013 to the long term mean of the period 1979 to 2011.

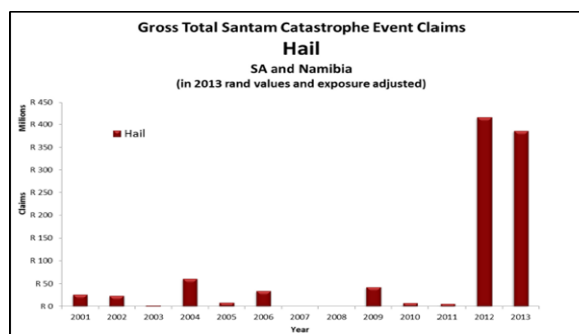


FIGURE 1: Yearly distribution of Santam's hail claims. Adapted from Melville (2014).

## Data and Methods

In this paper the hail season for Gauteng is defined as the spring and early summer months from September to December since most of the Gauteng hail claims occurred in this period and was confirmed by analysing Momentum Short Term Insurance claim data (Van der Merwe, 2014). The National Centre for Environmental Prediction (NCEP) reanalysis data (Kalnay, et al., 1996) were used to create average atmospheric circulation maps for both the climatological period (1979 to 2011) and the hail years (2012 and 2013). Temperature, geopotential heights, specific humidity and zonal and meridional winds were obtained at 850 and 500 hPa in the region surrounding South Africa. A qualitative analysis to identify anomalous circulation of the hail months was conducted.

Sounding data of the Irene weather office were used to identify significant anomalies in the thermodynamic properties of the atmosphere between the 2012/13 hail seasons and the climatological mean represented by all rain days. A rain day is defined as a day when at least 30% of the Gauteng rainfall stations received more than 1mm rain. No comprehensive list of thunderstorm days were available for the entire study period and defining a rain day by using a distribution of 30 % tries to capture days when thunderstorms occurred over at least a third of the province. The 1200 UTC were utilized for hail producing storms over Gauteng as it is closest to the time of maximum convection (Tyson and Preston-Whyte, 2012). Irene is almost in the centre of Gauteng and soundings from this location can be seen as proximity for the Gauteng area (Dyson et al., 2015). The sounding data used were obtained from the University of Wyoming website (<http://www.weather.uwyo.edu/>). The data used were temperature, dew point temperature, geopotential height and the wind speed and direction at all pressure levels from the surface to 300 hPa. The sounding parameters as depicted in Table 1 were calculated.

The averages of the sounding data and the sounding-derived indices were calculated for rain days of the 2012 and 2013 hail seasons and compared to the averages of the climate to statistically determined significant anomalies. The Student's t-test was used to determine the level of statistical significance of the anomalies. A confidence level of 95% was used.

### Results and Discussion

#### Synoptic circulation

The surface temperature patterns, show remarkable similarities for the 2012 and 2013 period (Fig. 2) while differing significantly from the climatological mean (CM). The temperatures were higher for each month of September to November in 2012 and 2013 than the CM (September not shown) over the entire southern Africa. The surface trough was also deeper as it extended to the interior of South Africa. During the hail season of 2012/13 the ridge of the Indian Ocean High over the interior was weaker compared to the CM. The flow of moist air therefore was more direct towards Gauteng. During the spring months the westerly surface winds were more to the south than normal as the Atlantic Ocean High was situated further to the south.

During most of the hail months of 2012 and 2013 a prominent temperature upper air trough was present to the north west of Gauteng (Fig. 3). This cold air trough, together with the prevailing westerly winds, may have caused colder upper air inflow towards Gauteng therefore increasing the conditional instability of the atmosphere.

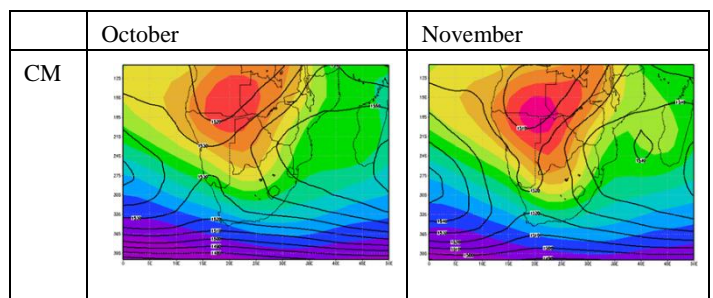
The inflow of warmer more moist air from the north-east during 2012 and 2013, together with inflow of colder upper air contributed towards the higher occurrence of hail.

Table 1: Sounding parameters and derived indices

Parameter	Abbreviation	Units
Freezing level height	FZ	m
Cloud depth below freezing level	FZD	m
Temperature lapse rate: surface to 500 hPa	Ts5	°C/km
Temperature lapse rate: 700 to 400 hPa	T74	°C/km
Average dew point at lowest 100 hPa	Td100	°C
Pressure at cloud base	CBP	hPa
Relative humidity surface to 500 hPa	RH05	%
Relative humidity 600 to 400 hPa	RH64	%
Temperature at 850 hPa	T850	°C
Dew point temperature at 850 hPa	Td850	°C
Temperature at 500 hPa	T500	°C
Dew point temperature at 500 hPa	Td500	°C
Temperature at 400 hPa	T400	°C
Wind speed at 300 hPa	WS3	m/s
Convective available potential energy	CAPE	J/kg
Bulk Wind shear – surface to 700 hPa	BWSs7	m/s
Bulk Wind shear – surface to 400 hPa	BWSs4	m/s
Bulk Richardson number	BRN	
Cloud base index	CBI	

#### Irene sounding parameters

Table 1 lists the 2012/13 thermodynamic parameters that were significantly different from the climate. They were the surface to 500 hPa temperature lapse rates (Ts5), the surface temperatures (T850), the freezing level depth (FZD) and the cloud base pressure (CBP). The higher surface temperatures correspond to the synoptic circulation analysis performed with NCEP data while steeper temperature lapse rates are also indicative of increased conditional instability.



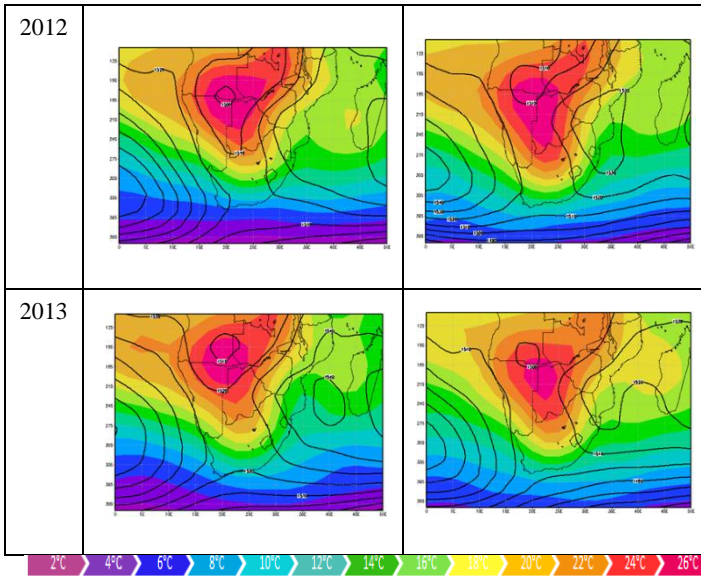


FIGURE 2: The monthly mean 850 hPa geopotential heights (solid black lines) and temperatures (shaded) for October and November for the climatological mean (CM) and, 2012 and 2013.

The cloud depth below freezing level was shallower for 2012 and 2013. The freezing level was consistently lower during 2012 and 2013 and significantly lower during the early summer months. The lower freezing level and higher cloud base (by virtue of lower CBP) indicate that the warm liquid part of clouds were smaller and therefore could have resulted in higher hail occurrence.

None of the selected sounding-derived indices were significantly and consistently higher or lower during 2012/13 compared to the climate. The CAPE and BRN values were however higher during the November/December period compared to the September/October period. The CAPE values of hail days compared to rain days were higher but not at a 95% significant level.

Poolman (1992) found that low values (below 85) of the cloud base index (CBI) increase the probability of hail growth. The CBI values during the spring months were much lower than during the early summer months, with values below 85. Although the average CBI values during 2012 and 2013 were lower than the climatological mean, it was not at a 95% significant difference level.

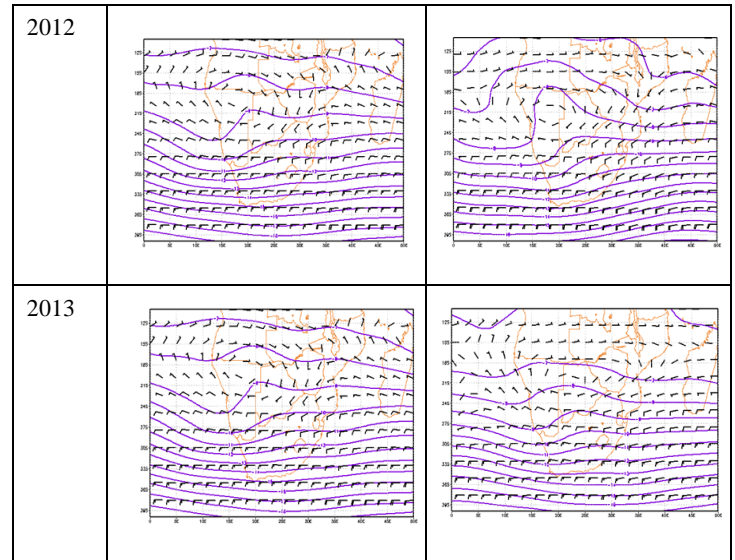
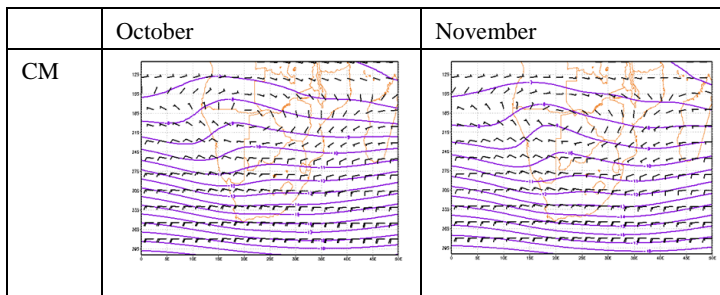


FIGURE 3: The monthly mean 500 hPa temperatures (solid blue lines) and wind in knots for October and November for the climatological mean (CM), 2012 and 2013.

TABLE 1: Listing of the mean values for September/October and November/December for rain days during 2012 and 2013 compared to the climatological mean where there is a significant difference.

	September/October			November/December		
	1979-2011	2012	2013	1979-2011	2012	2013
n	711	15	17	1452	42	44
FZ	4232	4205	4217	4580	4483	4491
FZD	78.2	71.5	52.0	121.9	106.1	103.3
Ts5	7.6	7.5	8.2	7.3	7.7	7.6
CBP	693	690	667	712	702	698
RH05	50.5	42.8	41.4	53.8	56.6	52.8
RH64	39.6	25.7	27.8	39.3	43.0	39.1
T850	22.3	21.2	24.5	23.9	25.0	24.8
TD850	8.2	7.4	8.1	11.8	12.0	11.4
TD500	-25.7	-33.3	-32.3	-24.2	-22.8	-23.6

Conclusions

Conditions needed for hail formation were enhanced during the 2012/13 hail seasons. In general the synoptic circulation patterns for 2012 and 2013 were very similar to one another and different from the climatological mean. Most notably were the temperature pattern differences at the 850 and 500 hPa levels. The surface temperatures were higher over the southern interior. Temperature troughs were present in both hail months west of Gauteng at 500 hPa, which resulted in colder upper air inflow. The analysis of the thermodynamics over Gauteng confirms that there was an increase in conditional instability as indicated by the higher surface temperatures and colder 500 hPa temperatures.

During 2012 and 2013 cloud depths below the freezing level were

shallower than the climatological mean. The freezing levels were also lower and the cloud bases, by virtue of lower cloud base pressures, were higher. This indicates that the warm liquid part of clouds were smaller and the possibility for hail growth higher. During the spring months of the hail seasons of 2012 and 2013, the atmosphere was significantly dryer than the climatological mean throughout the atmosphere. This correlates with previous findings that more intense hail seasons are often preceded by dry periods (Olivier, 1990).

By analysing the Momentum Short Term Insurance hail claim data it was interesting to note that the hail claim distribution correlated well with the climatology in terms of the highest hail occurrence during October and November. The geographical distribution of the hail is similar to the topography and the demographical distribution of Gauteng. The time of the day when hail peaks, late afternoon to early evening, is the same time as peak traffic on Gauteng roads and can be a factor in the amount of hail claims along the national roads.

In conclusion, the anomalies in circulation patterns and sounding data over Gauteng found in this study can be indicators of higher than normal hail seasons. It can assist forecaster to predict higher than normal hail periods and thereby assisting the users of such predictions, for example the Insurance Industry and exposed communities, to better manage the impact of hail. It is recommended that the study be expanded to include other years when significant hail events occurred in Gauteng as well as expanding it to include the rest of South Africa.

#### References

1. Dyson, L.L., van Heerden, J. & Sumner, P.D., 2015: A baseline climatology of sounding-derived parameters associated with heavy rainfall over Gauteng, South Africa. *International Journal of Climatology*, 2014. 35: 114–127.
2. Kalnay, E., Kanamitsu, M., Kistler, R., Collins, W., Deaven, D., Gandin, L., Iredell, M., Saha, S., White, G., Woollen, J., Zhu, Y., Leetmaa, A. & Reynolds, R., 1996: The NCEP/NCAR 40-year reanalysis project, *Bull. American Meteorological Society*, 77: 437-470.
3. Melville, J., 10 June 2014: *Hail! Hail! Hail! Insurance?* [http://www.iisa.co.za/images/stories/Seminars/may\\_2014/john\\_melville.pdf](http://www.iisa.co.za/images/stories/Seminars/may_2014/john_melville.pdf), 5 July 2014.
4. Olivier, J., 1990: 'Hail in the Transvaal, some Geographical and Climatological Aspects'. Phd Thesis, University of Johannesburg.
5. Poolman, E.R., 1992: 'Die Voorspelling van Haelkorrelgroei in Suid-Afrika'. MSc Thesis, University of Pretoria.
6. Rinehart, R.E., 2004: *RADAR for Meteorologists*. Fourth Edition, Rinehart Publishing; 154.6.
7. Tyson, P.D. and Preston-Whyte, R.A., 2012: *The Weather and*

*Climate of Southern Africa*. Eighth Impression, Oxford University Press: Cape Town, South Africa; 206.

8. Van der Merwe, M., 2014: Momentum Short Term Insurance hail claims data.

#### Acknowledgements

Employer - Momentum

Husband and family for continuous support

## Solar ultraviolet radiation levels measured under umbrellas in relation to ambient conditions and sun angle

Patricia N. Albers<sup>a\*</sup>, Caradee Y. Wright<sup>a,b</sup> and Martin W. Allen<sup>c</sup>

<sup>a</sup>Environment & Health Research Unit, South African Medical Research Council, Pretoria, South Africa.

<sup>b</sup>Department of Geography, Geoinformatics and Meteorology, University of Pretoria, Pretoria, South Africa.

<sup>c</sup>Department of Electrical and Computer Engineering, University of Canterbury, Christchurch, New Zealand.

\*Corresponding author. Email: patricia.albers@mrc.ac.za.

### Abstract

South Africa, a sunny country, receives high levels of solar ultraviolet radiation (UVR). UVR exposure is linked to several adverse health effects, including melanoma. In South Africa, handheld umbrellas are often used for sun and rain protection. This study endeavoured to measure solar UVR levels using electronic UVR dosimeter badges under three different coloured umbrellas, comparing these to ambient solar UVR levels. Data were analysed taking into account Solar Zenith Angle (SZA) and Solar Azimuth Angle (SAA). Results show considerably lower solar UVR levels under all three different umbrella types in comparison to ambient solar UVR levels. The umbrellas blocked up to 87.9% of ambient solar UVR, regardless of UVR badge location under the umbrella and SZA. Further, white umbrellas were least effective at reducing ambient solar UVR levels (76.6%) with solid blue performing the best (95.4%). Handheld umbrellas can potentially be considered as reasonable sun protection devices, however, this would depend on colour, the angle at which they are held, and their construction fabric and style.

**Keywords:** Solar zenith angle, Solar azimuth angle, Pretoria.

### 1. Introduction

In South Africa, the handheld umbrella is often used for personal shade on sunny days in addition to rain protection on wet days. One study in 2012 evaluated the solar ultraviolet radiation (UVR) protection provided by handheld umbrellas (McMichael, Veledar and Chen, 2013). They investigated umbrellas of different colours and patterns, and found that overall, umbrellas blocked about 77% of solar UVR and that black umbrellas offered the best protection. They did not consider the diurnal pattern of solar UVR levels in relation to solar zenith angle (SZA) in their analyses. Another study examined the social acceptability of handheld umbrellas for sun protection among females in the US and found moderate acceptability (McMichael, Ezirike, Veledar, Rice and Chen, 2014).

Here, we measure solar UVR levels at two positions (the face and directly beneath the umbrella fabric) under three different coloured (i.e. blue, white, and blue/white) umbrellas of the same fabric over the course of a day. We aimed to evaluate the overall average amount of solar UVR protection offered by the umbrellas, which colour umbrella offered the best protection, and the influence of SZA on solar UVR levels underneath the umbrellas.

### 2. Data and Methods

Data were collected from two instruments: electronic solar UVR dosimeter badges (Figure 1) and a UV-biometer (Figure 2). The UVR dosimeter badges were used to collect data during the field campaign underneath the umbrellas and at an exposed, horizontal site a few metres away from the umbrella set-up. Data from the biometer were used to calibrate the UVR badge data. The UVR dosimeter badges were developed at the University of Canterbury, Department of Electrical and Computer Engineering, New Zealand, to measure personal exposure to solar erythemal UVR (290-

400 nm) and have been described in detail elsewhere (Allen and McKenzie, 2013; Wright et al., 2007). They have been shown to be suitable instruments for use in solar UVR exposure studies (McKenzie et al., 2013; Seckmeyer et al., 2012; Seckmeyer et al., 2008).

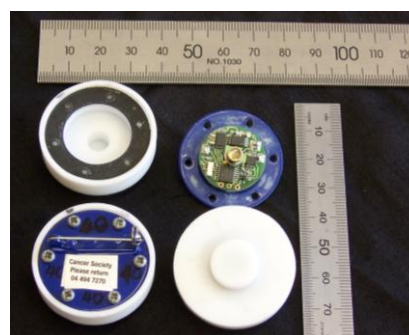


**Figure 1.** Two UVR badges showing inside of the Teflon cap (top left), sensor and circuit board (top right), back plate (bottom left) and front of Teflon cap (bottom right).



**Figure 2.** Location of the SAWS biometer on the roof of SAWS Head Office in Pretoria.

The main component of the UVR badge is a miniature solid-state AlGaN detector that measures erythemally-weighted UVR. The detector response is electronically converted into

a digital count (on a scale from 1 to 1024) that is proportional to the incident erythemally-weighted UVR irradiance. The detector is encased in a weatherproof polytetrafluoroethylene enclosure which also acts as a diffuser to ensure that the angular response of the instrument is close to the cosine response of human skin (Swift et al., 2010). The badge is powered by a small lithium coin cell battery (CR 1616, 3 V) and has a diameter of 35mm, thickness of 13mm, and weighs approximately 20.7 g. The badges were programmed to record UVR data every 60 seconds from 06h00 – 21h00 and they have sufficient on-board memory and battery capacity to store numerous days of data.

#### Calibration of UVR badges

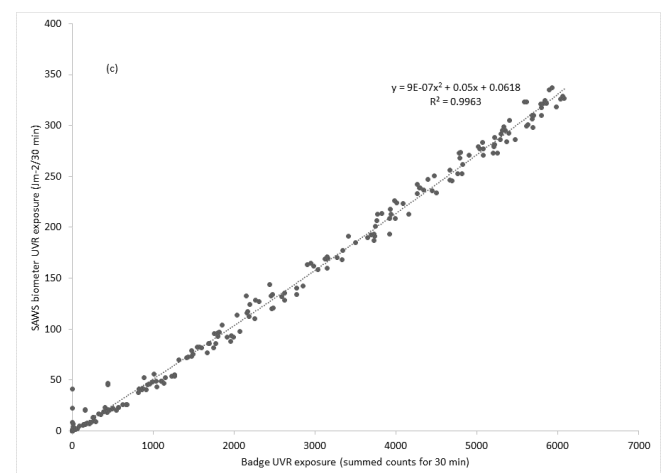
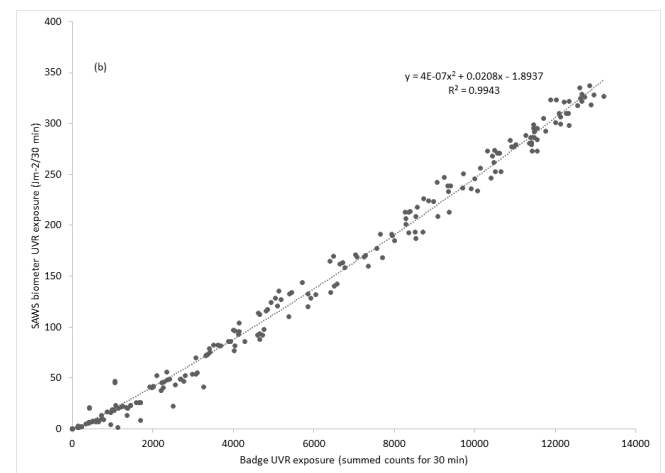
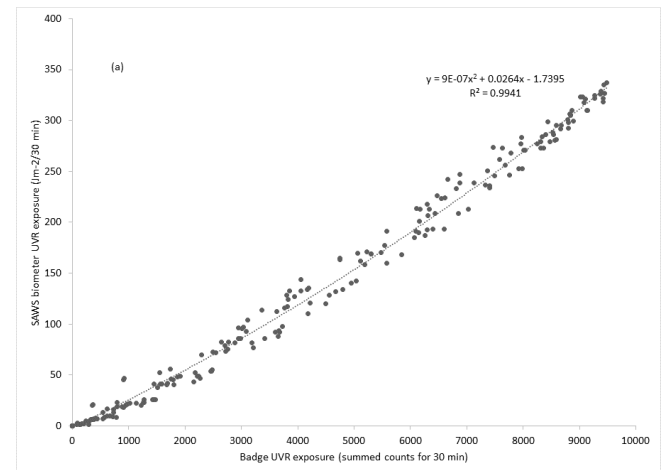
The badge counts measured by the UVR badges were converted to units of  $\text{Jm}^{-2}$  per 30 minute period ( $\text{Jm}^{-2}/30 \text{ min}$ ) in a calibration procedure using data from a UV biometer. The UV biometer (model 501) comprising a Robertson-Berger pattern UVR detector, digital recorder and control unit is used to measure ambient solar UVR levels at the South African Weather Service (SAWS) head office in Pretoria. The UV Biometer spectral response closely mimics the McKinley/Diffey Erythemal Action Spectrum (280-340 nm) (CIE, 1987). Calibration against the UV biometer enables the measured Minimal Erythemal Dose (MED) per 30 minute period to be converted into  $\text{Jm}^{-2}$  by dividing by 210 (Note: 1 MED = 210  $\text{Jm}^{-2}$  of erythemal UVR for skin phototype I) (Fitzpatrick, 1986). Recently, the UV biometer was inter-compared with a travelling standard instrument calibrated against the fast scanning spectro-radiometer SPECTRO 320D NO 15 that has traceability to the International Bureau of Weights and Measures. Analysis found the difference in the instrument pre- and post-calibration was less than 4%.

The calibration campaign took place from the 23 April to the 4 May 2015 in Pretoria. The four UVR badges used in the study were placed alongside the UV biometer and set to record every 60 seconds. On the 5<sup>th</sup> of May, the UVR badge and UV biometer data were downloaded to a personal computer. The UVR badge data were summed for every 30 minutes and compared to the UV biometer data in  $\text{Jm}^{-2}$  for the same 30-minute period. A second order polynomial equation was implemented for each UVR badge in relation to the UV biometer. The individual calibration equations are shown in Figure 3. For analysis of data from the measurement campaign, the badge counts were summed for every half an hour of the day and converted to  $\text{Jm}^{-2}$  using their individual calibration equations.

#### Procedures

The fieldwork campaign was held on the 11<sup>th</sup> of April 2015 from 7h00 to 16h30 in Pretoria. Two UVR badges were used to take measurements underneath the umbrellas and two UVR badges were used to measure ambient solar UVR conditions. Table 1 describes the location of the UVR badges beneath three different umbrellas: white, blue and blue/white striped at different time periods. The UVR badges were also moved to two different positions beneath the umbrella: just below the fabric, in the centre of the

umbrella and at a typical facial site in the centre of the umbrella.



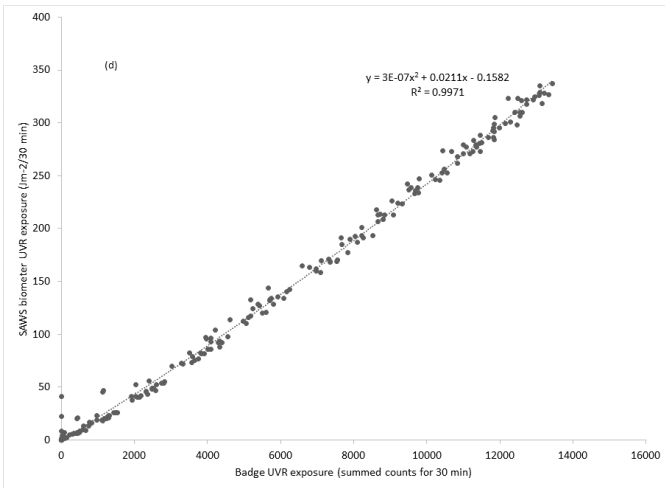


**Figure 3.** Calibration equations generated using UV biometer data plotted against UVR badge data for all four UVR badges (a) to (d).

#### Analysis

Analyses were carried out in Microsoft Excel and STATA 13.1. Solar UVR exposure data from under-umbrella sites were compared to ambient solar UVR levels. Data from all four badges are shown separately and averaged to calculate under-umbrella solar UVR as a percentage of the ambient solar UVR, as well as to estimate possible overall protection provided by the different umbrellas. In order to consider measured under-umbrella solar UVR levels in relation to the position of the sun, SZA and solar azimuth angle data were requested and provided by the National Institute for Water and Atmospheric Science (NIWA). The SZA is the angle

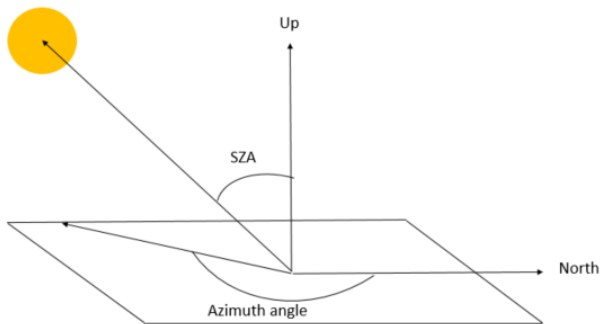


**Figure 4.** Diagrammatic sketch illustrating SZA and azimuth angle.

measured from the vertical to the sun's direct rays and the solar azimuth angle (SAA) is measured clockwise from North (Figure 4). Measured solar UVR levels were plotted against SZA to consider whether the position of the sun influenced the amount of solar UVR received underneath the umbrellas.

### 3. Results

A total of 76 data points from all UVR badges were included in this one day measurement campaign. Careful procedures were executed to ensure that the identical measurement period and duration were matched for both data streams. All units are in  $\text{Jm}^{-2}$ .

#### 3.1 Measured solar UVR levels at ambient and under-umbrella sites

Ambient solar UVR levels in relation to under-umbrella solar UVR levels are shown in Figure 5. The ambient solar UVR levels show a typical bell-shaped diurnal pattern indicative of changing sun elevation in the sky, rising in the morning, reaching its highest point around midday and returning to the horizon in the afternoon. Since it was a relatively clear-sky day, with only scattered clouds during the afternoon, the diurnal ambient solar UVR pattern shows little scatter. Midday ambient levels were between  $\sim 350 - 380 \text{ Jm}^{-2}/30 \text{ min}$ . The two UVR badges used to measure ambient solar UVR levels were mostly in agreement except between 11h00 and 14h00, likely due to sensitivity differences in relation to cloud influence on solar UVR.

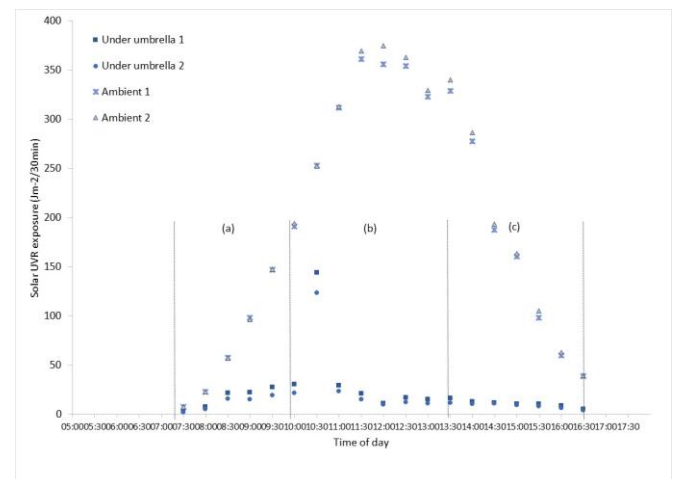


**Figure 5.** Diurnal pattern in solar UVR exposure measurements under (a) white, (b) blue and (c) blue/white umbrellas compared to ambient solar UVR exposure measurements on 11 April 2015.

Under-umbrella solar UVR levels were greatly reduced under all three different umbrella types in comparison to ambient solar UVR levels. Table 1 (column 6) shows the under-umbrella average of the two UVR badges' measurements for each half-hour period of the day. On average, under-umbrella solar UVR levels ranged between  $2.4$  and  $26.1 \text{ Jm}^{-2}$ . Despite such low values, the pattern in under-umbrella solar UVR levels still marginally reflects the typical diurnal, bell-shaped curve in solar UVR levels, except for the 12h00 measurement.

Table 1 (column 7) shows the under-umbrella solar UVR levels as a percentage of the ambient solar UVR levels for each half-hour period of the measurement campaign. Percentages ranged from 2.8 – 32.6 % depending on time of day, colour of umbrella and position of UVR badge under the umbrella.

### 3.2 Ambient and ‘under-umbrella’ solar UVR exposure measurements by SZA

SZA values (Table 1, column 8) change during the course of a day due to the changing position of the sun overhead and the SAA (column 9). Figure 6 compares SZA to measured ambient and under-umbrella solar UVR levels. As the SZA decreases (sun more directly overhead), ambient solar UVR levels increase. The same is not true for under-umbrella solar UVR levels where the umbrella acts as a barrier to the sun’s direct rays. While large SZAs when the sun is close to the horizon may lead to increased under-umbrella solar UVR levels depending on the angle of the umbrella, this could not be investigated in this study where the umbrellas were placed directly upright.

### 3.3 Position differences’ influence on under-umbrella solar UVR levels

The UVR badges were placed at two different sites under the umbrellas and differences in solar UVR levels are evident for these two positions. In general, the solar UVR levels under-umbrella as a percentage of the ambient solar UVR levels were higher under-umbrella when the UVR badge was placed directly underneath the umbrella fabric compared to when held at a typical face height under the umbrella. Increased shade effect at the lower height was the likely reason for this difference, ignoring SZA effect.

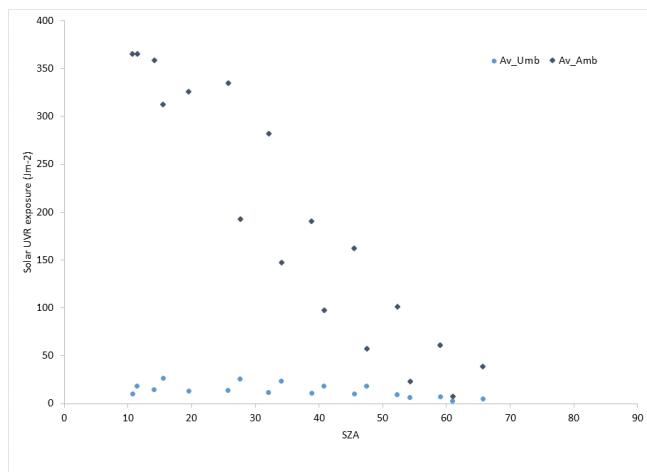


**Figure 6.** Solar UVR exposure measurements under-umbrella and ambient conditions by changing SZA.

### 3.4 Sun protection provided by umbrellas

Overall, umbrellas in this study, regardless of colour, UVR badge location under-umbrella and SZA, reduced ambient solar UVR levels by ~ 87.9%. White umbrellas were least effective at reducing ambient solar UVR levels at 76.6%. Blue and Blue/White umbrellas performed better and reduced ambient solar UVR levels by 95.4% and 91.9%, respectively.

## 4. Discussion

While this was only a one-day measurement campaign, it yielded relatively interesting results on an under-explored topic. Umbrellas are commonly used for shade in South Africa, yet little has been done to document their effectiveness. Some umbrellas are sold with a label describing their ultraviolet protection factor, however, there is no legislation in place to ensure umbrellas with the best quality fabric for ultimate sun protection are sold.

We found similar results as the one previously published study on handheld umbrellas (McMichael, Veledar and Chen, 2013); our umbrellas blocked 87% of ambient solar UVR, while their study reported 90%. We also confirmed their finding that white umbrellas perform worst in terms of sun protection. However, the umbrellas used in our study were large in comparison to the compact umbrellas their study used. We would need to perform additional measurements on multiple days to augment our data. It would also be useful to include black umbrellas, previously found to be the best at blocking solar UVR, and those with labelled UV protective fabric. Comprehensive data on umbrella diameter and canopy depth should also be recorded. Personal use of umbrellas, in terms of angle at which the umbrella is typically held, and position of the head beneath the umbrella are other variables to be considered.

## 5. Conclusion

Sun protection is an important personal behaviour to prevent excess solar UVR exposure and related adverse health effects. Handheld umbrellas may be considered reasonably useful sun protection devices depending on their colour, the angle at which they are held, and their construction style. It remains to be determined whether umbrellas are affordable and socially-acceptable for all population groups in South Africa as a practical means of sun protection.

## 6. Acknowledgements

Nicola Le Roux and Hennie Le Roux are acknowledged for carrying out the data collection. Dr Richard McKenzie and Dr Martin Allen are thanked for the loan of the UVR badges. Dr McKenzie is thanked for the provision of the SZA data. The UV biometer data for calibration were provided by the South African Weather Service.

## 7. References

- CIE, 1987. A reference action spectrum for ultraviolet induced erythema in human skin. *CIE Journal* 6, 17-22.
- Fitzpatrick, TB, 1986. Ultraviolet-induced pigmentary changes: Benefits and hazards. *Curr Probl Dermatol*. 1986;15:25-38.
- McMichael JR, Veledar E and Chen SC. UV radiation protection by handheld umbrella, 2013, *JAMA Dermatol* 149(6):757-758.
- McMichael JR, Ezirike J, Veledar E, Rice JE and Chen SC. The social acceptability of handheld umbrellas for sun protection, 2014, *Photodermatol Photoimmunol Photomed* 30(4):220-227.
- Allen, M and R. McKenzie (2013) Enhanced UV exposure on a ski-field compared with exposures at sea level. *Photochem. Photobiol. Sci.* 4, 429-437.

Wright, C.Y., A.I. Reeder, G.E. Bodeker, A. Gray and B. Cox (2007) Solar UVR exposure, concurrent activities and sun-protective practices among primary schoolchildren. *Photochem. Photobiol.* **83**, 749-758.

McKenzie, R., B. Liley, P. Johnston, R. Scragg, A. Stewart, A.I. Reeder and M.W. Allen (2013) Small doses from artificial UV sources elucidate the photo-production of vitamin D. *Photochem. Photobiol. Sci.* **12**, 1726-1737.

Seckmeyer, G., M. Klingebiel, S. Riechelmann, I. Lohse, R. L. McKenzie, J. B. Liley, M. W. Allen, A.-M. Siani, and G. R. Casale (2012) A Critical assessment of two types of personal UV dosimeters. *Photochem. Photobiol.* **88**(1), 215-222.

Seckmeyer, G., A. Bais, G. Bernhard, M. Blumthaler, C. R. Booth, K. Lantz, and R. L. McKenzie, *Instruments to Measure Solar Ultraviolet Radiation. Part 2: Broadband Instruments Measuring Erythemally Weighted Solar Irradiance*, World Meteorological Organization Global Atmosphere Watch, Report No. 164, WMO TD-No. 1289, Geneva, Switzerland, 55 pp., July 2008.

Swift, N., J. D. Hamlin, K. M. Nield, and R. L. McKenzie (2010) Characterisation of AlGaIn detectors for UV measurements, paper presented at NIWA UV Workshop, Queenstown, 7-9 April. Available at: [https://www.niwa.co.nz/sites/niwa.co.nz/files/algan\\_detectors\\_for\\_uv.pdf](https://www.niwa.co.nz/sites/niwa.co.nz/files/algan_detectors_for_uv.pdf)

**Table 1.** Timing, umbrella colour and location, measured solar UVR exposure and as a percentage of the ambient solar UVR exposure, and SZA and SAA for the campaign run on the 11 April 2015 in Pretoria.

Start time	End time	Umbrella colour	Location of UVR badge underneath the umbrella	Average ambient solar UVR exposure at exposed site (Jm <sup>-2</sup> )	Average solar UVR exposure under-umbrella (Jm <sup>-2</sup> )	UVR under the umbrella as percentage of ambient UVR (%)	Solar zenith angle (°)	Solar azimuth angle (°)
07:00	07:30	White umbrella	Under material	7.6	2.4	31.7	61.0	93.8
07:30	08:00	White umbrella	Under material	23.0	6.5	28.2	54.3	90.7
08:00	08:30	White umbrella	Under material	56.9	18.6	32.6	47.5	87.3
08:30	09:00	White umbrella	Face position	97.2	18.6	19.1	40.8	83.5
09:00	09:30	White umbrella	Face position	147.3	23.3	15.8	34.1	78.9
09:30	10:00	White umbrella	Face position	192.4	25.9	13.5	27.6	73.0
10:00	10:30	Umbrella fell over	-	-	-	-	-	-
10:30	11:00	Blue	Under material	312.3	26.1	8.3	15.5	50.1
11:00	11:30	Blue	Under material	365.4	18.0	4.9	11.4	24.2
11:30	12:00	Blue	Under material	365.1	10.3	2.8	10.7	346.1
12:00	12:30	Blue	Face position	358.5	14.5	4.0	14.1	315.8
12:30	13:00	Blue	Face position	325.9	13.1	4.0	19.5	298.9
13:00	13:30	Blue	Face position	334.5	14.0	4.1	25.7	289.0
13:30	14:00	White and Blue	Under material	282.2	11.7	4.1	32.1	282.4
14:00	14:30	White and Blue	Under material	190.5	11.1	5.8	38.8	277.5
14:30	15:00	White and Blue	Under material	161.9	10.0	6.2	45.5	273.5
15:00	15:30	White and Blue	Face position	101.3	9.1	8.9	52.3	270.0
15:30	16:00	White and Blue	Face position	61.2	7.4	12.1	59.0	266.9
16:00	16:30	White and Blue	Face position	38.8	4.5	11.6	65.7	263.9

# From a historical journey of air pollution to responsible choices that will mitigate climate change and improve the health of the nation

**Maria A. Oosthuizen**

*Council for Scientific and Industrial Research, Natural Resources and the Environment, Climate Studies, Modelling and Environmental Health Research Group, P.O. Box 395, Pretoria, 0001, South Africa.*

## Abstract

Air pollutants are emitted from both natural and man-made sources. Air pollution monitoring in the Vaal Triangle dates back as far as 1977, but has significantly improved since 1990, and more-so from 2006 when the area was declared the first air-shed priority area. Studies have shown that exposure to air pollution is associated with detrimental health effects. As air pollution is “inextricably intertwined” with climate change, this aspect is discussed in light of climate projections. Climate change is however, an abstract concept to the general public and needs to be addressed if it is a factor that influences their choices.

**Key words:** *Vaal Triangle, Human Health, South Africa.*

## <sup>1</sup>1. Introduction

The perception about air quality and air pollution has changed over the past centuries after it was realised that it could have an effect on human health. The quality of air depends on the presence or absence of pollutants in air. Air pollution can thus be defined as “the presence of substances in air at concentrations, durations and frequencies that adversely affect human health, human welfare or the environment” (Murray and McGranahan, 2003). Primary pollutants (gases and solid particles) may be emitted to air through natural (wind-blown dust, veld fires, lightning and plants) and anthropogenic or man-made (construction, mining and combustion processes) processes. Biological life contains elements such as carbon, hydrogen, oxygen, nitrogen, calcium, potassium, sulphur, some, such as manganese, copper and cobalt in small quantities. During combustion these elements will react and be released into the air. In addition, secondary pollutants may form in air from primary pollutants. For example sulphate and nitrate particles form from sulphur dioxide and nitrogen dioxide gases respectively and ozone from volatile organic compounds and or nitrogen dioxide under the influence of ultra violet rays from the sun.

## 2. History of air pollution management in the Vaal Triangle

In 2006 the Vaal Triangle Air-shed Priority Area (VTAPA) was declared the first air pollution priority area in South Africa. This action was deemed necessary due to the existence of air pollution sources and the exceedance of air quality standards in the area, which called for close management by authorities.

Air pollution (smoke and sulphur dioxide) monitoring in the main cities of South Africa commenced in 1959 (Ellerbeck et al., 1990), although air pollution was

formally addressed only when the Atmospheric Pollution Prevention Act (APPA) (Act number 45 of 1965) came into effect (Republic of South Africa, 1965). APPA aimed to control emissions at source through a permit system, which required industries regarded as potential air polluters (scheduled industries) to comply with the emissions stated in their permit. All potential sources of ambient (outdoor) air pollution were and still are represented in the Vaal Triangle. These include coal burning (from power stations, some industries and residential areas), industrial processes (such as petrochemical and metallurgical) and motor vehicles.

However, very little was done in the Vaal Triangle to combat air pollution during the period 1959 to 1970. There were no designated air pollution control officers and the only aspect of air pollution addressed was excessive smoke emissions, which through dissemination of information by health inspectors aimed at making people aware of air pollution (Department of Health, 1990). In 1970 a decision was taken by the municipal council of Vanderbijlpark to address smoke emissions under APPA. The first local regulations came into effect during 1973 and regulated fuel-burning apparatus that industries, hotels, dairies and dry cleaners were allowed to use. In the interim, approval was obtained from the minister to have some residential areas declared as smoke-free zones. The first came into effect on 28 July 1975 (Department of Health, 1990). The first designated air pollution control officer was appointed in 1976 and in the same year smoke and sulphur dioxide monitoring commenced in the Vaal Triangle. In July 1977, Section V of the APPA, which focused on the control of hazardous gasses emitted by diesel vehicles, came into effect in the Vaal Triangle. By 1981, five monitoring stations were in operation (Department of Health, 1990). Smoke was measured as the darkening ability that one cubic metre of air sampled over 48 hours had on filter paper and sulphur dioxide was sampled over 72 hours using the hydrogen peroxide method followed by chemically analysed in

<sup>1</sup> Email [Roosthui@csir.co.za](mailto:Roosthui@csir.co.za). Tel. 012 841 2035

the laboratory (Kemeny and Vleggaar, 1983). Both were thus manual methods.

The average results of the smoke and sulphur dioxide monitoring in Vanderbijlpark between 1977 and 1990 showed that concentrations of smoke and SO<sub>2</sub> remained more or less unchanged during these years (Department of Health, 1990) and were below the guidelines at the time (Ellerbeck et al., 1990).

By 1990, a perception existed amongst the public that the air in the Vaal Triangle was highly polluted and following repeated complaints from the public a meeting between the Department of Health, the Medical Research Council (MRC) and industries (including SASOL, ESKOM and ISCOR) was held. The outcome of the meeting resulted in an in-depth study aptly named the Vaal Triangle Air Pollution and Health Study (VAPS), funded by the Department and industries. This study sample included 14053 children and 46 primary schools from the area and commenced in August 1990.

During VAPS six monitoring stations monitored various pollutants (using direct reading instrumentation) as well as meteorological conditions. The main air quality findings from VAPS were (Terblanche, 1998):

1. Air pollution was worse during winter.
  2. The annual average of Total Suspended Particles (TSP) was up to 2.5 times the US-EPA health standard of 75 µg/m<sup>3</sup> (SA guideline 350 µg/m<sup>3</sup>) at the time and in coal burning townships concentrations were 4 to 6 times the US-EPA health standard.
  3. About 60% of the TSP was found to be small enough to be inhaled (10 µm or less in diameter) and the annual average of these smaller particles also exceeded the US-EPA health standard of 50 µg/m<sup>3</sup> (SA had no standard or guideline) at the time.
  4. Concentrations of sulphur dioxide were higher in winter than in summer but remained relatively low (below standards in residential areas).
  5. Concentrations of NO<sub>x</sub> remained below standards.
  6. Ozone concentrations exceeded standards < 1% of the time.
1. Depending on the annual rainfall between 1991 and 1993, pollen and fungal spores in the area also exceeded tolerance levels (Terblanche, 1991)

The situation remained more or less unchanged between 1993 and 2003; particulate matter was still the pollutant of concern, with sulphur dioxide sometimes exceeding the standard especially in industrial and coal burning areas while nitrogen dioxide remained below standards (Oosthuizen, 2004). It must however, be noted that the standards at the time were less stringent than current air quality standards.

In 2004 the APPA was replaced by the National Environmental Management: Air Quality Act (Act No. 39 of 2004), commonly known as the AQA. With the

new Act, the focus of air pollution control shifted from the source to control in the receiving environment. The Act also makes provision for areas where air pollution levels are exceeding standards or is foreseen to exceed standards to be declared as priority areas which are then closely monitored and managed. The Vaal Triangle was declared a priority area on the 26th of April 2006 by the then Minister of Environmental Affairs and Tourism.

### 3. Air pollution and health

In the late 1800s, the mayor of Middlesbrough in the United Kingdom had the following to say about the air pollution in the town: “The smoke is an indication of plenty of work and prosperous times... Therefore we are proud of our smoke” (Briggs, 1993). However, through the years we have learnt valuable lessons about the health consequences of air pollution, through incidences such as the 1952 “smog” incidence in London where subsequent re-analyses showed that 12 000 people died and not only 4000 as originally reported (Brunekreef and Holgate, 2002; Davis *et al*, 2002) as well as the more recent (2013) air pollution incidence in Beijing, China, during which the media reported that respiratory hospital admissions “rose 20%” (<http://za.news.yahoo.com/beijing-hospital-visits-rise-due-pollution-media-052431482.html>). In addition, several long and short-term epidemiology studies and studies under controlled conditions have shown detrimental health effects from exposure to air pollution (Krewski et al., 2009, Lepeule et al., 2012, WHO, 2013, Rich et al., 2013, Burnett et al., 2014). These health effects range from an increase in death rates in sensitive groups such as infants and the elderly, to chronic respiratory diseases, cardiovascular disease, including heart attacks, and impaired development and cancer. It is therefore not surprising that the 2010 Global Burden of Disease study ranked outdoor air pollution among the top 10 risks. A media release by the World Health Organization (WHO) furthermore stated that air pollution is “the world’s largest single environmental health risk” causing an estimated seven million deaths (in 2012) (WHO, 2014), compared to the estimated 1.9 million deaths from HIV/AIDS. South African studies in 2007 found that the burden of disease attributable to urban air pollution in 2000 were related to 0.9% of all deaths (Norman, et al., 2007) and indoor air pollution from the burning of solid fuels were related to 0.5% of all deaths (Norman, et al., 2007a) .

### 5. How does air pollution relate to climate change?

“Climate change and air pollution are inextricably intertwined” (Tibbetts, 2015). When it rains, air pollutants are washed out of the air through wet deposition and when there is evaporation of moisture from soil it has a cooling effect on the atmosphere

(Tibbetts, 2015). However, climate models project hotter and dryer conditions, including less moisture in soil, over South Africa (Personal communication Dr F Engelbrecht, CSIR). Higher temperatures and ultraviolet light leads to an increase in ozone levels at ground level. Although the sources of precursors for the formation of ozone are mainly found in cities, these precursors (which include nitrogen dioxide, volatile organic compounds and carbon monoxide) as well as ozone can travel hundreds of kilometres from source, affecting people in rural areas (Tibbetts, 2015).

Dry conditions and higher temperatures also increase the risk of veldfires, the smoke of which may contain more than 10 000 compounds (Tibbetts, 2015). It comes therefore as no surprise that emissions from veldfires are believed to be responsible for an annual number of about 340 000 premature (untimely) deaths globally (Tibbetts, 2015). The already-increased average temperatures recorded are associated with longer pollen-forming seasons, which may, in turn, increase the duration of the season for allergy-sufferers. In addition, as cooler areas are becoming warmer, plants that cause allergies may now also spread to these newly habitable areas. For example the American ragweed, a common allergen, can now also be found in areas of Europe (Tibbetts, 2015).

Another concern is that *in vitro* studies have shown when the relative humidity is high, nitrogen dioxide and ozone can react with certain types of pollen, modifying some of their proteins and in the process enhancing the allergic potential of the pollen (Tibbetts, 2015).

High atmospheric pressure over an area “traps” air pollution at ground level (Tibbetts, 2015), which could be one of the reasons why a higher incidence of heart attacks (one of the health effects of air pollution and specifically associated with particulate matter (Rich et al., 2013)) is recorded during such events (Tibbetts, 2015).

## **6. From climate change to responsible choices that will improve the health of the nation**

In the United States of America (USA) it was found that there is a huge knowledge gap between scientists and the general public around climate change and the threats of climate change (Weathers and Kendall, 2015). If that is the case in a first world country, why will it be any different in South Africa? As “climate change” is an intangible and abstract concept it is difficult to comprehend and relate to personal experience; rather it is seen as a vague global issue with huge uncertainty (Weathers and Kendall, 2015). In the USA it was also found that very few people thought climate change had any association with their health, until they were made aware of it, therefore the possible health effects of climate change are not even considered by the public

when making choices such as consumer’s choices (Weathers and Kendall, 2015).

The main reason for this phenomenon is two-fold. On the one hand in the USA media focus is on more critical national issues or dramatized news rather than climate change (Weathers and Kendall, 2015) and this may even be more the case in South Africa. For example in 2007/2008, a search of more than 2000 newspaper articles in the USA showed that less than 10% of them addressed health issues such as respiratory, and water and food-borne diseases. A similar survey in 2011/2012 showed that the number of climate change articles addressing public health dropped by 24% compared to the previous survey and those addressing respiratory, water, food and vector-borne diseases, remained below 10% but decreased even further in the second survey. Health effects that were addressed focused mostly on effects from extreme events such as heat waves and storms (Weathers and Kendall, 2015). On the other hand it is believed to be the manner in which information to the public is framed, namely as an environmental issue (with almost no visible link to public health) that affects areas, people and animals in far-away areas such as the Arctic (Weathers and Kendall, 2015).

If the public can be made aware of, not only the possible detrimental health effects of climate change but also the possible improvements in their health status when climate change is mitigated, or through adaptation measures, it will improve their knowledge on climate change and consequently their response. The public should know that the effects of climate change are not limited to hurricanes and sea level rise, which does not concern the general public in South Africa, but also include exacerbation of those illnesses and conditions familiar to the general public, such as asthma, allergies and food and vector-borne diseases (Weathers and Kendall, 2015).

Unpublished data from studies done by the CSIR showed that up to 56% of households tend to burn their refuse, thereby causing air pollution, even if it is collected on a regular (once a week) basis. In addition, the odds for having an upper respiratory illness was three times higher in those individuals living in households where refuse is burnt compared to those in households where this practice does not occur. The actions of the public are thus not only directly affecting their own health, but also contributing to climate change which is indirectly affecting their health.

As scientists we may think that our science should speak for itself as we are publishing in scientific peer-reviewed journals, which is read by other scientists and students. However, it must be kept in mind that it is expected of us to also publish popular articles and that we need to tell our stories in a way that will highlight the research, explaining it in way that tells people why they should be concerned (Davies, 2014).

In the USA it was found that people who understand climate change and its detrimental health effects are more supportive of climate change policies (Weathers and Kendall, 2015). Therefore, if the general public can relate climate change to possible personal health effects and how their daily activities may contribute to climate change, there is a much better chance for behavioural change and contribution to the mitigation of climate change (actions against the threat) (Weathers and Kendall, 2015).

## 7. Conclusion

Looking back, it is clear that the landscape or rather, the ‘airscape’ has changed since climate change has been brought into the equation. To collectively address the issue, it will be necessary to move away from merely disseminating science information, to addressing perceived needs, and towards developing the ability to understand, evaluate and evolve in response to these needs.

## Acknowledgements

Juanette John for valuable input and editing.

## 8. References

- Briggs, A.S.A., (1993). Victorian Cities. University of California Press. ISBN 0-520-07922-1.
- Brunekreef, B. and Holgate, S.T. (2002). Air Pollution and Health. *The Lancet* 360: 1233-42.
- Burnett, R.T., Pope, C.A. III, Ezzati, M., et al. (2014). An Integrated Risk Function for Estimating the Global Burden of Disease Attributable to Ambient Fine Particulate Matter Exposure. *Environmental Health Perspectives* 122 (4): 397-403.
- Davis, D.L., Bell, M.L. and Fletcher, T. (2002). A Look Back at the London Smog of 1952 and the Half Century Since. *Environmental Health Perspectives* 110(12): A734-75.
- Davies, B. (2014). Why is communicating Climate Change hard? *Bogology* Available: <http://bogology.org/2014/03/10/why-is-communicating-climate-change-science-hard/>
- Ellerbeck, R., Marinus, N. and Oosthuizen M.A. (1990). *Statistics on Smoke and Sulphur Dioxide Pollution in South Africa*. CSIR Report EMA-C 9020.
- Global Burden of Disease Report. (2010). Available: <http://www.thelancet.com/themed/global-burden-of-disease>
- Kemeny, E. and Vlegaar, C. (1983). *Statistics on Smoke and Sulphur Dioxide Pollution in South Africa*. ISBN 0 7988 2669 X.
- Krewski, D., Jerrett, M., Burnett, R.T., Ma, R., Hughes, E., Shi, Y., Turner, M.C., Pope, C.A. III, Thurston, G., Calle, E.E. and Thun, M.J. (2009). Extended Follow-Up and Spatial Analysis of the American Cancer Society Study Linking Particulate Air Pollution and Mortality.
- HEI Research Report 140. Health Effects Institute, Boston, MA.
- Lepeule, J., Laden, F., Dockery, D. and Schwartz J. (2012). Chronic Exposure to Fine Particles and Mortality: An Extended Follow-up of the Harvard Six Cities Study from 1974 to 2009. *Environmental Health Perspectives* 120 (8): 965-70.
- Department of Health (DoH). (1990). Information Brochure written by the Department for the Vaal Triangle Air Pollution and Health study. No number or author given.
- Murray, F. and McGranahan, G. (2003). Air pollution and Health in Developing Countries - The Context (In McGranahan, G. and Murray, F. (eds) *Air pollution & Health in rapidly developing countries* Earthscan London ISBN:185383985.
- Norman, R., Cairncross, E., Witi, J. and Bradshaw, D. (2007). Estimating the Burden of Disease Attributable to Urban Outdoor Air Pollution in South Africa. *South African Medical Journal* 97(8 Pt 2): 782-90.
- Norman, R., Barnes, B., Mathee, A. Bradshaw, D. (2007a). Estimating the Burden of Disease Attributable to Indoor Air Pollution from Household Use of Solid Fuels in South Africa in 2000. *African Medical Journal* 97(8 Pt 2): 764-71.
- Republic of South Africa, 1965. *The Atmospheric Pollution Prevention Act (Act number 45 of 1965)*. Government Printer, Pretoria.
- Rich, D.Q., Özkaynak, H., Crooks, J., Baxter, L., Burke, J., Ohman-Strickland, P., Thevenet-Morrison, K., Kipen, H.M., Zhang, J., Kostis, J.B., Lunden, M., Hodas, N. and Turpin, B.J. (2013). The Triggering of Myocardial Infarction by Fine Particles is Enhanced when Particles are Enriched in Secondary Species. *Environmental Science and Technology* 47: 9414-9423.
- Tibbetts, J.H. (2015). Air Quality and Climate Change A Delicate Balance. *Environmental Health Perspectives* 123(6): A148-A153
- WHO (World Health Organization) (2013). “Health risks of air pollution in Europe – HRAPIE” Project: Recommendations for Concentration–response Functions for Cost–benefit Analysis. Available: <http://www.euro.who.int/pubrequest>.
- WHO (World Health Organization). (2014). 7 million Premature Deaths Annually Linked to Air Pollution. Available: [http://www.who.int/mediacentre/news/releases/2014/air-pollution/en/?utm\\_source=health+care+without+harm&utm\\_campaign=8356d36629-hcwh+climate+health+news+april+4+2014+4+2014&utm\\_medium=email&utm\\_term=0\\_d34e902b88-8356d36629-82620853](http://www.who.int/mediacentre/news/releases/2014/air-pollution/en/?utm_source=health+care+without+harm&utm_campaign=8356d36629-hcwh+climate+health+news+april+4+2014+4+2014&utm_medium=email&utm_term=0_d34e902b88-8356d36629-82620853).

## Understanding of extreme temperature events by environmental health stakeholders in South Africa

J John<sup>1\*</sup>, RM Garland<sup>1,2</sup>, WA Landman<sup>1,3</sup>

<sup>1</sup>CSIR Climate Studies, Modelling and Environmental Health Research Group, Pretoria, South Africa;

<sup>2</sup>Climatology Research Group, Unit for Environmental Sciences and Management, North West University, Potchefstroom, South Africa; <sup>3</sup>Department of Geography, Geoinformatics and Meteorology, University of Pretoria, South Africa

### Abstract

The purpose of the work is to understand the potential need and use of extreme temperature forecasting products in the environmental health sector in South Africa by using an online questionnaire.

The majority of the 19 respondents agreed that industries and government currently do not have adequate heat-health action plans, with only one indicating that they had policies/plans in their work environment in the event of high temperature forecasts. However, 16 respondents would regard such a plan as useful.

Respondents did identify a need for a forecasting system but seem unsure about the range of capabilities that it can provide.

Keywords: Environmental Health, Climate, Weather Forecast, Practitioners

### Introduction

A changing climate can potentially have a large and negative impact on human health, especially in Africa where there are a large number of vulnerable people and an over-burdened healthcare sector (Confalonieri, 2007). In addition, the interior regions of southern Africa are projected to experience increases in temperature as great as 4-6°C under the A2 emission scenario, by the end of the century (Engelbrecht and Bopape, 2011). The warming atmosphere is expected to contribute to an increase in storms, floods, and other extreme weather events; thus scientists and meteorologists will need to rely more on advanced computing power (models) to develop medium-range forecasts that are accurate enough to save lives and property (Katz, 2015). Exposure to high ambient temperatures and heat waves can have large negative impacts on human health ranging from discomfort and fatigue, to heat stroke and death. Thus, the projected large increases in temperatures in Africa may lead to large negative health impacts. Also, temperature is also the easiest weather variable to predict; 'being more than 80% accurate if predicted 3-5 days in advance, moderately accurate (> than 60%) accurate, 5-10 days ahead, and a low degree of accuracy (40-60%) if predicted more than 10 days in advance' (Hughes et al., 2004).<sup>1</sup>

In order to mitigate the impacts of high temperatures on human health, many countries

utilize early warning systems and heat-health plans. The National Climate Change Response Plan has in fact highlighted the need for the creation of such plans. A key component of these plans includes weather forecasts, a tool that can be easily utilized by the health sector. Although under-utilised within public health, there is a growing recognition of the ability of weather forecasting to predict threats to health. (Hughes et al., 2004) The usefulness of these forecasts as a public health tool relies on the availability of accurate and timely information that is easily understood by the health sector and that is actionable. When developing forecasting products for early warning systems and heat-health plans, it is important to balance what metrics (i.e. maximum temperature) can be forecasted with certainty and what metrics are needed by the health sector.

In South Africa, the concept of forecasts, at weather and a seasonal scale is not well-understood by various sectors, including the health sector. This project surveyed environmental health researchers and practitioners about their potential need and use of extreme temperature forecasting products.

### Methods

An online questionnaire with 49 questions, developed through Google docs, was tailored to investigate and understand the potential current use and need of extreme temperature forecasting products in the environmental health sector in South Africa. Table 1 below highlights the topics that were covered in the questionnaire. The survey contained non-identifying questions about the respondents.

---

\* Tel 012 841 4189  
Email: jjohn@csir.co.za

Open-ended (5) and multiple choice (44) questions were used, of which 22 utilized a five-level Likert scale, ranking responses from strongly agree, agree, neither agree nor disagree, disagree to strongly disagree. Table 1 gives an overview of the types of questions and key variables, including the explored traits related to the perceptions of environmental health practitioners to the topics. The questionnaire was piloted before circulation. Ethics approval was granted by the CSIR Research Ethics Committee (Certificate Number: 71/2013).

Members of the Environmental Health Researchers Network (EHRN) were selected as study subjects, using a convenience sampling technique. The EHRN, developed in 2009, is a community of practice for those interested in environmental health research. The network includes researchers, Environmental Health Practitioners (EHPs) and government officials, at all levels, across South Africa. As participants in the group are working on and are interested in how the environment can impact human health in South Africa, it was deemed that they represent important health

stakeholders in the country that would be interested in using heat forecasts for health-planning purposes which could include the task of developing and implementing a heat-health plan or health early warning system. They were thus deemed to be appropriate subjects for the survey.

At the time during which the survey was circulated, the total membership of the network was ~143. As this number was tabulated in December 2013 and the survey was circulated in January 2014, it was assumed that the membership did not change significantly. The survey was circulated as an email through the EHRN listserv with the invitation to participate and the link to the survey. Participants who were not able to complete the online survey were sent an excel copy of the survey to complete. The survey was available online for one month and a reminder email was sent to the participants five working days before the closure of the survey. The results were captured into Excel and subsequently imported into Stata 13, a biostatistics package, for analysis. Tabulations, frequencies and contingency tables were used to analyse the data.

Table 1: Overview of survey topics and key variables

Overall topic	Variables	Question method
General information on respondent	Type of organization; Field of work; Years working in field; Location of work (by Province); Level of education	Categories
Perceived importance of heat on health currently and into the future	Currently receive weather warnings of extremely hot temp/ heat waves. Public/occupational health impacts from exposure to high temperatures currently not a problem <sup>1</sup> . Public/occupational health impacts not projected to be problem into the future <sup>1</sup> Knowing likelihood of above average temperatures occurring 1 wk-3 months ahead would aid to plan for preventing negative health impacts.	Binary (yes/no)  Likert scale
Current use of heat-health action plans	Industries/government currently have adequate heat-health action plans to protect workers/public. Set policies or plans in work environment to follow If high temp forecasted?	Likert scale  Binary (Yes/No)
Perceived need for heat-health action plans and early warning system	If none, would a set plan that would be tailored to your needs be useful in your opinion? How do you find out if high temperatures or heat waves are forecasted? How far in advance would you like to know if high temperatures or heat waves are forecasted?	Binary (Yes/No)  Categories (multiple responses)
Current use and perceived future needs for forecasting products	What sort of forecasted information related to heat-health would be most useful? What format would be most useful to display the forecasted information?	Categories (single response)
Feedback on example forecasting product	- helpful to show both "Observed" and "Forecasted" data as a comparison. - product would be useful in work if tailored for my area. - figure is confusing. - not helpful to see the historical data. - easy to understand main message of the figure.	Likert scale

<sup>1</sup> Used to derive Likert score "perceived heat-health score"

## Results and Discussion

A total of 19 responses were received; 16 of which were submitted electronically and three through an Excel version via email, corresponding to a 13% response rate. Demographics of the participants indicated the predominant field of work as environmental health, with most of the respondents (12) from government, with their place of work representing five provinces. The years in the field varied between 1 and 34 years, with 21% having 7 years or less experience. Almost half of the respondents (8) had post-graduate training.

### Perceptions of heat and health and impact

Only seven respondents indicated that they currently receive warnings of extremely heat and heat waves. However, 11 respondents indicated that they know someone whose health had been affected by high temperature. Most respondents disagreed that public and occupational health impacts from exposure to high temperatures are not or will not be a problem in future (Table 2). As the combination of these four questions measured the underlying characteristic regarding the perception of heat-health impacts, the scales were combined into a Likert score (or 'heat-health perception score'). This score (see Table 3) indicated that more than half of the respondents believed that health impacts from exposure to high temperature are currently and will be a problem in future.

Table 2: Responses to statements on health impacts from exposure to high temperatures.

Statement	Response		
	Agree <sup>1</sup>	Neutral	Disagree <sup>1</sup>
a. Public health impacts currently not problem.	1	2	16
b. Occupational health impacts currently not problem.	2	1	16
c. Public health impacts not problem in future	4	5	10
d. Occupational health impacts not problem in future.	5	1	13
"Heat-health perception score" (comb a-d)	1 (0-10) <sup>2</sup>	7 (11-15) <sup>2</sup>	11 (16-20) <sup>2</sup>

<sup>1</sup> combined strongly and somewhat      <sup>2</sup> score sum

### Policies and plans on heat-related health

Fourteen respondents agreed that industries in general currently have adequate heat-health action plans to protect their workers from extremely high temperatures and heat waves, while nine

respondents agreed that government currently have such plans to protect the public. However, only one respondent indicated that there were in fact set policies or plans in their work environment that must be followed in the event of high temperatures being forecasted with 12 indicating that there were not (six did not know). Nonetheless, 16 respondents were of the opinion that a set plan, tailored to their needs would be useful. Some aspects deemed useful for such a plan include:

- Information on expected symptoms and awareness-creation of health impacts of high temperature.
- Regulation of working conditions to protect employees against the effects of high temperature, including the average time to be spent in a very hot environment, measures to prevent and treat heat-related symptoms, availability of resource for hydration and sun protection.
- Procedures to follow in the case of an event to be aligned to current health and safety plan.
- Short and long-term action points, including reporting of incidents.

### Knowledge and use of forecasting products and information: weather and seasonal time-scale

Nine respondents agreed that seasonal forecasts providing information on the likelihood of extremely high temperatures would be helpful. Eight of the 10 respondents who agreed that knowing one week or more ahead would aid in planning to prevent negative health effects, indicated a temperature range as being the most useful forecasted information related to heat-health, followed by temperature scale linked to possible health outcomes at each scale (7). Most respondents who preferred to know one week or more ahead indicated that they would use either TV (8) or radio (7) as means to get forecasts.

Eight respondents indicated that a map will be most useful for presenting forecasted information. An action or piece of advice and a table was the least preferred formats.

An example of a forecasting product for a South African town were included in the questionnaire (Fig. 1). This figure showed percentage of days "observed" and "forecasted" where the maximum temperature is expected to exceed different temperature thresholds (x-axis) for the October-December season. The "observed" values were historical, multi-year average of measured maximum temperatures in the town for previous seasons. This provided an indication of what the distribution of temperatures is on average in the town during the October-December season. The "forecasted" values were from a forecast created

for an upcoming season three months before the start of the season (i.e., the forecast was created in July for the period of October –December). , followed by statements on its usefulness. Respondents were then asked to respond to statements relating to the figure. Responses to these statements are shown in Table 3.

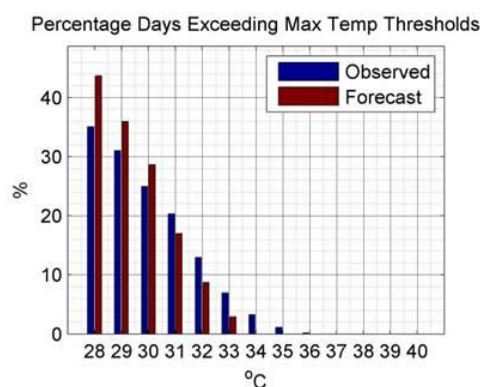


Figure 1: Example of a forecasting product comparing days “observed” (previous seasons) and “forecasted” (upcoming season) where the max temperature is expected to exceed different temperature thresholds.

Table 3: Responses to statements on the usefulness of the example forecasting product.

Question	Statements	No of Responses
Feedback on usefulness of example forecasting product (somewhat or strongly agreed)	- Show “Observed” and “Forecast”	13
	- Useful in work if tailored	15
	- Figure not confusing.	10
	- Helpful to see historical data	9
	- Easy to understand message	10

One of the main points from the survey was that people were interested in forecasting material, including on a seasonal scale, but did not actually understand what was possible – e.g. they want to know on day x three months in future the temp will be Y. It was also indicated that the product should be readily available without subscription or a fee.

This survey tested the knowledge of and perceived need in the health sector for forecasting products of extreme temperatures with different lead times that could aid this sector in their development of heat-health action plans and policies. The response rate was very low. There seems to be a perception that both government and industry have adequate heat-health plans in place. No set policies or plans are in place in the work environment to deal with forecasted high temperatures, or if these do exist,

the level of awareness about them was very low. Most respondents indicated that they would find both a tailor-made set plan, as well as information on the likelihood of extreme temperatures useful, pointing to the need for timeous information that could be applied by professionals in the health sector.

Weather forecasting techniques have the potential to contribute to timely public health information and to the achievement of adequate access and care, and combined, may reduce levels of mortality and health inequalities caused by weather variability. An improved understanding of the relationships between weather and health, together with appropriate transmission tools can assist in predicting and communicating the public health impact of future climate change.

## References

- Betts, K. and Sawyer, K. (2015). Modeling the health risks of climate change: Workshop summary. National Research Council. National Academies Press, Washington, DC. Available: <http://www.nap.edu/catalog/21705/modeling-the-health-risks-of-climate-change-workshop-summary>
- Confalonieri, U., Menne, B., Akhtar, R., Ebi, K.L., Hauengue, M., Kovats, R.S., Revich, B. and Woodward, A. (2007). ‘Human health’ Climate Change 2007: Impacts, adaptation and vulnerability. In Parry, M.L., Canziani, O.F., Palutikof, J.P., van der Lindern, P.J. and Hanson, C.E. (Ed.) Contribution of Work Group II to the Fourth Assessment Report of the Intergovernmental Panel on Climate Change, Cambridge University Press, Cambridge, UK, p. 391–431. Available: [https://www.ipcc.ch/publications\\_and\\_data/ar4/wg2/en/ch8.html](https://www.ipcc.ch/publications_and_data/ar4/wg2/en/ch8.html)
- Engelbrecht, F. and Bopape, M.J. (2011). High resolution projected climate futures for southern Africa. In *27th Annual Conference of South African Society for Atmospheric Sciences: The Interdependent Atmosphere, Land and Ocean*, 22–23 September 2011, Hartbeespoort, North-West Province, South Africa.
- Hughes, S., Bellis, M.A., Bird, W. and Ashton, J.R. (2004). Weather forecasting as a public health tool. Available: <http://www.cph.org.uk/wp-content/uploads/2012/08/weather-forecasting-as-a-public-health-tool.pdf>
- Katz, C. (2015). As extreme weather increases, a push for advanced forecasts. Available: [http://e360.yale.edu/feature/as\\_extreme\\_weather\\_increases\\_a\\_push\\_for\\_advanced\\_forecasts/2845/](http://e360.yale.edu/feature/as_extreme_weather_increases_a_push_for_advanced_forecasts/2845/)